NONDESTRUCTIVE TESTING OF REINFORCED CONCRETE BRIDGES USING RADAR IMAGING TECHNIQUES

By Dryver Huston, Peter Fuhr, Ken Maser, and William Weedon

Prepared for
The New England Transportation Consortium
July 1, 2002

NETCR19 Project No. 94-2

TECHNICAL REPORT DOCUMENTATION PAGE

1. Report No. NETCR 94-2	2. Government Accession No. N/A	3. Recepient's Catalog No. N/A
4. Title and Subtitle Nondestructive Testing of Reinforced Concrete Bridges using Radar Imaging Techniques		5. Report Date July 1, 2002
		6. Performing Organization Code N/A
7. Author(s) Dryver Huston, Peter Fuhr, Kenneth Maser, William Weedon		8. Performing Organization Report No. NETCR 94-2
9. Performing Organization Name and Address Department of Mechanical Engineering College of Engineering & Mathematics University of Vermont Burlington, VT 05405-0156		10 Work Unit No. (TRAIS) N/A
		11. Contract or Grant No. N/A
12. Sponsoring Agency Name and Address New England Transportation Consortium 179 Middle Turnpike University of Connecticut, U-5202 Storrs, CT 06269-5202		13. Type of Report and Period Covered Final Report
		14. Sponsoring Agency Code NETC 94-2 Nondestructive Testing of Reinforced Concrete Bridges using Radar Imaging Techniques
15 Supplementary Notes N/A		

16. Abstract

The goal of this project was to examine the critical issues related to the use of GPR in the inspection of concrete bridge deck roadways. The research included: 1. The state of the assessment of GPR inspection of concrete roadways. 2. Numerical modeling of GPR interactions with concrete. 3. Laboratory tests of GPR interactions and inspection of concrete in 0.5 to 6 GHz range. 4. Field tests of GPR inspection of concrete including the use of a handheld system. 5. Recommended specifications for a field test system.

17. Key Words ground penetrating radar, GPR, bridges, inspection, concrete, pavement, nondestructive evaluation, NDE	18. Distribution Statement No restrictions. This document is available to the public through the National Technical Information Service, Springfield, Virginia 22161.		
19. Security Classif. (of this report) Unclassified	20. Security Classif. (of this page) Unclassified	21. No. of Pages 182	22. Price N/A

Form DOT F 1700.7 (8-72) Reproduction of completed page authorized

2. ACKNOWLEDGEMENTS

Many people and organizations contributed to the completion of this project. The authors of this report are extremely grateful for their help. The University of Vermont graduate students Chris Adam and Jing Qiong Hu conducted a large portion of the experimental and numerical tests reported here. Other contributors from the University of Vermont were Peter Bergendahl, Brian Esser, Aaryn French, Xuling Luo, Xun-Sha Ma, Noel Pelczarski, Victor Rossi, Xiangdong Zhao, and Jason Zietz. Dr. John Aurand of the Sandia National Laboratories provided considerable assistance in antenna design and in the understanding of electromagnetic principles. J.B. McCarthy and Shauna Clifford of the Vermont Agency of Transportation provided access to roads for testing. William Payne of Concorr, Inc. demonstrated their bridge inspection system, which aided our research efforts. The New Hampshire Department of Transportation provided access to an interstate bridge.

3. TABLE OF CONTENTS

4. LIST OF FIGURES

5. LIST OF TABLES

6. SUMMARY

The goal of this project was to examine the critical issues related to the use of GPR in the inspection of concrete bridge deck roadways. The project involved numerical, laboratory and field studies of GPR interactions with reinforced concrete roadways. Some of the key results are:

1. *The state of the art in GPR inspection of concrete roadways was examined.* This included an identification of damage mechanisms in concrete, and the various associated evaluation techniques. The conclusion of the survey was that GPR is a potentially powerful method of bridge deck inspection, but that the technology needs some more development before it can be used.
2. *Numerical modeling* – Numerical 1-D and 2-D models indicated that GPR waves can potentially reflect subsurface cracks and air-filled delaminations.
3. *Laboratory tests* – The results of the laboratory tests were that subsurface air-filled delaminations could be identified with a 0.5 – 6 GHz system, and that a 0.5 – 20 GHz system would work even better, when the penetration depth was sufficient.
4. *Field tests* – Various versions of the system was tested several times on local bridges, retaining walls and columns. Subsurface rebars could be identified. Delaminations were identified based on weak rebar reflections and were correlated with hammer tap results.
5. *Recommended specifications* for a field test system have been formulated. New FCC regulations on ultrawideband instruments will have to be incorporated in all new systems.

7. INTRODUCTION

7.1 OVERVIEW

The overall goal of this project was to advance the state-of-the-art in GPR techniques so that it can become a more practical and reliable tool for assessing the integrity of reinforced concrete bridge decks, with particular attention directed towards the specific problems of the bridges in New England. This project was conducted with funding by the New England Transportation Consortium (NETC) Project 94-2 “Nondestructive Testing of Reinforced Concrete Bridges Using Radar Imaging Techniques.” The project involved numerical, laboratory and field studies of GPR interactions with reinforced concrete roadways.

A multidisciplinary team of investigators with experience in GPR, electromagnetics, structural engineering and scientific instrument development, from the University of Vermont and consultants from Massachusetts worked on the project. The investigators from the University of Vermont included Professors Dryver R. Huston and Prof. Peter L. Fuhr and several graduate and undergraduate students. The Massachusetts-based investigators were Dr. Kenneth Maser of Infrasense, Inc. and Dr. William Weedon of Applied Radar, Inc.

The overall result of the project was that most of the proposed objectives were met. A working high-frequency (0.5 – 6.0 GHz) system was built and tested on damaged and undamaged slabs in both the laboratory and the field. Damage in the form of thin air-filled delaminations and accelerated corrosion was identified in the laboratory. The field results are a little less certain because of the unknown state of the underlying roadway. The state of the art for GPR has advanced considerably in the past several years. Some of the modern imaging techniques show promise for routine use in GPR surveys of bridge decks. It is recommended that future GPR systems for roadways operate at frequencies above 2 GHz and that they include synthetic aperture radar imaging techniques.

7.2 SIGNIFICANCE OF PROBLEM

The bridge infrastructure of the United States is distressed. The United States Department of Transportation estimated in early 1994 that as many as 40% of the total number of bridges in this country are structurally deficient, with repair costs estimated in the billions of dollars (Smith, 1995; and Halabe et al. 1995). The leading cause is the deterioration of the bridge deck. Deterioration is due primarily to two mechanisms: 1) Freeze/thaw damage to the concrete (punky concrete), and 2) Corrosion-induced delamination resulting from infiltration of chlorides introduced by winter road salting operations or by ocean spray. Unfortunately, bridge deterioration – including rebar corrosion, delaminations and disintegrating concrete – is often hidden under an asphalt overlay (Maser and Kim Roddis, 1990). Efficiently managing maintenance activities for bridge decks requires tools that can assess the integrity or state of deterioration. One of the major problems with concrete deterioration is that its severity and extent is difficult to assess. The mechanisms of deterioration occur below the surface, and their manifestations are not readily seen in visual inspections. Consequently, agencies are forced to program, prioritize, and set budgets for the repair and replacement of many structures whose conditions are virtually unknown. This has led to "surprises" during construction, and to cost overruns and excess repairs.

Current techniques for condition assessment are slow, labor intensive, intrusive to traffic, and do not produce an accurate estimate of the quantity of deteriorated concrete. These techniques, which include core sampling, corrosion (half-cell) potentials, and chloride ion measurements, are well documented (NCHRP, 1979). Corrosion potentials and chloride ion measurements infer corrosion, but do not address unseen freeze/thaw damage. A more reliable technique, the chain drag, does not work with either asphalt overlays or in heavy traffic conditions with high ambient noise. Alternative non-destructive evaluation (NDE) techniques offer the possibility of more efficiently and effectively assessing the state of a bridge deck.

To date, however, NDE measurement methods have not been widely adopted. The reasons for this are twofold: 1. The state-of-the-art has not been developed to the point where the techniques are routinely implemented in the field; and 2. There has been a lack of well planned and thought out programs to obtain the kind of basic measurements and theory that are essential to evaluating proposed non-destructive techniques (Al-Qadi et al., 1995b). Since NDE is a powerful tool in assessing the performance and characteristics of constructed facilities, the development and implementation of an accurate and widely accepted non-destructive method of assessment is desirable.

GPR is one of several NDE methods for bridge decks that has been proposed and tested over the last couple of decades. One of the potential advantages of GPR is that it is able to analyze a bridge deck rapidly without having to contact the slab. This enables configuring a test system that can evaluate bridge decks with a minimal disruption to traffic.

7.3 BRIDGE DECK DAMAGE MECHANISMS

The leading cause of deterioration in reinforced concrete bridge decks is believed to be a progressive breakdown that begins with the application of deicing salts and harsh environmental and loading conditions and ends with the disintegration of the roadway. The intermediate steps are: 1. The diffusion of chloride ions, from these chemicals, into the concrete. 2. Once the chloride ions penetrate to the rebar surface, they break down the passive iron oxide film that normally protects the steel. 3. The breakdown of the passivation layer enables rebar corrosion to initiate. 4. As rebar steel corrodes, it expands, sometimes with an increased volume ratio of five. 5. The expansion of the corroded rebar steel causes tensile forces in the concrete, which, in turn causes cracks in the concrete. 6. The appearance of cracks in the concrete promotes further chloride ion, water and oxygen penetration to the rebars, which accelerates the corrosion process. 7. The corrosion and cracking process continues with end result being the formation of large cracks, commonly referred to as delaminations. The delaminations often run horizontally in the bridge deck from rebar to rebar, but eventually emerge at the surface in the form of large spalls, or potholes (Joyce, 1984; Manning and Holt, 1980; and Escalante et al. 1984).

In colder states, such as those in New England, the condition of concrete disintegration due to cycles of freezing and thawing appears to be as prevalent as delamination due to rebar corrosion (Maser, 1989). Concrete disintegration caused by freeze thaw damage to the cement matrix is known as scaling, and reduces the concrete to a gravely matrix which may contain either air or water (Maser and Kim Roddis, 1990; and (Maser and Kim Roddis, 1990; and Carter et al., 1986). In this mode of disintegration, moisture accumulates within the bridge deck. As the moisture freezes it expands. When the tensile force due to this expansion exceeds the tensile strength of the concrete cracking occurs. This leads to a "waterfall" effect in which the cracks grow, allowing them to retain more water that causes them to grow more. Subsurface moisture may also cause delamination between pavement layers, allowing heavy traffic to dislodge chunks of surface pavement from the weakened road, resulting in the condition referred to as spalling (Smith,1995).

7.4 COMMONLY-USED EVALUATION PROCEDURES

Existing procedures for analyzing the condition of concrete bridge decks require a thorough visual inspection, supplemented by physical testing that includes a chain drag survey and the measurement of electrical potentials and possibly coring.

7.4.1 CHAIN DRAG

The chain drag is the traditional method of identifying delaminations in exposed concrete bridge decks. It has proven useful in locating delaminations in the medium and severe stages of development (Manning and Holt, 1984; and Joyce, 1984). This procedure is based on identifying the distinctly different sounds that emerge from a bridge a bridge deck as a set of chain links are dragged across the surface, depending on whether the underlying surface is delaminated or intact. Unfortunately, the chain drag technique is only useful when the deck does not have an asphalt overlay or when the asphalt has been removed as the first step in the repair process. The chain drag technique is also difficult to use in noisy environments, such as that due to nearby heavy traffic.

7.4.2 CORING AND VISUAL INSPECTION

Visual inspection of the bridge deck as a whole may also be conducted to assess deterioration. This type of inspection can reveal cracking and other surface distresses as well as areas of whitish staining (efflorescence) and rust stains on the underside of the deck (Maser, 1989). It was found that surface distresses do not necessarily indicate subsurface deterioration, however, areas where staining has occurred are usually indicative of scaling and delamination.

The visual inspection and strength testing of cores, in addition to the visual inspection of the entire deck, is a highly accurate means of assessing delamination, scaling, and debonding (Manning and Holt, 1980). The method is limited by being slow and labor intensive. Core samples of the bridge deck can be tested for strength, chloride and air content, as well. Maser (1989) reported, however, that there is no significant correlation between chloride content and percent deterioration due to the fact that chloride content measurements are generally too few and not representative of the overall conditions.

7.4.3 HALF CELL

The half cell technique is an electrochemical method that measures the presence of corrosion activity by creating an electrochemical cell between a rebar and a concrete surface (Scannell et al. 1996). The method can be quite effective if the corrosion is actively underway during the test. The method has difficulty detecting corrosion that has already occurred, but is now in a passive state.

7.4.4 ULTRASOUND

Ultrasonic techniques utilize the propagation of high frequency acoustic waves within the material to identify distressed areas of concrete (Manning and Holt, 1980 and 1984) Ultrasound works well for the characterization of certain homogeneous media, such as steel, or those with favorable transmission and scattering characteristics, such as soft tissue in the human body. Unfortunately, the high levels of absorption and scattering in concrete, along with the requirement of directly coupling the ultrasound transducer to the roadway, makes ultrasound an impractical alternative for NDE testing of concrete decks.

7.4.5 IMPACT ECHO

Impact echo testing involves sending transient stress waves into a test object by mechanical impact and monitoring displacements caused by the arrival of reflected waves from internal defects and external boundaries (Sansalone and Carino, 1988). Using this method, it is possible to determine the depth of the asphalt concrete overlay as well as the location and depth of delaminations (Sansalone and Carino, 1989). Impact-echo testing is relatively slow, requires good contact between the source/receiver and the surface being tested, and requires careful control and tuning of the impact pulse parameters for it to work. As a result, impact-echo testing is relatively impractical for concrete bridge deck testing.

7.4.6 RADIOGRAPHY

Radiography is the technique of obtaining a shadow image of a solid object using penetrating radiation such as x-rays or gamma rays (γ-rays) (Cartz, 1995). Radiography offers several advantages as a non-destructive method of evaluation, including high penetration depth and internal feature resolution. Despite these advantages there are several drawbacks which hinder the use of radiography for the assessment of bridge decks including the geometric problem of having to be positioned on opposite sides of the bridge deck and obvious safety problems.

7.4.7 INFRARED THERMOGRAPHY

Infrared thermography attempts to detect features underlying the surface of an object, such as a delamination, based on measuring subtle temperature differences on the surface. Under the appropriate circumstances of surface conditions, and solar heating, infrared thermography is an effective tool for identifying underlying delaminations. However, it is difficult to consistently obtain the ideal conditions in the field that are necessary for the procedure to work.

7.4.8 GROUND PENETRATING RADAR

Radar is the electromagnetic analog to ultrasound, and it has four properties which make it very practical for non-destructive testing of reinforced concrete: (1) the ability to penetrate dielectric materials (e.g. concrete) (2) reflection from conducting bodies (e.g. steel rebars) and interfaces (3) polarizability of the microwave signal (4) relatively small wavelengths which render small probe sizes (Maser, 1989; and Zoughi et al. 1991). GPR has the ability to evaluate the properties of materials composed of a mixture of several constituents, and radar technology offers the capability of collecting data at highway speeds (Maser, 1990; Sansalone and Carino, 1989).

The data that are gathered from a GPR system can be quite complex. Processing and interpreting the data can be a formidable challenge. A variety of data processing techniques have been developed to aid in the interpretation of the data. These range from color and graphical enhancements of the plots of the raw data (Russ, 1999; Hunt et al. 2000) to reflection measurements (Saarenketo and Roimela, 1998) to complex systems that use synthetic aperture radar techniques that reconstruct underlying features from the data (Johansson and Mast, 1994a).

A second barrier lies in the inherent limitations of commercially available radars used for bridge deck and other civil engineering applications. Maser (1989) reported that because these radar systems operate at wavelengths on the order of 10cm (frequency of 1GHz) in concrete, as seen in Table 8.2, small (~1mm) air-filled delaminations are not directly detectable by radar. However, it has been found that these cracks are detectable if they and the adjacent concrete are filled with moisture, or if the properties of the concrete abruptly change in going from above to below the delamination. Since a large number of delaminations are small air filled cracks, detection presents a dilemma which is as challenging as that of data processing, and must be over come in order to create an accurate means of bridge inspection.

7.5 PREVIOUS NETC GPR PROJECT

In recognition of the need for further development of GPR techniques for bridge deck assessment, the NETC initially sponsored a program carried out by the Massachusetts Institute of Technology (MIT) from 1986 to 1990 to investigate the potential of new technology for asphalt overlaid bridge decks. The specific objective of this first NETC program was to investigate two new technologies for bridge deck assessment – Ground Penetrating Radar and Infrared Thermography. The approach was to conduct Radar and Infrared surveys on a group of asphalt-overlaid decks that were scheduled for maintenance. During maintenance, the asphalt was removed and the concrete surface observed and chain-dragged to determine deterioration quantities for removal. These quantities were correlated with the predictions from the radar and infrared surveys.

These field correlations were carried out on 28 decks in the New England area. The field study was complemented by theoretical studies (Maser, 1990) and by laboratory studies on deck slabs recovered from the field. The results of this study led to the establishment of a radar-based technique that produced accurate correlations with observed deterioration. Analysis techniques were developed for the prediction of concrete deterioration from variations in the concrete dielectric constant as computed directly from the radar waveforms. The computation was used to predict overall deterioration for each deck and each major span. This prediction was then correlated with the actual deck deterioration determined when the asphalt overlay was removed, and the bare concrete was visually examined and chain dragged.

The results for this first NETC project were limited to estimation of total quantities of deteriorated concrete for asphalt overlaid decks. The techniques developed during this project were based on overall deck averages, and were not able to clearly identify the location or the severity of the deterioration. Also, the techniques developed were limited to asphalt overlaid decks.

The project described here focuses on advancing the state of the art of GPR for concrete evaluation. The advances are based on (a) an improved understanding of the electromagnetic properties of concrete; (b) advances in signal processing; and (c) advances in radar antenna equipment. These advances can derive from a number of sources. For example, the first NETC program stimulated a wide range of GPR research efforts within different universities that have subsequently produced significant results. Also, similar research has been independently pursued by other agencies such as the Ontario Ministry of Transportation and the Strategic Highway Research Program. Finally, other organizations specializing in electromagnetic wave theory and technologies have taken a greater interest in applying their know-how to the infrastructure area.

7.6 DESCRIPTION OF PROPOSED RESEARCH PROGRAMS

In response to the request for proposals from the New England Transportation Consortium entitled “94-2 Nondestructive Testing of Reinforced Concrete Bridges Using Radar Imaging Techniques,” the UVM project team proposed the items described in the remainder of this section.

7.6.1 PHASE I - NUMERICAL MODELING

Electromagnetic models for the propagation of radar waves within concrete are to be used to predict the fundamental properties of the radar waveform and the potential bases for creating images from these waveforms. This work is primarily an adaptation of existing numerical models to the particular needs of this research program. Models have already been developed for this purpose by other researchers (Halabe et. al., 1989; Chew, et. al., 1994). These numerical models are available to the research team.

One key question in the use of waveform or imaging models is the determination of the electromagnetic representation of the materials being modeled. Deterioration (e.g., delamination, chloride contamination, freeze-thaw damage, debonding, etc.) and other ordinary concrete and asphalt properties must be represented by material dielectric properties and by geometric discontinuities. Other researchers (Halabe, et. al., 1993), have already developed analytic models of dielectric properties. Experimental work has also been carried out (Zoughi, *et. al*, 1995) and is ongoing to relate concrete dielectric properties to more familiar material. These physical properties are to be used to develop input into the numerical modeling to be carried out under this phase of the work.

A series of numerical parameter studies are to be carried out using the available models and material characterizations described above. The objective is to quantify changes in the GPR signal response as they are related to concrete material property changes. A second consideration in these studies is the characteristics of the input antenna signal. The goal is to determine the antenna characteristics that are most effective in revealing the concrete properties of interest.

7.6.2 PHASE II - DESIGN AND CONDUCT OF LABORATORY EVALUATIONS

The results of the numerical modeling of Phase I are to be verified and evaluated with laboratory measurements on concrete specimens in which various forms of deterioration have been induced. Laboratory specimens are to be fabricated of sufficient size to be evaluated by radar, and yet be sufficiently small to be exposed to and affected by simulated forces and effects of the external environment. Three major environmental exposures will be considered: moisture and chloride intrusion, freezing and thawing, and corrosion of reinforcing steel. Accelerated rebar corrosion will be induced in laboratory concrete samples using inverse cathodic protection.

The data acquisition is to consider different antenna/sample geometries: for example: a) A *monostatic geometry*, in which the antenna will both transmit and receive radar pulses and echoes (most typically used in the field). The samples are to be placed directly below the radar antenna. The sample antenna distance is to be varied to determine the optimum sample antenna distance; and b) *A bistatic geometry*, in which two antennas are used, one transmitting pulses while the other receiving echoes. The added flexibility of using two antennas permits the study of oblique transmission and reflections angles. This arrangement allows reflection tomography, direct transmission and refraction measurements to be made.

Two types of equipment are available for these laboratory tests - commercial equipment and laboratory prototypes. The commercial equipment can be rented from Geophysical Survey Systems, Inc. They manufacture 1.0 and 2.5 GHz horn antennas that are potentially useful in this work. It is possible, however, that this equipment is not optimal for this project. Rather than be constrained by the limitations of current commercial equipment, the intent is to explore other types of antennas with more suitable properties.

7.6.3 DEVELOPMENT OF RADAR DATA PROCESSING SOFTWARE

One of the biggest problems preventing the routine use of GPR as a routine tool for pavement evaluation is that the waveforms can be complex and require highly-skilled personnel to interpret the waveforms. The main purpose of this phase of the project is to develop automated pattern and image processing techniques that are capable of classifying the waveforms so that they can be readily identified as corresponding to particular events, i.e. damage or deterioration in the concrete decks. The main feature in such an effort is to identify the physics and the actual form of the event signatures from both the numerical and laboratory studies of Phases I and II. Once the actual event signatures corresponding to particular concrete conditions are identified, then software can be written to automate the process. The actual form and structure of the image identification software will depend on the results of Phases I and II. Some of the algorithmic options include: heuristic if-then structures, neural networks, genetic algorithms and wavelet analysis. It is anticipated that this software development work will require considerable interaction with other phases of the project.

7.6.4 CORRELATION OF SOFTWARE WITH LABORATORY AND FIELD DATA

A necessary phase in the development of GPR techniques is to ascertain the level and the nature of the correlation between the numerical studies, laboratory data, and field data. Therefore, it is necessary to conduct field measurements of concrete conditions by both GPR and conventional techniques. The proposal request for this project (NETC 94-2) has specific requirements for the field testing. They are as follows:

1. **Radar Data Collection.** Structural reinforced concrete elements will be evaluated using the developed radar system. The elements to be evaluated are: columns, pier caps, wells (solid shaft walls and abutments), arches, unsurfaced concrete decks, and slabs with bitumen concrete and membrane waterproofing. The researcher shall execute a minimum of five (5) different tests for each element, which will be selected from a minimum of five (5) different sites. No more than two (2) radar scans shall be conducted for a particular element at any site. Sites may be selected by the proposer, subject to approval by the Technical committee or may be selected jointly with the Committee.

2. **Reference Data Collection.** The verification and correlation of radar results with true concrete condition shall be determined by a traditional analysis of each element analyzed in Part I above. True concrete condition may be determined by the following methods, including but not limited to: laboratory testing and cored samples; laboratory testing of slabs, on-site chain drag test; visual inspection of cored holes and external surfaces; hammer soundings; and half-cell measurements.

The proposed laboratory testing program should quantify the state of deterioration through the following parameters: compressive strength, permeability, moisture content, and chloride content. The proposed laboratory and field inspections shall quantify, at a minimum, the degree of microcracking, spalling, delamination, and rebar corrosion.

3. Verification and Correlation of Radar Analysis with Reference Lab/Field Data. Concrete condition data obtained through the radar system (Part 1) will be correlated with actual concrete material and strength properties derived in Part 2. The proposer shall analyze the relationship of the data to true concrete condition.

The next phase in the correlation process will be to evaluate the structural elements through the traditional methods of examining field conditions and core sections for microcracking, spalling, delamination, and rebar corrosion.

The data derived from the numerical, laboratory, and field studies are to be correlated to examine the validity of the GPR test procedures. This correlation study involves both an examination of the observability of physical phenomena under both field and laboratory conditions, and the modification, adaptation or calibration of the software that is necessary to create a reliable system for field use.

7.6.5 IMPLEMENTATION OF RESEARCH RESULTS

Phase V of this project will be to develop documentation so that the technology that is developed as part of the research program will be readily transferable to state highway agencies. This will involve the writing of a procedure manual and equipment manual for the study's findings. Other deliverables will include the concrete classification software developed, specifications for the radar system, and procedural manuals suitable for State transportation agencies to obtain proposals from testing firms.

7.6.6 PROJECT MANAGEMENT

The key personnel on this project are: 1. The Principal Investigator - Prof. Dryver Huston of the Mechanical Engineering Dept. at the University of Vermont; 2. Prof. Peter Fuhr of the Dept. of Electrical Engineering and Computer Science at the University of Vermont; 3. Dr. Kenneth Maser of Infrasense Inc., Arlington, MA; 4. Dr. William Weedon of the Center for Electromagnetics Research and Electrical and Computer Engineering; and 5. A graduate student and possibly some undergraduates from the University of Vermont.

The division of effort and responsibility on this project is as follows: 1. The Principal Investigator, Dr. Dryver Huston, will be responsible for the overall conduct and management of the project; 2. The laboratory studies and analyses will be conducted at the University of Vermont under the direction of Profs. Huston and Fuhr; 3. The numerical analysis and software development will be carried out at the University of Vermont's computer facilities. Dr. Weedon and Dr. Ken Maser will provide technical help in the software and algorithm development; 4. Investigators from the University of

Vermont will conduct the field testing, with the advice of Dr. Ken Maser, who has considerable expertise in the use of ground penetrating radar to evaluate highway pavements. 5. Report preparation - The contract requirements of quarterly reports and the staff at the University of Vermont will complete a final report. 6. Communication - All of the investigators are on the Internet so that email and electronic data and document transfer is readily available. A minimum of one face-to-face total group meeting of the team is planned per year. Additional meetings will be scheduled on an as needed basis.

7.7 MODIFICATIONS TO WORK PLAN

The major modification to the work plan was to develop a GPR system at UVM rather than rent one from GSSI. The advantages of this modification were: 1. The equipment would be available to the project investigators throughout the course of the project. The original plan of renting would have made the equipment available to the investigators for only one month during the project. 2. The frequency range of the UVM system is 0.5 – 6 GHz. This is higher than the 1 GHz centerband system available for rent. (A 2 GHz centerband system has recently become available for rent.) 3. Developing the system internally would create a better opportunity for a more thorough understanding of GPR systems. The disadvantages of developing a system at UVM versus renting one are: 1. It will take longer to put together; and 2. The system may not be as reliable or high-quality as the rented system. An unexpected disadvantage of building an in-house system was that contractual difficulties between UVM and NETC held up the purchase of the major instrument required for the system (HP 8753D Network Analyzer) for about a year. Based on the perceived advantages and disadvantages of building versus renting a GPR system, it was decided to build (assemble) one in-house.

7.8 PRIMARY RESULTS

The primary results of this project are that most of the project objectives were accomplished. Details about the project activities can be found throughout this report . A summary is listed below.

7.8.1 SURVEY OF THE STATE OF THE ART

Assessing the state-of-the-art in GPR inspection of roadways was a fairly major portion of this project. GPR is a moderately mature technology. Articles on GPR started to appear in open literature about three decades ago. The roots of radar technology can be traced to the early days of radio and aerospace. Most of the key developments have been closely held military secrets that gradually diffused into open literature. An excess of three hundred technical articles and reports specifically related to GPR were studied. In addition, to the literature survey, several conferences and trade shows on the nondestructive evaluation of materials and GPR were visited.

The main results of the literature survey were that it was determined that GPR is capable of determining bulk properties of concrete. Under the appropriate circumstances, GPR can be used to identify features, such as rebars and pavement layer depths. Reliably detecting the condition of the pavement and identifying air-filled delaminations has not been consistently demonstrated. In addition, it was determined that the commercial GPR field is highly fragmented, with a variety of incompatible systems that all have proprietary software and hardware.

7.8.2 NUMERICAL STUDIES

Numerical studies were conducted in an effort to simulate the interactions of GPR waves with bridge decks. The primary purpose of these studies was to examine the theoretical capability of GPR systems to identify and interact with subsurface features. The simulations involved both 1-D and 2-D models. The 1-D models showed that it is possible to detect small 1 mm thick air-filled delaminations. The 2-D models showed that the signals can be sensitive to the height of the antenna, and rebar placement.

7.8.3 LABORATORY TESTS

A series of laboratory tests were conducted to evaluate the performance of various radar system and component designs and to evaluate various effects, such as those resulting from simulated and real damage to concrete, on reflected and transmitted radar signals. The bulk of the results of the laboratory tests are described in Chapter 8, and in Adam (1997), Hu et al. (1999), Hu (2000), and Huston et al. (1997, 1998, 1999a, 1999b).

The primary results of the laboratory studies are:

1. High-frequency, wide-band (0.5-6 GHz or 0.5-20 GHz) antennas can be built out of inexpensive components.
2. The 0.5-6 GHz system can penetrate through several inches of concrete and through a 50 mm thick asphalt overlay.
3. Embedded Styrofoam simulated defects can be located.
4. 1 mm thick air-filled delaminations can be identified.
5. Corrosion produces measurable effects.
6. Freeze-thaw testing produced a decrease in dielectric constant.

7.8.4 FIELD TESTS

The results of the field tests of bridge decks were:

1. Several bridges were tested. These included:
   a. A thick concrete bridge deck under construction in Milton, VT
   b. A distressed bridge deck on Bostwick Rd. in Shelburne, VT
   c. A relatively new and undamaged bridge deck on Turkey Lane in Hinesburg, VT
   d. An interstate highway bridge deck on I-89 near Sunapee, NH undergoing rehabilitation before and after the removal of an asphalt overlay
   e. The concrete column of an interstate overpass bridge for I-189 on Spear St. in South Burlington, VT
   f. The concrete retaining wall of an interstate overpass bridge for I-189 on Farrell St. in South Burlington, VT.

2. Features under the deck, such as rebars, can be detected. However, imaging through bare concrete is easier.
3. The magnitude of the initial reflected pulse, i.e. the dielectric parameter of the top surface can be used as an indication of the overall quality of the concrete. However, it does not seem to be a good indication of delaminations.
4. The degradation of the return signals from the rebars correlated well with delaminations.

7.8.5 SOFTWARE

A software system was developed to control the GPR system, collect the data, and present the data in real time in a B-scan format. Imaging software using migration or synthetic aperture radar methods appears to be a promising technique.

7.8.6 RECOMMENDED SYSTEM

A set of performance specifications and a generic recommended system have been developed. New FCC regulations governing GPR systems have been summarized.

8. PRINCIPLES OF GROUND PENETRATING RADAR

8.1 OVERVIEW OF OPERATING PRINCIPLES

GPR operates by transmitting high-frequency electromagnetic waves into pavement using an antenna attached to a survey vehicle. The waves are reflected back to the antenna with an arrival time and amplitude that is related to the location and nature of dielectric discontinuities in the material (air/asphalt or asphalt/concrete, reinforcing steel, etc.). The reflected energy is captured, processed and displayed in a manner that illuminates the underlying dielectric properties of the pavement, which are an indication of the properties of the pavement. Figure 8.1 indicates how an electromagnetic wave can reflect off of features inside a bridge deck and be indicated in the reflected waveform. Table 8.1 contains the typical frequencies of GPR and standard radar bands. Table 8.2 lists wavelengths that are typically encountered in the use of GPR in various media.

BAND	FREQUENCY RANGE	PRINCIPAL APPLICATIONS
HF	3 - 30 MHz	Over-Horizon Radar
VHF	30 - 300 MHz	Long-range Search
W	0.3 - 6000 MHz	Ground Penetrating Radar
UHF	0.3 - 1 GHz	Long Range Surveillance
L	1 - 2 GHz	Long Range Surveillance
S	2 - 4 GHz	Air Traffic Control
C	4 - 8 GHz	Instrumentation Tracking
X	8 - 12 GHz	Air-to-Air Missile Seeker
Ku	12 - 18 GHz	Remote Sensing
Ka	27-40 GHz	Weapon Guidance (Remote)
V	40-75 GHz	Weapon Guidance (Remote)
W	75-110 GHz	Remote Sensing Guided Weapons

Table 8.1 Standard radar frequency bands.

The interactions of electromagnetic waves with physical media can be quite complex. In an effort to gain an understanding of these interactions, a wide variety of approximate theories have been developed, each of which works quite well under the appropriate circumstances. The most exact models known for electromagnetic interactions use quantum mechanics (Feynmann, 1977). At the moment, there are very few, if any, situations where the power and complexity of quantum mechanics

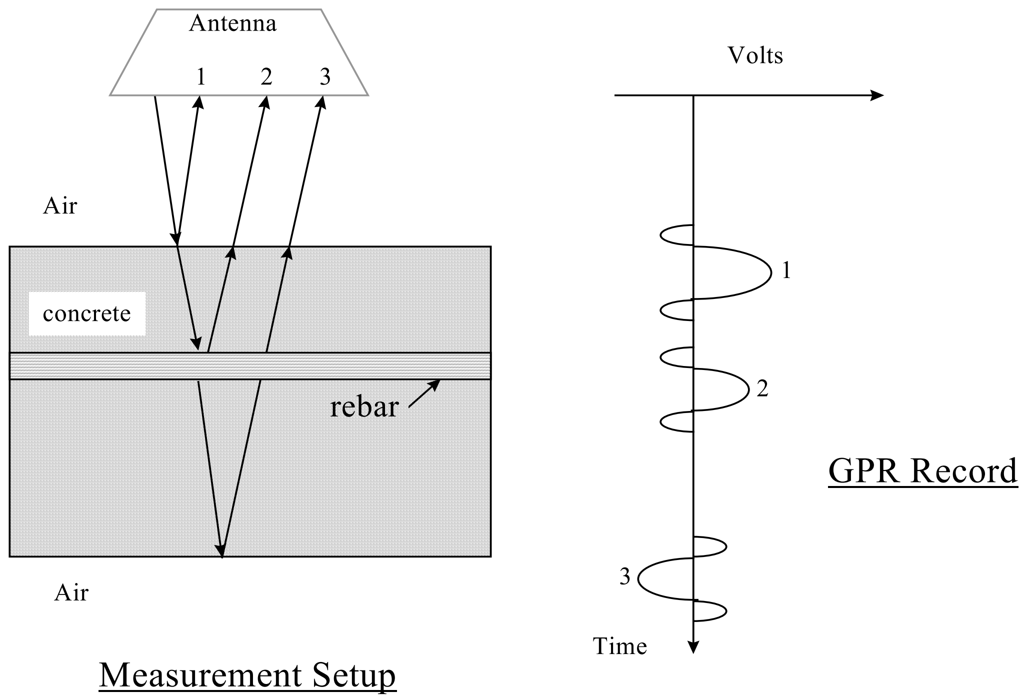

Figure 8.1 *Electromagnetic wave interactions with a concrete bridge deck.*

Frequency (GHz)	Wavelength (m)			
	Air $\varepsilon_r = 1.0$ velocity = 3E+8	**Asphalt** $\varepsilon_r = 5.0$ velocity = 1.34E+8	**Concrete** $\varepsilon_r = 7.5$ velocity = 1.09E+8	**Water** $\varepsilon_r = 78.0$ velocity = 3.39E+7
0.5	0.600	0.268	0.218	0.068
1	0.300	0.134	0.109	0.034
2	0.150	0.067	0.055	0.017
3	0.100	0.045	0.036	0.011
4	0.075	0.034	0.027	0.008
5	0.060	0.027	0.022	0.007
6	0.050	0.022	0.018	0.006

Table 8.2 - Electromagnetic wavelengths as a function of frequency for different media.

has been used on GPR problems. An approximation to the quantum representation is that given by Maxwell's equations (Feynmann, 1977). Maxwell's equations treat the electromagnetic interactions in terms of electric and magnetic field vectors that propagate and reflect as waves. Often, the propagation of electromagnetic waves can be represented by scalars instead of vectors, which simplifies the mathematics at the expense of a loss of directional information, such as polarization. If the waves are approximated as plane waves, then a geometric ray tracing model can be used. Ray tracing replaces the differential wave equations with geometric and trigonometric relations. A further simplification occurs if the media appear as a multi-layered planar structure with the wave direction being normal to the surface of the planes. This forms what is called a 1-D multi-layered model.

8.2 PRIOR RESEARCH

Interest in radar as a possible non-destructive evaluation tool stemmed from radar development work by the Calspan Corp. in the mid-1960's, under a U.S. Army contract, to detect buried non-metallic mines. Subsequent modifications allowed it to be used in the early 1970's to detect voids under pavements. Follow up studies of this radar development work by the Port Authority of New York and New Jersey (PANYNJ) Engineering Research and Development Staff in 1974 led to a program of radar non-destructive evaluation testing and development which has continued through the 1980's and early 1990's. (Steinway et al. 1981; Alongi et al., 1982)

Ulriksen (1982) studied the detection of deteriorated concrete in asphalt overlaid bridge decks by correlating concrete deterioration with chloride content. This work detected an increase in the amplitude of the reflection from the asphalt concrete boundary with higher concrete chloride content. Alongi et al. (1982) conducted laboratory and field tests with a van-mounted radar antenna suspended over a bridge deck. Waveforms were correlated with core samples. It was noted that good concrete exhibited a "smoother" waveform than distressed concrete.

Manning and Holt (1984) conducted field investigations on overlaid bridge decks using radar equipment similar to that used by Alongi. They verified the ability of the radar to detect the asphalt/concrete interface. They also suggested that waveforms corresponding to delaminated concrete contain an intermediate reflection between the asphalt concrete interface and the reflection from the top rebar cover.

Chung *et al.* (1984) developed signal processing techniques to automate the interpretation of waveform data. The algorithm for identifying asphalt/concrete debonding and concrete surface scaling was developed based on amplitude ratios of waveform peaks.

Clemena (1984) analyzed the condition of bridge decks by utilizing the graphic black/white "B-scan"(Brightness-scan) radar output. Areas in the B-scan with significantly different intensity patterns indicated areas with delaminations and other forms of deterioration. Joyce (1984) investigated the feasibility of using radar for high speed surveys of bare and overlaid bridge decks. He conducted laboratory and field tests to note the effect of delaminations on the radar waveform. The laboratory data suggested that delaminations modeled as planar air filled cracks (3mm thick) resulted in a slight intermediate reflection, and resulted in an early radar return from the bottom of the slab. Data from field tests failed to confirm the existence of any intermediate reflections. The study indicated that radar surveys could be conducted at speeds of up to 70 km/hr.

Maser (1989) reported a high correlation between the total deterioration observed on asphalt-overlaid bridge decks, and predictions from radar data. Deteriorated areas were determined based of a waveform-based calculation of the dielectric constant of the concrete immediately below the asphalt layer. Areas were denoted as deteriorated if the calculated dielectric constant was greater than 130% of the mean dielectric constant of the specific pass. This procedure resulted in good correlation with observed deterioration in the field.

Halabe et al. (1990) demonstrated the theoretical feasibility of calculating the bulk physical properties of concrete directly from the radar waveform. Halabe determined the physical properties of the sample through a least square error inversion approximation.

With the promise of becoming a widely accepted non-destructive evaluation method, a large amount of research was conducted in the late 1980's and early 1990's in an attempt to understand more fully ground penetrating radar. A three year project funded by the New England Transportation Consortium was subsequently undertaken in the late 1980's to investigate and propose improved methods for bridge deck assessment (Maser, 1989 and 1990). Several conclusions were drawn from this project, the most important of which was that radar could stand alone as an accurate method of non-destructive evaluation. It was also found that the radar waveform is sensitive to changes in the moisture and chloride content of the asphalt and concrete, due to changes in the material dielectric constant and conductivity. It was found that there is a dramatic increase in signal attenuation in going from low to high chloride values. One drawback which was discovered in this study, using both analytic and experimental analysis, was that small (~1mm thickness) air filled delaminations did not have an appreciable effect upon the resulting waveform. However it was found that an increase in moisture content has the desired effect of making a delamination of this magnitude detectable with pulse radar even if it was undetectable by this means when dry (Moffatt and Puskar, 1976).

The advent of modern synthetic aperture radar signal processing algorithms has opened up the possibility of processing the returned waveforms to produce images of features in reinforced concrete bridge decks (Soumehk, 1999). These techniques were initially demonstrated on laboratory specimens by Mast (1993), Mast and Johannson (1994), and Johannson and Mast (1994). The technique was further demonstrated on roadways using the FHWA PERES and HERMES systems (Chase, 1999).

Halabe *et al*. (1989) conducted a numerical study of the sensitivity of the concrete reflectivity to moisture and chloride content. The study used electromagnetic models for predicting radar waveforms from concrete and asphalt material properties. The results were that both moisture and chloride content increase the reflectivity of the concrete.

Other indicators of concrete deterioration have been proposed (Carter et. al., 1986; Manning and Holt, 1980; Ulricksen, 1982; Alongi et. al., 1982; Clemena, 1984). These other indicators, however, are all sensitive to the cross sectional geometry of the deck, including asphalt thickness and rebar spacing and depth. The geometric sensitivity of these indicators decreases their usefulness as indicators of deterioration, since geometry will vary within a deck and from deck to deck. The concrete reflectivity, however, is unaffected by cross section geometry except when interference occurs due to thin asphalt (less than 51mm) and to shallow rebar cover (less than 25mm). Under these circumstances, signal processing techniques are required to reveal the true value of the concrete reflectivity. The use of the strength of the reflections from rebars was described by Nayranan et al. (1998). The results were promising, but not definitive.

8.3 ELECTROMAGNETIC WAVES

Electro-magnetic fields can be described in vector form by the intensity of the electric field, $\vec{E}$; the intensity of the magnetic field, $\vec{H}$; the electric displacement, $\vec{D}$; and the magnetic induction, $\vec{B}$. These vectors are assumed to be finite throughout the entire field, and at all ordinary points to be continuous functions of position and time, with continuous derivatives (Stratton, 1941). At every ordinary point in space these field vectors are subject to Maxwell's equations:

$$\nabla \times \vec{H} = \left(\frac{\partial \vec{D}}{\partial t}\right) + \vec{J}_s + \vec{J}_c \tag{8.3.1}$$

and,

$$\nabla \times \vec{E} = -\left(\frac{\partial \vec{B}}{\partial t}\right) \tag{8.3.2}$$

Where $\vec{J}_s$ is the source current density and $\vec{J}_c$ is defined as the conductivity current density ($\vec{J}_c = \sigma \vec{E}$). In an isotropic medium, $\vec{D}$ is parallel to $\vec{E}$,and $\vec{H}$ is parallel to $\vec{B}$,

$$\vec{D}(\vec{r},\omega) = \varepsilon \vec{E}(\vec{r},\omega) \tag{8.3.3}$$

and,

$$\vec{B} = \mu_0 \vec{H} \tag{8.3.4}$$

Where ε and μ_o can be defined as the relative permittivity and the relative permeability ($\mu_o = 4\pi x 10^{-7}$ N/A^2) respectively. It should be noted that the equation for **D** is for that of a non-dispersive media. For dispersive media ε is a function of frequency and the equation can be re-written as follows:

$$\vec{D}(\vec{r},\omega) = \varepsilon(\omega) \vec{E}(\vec{r},\omega) \tag{8.3.5}$$

For nonconducting homogeneous media, Maxwell's equations can be written as (Slater and Frank, 1969):

$$\nabla \times \vec{H} = \varepsilon \frac{\partial \vec{E}}{\partial t} \qquad (8.3.6)$$

$$\nabla \times \vec{E} = -\mu \frac{\partial \vec{H}}{\partial t} \qquad (8.3.7)$$

$$\nabla \cdot \vec{H} = 0 \qquad (8.3.8)$$

$$\nabla \cdot \vec{E} = 0 \qquad (8.3.9)$$

where $\vec{H}$ = the magnetic field vector, $\vec{E}$ = the electric field vector, ε = the relative permittivity or dielectric constant, and μ = the relative permeability. For a vacuum (or air) $\varepsilon_o = 8.854 \times 10^{-12}$ farad/m and $\mu_0 = 4\pi \times 10^{-7}$. A manipulation of these equations converts them into wave equations, which indicate that the medium can support electromagnetic waves. This is accomplished by first taking the curl of eqs. (8.3.6) and (8.3.7) to yield

$$\nabla \times \nabla \times \vec{H} = \varepsilon \frac{\partial (\nabla \times \vec{E})}{\partial t} \qquad (8.3.10)$$

$$\nabla \times \nabla \times \vec{E} = -\mu \frac{\partial (\nabla \times \vec{H})}{\partial t} \qquad (8.3.11)$$

Noting that for any arbitrary vector

$$\nabla \times \nabla \times \vec{A} = \nabla \nabla \cdot \vec{A} - \nabla^2 \vec{A} \qquad (8.3.12)$$

and inserting eqs. (8.3.6) and (8.3.7) into eqs. (8.3.10) and (8.3.11), respectively yields the wave equations

$$\nabla^2 \vec{H} = \varepsilon \mu \frac{\partial^2 \vec{H}}{\partial t^2} \qquad (8.3.13)$$

$$\nabla^2 \vec{E} = \varepsilon \mu \frac{\partial^2 \vec{E}}{\partial t^2} \qquad (8.3.14)$$

The wave equations indicate that a wide variety of different shapes of electromagnetic waves can propagate through a medium. A wave with a simple form that appears in many GPR models is the plane wave with the representation

$$\vec{H} = \vec{H}_0 \exp[i(\vec{K} \cdot \vec{r} - \omega t)] \qquad (8.3.15)$$

$$\vec{E} = \vec{E}_0 \exp[i(\vec{K} \cdot \vec{r} - \omega t)] \qquad (8.3.16)$$

where $\vec{K}$ is the wavenumber vector, $\vec{r}$ is position, and ω is circular frequency. Substituting (8.3.15) and (8.3.16) into (8.3.13) and (8.3.14), and using the relations

$$\nabla = i\vec{K} \tag{8.3.17}$$

$$\frac{\partial}{\partial t} = -i\omega \tag{8.3.18}$$

indicates that the plane waves will propagate if

$$f = \frac{c}{\lambda} \tag{8.3.19}$$

where f = frequency, c = speed of light in the medium, and λ = wavelength.

In homogeneous media, plane waves propagate in a straight line, in a direction indicated by the wavenumber vector $\vec{K}$. This allows a simplified representation of plane wave propagation with a ray that is points in the direction of propagation. Substituting the relations (8.3.17) and (8.3.18) into (8.3.6) yields

$$i\vec{K} \times \vec{H}_0 = -i\omega\varepsilon\vec{E}_0 \tag{8.3.20}$$

The cross-product in (8.3.20) indicates that the direction of propagation, the magnetic field vector and the electric field vector are all mutually perpendicular. The directions and phasing of the magnetic and electric field vectors determine the polarization.

When electromagnetic waves travel through inhomogeneous media, the waves can reflect, transmit, and scatter in complex patterns. The situation is fairly simple when a plane wave travels through two different media that are joined by a continuous planar surface. Three waves form in this case: an incident wave with wavenumber vector $\vec{K}_i$, a transmitted wave with wavenumber vector $\vec{K}_t$, and a reflected wave with wavenumber vector $\vec{K}_r$. The relative wave speeds of the two media determine the nature of the interactions between these three vectors, Figure 8.2. It is customary to describe the wave speed in terms of the index of refraction $n_i = c_0/c_i$, where c_0 = speed of light in a vacuum (3.0 x 10^8 m/s) and c_i = speed of light in medium i ($<c_0$).

The continuity of the electric and magnetic fields across the boundary of the two media, requires that the wavenumber vectors for all three waves must be equal at the boundary

$$\vec{K}_i \cdot \vec{r} = \vec{K}_r \cdot \vec{r} = \vec{K}_t \cdot \vec{r} \tag{8.3.21}$$

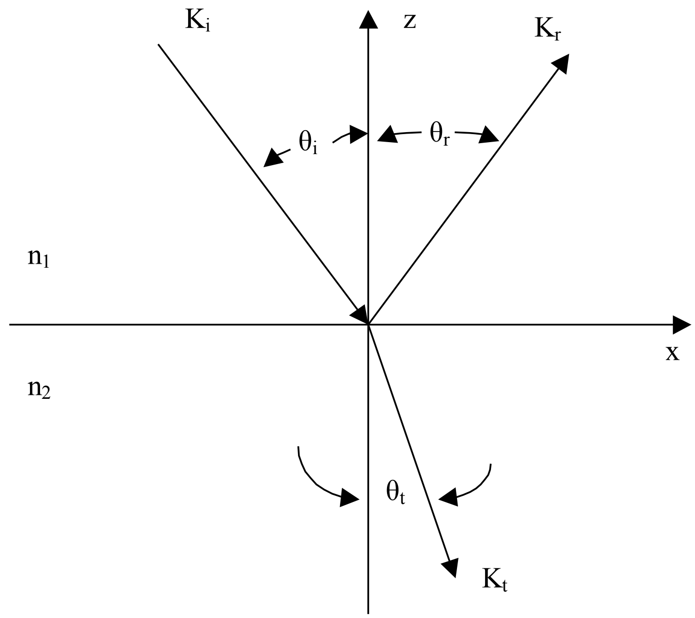

Figure 8.2 *Geometry of incident, reflected and transmitted waves interacting with two different media.*

For the boundary being along the x-axis

$$K_i \sin\theta_i = K_r \sin\theta_r = K_t \sin\theta_t \qquad (8.3.22)$$

Combining eqs. (8.3.19) with (8.3.21) gives

$$\theta_i = \theta_r \qquad (8.3.23)$$

i.e. the angle of the incident wave equals that of the reflected wave, and

$$\frac{\sin\theta_i}{\sin\theta_t} = \frac{n_2}{n_1} \qquad (8.3.24)$$

which is known as Snell's law.

If the electromagnetic wave is polarized so that the electric field vector lies in the x-y plane and the magnetic field vector lies in the x-z, the wave is called a transverse electric (TE) polarized wave. If the wave is polarized so the that the magnetic field vector lies in the x-y plane and the electric field vector lies in the x-z plane, then the wave is called a transverse magnetic (TM) polarized wave. TE waves and TM waves interact differently with a boundary, producing different amplitudes in the reflected and transmitted waves (Udd, 1991). The reflection (R) and transmission (T) coefficients are

$$R_{TE} = \left(\frac{E_r}{E_i}\right)_{TE} = \frac{n_1 \cos\theta_i - n_2 \cos\theta_t}{n_1 \cos\theta_i + n_2 \cos\theta_t} \tag{8.3.25}$$

$$T_{TE} = \left(\frac{E_t}{E_i}\right)_{TE} = \frac{2n_1 \cos\theta_i}{n_1 \cos\theta_i + n_2 \cos\theta_t} \tag{8.3.26}$$

$$R_{TM} = \left(\frac{E_r}{E_i}\right)_{TM} = \frac{n_2 \cos\theta_i - n_1 \cos\theta_t}{n_1 \cos\theta_t + n_2 \cos\theta_i} \tag{8.3.27}$$

$$T_{TM} = \left(\frac{E_t}{E_i}\right)_{TM} = \frac{2n_1 \cos\theta_i}{n_1 \cos\theta_t + n_2 \cos\theta_i} \tag{8.3.28}$$

If the angle of incidence $\theta_i = 0$, the situation corresponds to testing in a monostatic mode with layered media. The equations (8.3.25-28) simplify to

$$R_{TE} = -R_{TM} = \frac{n_1 - n_2}{n_1 + n_2} \tag{8.3.29}$$

$$T_{TE} = T_{TM} = \frac{2n_1}{n_1 + n_2} \tag{8.3.30}$$

If the two media are dielectric and if can be assumed that the change in wavespeed is due to changes in the dielectric constant (rather than the permeability), the reflection and transmission coefficients for a wave traveling from medium 1 to 2 are

$$R_{12} = \frac{\sqrt{\varepsilon_1} - \sqrt{\varepsilon_2}}{\sqrt{\varepsilon_1} + \sqrt{\varepsilon_2}} \tag{8.3.31}$$

$$T_{12} = \frac{2\sqrt{\varepsilon_1}}{\sqrt{\varepsilon_1} + \sqrt{\varepsilon_2}} \tag{8.3.32}$$

If medium 1 has a smaller relative dielectric constant than medium 2, then R_{12} has a negative value. If medium 1 has a larger relative dielectric constant than medium 2, then R_{12} is positive. The magnitude of the reflection coefficient dictates the amplitude of the reflected wave, and the sign of the reflection coefficient dictates the phase shift of the returning wave. When R_{12} is negative the incident wave will undergo a 180 degree phase shift when it is reflected, and when R_{12} is positive, no shift in phase occurs (Carter et al., 1986).

The reflection from a metal surface can be modeled by setting the dielectric constant ε_2 to infinity. In this case $R_{12} = -1$ and $T_{12} = 0$.

The different reflectivities of a dielectric surface and a metallic surface can be exploited to determine the dielectric constant of a roadway surface. If A is the amplitude of the reflection from a normal incidence wave off of the surface of the roadway and A_{PL} is the amplitude of the reflection off of a metal plate placed on the roadway surface, then the dielectric constant for the roadway can be calculated with

$$\varepsilon_1 = \quad [(1 + A/A_{pl})/(1 - A/A_{pl})]^2 \qquad (8.3.33)$$

8.4 ELECTROMAGNETIC INTERACTIONS WITH MATERIALS

The interactions of electromagnetic waves with materials can be quite complex, with the interactions often being highly dependent on wavelength and physical properties of the medium, such as moisture content, chloride ion content, and temperature. For GPR, usually only four types of models of electromagnetic interactions with media are commonly used: 1. *vacuum or air*, 2. *dielectric*, 3. *lossy dielectric*, and 4. *metallic reflective.*

8.4.1 VACUUM OR AIR

The electromagnetic properties of air and a vacuum are virtually identical for the frequencies and transmission distances commonly encountered in GPR. Electromagnetic waves propagate through air with minimal losses.

8.4.2 DIELECTRICS

Dielectrics are insulating materials containing dipoles. When the material is subjected to an electric field, the dipoles will set up dipole moments that are proportional to the strength of the field. This is expressed by the relation

$$\vec{D} = \varepsilon_r \vec{E} \qquad (8.4.1)$$

where $\vec{D}$ is the electric displacement vector, ε_r is the dielectric constant for the material, and $\vec{E}$ is the applied electric field. The permittivity of air is often normalized to unity and the dielectric constant ε_r is also normalized, with a value that is always greater than or equal to one.

8.4.3 LOSSY DIELECTRICS

Ideal dielectrics allow the propagation of electromagnetic waves without any losses. All real passive materials produce losses, which convert the electromagnetic energy into heat and attenuate the amplitude. This loss mechanism is usually described by a linear model where eqs. (8.3.12) and (8.3.13) are modified to have complex-valued permittivities and permeabilities, $\varepsilon^* = \varepsilon' + i\varepsilon''$ and $\mu^* = \mu' + i\mu''$, (Condon and Odishaw, 1967) i.e.

$$\nabla^2 \vec{E} = \varepsilon^* \mu^* \frac{\partial^2 \vec{E}}{\partial t^2} \qquad (8.4.2)$$

If the propagation factor, γ, is defined as

$$\gamma = i\omega[\varepsilon^* \mu^*]^{1/2} = \alpha + i\beta \qquad (8.4.3)$$

then α is the attenuation factor (α=0 for loss-free media) and β is the phase factor, which is indicative of the phase velocity of the wave. For most dielectric materials, the loss factor is modeled by absorbing the complex part into the permittivity ε^*. A useful descriptive quantification of the loss factor is the loss tangent, $\delta = \varepsilon''/\varepsilon'$, because it is a relatively easy to measure.

8.4.4 METALLIC MATERIALS

Metallic materials conduct electricity with a resistance R. In this case Maxwell's equations need to include the current terms, as in eq. (8.3.1) Metallic materials appear in GPR applications as reflective elements, such as metallic plates and rebars, and in antennas. Metal surfaces are strong reflectors of electromagnetic waves. The reflection from a metallic surface, such as a rebar, is often stronger than that resulting from a change in dielectric properties. Since metals are such good conductors, they make excellent materials for antennas. Copper is often the material of choice. Since metals are also strong reflectors, the analysis and design of antennas can be quite complex (Balanis, 1997).

8.5 ELECTROMAGNETIC PROPERTIES OF CONCRETE AND ASPHALT

8.5.1 DETERIORATION MECHANISMS

Road pavements, especially bridge decks, are heavily loaded structural elements with expected lifetimes of decades. In addition to repeated heavy traffic loads, pavements are subjected to the stresses of corrosion, freeze-thaw action and differential thermal expansion.

Corrosion of the reinforcing steel in concrete bridge decks is a serious maintenance problem. Prior to 1980, virtually every concrete bridge deck was constructed with bare reinforcing steel with no protective coatings for corrosion. In most cases, the alkali nature of concrete forms a passivation layer around the bare steel that effectively impedes corrosion. The primary initiating mechanism of rebar corrosion is that chloride ions breakdown the passivation layer. Chloride ions usually come from the application of deicing salts, but can also come from sources such as ocean spray, or defective concrete mixes. The products of this corrosion process – principally iron oxide – expand and exert sufficient force on the concrete to cause severe damage and to weaken the bond of the concrete to the steel. Early detection of this process can make it possible to arrest the corrosion process and prevent the necessity of replacing the concrete deck.

The concrete used in bridges is heavily exposed to the destructive forces of freezing and thawing – a factor that is critical to its durability. The concrete is often saturated with water prior to freezing, which can generate large stresses due to the expansion and contraction of water as it freezes and thaws. Field observation of asphalt covered bridge decks (Maser, 1989) have shown extensive freeze-thaw damage occurs even when air-entrained concrete was specified in the original construction.

The *alkali-silica reaction* involves certain forms of silica and siliceous materials that cause deleterious expansion and cracking of concrete by interaction with alkalis released during the hydration of Portland cement. The most active aggregates have been found to be those containing opal, chalcedony, certain forms of chert, volcanic glasses, rhyolite, and basalts. In order for such aggregate to be destructive, there must be sufficient alkalis in the cement and the concrete must be either continuously or intermittently wet. If the alkali concentration in the cement can be kept down to less than 0.6%, usually no damage occurs.

Deterioration in *asphalt concrete* is primarily due to separation of the aggregate from the asphaltic binder, and to aging and *embrittlement* of the binder. Since mineral aggregates constitute about 80 percent by volume of asphaltic concrete mixes, their influence on the properties and performance of mixes is great. As far as deterioration is concerned, the porosity and nature of the aggregate surface are especially important to aggregate-asphalt interaction. The asphalt must adequately cover the aggregate and adhere to the aggregate surface. A lack of proper asphalt-aggregate adhesion may occur with smooth aggregate surfaces of very low porosity or those that do not bond well to asphalt because of surface chemistry. Adhesion is particularly important during periods when the mix is exposed to water. If the aggregate is of a type that wets well with water, water may successfully compete with the asphalt for adsorption onto the aggregate surface and aggregate-asphalt separation, known as stripping, results. Stripping can be aggravated as the asphalt ages and oxidizes with time and becomes more brittle in nature. Aggregate stripping is the most serious mechanism of deterioration of asphaltic concrete mixtures.

8.5.2 RELATIONSHIP OF DETERIORATION TO ELECTROMAGNETIC PROPERTIES

The deterioration of concrete and asphalt often changes their electromagnetic properties. These changes may occur in the fine structure of the material, such as the formation of additional interfaces and dielectric discontinuities created by delaminations, stripping, and freeze thaw damage; or they may occur in the bulk properties of the material, such as an increase in the dielectric constant (decreased velocity) or an increased in the attenuation due to higher moisture content, chloride content, and porosity.

Commercial radar systems operating at frequencies centered around 1 GHz yield a maximum spatial resolution of from 5-10 mm in concrete to 10-15 mm in asphalt (Table 8.1). This fundamental limitation in resolution significantly reduces the ability of radar to directly detect the fine dielectric discontinuities that result from deterioration mechanisms. In spite of this limitation, field data from various sources support the claim that deterioration may be detected by focusing on bulk conditions that promote or are associated with deterioration, such as high moisture or chloride content (Maser, 1989). Other forms of deterioration, such as the porosity changes associated with freeze-thaw damage, may also be detected by focusing on the electromagnetic properties of the bulk sample (Halabe et al. 1990 and 1993).

Tables summarizing the dielectric properties of a variety of homogeneous materials have been compiled by many researchers, e.g. Zoughi, et al. (1995). However, the dielectric properties of multi-phase, heterogeneous materials, such as Portland cement concrete and asphalt, have not been as systematically investigated.

Halabe, et al. (1990) developed a model to characterize the complex dielectric constant of asphalt and concrete mixtures as a function of wave frequency, sample temperature, moisture content, chloride content, and mix constituents. The model calculates the dielectric permittivity of concrete from the known permittivity of its discrete constituents (i.e., aggregate, air, water, chloride, cement paste). Although water and salt compose a relatively small percentage of a given concrete or asphalt pavement sample, the effect on the permittivity can be quite large. Unbound water molecules cause an increase in the average dielectric constant of the material. Salt and other ionic substances cause an increase in the attenuation of the traveling EM waves. The influence of these substances upon the propagation of radar waves has been verified by numerous field and laboratory measurements. (Maser 1990, Sotoodehnia 1989).

The mixture models developed by Halabe et al. (1990*)* are valid only in regimes where the particles within the medium are small compared to the wavelength of the radar. The use of high-frequency short-wavelength GPR waves to identify features such as delaminations, freeze thaw damage, and stripping involves reducing the wavelength to values where localized inhomogeneities, such as that due to aggregates, can produce significant amounts of scattering.. As the frequency of the radar is increased, scattering from both inherent inhomogeneities of the sample and deterioration products can significantly influence the propagation of the radar pulse and should be included in the electromagnetic model of the media. However the scattering of a radar pulse within concrete and asphalt has not been well studied.

Models have been proposed to account for scattering losses through random discrete media (Kong, 1986) by characterizing the medium with a gross effective permittivity. As the frequency of the incident electromagnetic wave increases, losses due to multiple scattering are included in the imaginary part of the effective permittivity of the medium to account for the attenuation.

8.5.3 MODELING THE DIELECTRIC PROPERTIES OF CONCRETE

Concrete is a complex medium that is formed as a mixture of several constituents, including cement, aggregate, entrained air, free and bound water, ions, and steel reinforcement. Matthews et al. (1998) found that the dielectric permittivity increased with moisture content and ranged from 5.2 to 11. Modeling the electromagnetic properties of concrete requires balancing the complexity of the physics with the need for a computationally efficient model.

Several models, which have been developed and verified for partially-saturated rocks, exist for predicting the dielectric properties of a mixture from the properties and volumetric proportions of the constituents (Halabe et al. 1993 and 1995a). The components in these models include coarse and fine aggregate, cement paste, air, water, and salt. Of these components it has been found that water and salt, only when dissolved in solution, have the greatest effect on the dielectric constant. The relative dielectric permittivity of salt water (ε_{sw}) can be written using the DeBye expression of the form

$$\varepsilon_o = \varepsilon_\infty + \frac{\varepsilon_o - \varepsilon_\infty}{1 - i2\pi\tau f} + i\frac{\sigma}{2\pi\varepsilon_o^* f} \qquad (8.5.3.1)$$

where,
ε_o = static dielectric constant of the solvent
ε_∞ = high frequency dielectric constant of solvent
τ = relaxation constant
σ = conductivity of water, and
f = electromagnetic frequency.

The expressions for ε_o, ε_∞, and σ as a function of water's salinity, temperature, and the frequency of electromagnetic wave propagation, have been developed by Stogryn (1971) using linear regression of tabulated values for these dielectric properties. These equations were later modified by Klein and Swift (1977) and have also been reproduced by Ulaby et al. (1986).

Water plays such a large role because the dielectric constant of water (81) is much greater than that of dry natural rock, soil, and concrete (2.5-8.0) (Maser and Kim Roddis, 1990). For the purpose of the models proposed by Halabe et al. (1993 and 1995a) the coarse and fine aggregate are considered to have a dielectric constant between 4.0 and 7.0. Coarse aggregate has a low porosity (1-2%). It does not hold much water. The mortar mixture is very porous, with the saline water contained within the pores being the primary constituent contributing to the loss factor. Concrete can be modeled as a three-phase mixture consisting of solid particles and air having a real dielectric permittivity, and saline water having a complex permittivity. A brief description of three models can be found in the following paragraphs. A more in depth description can be found in Halabe et al. (1993).

8.5.3a Complex Refractive Index Method (CRIM) – The refractive index η_t for a medium is defined as

$$\eta_t = c_o\sqrt{\mu_t\varepsilon_o\varepsilon_r} \qquad (8.5.3.2)$$

where,

c_o = velocity of electromagnetic waves in a vacuum = 3 x 10^8 m/sec
μ_t = permeability of medium = μ_o = 4π x 10^{-7} henry/m for vacuum and most dielectric materials
ε_o = dielectric permittivity of vacuum = 8.854 x 10^{-12} farad/m, and
ε_r = relative complex dielectric permittivity of medium.

The CRIM method asserts that the complex refractive index for the mixture is given by the volume average of the complex refractive indexes of the constituents. The relative dielectric constant for a given mixture can then be expressed as a volume average of the dielectric constants of the constituents

$$\sqrt{\varepsilon_r} = (1-\phi)\sqrt{\varepsilon_m} + (1-S)\phi\sqrt{\varepsilon_a} + \phi S\sqrt{\varepsilon_{sw}} \qquad (8.5.3.3)$$

where,
ϕ = porosity of concrete = (volume of voids)/(total volume of concrete)
S = degree of saturation = (volume of water)/(volume of voids)
ε_m = relative dielectric permittivity of concrete solids ~ 5.0 (real)
ε_a = relative dielectric permittivity of air = 1.0 (real)
ε_{sw} = relative complex permittivity of water, and
ε_r = relative dielectric permittivity of resulting concrete mixture = $\varepsilon^{I} + i\varepsilon^{II}$.

This method has been widely used because of its simplicity, however it has little theoretical basis and contains no geometrical information on grain shape (Feng and Sen, 1985). It gives reasonable results when the ratio of the imaginary to the real part of the dielectric constant is close to one, however when the salinity is high or the frequency is low, this ratio becomes much greater than one and the results become highly inaccurate.

8.5.3b Continuous Grain Size Distribution Model – This model assumes that the solid grains and air molecules are spherical particles with a continuous size distribution. The model has been derived by Feng and Sen (1985) based upon the effective medium theory (also called equivalent media theory), which asserts that the effective complex relative dielectric constant of a mixture ε_r is given by

$$\Sigma\, v_i \left[(\varepsilon_r - \varepsilon_l) / (2\varepsilon_r + \varepsilon_i)\right] = 0 \qquad (8.5.3.4)$$

where ε_i denotes the dielectric permittivity of the individual constituents and v_i is the corresponding volume fraction of the components. This theory is limited by the fact that it predicts that the DC conductivity becomes zero when the volume fraction of the conducting phase drops below a critical value of thirty three percent. This prediction presents a problem for concrete since the volume fraction of water, which is the conducting phase in rock and concrete, is almost always below this critical value. This limitation can be removed by a systematic procedure in which one starts with a background matrix of water where small amounts of solid particles and air molecules are added in a number of steps starting with the smallest particles. At each step the effective complex dielectric constant is calculated using equation (8.5.4.4) and the resulting mixture serves as the background for the next step. It should be noted that the solid particles and air molecules can be added at any rate, with the only constraint being that the final values of $v_m : v_a : v_{sw} = (1-\phi) : (1-S)\phi : S\phi$.

8.5.3c Discrete Grain Size Distribution Model – Another model using the equivalent medium theory which considers a discrete particle size distribution of spherical grains was proposed by Madden and Williams (1993) . This model assumes that a discrete particle size distribution is more realistic than the continuous size distribution model because it allows for the differentiation between fine and coarse grained aggregates. This distinction in turn affects the internal structure of the model that greatly affects its dielectric properties.

The discrete model differs from the continuous model in that it deals with complex conductivities as opposed to complex relative dielectric constants. The two can be related using

$$\varepsilon_r = \varepsilon^{I} + i\varepsilon^{II} = \varepsilon^{I} + i\sigma/(\omega\varepsilon_o) \qquad (8.5.4.5)$$

Here σ ($=\omega\varepsilon_o\varepsilon^{II}$) denotes the dielectric conductivity of the medium. The complex conductivity σ_c is defined as

$$\sigma_c = \sigma - \imath\, \varepsilon^{I}\, \varepsilon_o\, \omega \qquad (8.5.4.6)$$

From eq.(8.5.4.5) and (8.5.4.6), the relationship between ε_r and σ_c can be obtained as

$$\sigma_c = -i\omega\, \varepsilon_r\, \varepsilon_o \qquad (8.5.4.7)$$

Which can be used to derive the following formula for the iterative mixture law for the discrete case (Halabe et al., 1993)

$$\sigma_n = \sigma_{n-1} - \Sigma[3(\sigma_{n-1} - \sigma_j)P_j\sigma_n] / (\sigma_j + 2\sigma_n) \qquad (8.5.4.8)$$

where the summation is taken from j=1 to k^{I} and,
σ_n = complex conductivity of mixture to the nth step
σ_{n-1} = complex conductivity of mixture up to (n-1)th step
σ_j = complex conductivity of jth inclusion (i.e., air or solid particles)
P_j = volume fraction of the jth inclusion, and
k^{I} = number of inclusions at each step (which can be any desired number).

8.5.5 MODELING PROPERTY VARIATION WITH DEPTH

As noted in the previous section, the dielectric properties of concrete are highly dependent on the porosity, chloride content, saturation, and temperature, which can vary significantly with depth. The following paragraphs summarize the models for each of these properties.

8.5.5.a Porosity – Cady and Weyers (1983) found that the porosity is dependent upon the water/cement (w/c) ratio, with field porosity measurements for bridge deck specimens falling between 17.5%(w/c ratio of 0.4) and 23.8%(w/c ratio of 0.5). At present little information is available about the variation of porosity with depth in a concrete bridge deck. Halabe et al. (1995a) assumed that the porosity is constant through the thickness.

8.5.5.b Chloride Content **–** Cady and Weyers (1983) found that the chloride content of a bridge deck increases with age, with the maximum chloride content occurring at a depth of 12.7 mm below the concrete surface. In order to account for this, the synthesis program divides the top one inch of concrete into 6.4 mm, 12.7 mm and 6.4 mm thick layers, while the remaining portion is divided into equal thickness layers. Based upon the properties of the top layer, the chloride content for the remaining layers is then determined as follows as outlined by (Halabe et al., 1995a).

The second layer has the maximum chloride content, which is computed by multiplying the top surface content with a factor of 1.15. The chloride content of the third layer is calculated by multiplying the top surface chloride content by 1.025. The chloride content for the remaining layers is then calculated using the following formula:

$$Cl^-(l) = Cl^-_{max} / (1.15\text{x } D(l\text{-}1)) \qquad (8.5.5.1)$$

or 0.0125%, whichever is greater

where,

$Cl^-(l)$ = chloride content of layer (l)% by weight of dry concrete

Cl^-_{max} = maximum chloride content = 1.15 x top surface chloride content, and

$D(l\text{-}1)$ = distance from top surface of deck to top layer (l in inches).

The radar waveform synthesis model computes the dielectric permittivity of concrete by using salinity in parts per thousand (ppt) by weight and not by chloride content. Therefore the chloride content needs to be converted into salinity using the following equation

$$S_{sw}\,(\text{ppt}) = Cl^- \text{ x } (58.5/35.5) \text{ x } 1/w \text{ x } 1000 \qquad (8.5.5.2)$$

where,

S_{sw} = salinity (NaCl equivalent) in parts per thousand by weight of water

Cl^- = chloride content in % by weight of dry concrete

w = water content in % by weight of dry concrete

58.5 = molecular weight of NaCl, and

35.5 = Molecular weight of Cl^-.

8.5.5.c Saturation – The amount of moisture in a bridge deck strongly affects the dielectric properties and wave propagation of a radar wave. Increased saturation leads to an increased dielectric permittivity, increased attenuation and reduced velocity of radar waves. For the synthesis model, the maximum saturation is assumed to occur at mid-depth. It is approximated as 1.5 times the top surface saturation. Applying this assumption, two different models are used in the synthesis program based upon the saturation of the top layer of the deck. If the saturation of the top layer exceeds 50%, a model proposed by Carrier et al. (1975) is used. In this model the saturation is decreased by about 1% for each layer, excluding the top and bottom layers, starting from the mid-depth layer and moving outward towards the top and bottom layers. For the top 25 mm of the deck, which is divided into three layers for the purpose of the chloride content, the top 6 mm is taken as the top surface saturation and the saturation for the next two layers is increased by 5% and 10% respectively. For the bottom layer, the saturation is taken as the top surface saturation plus 5%.

A second model is used when the saturation of the top surface falls below 50%, because the model proposed by Carrier et al. (1975) does not work well for decks with low saturation. In this case the saturation is assumed to be symmetrical about the mid-depth saturation, where the saturation decreases linearly to the top and bottom surfaces of the deck (Halabe et al. 1975).

8.6 1-DIMENSIONAL LAYERED MEDIA MODEL

Halabe et al. (1993, 1995a and 1995b) Bhandarkar (1993) developed a theoretical model for the analysis of the interaction of radar waveforms with concrete bridge decks. The model includes both a synthesis (forward) model for the generation of theoretical waveforms, and an inversion model for the prediction of concrete deck properties from a field radar waveform. For the inversion model, four parameters for a concrete bridge deck are treated as unknown 1. porosity of concrete, 2. degree of saturation of concrete, 3. pore water salinity, and 4. the top reinforcing bar cover. This approach starts with an initial guess for the unknown parameters and uses a least squares method to modify the parameters at each step of the iteration. A synthetic waveform is generated for each iteration and the iteration process continues until a convergence between the field waveform and the synthetic waveform is achieved. In a numerical study of the inversion model it was found that while the total water content and top reinforcing bar cover converged to their true values, there was a high degree of non-uniqueness with respect to the other parameters describing the physical condition of the concrete. A detailed description of the inversion model can be found in the paper by Halabe et al.(1995b).

The synthesis model considers the bridge deck or pavement as a multi-layered medium, with cylindrical inclusions (rebars). The model accounts for the effects of several parameters such as porosity, saturation, chloride content, temperature and frequency on the complex dielectric permittivity of concrete. In this model, the reflection coefficient for each layer is computed recursively, working from the bottom interface and proceeding upwards. These computations are performed in the frequency domain to account for the multiple reflections from all of the interfaces. Reflections from the longitudinal rebars are accounted for in the time domain. This model ignores the reflections from the transverse rebars since they are usually perpendicular to the polarization direction of the radar antenna's electric field in a typical bridge deck survey. For more details see Halabe et al. (1993, 1995a, and 1995b).

Halabe et al.(1995a) performed a numerical study using each of the three models presented in the preceding sections, and compared the results with actual experimental results. It was found that all three models predict the real part of the complex dielectric constant within 10 percent of the values obtained experimentally. Further, it was found that the CRIM model and the discrete model result in a more accurate prediction of the attenuation coefficient. The CRIM model was found to break down and provide unrealistic results at low frequencies (in the MHz range) or when the salinity and conductivity of the mixture is high ($\varepsilon^{II} / \varepsilon^{I} > 1$). Overall, the CRIM and discrete models are in good agreement with each other, and with results obtained experimentally. The CRIM model offers the advantage of being simpler to use. The discrete model, on the other hand, provides reasonable predictions over a wide range of conditions (including very low frequencies).

8.6.1 MODELING THE REFLECTION FROM REBARS

Since the reinforcing bar reflections are superimposed on the reflections from other irregular subsurface anomalies (i.e., delaminations, deteriorated concrete), it is very important to incorporate the effect of rebars in any analytic model (Halabe et al., 1995b). A rebar can be treated as a regular cylindrical subsurface anomaly with a uniform depth and spacing. The reflection from the rebar is modeled using geometric optics for the reflection of EM waves. Davis (1979) proposed the following expression for the scattering attenuation function (SAF), which is defined as the ratio of reflection from a cylinder oriented along the polarization direction of the antenna's electric field to that from an infinite flat metal plate at the same distance from the antenna

$$\mathrm{SAF} = \sqrt{[r / (r + d)]} \qquad (8.6.1.1)$$

where r is the radius of the reinforcing bar or cylinder, and d is the distance from the radar antenna to the top of the reinforcing bar or cylinder. Equation (8.6.1.1) is based on the assumption that the antenna is a point source transmitting spherical waves, and the rebars have a diameter that exceeds one-fifth of the wavelength. It should be noted that experimental results indicate that when the antenna is oriented longitudinally, the dominant transverse rebar will have a relatively small effect on the radar waveform, and can be ignored for the purposes of modeling.

Equation (8.6.1.1) is valid for a single rebar. For a rebar grid, equation (8.6.1.1) can be written as

$$\mathrm{SAF\ (rebar\ grid)} = \left(\sqrt{[r / (r + d)]}\right) \cdot \left(\text{effective cone width/longitudinal rebar spacing}\right) \qquad (8.6.1.2)$$

Where the effective cone width refers to the width of the radiation cone at the level of the reinforcing grid. This width can be calculated using Snell's Law, eq. (8.3.25), and the initial width of the radiation cone emitted from the antenna.

The effect of the presence of a rebar grid upon the reflection from subsequent layers was also examined by Halabe et al. (1995b). It was found that the reduction in amplitude of reflections from subsequent interfaces, due to the presence of a rebar grid could be approximated within 15 to 20 percent, using

Reflection from subsequent layer interface in presence of the rebar grid = [1 - SAF(for rebar grid)] • reflection from subsequent layer interfaces in absence of rebar grid (8.6.1.3)

It should be noted that equations (8.6.1.2) and (8.6.1.3) are applicable only in the time domain. The following section describes how these equations can be combined with equations developed in the frequency domain for the modeling of saline water and concrete.

8.6.2 RADAR WAVEFORM SYNTHESIS

As previously discussed, the deck is idealized as a multi-layered medium with cylindrical metal inclusions. Each layer is considered to have homogeneous dielectric properties that can be calculated with the methods of the preceding sections. The computed waveform for the bridge deck, accounting for the top and bottom rebar grids, can be obtained by a weighted linear superposition of waveforms from three separate models, as seen in Figure 8.3. The first model contains no reinforcing bars. In the second model, a metal plate replaces the top reinforcing layer, so that the incident EM wave does not penetrate past. The third model has no top reinforcing bars and a metal plate replaces the bottom reinforcing layer. The radar waveforms are synthesized in the frequency domain and then converted into the time domain using discrete Fourier transforms. The waveforms in the time domain can now be combined, where the waveform from each model is weighted based upon the SAF function, as outlined by Halabe et al. (1995b).

8.7 2-DIMENSIONAL EFFECTS

Many situations arise when it is useful to consider the 2-D nature of GPR interactions with subsurface features. This is particularly important when the GPR measurements are taken at different locations across the surface. Figure 8.4 shows the 2-D geometry of a set of scans taken with an isolated reflector, such as a rebar, at location x_r, y_r. The lateral position of the antenna is indicated by the coordinate ξ. The position of the reflector is indicated by the lateral, or cross-range, coordinate x; and by the vertical, or down range, coordinate y.

A common measurement technique is to take a series of GPR measurements at positions that are spaced equally along a straight line across the surface of the structure. This can be assembled into a 2-D graph of the return signals. When the 2-D graph is plotted in terms of amplitude vs. brightness, it is called a B-scan (brightness scan).

The oscillating electromagnetic field produced by an antenna can be quite complex, particularly in the near field. A reasonable approximation is to assume that the antenna produces circular (spherical in 3-D) waves. These waves propagate through the medium, reflect off of features and are then picked up by the receiving antenna. The location of a reflective feature is determined by measuring the time, Δt that it takes for a wave to travel from the antenna to the reflective feature and then back to the antenna, i.e.

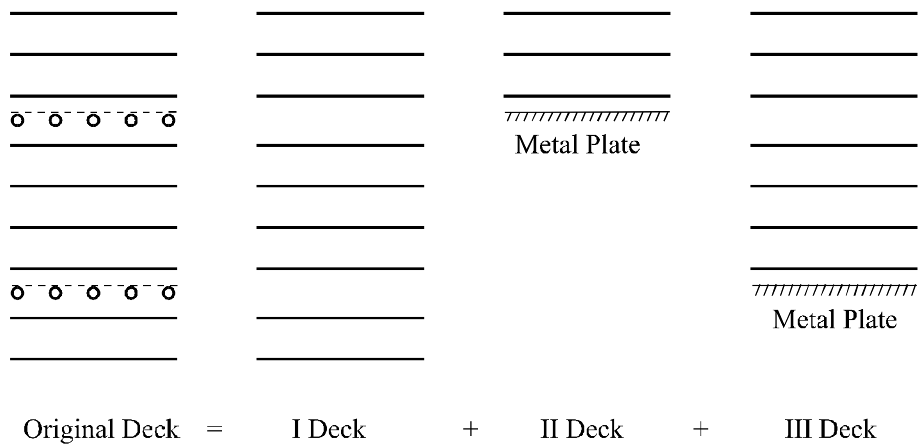

Figure 8.3 *Multilayered bridge deck model with reinforcing bar layer (Halabe et 1995b)*

$$r = \frac{1}{2} c_m \Delta t \tag{8.7.1}$$

where r is the distance from the antenna to the reflector, and c_m = the speed of light in the medium. The factor of ½ appears in (8.7.1) because the wave has to make a round trip. Equation (8.7.1) is particularly useful if the reflector is known to be directly downrange of the antenna, or if the reflector is planar, such as a layer of material with a refractive index that is different than the one above it. If the reflector is isolated and is positioned laterally from the source antenna, then (8.7.1) is still valid, but the travel distance, r, is the diagonal distance from the antenna to the reflector.

$$r = [(x_r - \xi)^2 + y_r^2]^{1/2} \tag{8.7.2}$$

From a single trace, it is not possible to discern simultaneously the cross range and down range position of an isolated reflector. If it is erroneously assumed that a reflector is immediately downrange from the antenna, when its position actually has a cross-range component as well, then the apparent position of the object is directly downrange at a distance equal to combined downrange and cross-range position, Figure 8.4.

If the antenna is slewed across the surface of the material under examination and a series of scans are taken, the time for a signal to travel round-trip from the antenna to the reflector is

$$\Delta t = \frac{2}{c_m}[(x_r - \xi)^2 + y_r^2]^{1/2} \tag{8.7.3}$$

For a fixed reflector position, equation (8.7.3) forms a hyperbola in ξ, and Δt. Figure 8.5 shows the hyperbolae that result from having a reflector at various depths. The deeper the reflector, the flatter the hyperbola appears. Figure 8.6 shows a B-scan image that results from the reflections off of a round aluminum bar that is being held in the air.

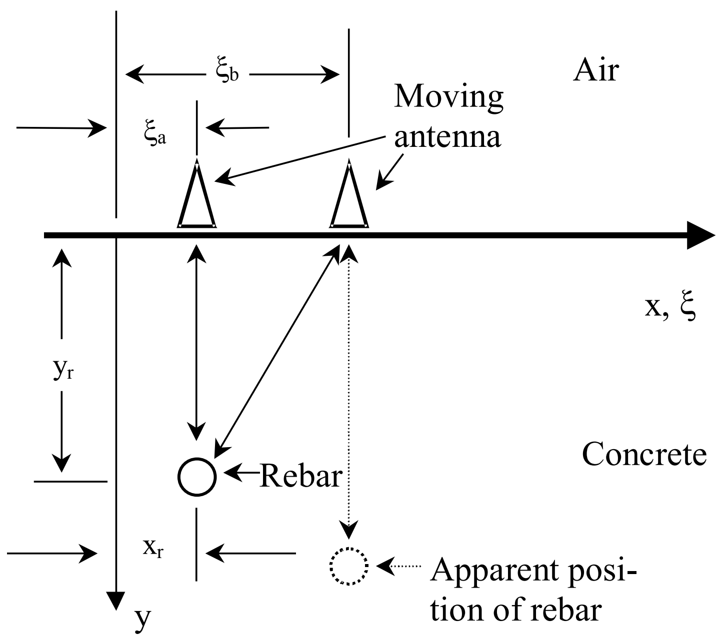

Figure 8.4 *2-D geometry of moving monostatic antenna and hyperbolic nonlinear distortion.*

The processing of the B-scan signals to remove the hyperbolic nonlinearity distortion has been the subject of much investigation by geophysicists and radar engineers over the past thirty years. A whole group of techniques that go by the names 'migration' and 'synthetic aperture radar' have been developed. These techniques will be discussed in more detail in Chapter 10.

The ability to resolve isolated features by reflecting radar waves is limited by the wavelength of the transmitted wave (or equivalently, the bandwidth of the system) and the geometry (Soumekh, 1999). The smallest dimension, Δ_y that can be resolved in the downrange, y, direction is

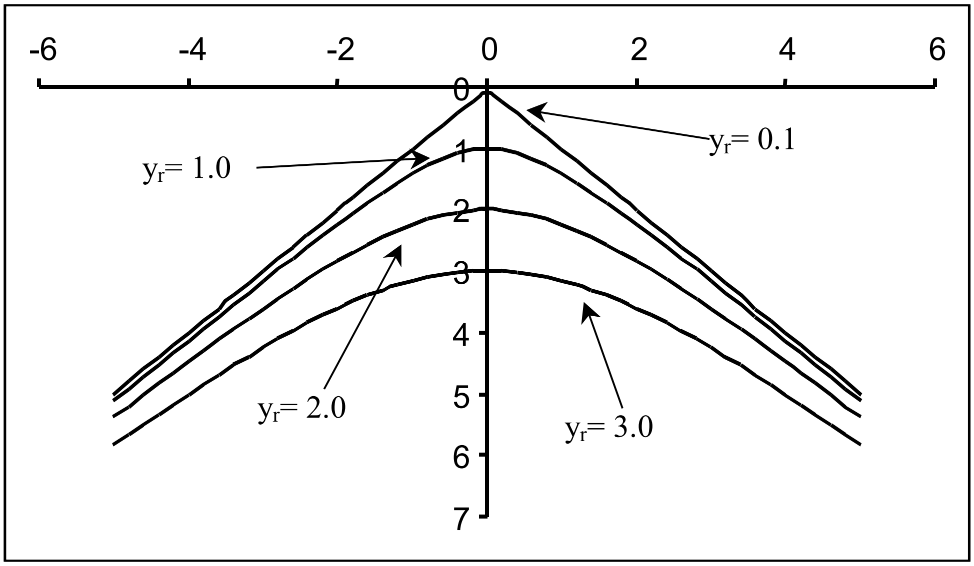

Figure 8.5 *Hyperbolic nonlinearity that results from moving an antenna relative to a fixed reflector at various depths. (Reflector cross-range x_r = 0)*

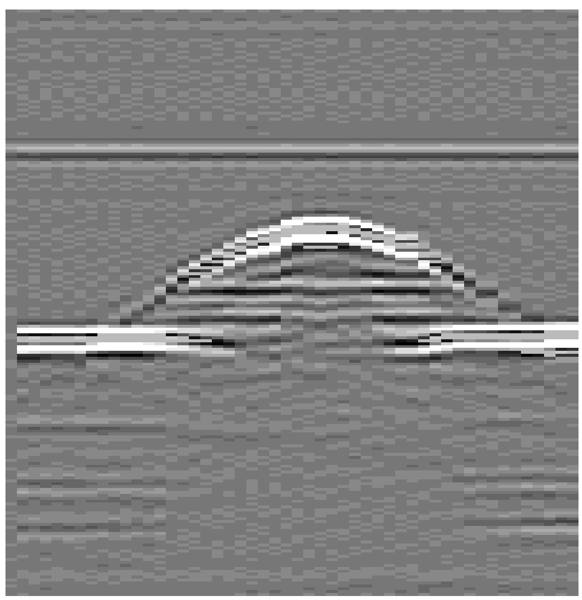

Figure 8.6 *B-scan of an aluminum bar in air over a piece of Echosorb™.*

$$\Delta_y = \frac{c}{4B_0} \qquad (8.7.4)$$

where c is the wavespeed, and B_0 is the bandwidth of the system. For a system with a bandwidth of 5.5 GHz in concrete with a relative dielectric constant of 5, the downrange resolution is 6mm. The smallest dimension, Δ_x that can be resolved in the crossrange, x, direction is

$$\Delta_x = \frac{c}{2f_{\max}} \tag{8.7.5}$$

where f_{max} is the maximum frequency. For a system with a maximum frequency of 6 GHz in concrete with a relative dielectric constant of 6, the crossrange resolution limit is 11 mm. It should be noted that these resolution limits are based on ideal conditions and assumptions. For real systems, the resolution limits are larger.

8.8 2-DIMENSIONAL FINITE DIFFERENCE MODEL

Numerical solutions to Maxwell's equations for electromagnetic wave propagation can be obtained by finite difference procedures. The finite difference technique approximates differential equations over continuous fields with difference equations acting on a grid of points (Taflove 1988). The finite difference algorithm used in this project is a two-dimensional version that was developed by Weedon (1994). It is based upon the finite difference time domain (FDTD) algorithm (Yee, 1966). The Yee FDTD algorithm applies second-order accurate central difference approximations for the space and time derivatives of the electric and magnetic fields, and can be used to calculate either scattered fields or total fields (Shlager, and Schneider, 1995). The algorithm includes a perfectly matched boundary layer which allows Maxwell's equations to be solved for problems involving theoretically infinite domains by the absorption of electro-magnetic waves at the boundaries of the computational domain (Taflove, 1988). The following sections summarize the derivation of the FDTD algorithm in 2D, and discuss the uses and limitations of such a model.

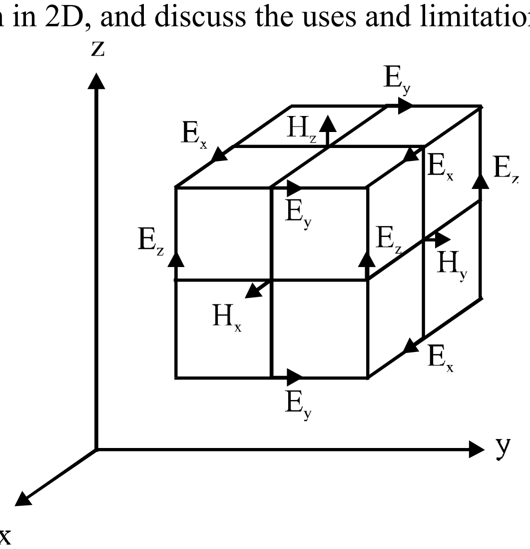

Figure 8.7 *Lattice unit cell in Cartesian coordinates Taflove, 1988).*

8.8.1 MAXWELL'S EQUATIONS IN 2-DIMENSIONS

Several assumptions which are used when Maxwell's equations are solved in 2D with the FDTD algorithm. It is assumed that the field components do not depend on the z-coordinate of a point, ε and μ are constant and the current J≡0. With these assumptions stated, the source in the problem is an incident wave that will be scattered after it encounters some obstacle. This problem can be further simplified if it is observed that in the EM field can be decomposed into transverse electric (TE) and transverse magnetic (TM) fields when ε and μ are held constant.

TE waves take the form

$H_x = H_y = 0, \quad E_z = 0,$

$$\frac{\partial H_z}{\partial t} = \frac{1}{\mu_o} \cdot \frac{\partial E_y}{\partial x} - \frac{1}{\mu_o} \cdot \frac{\partial E_z}{\partial y}, \tag{8.8.1.1}$$

$$\frac{\partial E_x}{\partial t} = \frac{1}{\varepsilon} \cdot \frac{\partial H_z}{\partial y} - J_{sx}, \quad \frac{\partial E_y}{\partial t} = \frac{1}{\varepsilon} \cdot \frac{\partial H_z}{\partial x} - J_{sy}$$

TM take the form

$E_x = E_y = 0, \quad H_Z = 0,$

$$\frac{\partial E_z}{\partial t} = \frac{1}{\varepsilon} \cdot \frac{\partial H_y}{\partial x} - \frac{1}{\varepsilon} \cdot \frac{\partial H_z}{\partial y} - J_{sz}, \tag{8.8.1.2}$$

$$\frac{\partial H_x}{\partial t} = -\frac{1}{\mu_o} \cdot \frac{\partial E_z}{\partial y}, \quad \frac{\partial H_y}{\partial t} = \frac{1}{\mu_o} \cdot \frac{\partial E_z}{\partial x}$$

Letting

$$\tau = ct = \sqrt{\frac{1}{\mu \varepsilon}}\, t \tag{8.8.1.3}$$

and,

$$Z = \sqrt{\frac{\mu_o}{\varepsilon_o}} = 376.7 \tag{8.8.1.4}$$

yields the finite difference equations for both the TE and TM cases.

For TE waves:

$$H_z^{n+1/2}(i+1/2, j+1/2) = H_z^{n-1/2}(i+1/2, j+1/2)$$
$$-\frac{1}{Z}\frac{\Delta \tau}{\Delta x}[E_y^n(i+1, j+1/2) - E_y^n(i, j+1/2)] \quad (8.8.1.4)$$
$$+\frac{1}{Z}\frac{\Delta \tau}{\Delta y}[E_x^n(i+1/2, j+1) - E_x^n(i+1/2. j)]$$

$$E_x^{n+1}(i+1/2, j) = E_x^n(i+1/2, j)$$
$$+Z\frac{\Delta \tau}{\Delta y}[H_z^{n+1/2}(i+1/2, j+1/2) - H_z^{n+1/2}(i+1/2, j-1/2)] - J_{sx} \quad (8.8.1.5)$$

$$E_y^{n+1}(i, j+1/2) = -Z\frac{\Delta \tau}{\Delta x}[H_z^{n+1/2}(i+1/2, j+1/2)$$
$$- H_z^{n+1/2}(i-1/2, j+1/2)] - J_{sy} \quad (8.8.1.6)$$

For TM waves:

$$E_z^{n+1}(i, j) = E_z^n(i, j)$$
$$+Z\frac{\Delta \tau}{\Delta x}[H_y^{n+1/2}(i+1/2, j) - H_y^{n+1/2}(i-1/2, j)] \quad (8.8.1.7)$$
$$-Z\frac{\Delta \tau}{\Delta y}[H_x^{n+1/2}(i, j+1/2) - H_x^{n+1/2}(i, j-1/2)] - J_{sz}$$

$$H_x^{n+1/2}(i, j+1/2) = H_x^{n-1/2}(i, j+1/2)$$
$$-\frac{1}{Z}\frac{\Delta \tau}{\Delta y}[E_z^n(i, j+1) - E_z^n(i, j)] \quad (8.8.1.8)$$
$$H_y^{n+1/2}(i+1/2, j) = H_y^{n+1/2}(i+1/2, j)$$
$$+\frac{1}{Z}\frac{\Delta \tau}{\Delta x}[E_z^n(i+1, j) - E_z^n(i, j)] \quad (8.8.1.9)$$

The initial field values are determined by the source current. For example, the initial $\vec{E}$ and $\vec{H}$ components for the TM case are calculated using Ampere's Law and the initial value for the source current.

8.8.2 BOUNDARY CONDITIONS

For the FDTD method, Yee (1966) modeled the boundary of the computational domain as a perfect conductor, which implies that the tangential components of the electric field vanish and that the normal components of the magnetic field vanish on the surface. The conducting surface will therefore be approximated by a collection of surfaces of cubes, the sides of which are parallel to the coordinate axes. In order to achieve this boundary condition, plane surfaces perpendicular to each of the coordinate axes, and containing points where the electric field vectors along the other axes are defined, are chosen. For example, a plane surface perpendicular to the x-axis is chosen so as to contain points where E_y and E_z are defined.

8.8.3 GRID SIZE AND STABILITY CRITERION

The FDTD method is restricted by the grid size, because over one increment in the space grid, the electromagnetic field cannot change. This means that in order to obtain meaningful results, it becomes necessary for the linear dimensions of the grid to be only a fraction of the wavelength. This requirement puts a restriction upon the time step (Δt) for the chosen grid dimensions (Δx, Δy, Δz) (Yee, 1966). If ε and μ are allowed to be constant, this restriction, known as the stability criterion, can be expressed as,

$$\left(\frac{1}{\Delta x^2}+\frac{1}{\Delta y^2}+\frac{1}{\Delta z^2}\right)^{\frac{1}{2}} > c_{\max}\Delta t \qquad (8.8.3.1)$$

Where c_{max} is defined as the maximum wave velocity through a given medium. This velocity can be further defined as ($c_o/\sqrt{\varepsilon_r}$), where c_o=2.997x10^8 m/s and ε_r = the relative permittivity of the medium.

8.8.4 PERFECTLY MATCHED BOUNDARY LAYER

The FDTD technique is limited by the fact that Maxwell's equations need to be solved in a discretized where the overall dimensions are limited. Nevertheless, problems involving infinite space domains can be modeled with the use of special conditions on the boundaries of the computational domain that absorb the outgoing waves (Berenger, 1994). Yee's method proposed placing a perfectly conducting surface on the boundary of the computational domain to allow for the absorption of outgoing waves. However, this and other techniques of outgoing wave absorption simulation are not faultless. A wave is absorbed without reflection in particular cases only, for instance, if it is plane and propagates perpendicular to the boundary. This will in turn lead to restrictions, namely, forbidding the treatment of some problems and placing constraints on others. Berenger (1994) overcomes many of the difficulties associated with boundaries by using the perfectly matched layer (PML) technique. In this case the finite difference computational domain appears in Figure 8.8.

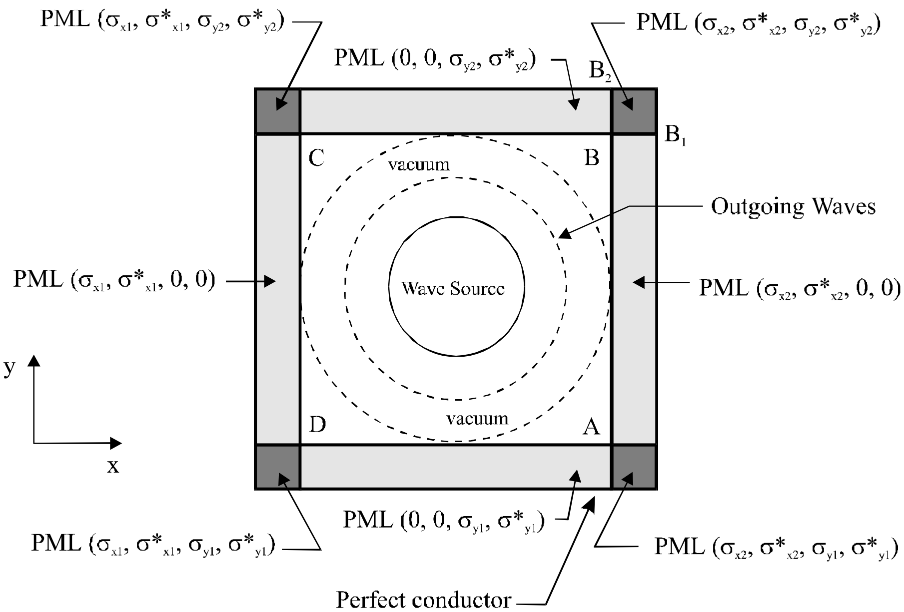

Figure 8.8 *The PML technique (Berenger, 1994*).

8.9 SYSTEM REQUIREMENTS

8.9.1 SYSTEM COMPONENTS

A GPR system has five main components: transmitter, isolator, antenna, receiver and signal processor. The function of the transmitter is to produce a rapidly-varying voltage signal that has sufficient power to be transmitted. The signal is usually either a narrow pulse, sinusoid with a duration ranging from 0.1 nanosecond to 1 nanosecond, or a high-frequency sine wave. The sine wave can be gated after a limited number of cycles, or swept through a range of frequencies, as in the step-frequency or continuous wave technique. The transmit signal is then sent to the antenna via high-fidelity cables. The cables are matched with respect to impedance so as to avoid any internal reflections that distort the echoes from the target. High-quality cables are also resistant to impedance changes and phase shifts when the cable is flexed. In the case of a mono-static system, where one antenna is used to both transmit and receive the electromagnetic pulse, an isolator is used to connect the transmitter to the antenna during the transmission mode. Once the system is switched from the transmit to the receive mode, the isolator blocks any electromagnetic power which may “leak” from the transmitter, thus protecting the sensitive receiver components from overload and damage (Lau, 1991). The receiver detects the reflected pulses from the target and amplifies them so that they may be processed.

8.9.2 TRANSMIT SIGNAL

The successful application of GPR for subsurface inspection requires selecting and tuning the operational parameters for a particular application (Moffatt and Puskar, 1976). The relatively small dimensions of delaminations and other features of bridge decks require an instrument with a high degree of resolution (Manning and Holt, 1984). Increasing the frequency will reduce the wavelength and produce the desired effect of improving resolution. However, as the wavelength approaches the physical dimension (diameter) of the reinforcement, a larger fraction of the inspection wave will be reflected producing larger interference signals. Also the signal attenuation with respect to the depth of penetration in the concrete often increases exponentially with frequency (Joyce, 1984).

Another factor which plays an important role in the resolution of a radar system is the shape of the transmit pulse. A transmit pulse which contains a high degree of "ringing" leads to distortions in the return waveform making data interpretation difficult.

8.9.3 NETWORK ANALYZER

Two primary methods are used to produce source pulses. The first uses a customized circuit to produce a specified pulse shape. This has the advantage of testing in the time domain. However the use of a specialized circuit is limited in flexibility with regards to the shape of the source pulse. The second option, which was chosen for the majority of the work in this project, is the step-frequency technique. An ideal instrument for low power step-frequency measurements is to use a network analyzer. A network analyzer produces sine waves at specified frequencies and amplitudes that can be combined to synthesize the desired source pulse. This method is fairly flexible in that it allows for the shape of the source pulse to be specifically designed and changed if necessary. Another advantage of the network analyzer is that it functions as the transmitter, receiver, and signal processor. When used in radar analysis, the network analyzer scans a selected frequency range and measures the amplitude and phase of the return waves at the frequencies corresponding to the original sine waves. This measured response is then used to produce the radar return waveform.

In using the network analyzer, the shape of the source pulse in the time-domain is essentially arbitrary, with the requirement that the pulse is limited to the bandwidth of the analyzer. When a pulse is synthesized, the network analyzer takes the source pulse in the time domain and converts it into the frequency domain using the discrete Fourier transform (DFT). The function in the frequency domain, which is a complex number, is then converted into a magnitude and phase. For each magnitude and phase, the network analyzer then produces a sine wave and the response is measured. In order to synthesize the return pulse in the time domain, each response in the frequency domain is then transformed using the inverse DFT. Usually the frequency domain representation of the source pulse is a tapered broadband amplitude spectrum with zero phase shift. This produces a single sharp time domain pulse. If the frequency amplitude spectrum is a Gauss-Hermite function, such as the Gauss bell curve or the Mexican hat function, the time domain representation will have the same shape (Wiener, 1958)

8.9.4 ANTENNA

The purpose of the antenna is to transmit an electromagnetic pulse into a medium and to receive the reflected waves. The ideal system would have an infinite frequency bandwidth. However, all radar systems are limited in bandwidth at both high and low ends. The highest frequency of the range limits the resolution of the system. The lowest frequency usually limits the penetration depth. The challenge is to design a GPR antenna with a wide frequency range.

The production of electromagnetic waves by an antenna is a complex interaction of the geometry of the antenna with dynamically varying electric and magnetic fields (Serway, 1990; and Balanis, 1997). The operating principle is that an alternating electromagnetic field is induced in the antenna, which causes charged particles (electrons) to oscillate and accelerate. The accelerated particles radiate energy in the form of electromagnetic waves. The geometry and coherence of the motion of the charged particles within the antenna governs the shape and strength of the radiated waves.

Radar systems use two main types of antenna configurations. One type is where separate antennas are used to transmit and receive the signals. This is known as a bistatic configuration. The second type is where a single antenna is used as both the transmitter and receiver. This is known as a monostatic configuration. More complex multiple antenna configurations are also possible. Each design has its draw backs. When a single antenna is used, it is difficult to switch between the transmit and receive modes. The switching device produces a less than optimum signal to noise ratio and causes signal loss on both transmission and reception. Alternatively, bistatic systems are larger, heavier, and more expensive (Smith, 1995).

Impedance matching is one of the key features that affects the performance of radar antennas. Impedance mismatches causes reflections. When the impedance mismatches occur inside the medium that is being examined, the reflections contain valuable information concerning the type and geometry of embedded features. When the impedance mismatches occur in the cabling and the antenna, the reflections do not contain useful information. Signal processing can easily discard the spurious reflections. However, the spurious reflections are a source of power loss, which reduce the penetrating depth and effective resolution of the system.

A standard quantitative assessment of impedance matching is the Standing Wave Ratio (SWR or VSWR for voltage standing wave ratio). When reflected waves exist within a waveguide, a standing wave will be formed by the transmitted and reflected wave. When a reflected wave is present in the antenna, it interferes with the original wave and causes a standing wave. The maximum value of the standing wave pattern occurs where the incident and reflected waves are in phase. The minimum value corresponds to destructive interference. When two waves have an opposite phase, the ratio of the maximum value to the minimum value of the standing wave within the antenna is defined as the voltage standing wave ratio **S** (VSWR or SWR). Equation (3) gives the definition of VSWR and its relationship with the voltage reflection coefficient (Γ). Γ was defined as the ratio of the amplitude of the reflected voltage wave to the amplitude of the incident voltage wave. When the value of the SWR closely approaches

1, the impedance match is satisfactory. If the impedance is totally mismatched, Γ is 1, and S approaches infinity (∞).

$$S = \frac{\left|\tilde{V}\right|_{\max}}{\left|\tilde{V}\right|_{\min}} = \frac{1+\left|\Gamma\right|}{1-\left|\Gamma\right|} \qquad (8.9.4.1)$$

The two most common antenna configurations are the horn antenna and the bowtie antenna. The horn antenna, which is the larger of the two, launches waves into the air and then into the pavement. The bowtie antenna is usually smaller and is placed directly on the ground. Figure 8.9 is a rendering of the horn and bowtie antennas (Smith, 1995).

In the GPR analysis of pavement analysis, air launched antennas are more effective than ground coupled antennas because they can be moved over the pavement at highway speeds. Friction and wear restricts ground coupled antennas to a normal walking speed. However, impedance mismatching of the horn antenna with the air causes losses. Another drawback to using air launched antennas is that as much as 50% of the pulsed energy bounces off the surface and never penetrates to the subsurface (Smith, 1995).

Despite these limitations, single air coupled horn antennas have proven to be the antenna of choice for evaluating pavement. The reason is that the radar only has to penetrate a few feet into the highway roadbed, therefore making signal losses due to a high s/n ratio and a 50% reflection from the surface acceptable, without sacrificing a great degree of resolution. This combined with the advantage of the horns traversing speed, improved impedance matching, and resolution make the horn antenna attractive. Additionally, for this application, the size is manageable.

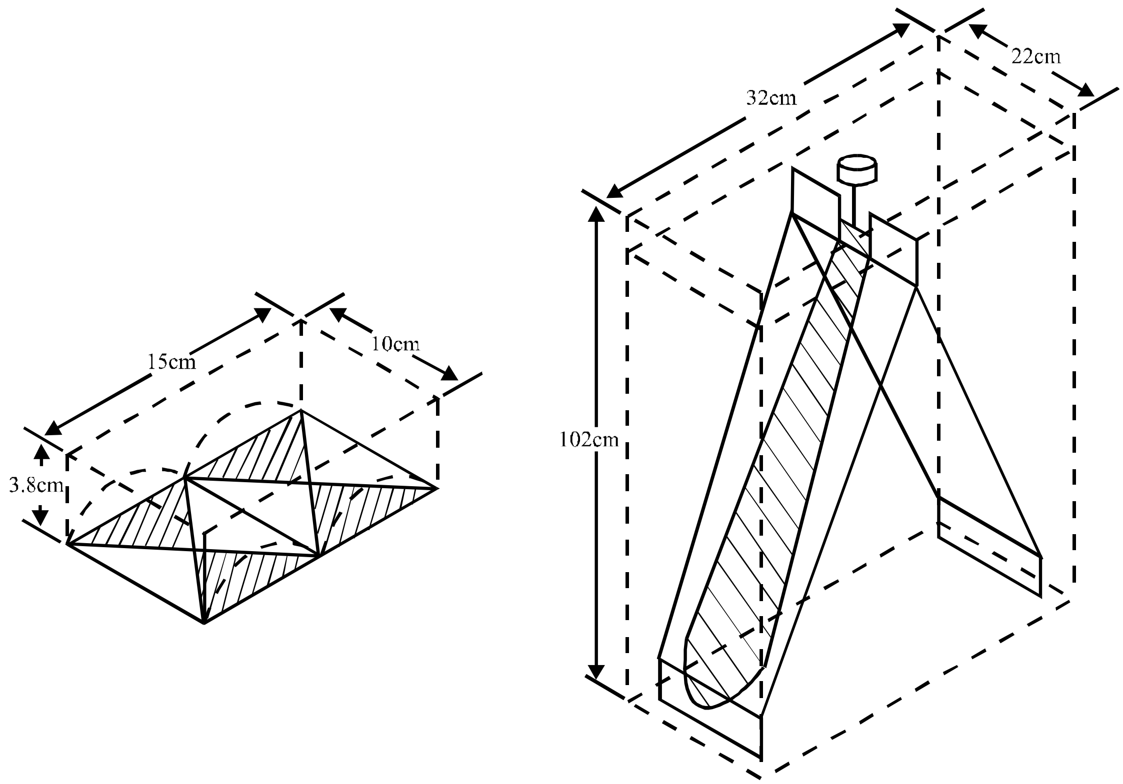

Figure 8.9 *Relative sizes of a 1 GHz bow-tie antenna (left) and a 1 GHz TEM horn antenna (Smith, 1995).*

9. NUMERICAL SIMULATION RESULTS

9.1 OVERVIEW

Numerical simulations were carried out to assess the potential performance of GPR systems for detecting features and damage in concrete pavements. Two sets of simulations were conducted. The first set of simulations used the 1-D layered media model developed by Halabe et al. (1997). The purpose of the 1-D model was two fold. The first objective was to examine whether small (~1 mm) delaminations, which are commonly seen in bridge decks, could be detected. The second was to examine possible methods of data representation that would allow these cracks to be seen clearly. In addition, this study included an initial examination of the role that antenna height plays in the detectability of these cracks, as well as the overall effect that it has on the reflected wave form. The second set of simulations used a two-dimensional finite difference time domain technique to model the propagation of waves in a planar representation of the GPR interactions with air, concrete, reinforcing bars, and damage. Since a fairly large number of approximations were incorporated in the use and development of the 1-D and 2-D simulations, the results of the simulations should be viewed only as an indicative guide as to the behavior of a GPR system. The data from the actual test results include non-idealized effects that can be significant.

The overall result of the 1-D simulations was that the reflections from air-filled delaminations could be detected, but that the alterations to the reflected signal were not real strong. The 2-D model results indicated that the reflections of the EM waves could be sensitive to antenna position.

9.2 1-D LAYERED MEDIA MODEL RESULTS

The Halabe model generates a single reflected waveform based upon a set of input parameters. This means that the waveform represents a single point along a bridge deck at one instant in time and does not include 2-D effects, such as cross-range reflections. Actual use of a GPR system in the field generates a large number of waveforms, one for each measurement location. The spatial variation of radar reflection signals that occurs in field situations was simulated by assembling an array of waveforms from 1-D simulations with corresponding spatial variations in the individual material properties in the 1-D simulations. A method of data processing that used the differences in the 1-D waveforms to indicate changes in the underlying material properties, i.e. a delamination, was examined.

Five different simulations were generated with variations in crack dimensions and properties, as well as antenna height. The purpose of the first three simulations was to examine the effect that a delamination of varying thickness had on the return waveforms. Each simulation contained one hundred waveforms, of which the first and last twenty five waveforms were created with a no-delamination condition and the middle fifty contained a symmetric delamination. This delamination gradually increased from 0.1 to 1.0 mm and then back to 0.1 mm in a manner that was laterally symmetric about a centerline. The simulations differed by the amount of water that was contained in the delaminated layer. These included a water-filled delamination, an air-filled delamination, and a delamination which contained fifty percent water and fifty percent air. Since the purpose of these simulations was to examine the detectability of small delaminations, all other parameters were held constant.

The 1-D program from Halabe allows the user to generate a simulated waveform in one of two ways. The first is through the use of the pre-processor, which allows the user to define a given set of parameters. Once this is done the program generates an input file and runs the simulation. Because the pre-processor does not allow for the inclusion of delaminations, it was necessary to generate individual input files independent of the pre-processor. This constitutes the second method of generating a waveform. The input files were set up using the CRIM model to compute the dielectric constant of the concrete. The porosity was set at a constant value of 0.180, and the variations for salinity, temperature and saturation followed the models described in Chapter 7. The antenna was set at a height of 203 mm (8"), the asphalt thickness was 80 mm (3.15"), and the dielectric constant of the asphalt was 5.00. The simulations were set up with two layers of rebar. Each layer of rebar had a diameter of 15 mm (.59") and a spacing of 150 mm (5.9"). For the input files that contained a delamination, an extra layer was added between the fourth and fifth layers of the no-delamination case. Half of the thickness of this layer was then subtracted from both the layer above and below so as to maintain a constant overall value for the thickness of the simulated deck.

The Halabe software uses a 1 GHz source pulse (Bhandarkar, 1993). The original pulse was contained in an ASCII file with 73 data points. Initial work with this pulse resulted in waveforms in which the return peaks were overlapped and difficult to differentiate. In order to "clean up" the return signals, and to simulate field conditions more realistically, a 2 GHz pulse was used that was created by eliminating every other data point from the 1 GHz ASCII file. This effectively doubled the frequency of the input pulse.

An examination of the individual waveforms for each group of simulations showed the water-filled and 50% water filled delaminations were clearly visible. However, the air-filled delamination was not. A single waveform from each simulation group can be seen in Figures 9.1 through 9.4. The delaminations which contained water showed up on the waveforms as an extra peak occurring just prior to the peak from the first layer of rebar. In addition, in the waveforms which had delaminations containing water, the peak from the first layer of rebar occurred later in time relative to the same peak occurring in the waveforms without a delamination. This time shift was due to the radar waves traveling much slower through water than concrete, which is indicated by the large difference in the dielectric constants of the two materials.

The next step was to examine possible methods of data representation and filtering which would enhance cracks detection. To this end the data for each simulation were put into a single array and plotted using Matlab. 2-D plots were generated in which time was represented by the y-axis. Waveform number, or distance along the deck, was represented along the x-axis. Amplitude was represented by a color. The resulting plots, as seen in Figures 9.5(a), 9.6(a), and 9.7(a), showed various attributes contained within the deck as stripes of color, or lightened bands in these black and white versions. The top surface of the deck, the asphalt- concrete interface, and the rebars could all be seen clearly, however only delaminations which contained water were visible in this format. Because the air filled delamination presented the greatest detectability problem, attention was centered around locating this defect. In an attempt to find the air filled crack, two filtering techniques were used. The first technique subtracted a baseline waveform containing the no-delamination condition from each of the one hundred waveforms contained in the simulation. This resulted in a zero amplitude for the waveforms that did not contain a delamination and caused the air filled delamination to become clearly defined. The plot generated using this technique for an air-filled delamination can be seen in Figure 9.5(b). The second filtering technique subtracted an average waveform from each of the one hundred waveforms contained within the simulation. Again the result, which can be seen in Figure 9.5(c), clearly showed the location of the air filled delamination. In addition to showing the delamination, these filtering techniques also demonstrated the ability of this model to simulate the resonance effects caused by the cracks.

These filtering techniques were also used for the simulations containing a water filled crack and a crack containing 50% moisture, as seen in Figures 9.6(b), 9.6(c), 9.7(b), and 9.7(c). Again, the cracks became clearly defined, and the resonance effects were visible.

These simulations illustrate the possibility of using a filtering technique to detect smaller amplitude reflections caused by cracks on the order of 1 mm in thickness. Of the two filtering techniques that were examined, the method of subtracting an average waveform as the baseline seems to be more applicable to actual field data.

Because the filtering techniques allowed the detection of air-filled delaminations, the next step was to examine the effect which antenna height had upon the return signals. To this end a second set of simulations were generated with an air-filled delamination identical to that described for the first set of simulations. The input files for these simulations were set up the same as for the first three simulations, with the only differences being the height of the antenna. Three sets of waveforms, each containing one hundred waveforms, were analyzed. The first simulation had the same set-up as that for the air-filled delamination case in the first group of simulations, and was therefore not repeated. The other two simulations looked at antenna heights of 102 mm (4”) and 305 mm (12”). A representative waveform at antenna heights of four inches and twelve inches can be seen in Figures 9.8 and 9.9, respectively.

Once again the resulting waveforms were grouped together into an array, and two dimensional color plots were generated using Matlab. The plots showed the only effect of changing antenna height to be an overall time shift of the resulting waveforms. This time shift correlates with an increase or decrease in the time of flight of the radar wave as a result of moving the antenna further from the deck or closer too it, respectively. The intensity of the return waveform was unaffected by any vertical change in the location of the antenna.

These plots were also filtered using both the undamaged and average slab waveform baseline subtraction techniques. As with the first group of waveforms, these filtering techniques allowed the delaminated areas to be seen clearly. In addition, the resonance effects associated with the reflection of the radar waves from the delaminated areas were clearly in evidence. The color (black and white) plots for each of these additional cases can be seen in Figures 9.10 and 9.11.

It should be noted that the use of this program to examine antenna location is limited by the fact that the transmitter and receiver are in the co-located monostatic configuration and can only be moved in the vertical plane. As a result, it was not possible to examine the effect of changing the horizontal separation between the transmitter and receiver.

9.3 2-D FINITE DIFFERENCE MODEL

Because delaminations in reinforced concrete bridge decks commonly occur close to the rebars themselves, they are difficult to detect using GPR. This is because the smaller reflections from the delaminations are masked by larger rebar reflections. It is attractive to minimize, or ideally eliminate, the rebar reflections. One method is to use a baseline subtraction filter as discussed in the previous section. A second method is to look more closely at the reflected signals from each component of the deck in order to optimize the radar configuration. Ideally this would result in an enhanced reflection from the delamination and a smaller reflection from the rebar. The 2-D program was used to look at the reflected signals, in both the time and frequency domain, from the rebar and a 1 mm delamination as a function of transmitter/receiver location.

9.4 GENERATION OF REFLECTED FIELDS

The 2-D finite difference code was set up to produce a total field for any given receiver location. The total field contains the incident field as well as the reflected field from any objects contained within the simulation grid. The incident field can be defined as the field generated when the object of interest is not present. To examine the reflected field from an object, it is necessary to generate an incident field without the object of interest and a total field with the object of interest in place. The two can then be subtracted in order to obtain the reflected field from the object of interest. Therefore in order to obtain the reflection caused by the rebar layer, it was necessary to generate a waveform for a bridge deck with rebar (total field) and a bridge deck without rebar (incident field). By subtracting the two, the resultant waveform was the reflection from the rebar alone. This same procedure was followed to examine the reflection from a delamination.

9.5 SCATTERING AMPLITUDE SPECTRUM AND REFLECTED ENERGY

In order to examine the reflected fields from different components of the bridge deck, such as delaminations and rebars, it was necessary to develop a method of comparison. The scattering amplitude spectrum for each combination of variables was computed, which can be defined as the spectrum of the reflected field from the element normalized by the spectrum of the reflected field from the entire deck without the given component. The spectra were calculated by taking the Fast Fourier Transform (FFT) of the time domain signals. The scattering amplitude spectrum gives a quantitative value, in dB, for the detectability of the object and the frequency at which this detectability is optimized.

In addition to looking at the scattering amplitude spectrum for a given component, the energy contained within the reflected wave from that component, normalized by the reflected energy from the entire deck, was also examined. By calculating the normalized reflected energy, it became possible to optimize the transmitter and receiver locations based upon a single quantitative value. This energy value was obtained by calculating the area under the reflected wave from a single component (i.e. a delamination), and then dividing that number by the area under the reflected wave from the entire deck. The resulting number was the fraction of energy reflected by the single component relative to the total amount of energy reflected by all of the components in the deck. Based upon this calculation it was then possible to examine the reflected energy at each transmitter/receiver separation. This enabled maximizing the amount of energy being reflected from a delamination and minimizing the energy being reflected from other deck components.

9.6 SIMULATION SET 1

The first set of simulations were set up to examine the transmitter/receiver separations of 64 mm and 130 mm at a constant transmitter/receiver height of 25 mm (~1.0”) above the asphalt surface. The grid contained 198 grid points in the x direction and 332 grid points in the y direction, where Δx and Δy were set at 2.00 mm and 1.00 mm, respectively. The time step (Δt) was set at 2.35e-12 seconds in order to satisfy the stability criteria. The absorbing boundary condition was set at 8 grid points in the x direction and 16 grid points in the y direction so as to maintain a uniform thickness of 16 mm. The deck itself included a 50 mm (1.97”) thick layer of asphalt, a 150 mm (5.9”) thick layer of concrete, and three rebars 160 mm (.63”) in diameter which were set 50 mm (1.97”) below the top surface of the concrete and 130 mm (5.1”) apart on center. A sketch of the simulation grid, including relative transmitter and receiver locations can be seen in Figure 9.12. The asphalt was assigned a dielectric permittivity of 5.0 and a conductivity of 0.0. The concrete was assigned a dielectric permittivity of 7.5 and a conductivity of 0.15. The free space surrounding the deck was assigned a dielectric permittivity of 1.0 and a conductivity of 0.0.

In order to create the delamination condition, a fourth layer was added to the simulation grid. This layer was 1 grid point (1 mm) in thickness and it was located 2 mm above the rebar layer and 48 mm (1.9") below the top surface of the concrete. The dielectric properties assigned to this layer depended upon the type of delamination that was being simulated. For the air-filled delamination the dielectric constant, ε_r, was set at 1.0 and the conductivity, σ, was set at 0.0. The water-filled delamination was assigned a dielectric constant, ε_r, of 78, assuming the water to be at room temperature, and a conductivity, σ, of 0.88. The conductivity value was determined using the equation for conductivity reported by Klein and Swift (1977) and assuming a salinity of 5.0 ppt.

For the first set of simulations the transmitter was set up at the mid-point of the grid in the *x* direction, and 25 mm (1") above the top surface of the asphalt in the *y* direction. Five receivers were used, the first being co-located with the transmitter, and the other four were located 64 mm (2.5") and 130 mm (5.1") away from the transmitter in either direction and at the same height.

9.7 SIMULATION SET 2

The second set of simulations were used to look at transmitter/receiver separations of 194 mm (7.6") and 260 mm (10.2") at a constant height of 25 mm (1") above the asphalt surface. The simulation grid was identical to that used for the first group of simulations.

9.8 SIMULATION SET 3

The third set of simulations were used to look at transmitter/receiver separations of 64 mm (2.5") and 130 mm (5.1") at a constant height of 75 mm (2.95") above the asphalt surface. In order to accommodate the increased height of the antennas, it was necessary to modify the simulation grid. This modification involved increasing the number of grid spaces in the y direction to 457 as opposed to the original 332. This simulation only required an increase of 50 grid points in order to accommodate the increased height, however subsequent simulations would require more grid cells. In order to simplify future simulations, the number of grid cells in the y direction was modified to accommodate a maximum transmitter/receiver height of 152 mm (5.98"). All other attributes of the simulation grid were maintained.

9.9 SIMULATION SET 4

The set-up for this set of simulations was identical to that for Set 3. This set examined transmitter/receiver separations of 194 mm (7.6") and 260 mm (10.2") at a constant height of 75 mm (2.95").

9.10 SIMULATION SET 5

For this group of simulations the height of the transmitter and receivers was increased to 152 mm (5.9") above the top of the asphalt layer. The separation between the transmitter and the receivers was 64 mm (2.5") and 130 mm (5.1") in either direction. The simulation grid remained constant.

9.11 SIMULATION SET 6

The set-up for this set of simulations was identical to that of Set 5. This set examined transmitter/receiver separations of 194 mm (7.6") and 260 mm (10.2") at a constant height of 152 mm (5.98").

9.12 RESULTS

Five simulations were run for each of the six set-ups described above. These included the entire deck with rebar, the entire deck without rebar, the entire deck with rebar and a water-filled delamination, the entire deck with rebar and an air-filled delamination, and an empty grid. The purpose of the empty grid was to simulate wave propagation through air. This collection of simulations allowed for the examination of the reflections from an air-filled delamination, a water-filled delamination, and the rebar layer individually at each transmitter/receiver separation distance. In addition it was possible to generate waveforms similar to those generated by the 1-D model, in which the reflections from all of the elements contained within the deck were visible on one waveform.

The scattering amplitude spectrum and reflected energy for the water-filled delaminations and the air-filled delaminations were also computed in order to examine the detectability of these defects. This detectability was investigated as a function of transmitter/receiver separation distance in an attempt to determine what separation distance maximized the reflected signal from these defects.

For each antenna height there were five different combinations of transmitter/receiver separations, resulting in fifteen scattering amplitude spectrum plots. Because of similarities in the spectra it was difficult to determine the optimal conditions based upon these spectra alone. For this reason the relative reflected energy value was used to determine the transmitter/receiver locations for each antenna height at which the largest fraction of energy was reflected from a given delamination. The scattering amplitude spectrum at the optimal location was then analyzed to examine the spectral content of the reflected energy.

Plots of the relative reflected energy as a function of transmitter/receiver separation distance for a water-filled delamination and an air-filled delamination can be seen in Figures 9.13 and 9.14, respectively. At antenna heights of 25 mm and 75 mm, there is a very distinct energy peak at a separation distance of 130 mm. This separation distance corresponds to the separation distance between the rebars contained within this model. This would suggest that at either of these heights, a transmitter/receiver separation of one increment of rebar separation results in an optimal detectability of a delamination on the order of 1 mm.

An examination of the reflected wave from the entire deck reveals another advantage to a transmitter/receiver separation of one increment of rebar separation. Due to geometric effects, as the transmitter and receiver are separated, the reflection from the rebar layer is minimized. When the transmitter and receiver are co-located above a rebar, the receiver picks up a reflection from the rebar, as well as from the neighboring rebars located equal distances apart on either side. Because of the different distances that the wave must travel, as demonstrated in Figure 9.15, the receiver picks up a reflected signal from the rebar located directly below it. At some point later in time a second signal appears as a result of the neighboring rebar. By separating the transmitter and receiver by a distance equal to the rebar separation, the distance that the wave travels can be equalized. This results in a single reflected peak. Separation past one increment of rebar separation serves to further decreases the reflection from the rebar layer further. The effect which transmitter/receiver separation has upon the reflected waveform from a sound deck can be seen in Figure 9.16.

At an antenna height of 152 mm, the maximum reflected energy values occur at separation distances of 65 mm and 260 mm. These separation distances correspond to one half the separation distance between the rebars and twice the separation distance between the rebars respectively. In this case in order to determine the optimal locations for the transmitter and receiver it was necessary to examine the reflected waves from the entire deck. At a separation distance of 260 mm, the peak occurring as a result of the reflection from the rebar is slightly smaller in magnitude than the reflection occurring at a separation distance of 65 mm. Additionally at 65 mm, there is a double peak corresponding to the reflections occurring as a result of neighboring rebars. This neighboring effect is minimized at a separation distance of 260 mm.

Further examination of the reflected waveforms for an antenna height of 152 mm and a transmitter/receiver separation of 260 mm reveals another positive result. In this configuration there is a slight, but noticeable change in the reflected waveform as a result of the presence of an air filled delamination. Because this change is noticeable, this suggests that the use of a filtering technique, such as was used with the 1-D simulations, would allow for a positive identification of air-filled delaminations on the order of 1 mm in thickness. The water-filled delaminations are much more noticeable in the reflected waveforms when compared to the reflections from a sound deck. A comparison of all three waveforms can be seen in Figure 9.17.

Based upon relative reflected energy values and an examination of the reflected waveforms, the optimal transmitter/receiver separation would be 260 mm at a height of 152 mm. In addition to maximizing the relative reflected energy, this antenna height is also advantageous in that it allows for the incident signal to be easily differentiated from the reflected signal. When a bi-static system is used, the receiving antenna will detect both the incident signal generated by the transmitting antenna, as well as the reflected signal from the object under test, which in this case is the bridge deck. If the time of flight for the incident wave is greater than the two way travel time of the reflected wave, the two will overlap leading to a distorted signal coming from the bridge deck. It is a simple procedure to remove the incident signal through processing, however elimination of this step and the use of a time window would allow for easier data processing. At the proposed antenna locations, the incident signal is clearly identifiable.

The scattering amplitude spectra for an air-filed delamination and a water-filled delamination at these optimized antenna locations can be seen in Figure 9.18. In both cases these spectra are relatively flat across the frequency span. This would indicate that there is no dominant frequency that sets up a resonant condition. These plots also show that the magnitude of the reflected peak from the air-filled delamination is 20 dB lower than that of the reflected peak from the water filled delamination. This difference in magnitude is the reason for the difficulty in detecting air-filled cracks with a thickness on the order of 1 mm.

In conclusion, although difficult to detect, the results of these simulations do show that by optimizing antenna locations and using a filtering technique it is possible to positively identify these cracks.

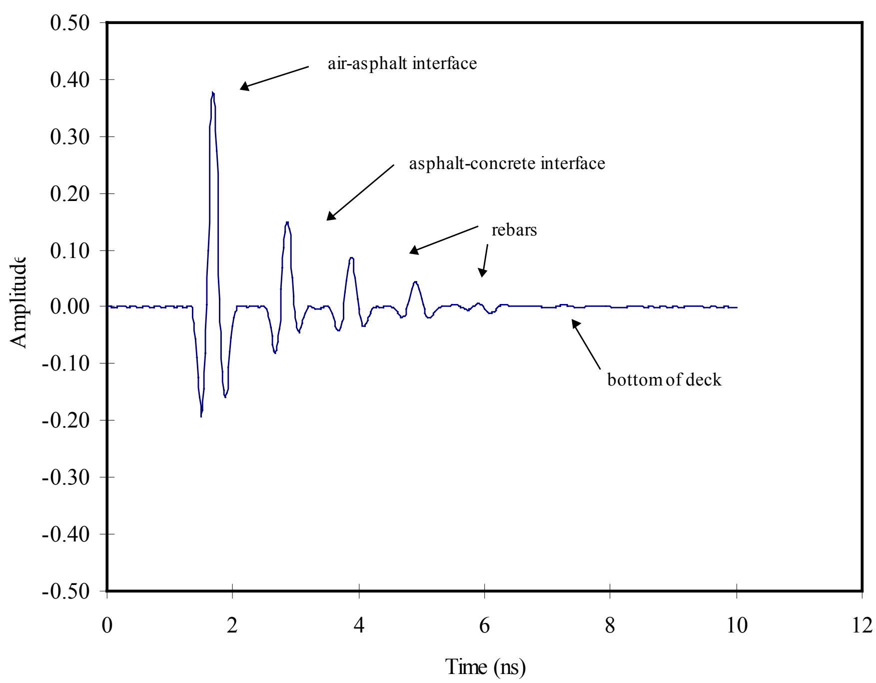

Figure 9.1 Waveform generated for a sound bridge deck.

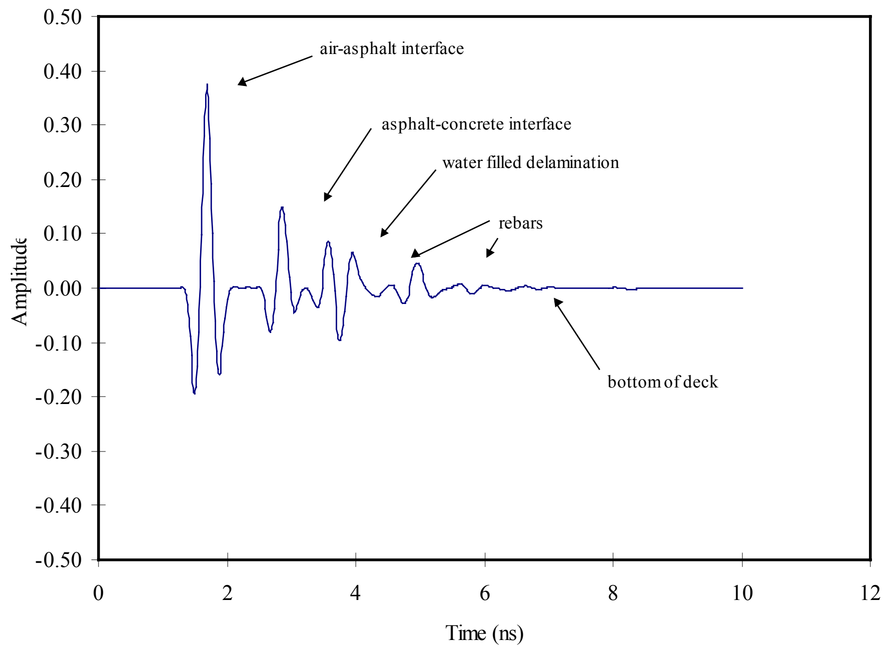

Figure 9.2 Waveform generated for a 1mm water-filled delamination.

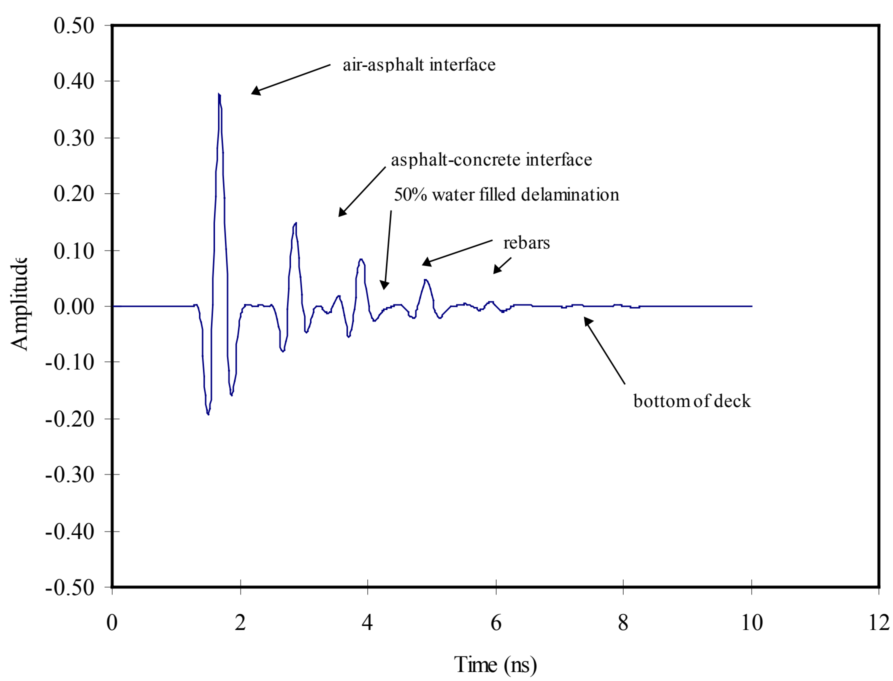

Figure 9.3 Waveform generated for a 1mm 50% water-filled delamination

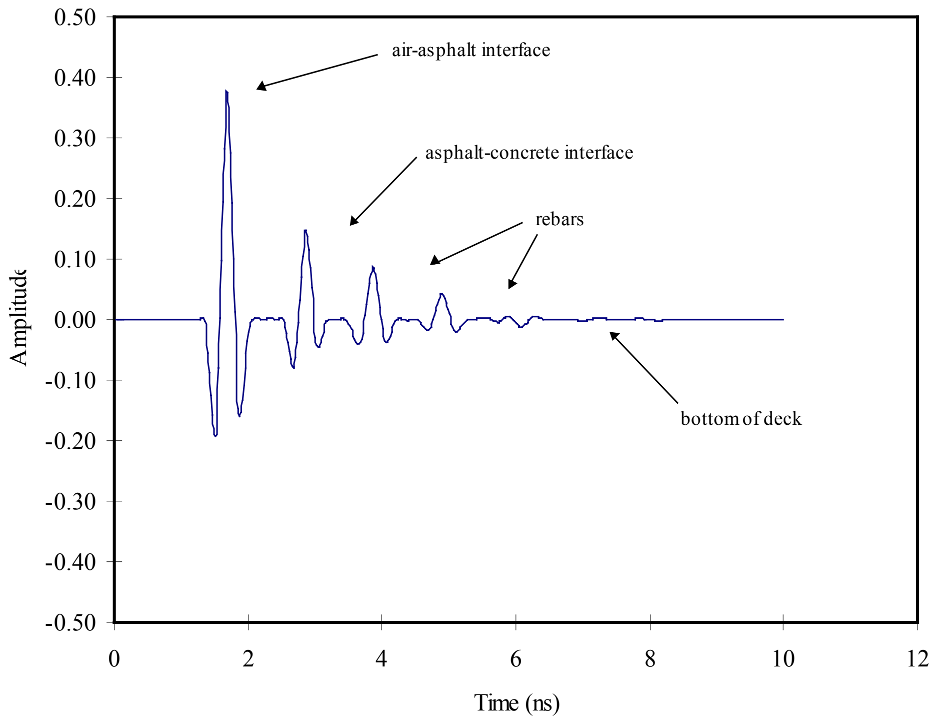

Figure 9.4 Waveform generated for a 1mm air-filled delamination.

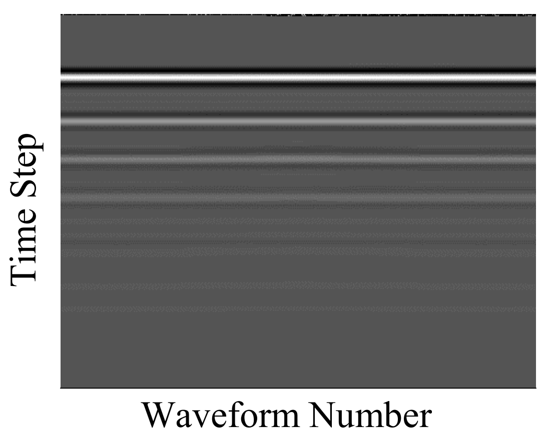

Figure 9.5a *Unfiltered intensity plot for air-filled delamination.*

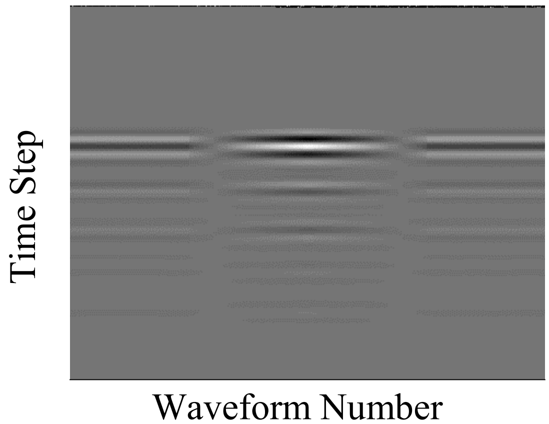

Figure 9.5b *Intensity plot for air-filled delamination using average waveform filter.*

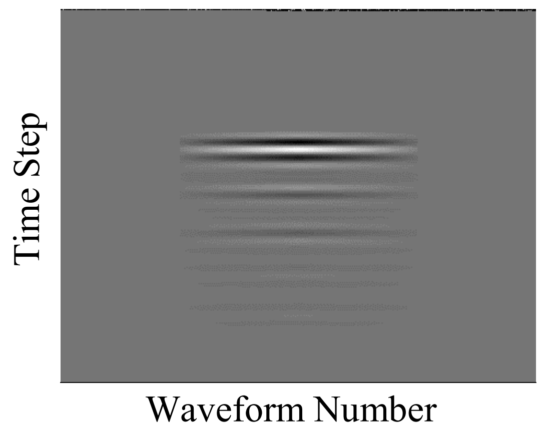

Figure 9.5c *Intensity plot for air-filled delamination using first waveform filter.*

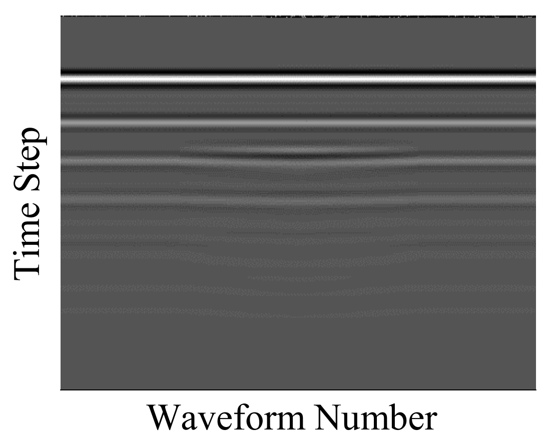

Figure 9.6a *Unfiltered intensity plot for water-filled delamination.*

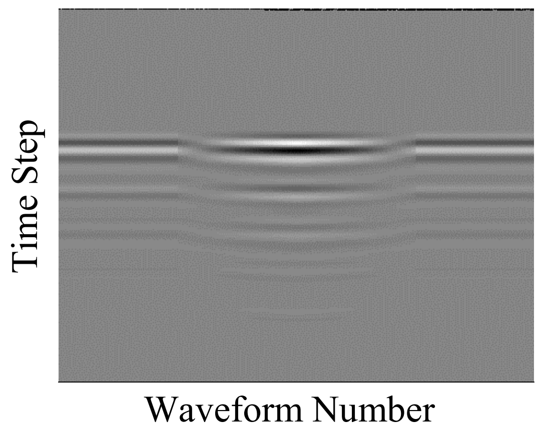

Figure 9.6b *Intensity plot for water-filled delamination using average waveform filter.*

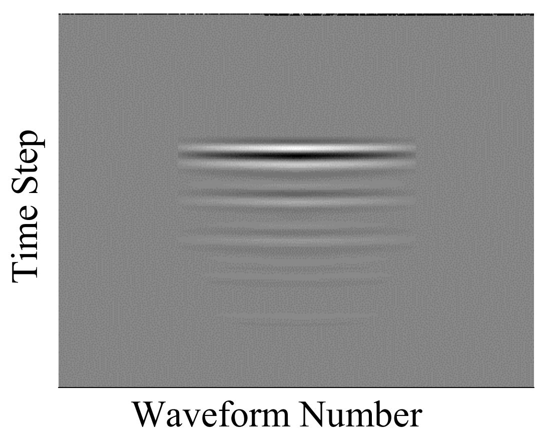

Figure 9.6c *Intensity plot for water-filled delamination using first waveform filter.*

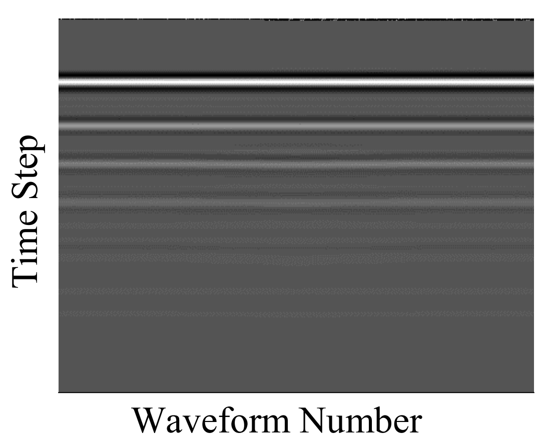

Figure 9.7a *Unfiltered intensity plot for 50% water-filled delamination.*

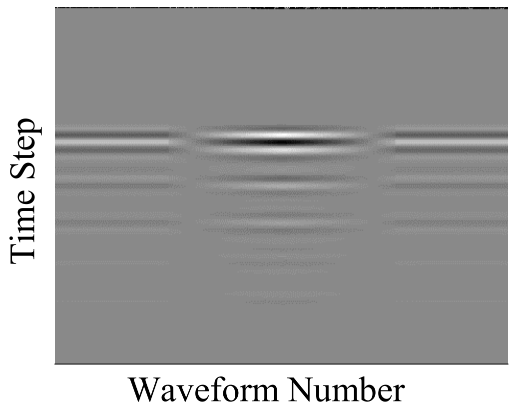

Figure 9.7b *Intensity plot for 50% water-filled delamination using average waveform filter.*

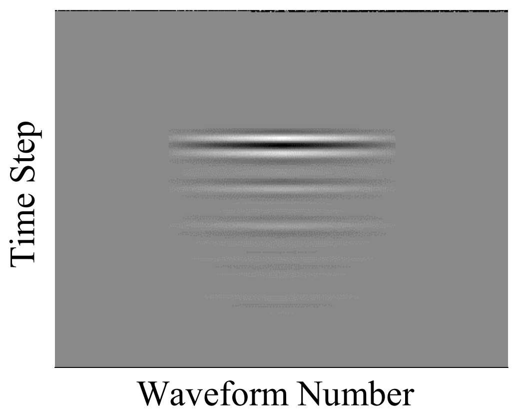

Figure 9.7c *Intensity plot for 50% water-filled delamination using first waveform filter.*

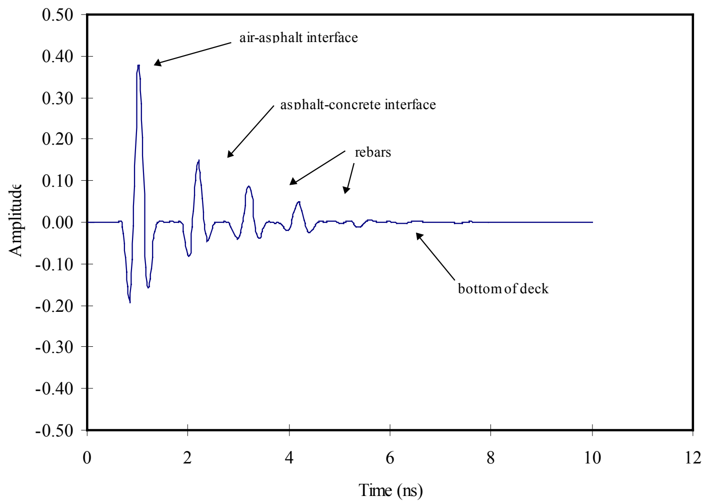

Figure 9.8 *Waveform generated for a 1 mm air-filled delamination, antenna height =102 mm (4in)*

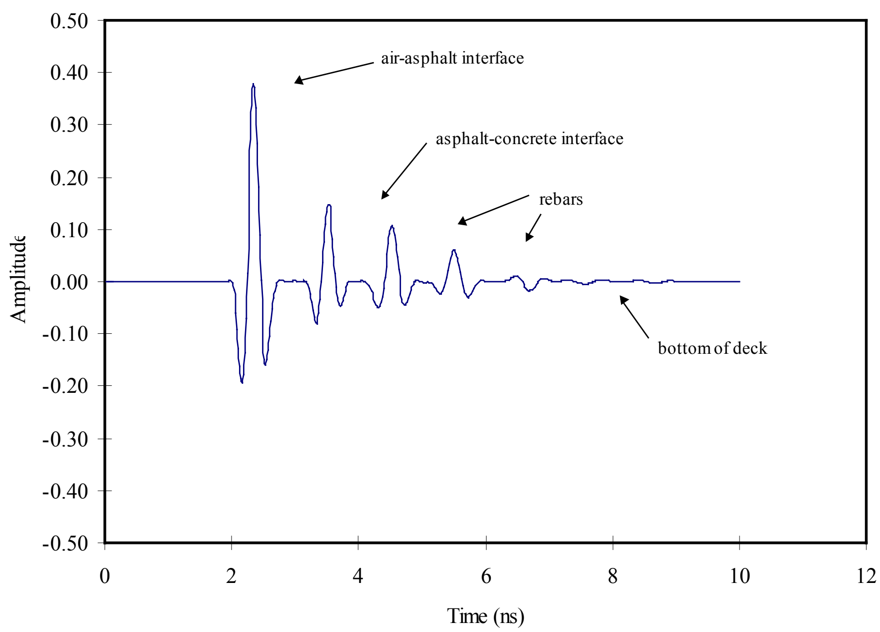

Figure 9.9 *Waveform generated for a 1 mm air-filled delamination. (antenna height =305 mm =12in)*

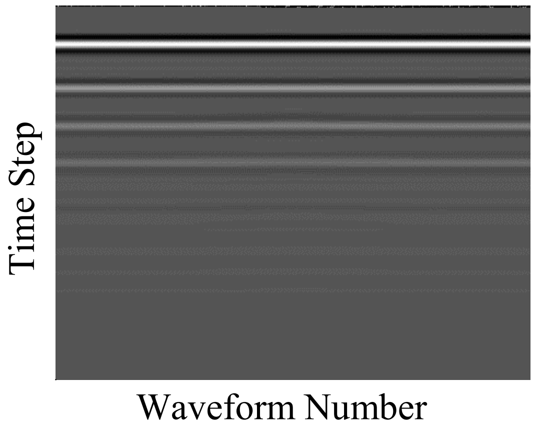

Figure 9.10a *Unfiltered intensity plot for air-filled delamination, antenna height = 102 mm (4")*

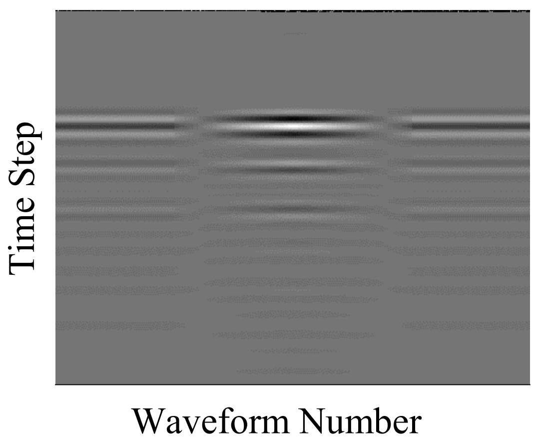

Figure 9.10b *Intensity plot for air-filled delamination using average waveform filter, antenna height = 102 mm (4").*

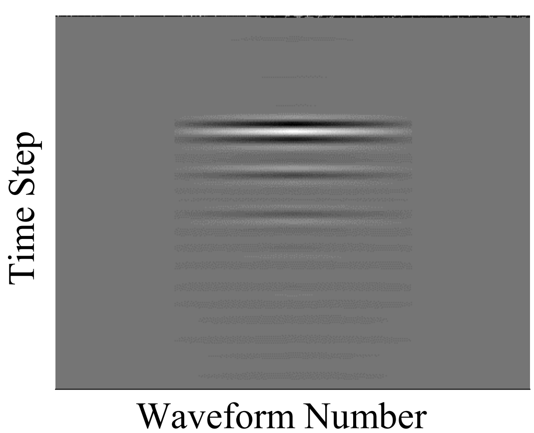

Figure 9.10c *Intensity plot for air-filled delamination using first waveform filter, antenna height = 102 mm (4")*

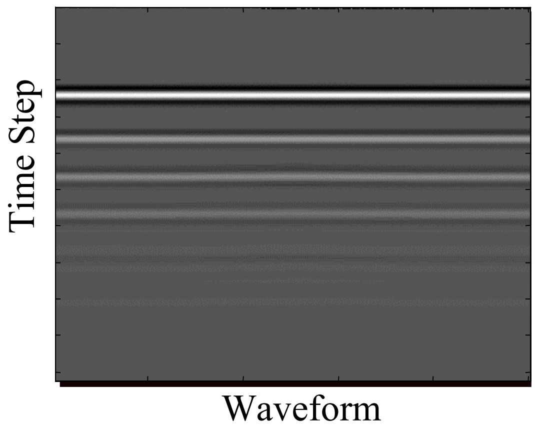

Figure 9.11a *Unfiltered intensity plot for air-filled delamination, antenna height = 305 mm (12").*

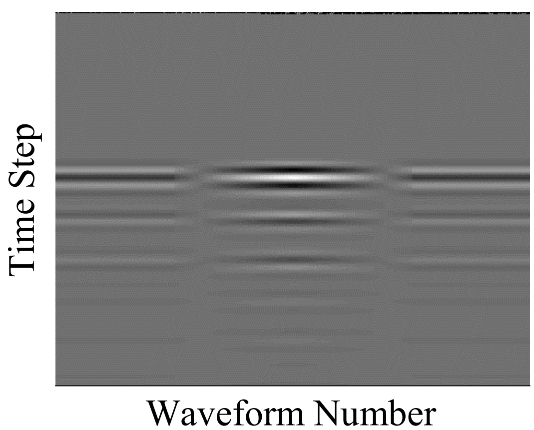

Figure 9.11b *Intensity plot for air-filled delamination using average waveform filter, antenna height = 305 mm (12").*

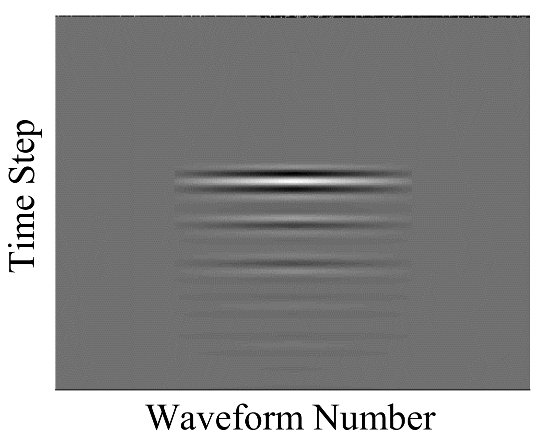

Figure 9.11c *Intensity plot for air-filled delamination using first waveform filter, antenna height = 305 mm (12").*

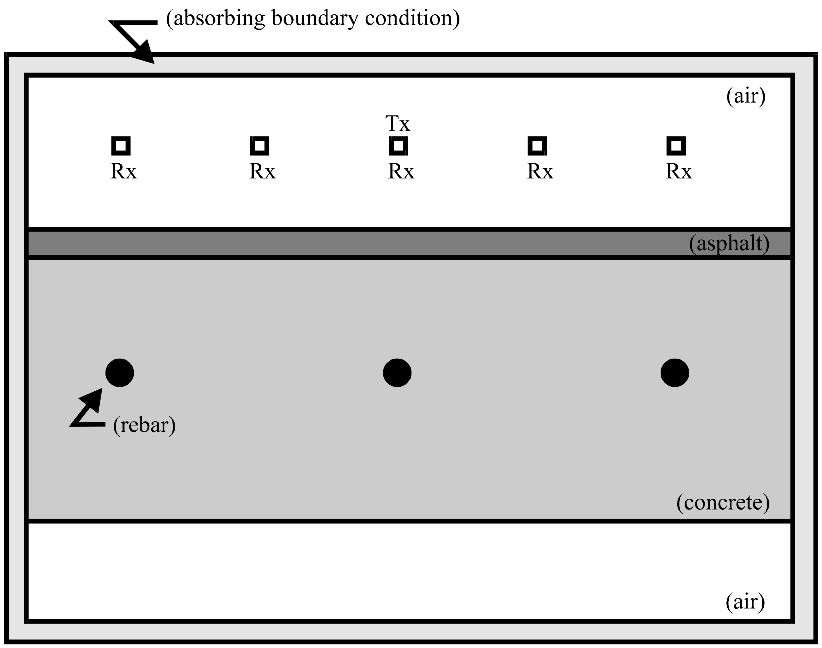

(a)

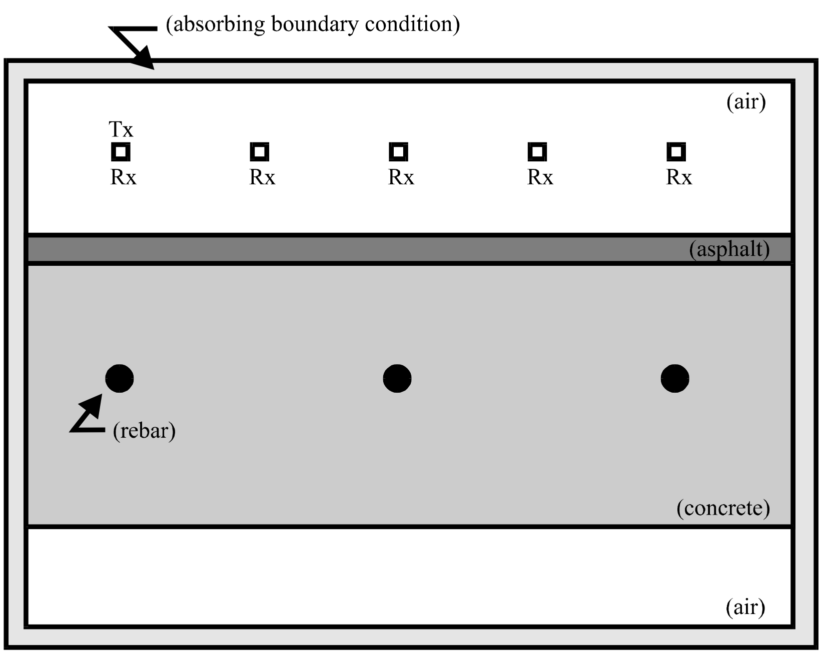

(b)

Figure 9.12 *Sketch of simulation space for 2-dimensional FDTD model relative transmitter/receiver locations for simulations 1, 3, 5 relative transmitter/receiver locations for simulations 2, 4, 6.*

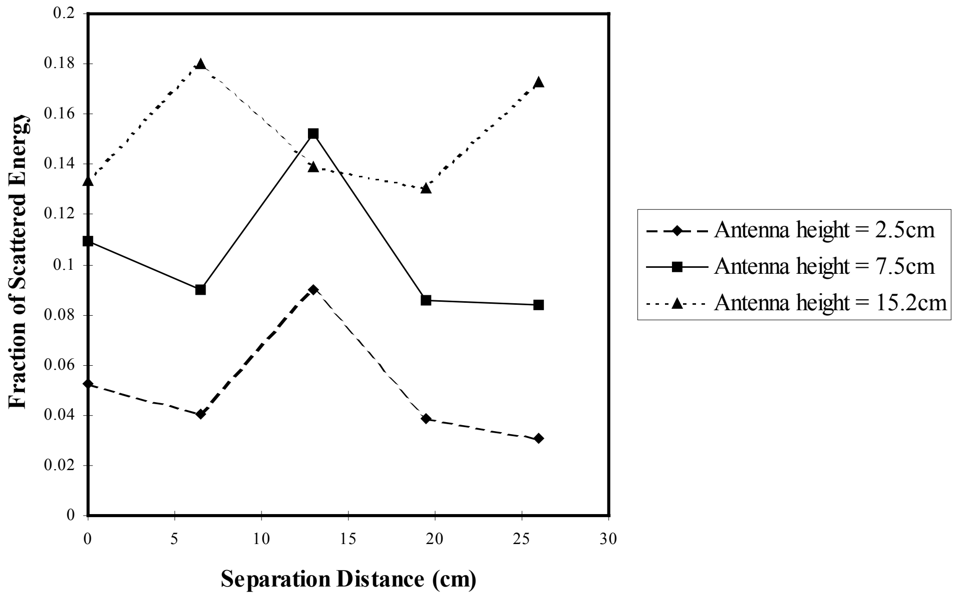

Figure 9.13 *Relative reflected energy as a function of antenna separation for a water-filled delamination.*

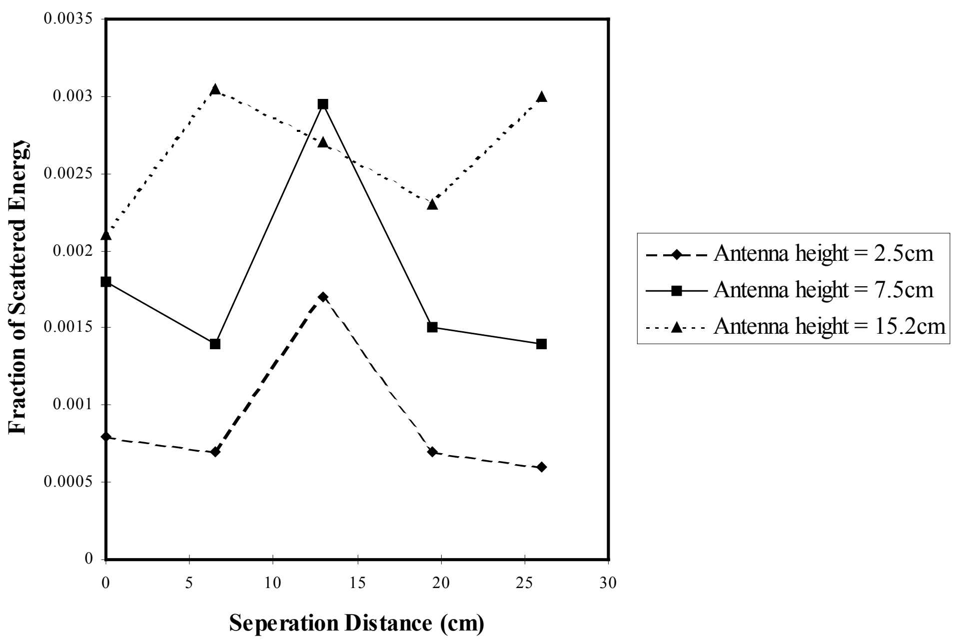

Figure 9.14 *Relative reflected energy as a function of antenna separation for an air-filled delamination.*

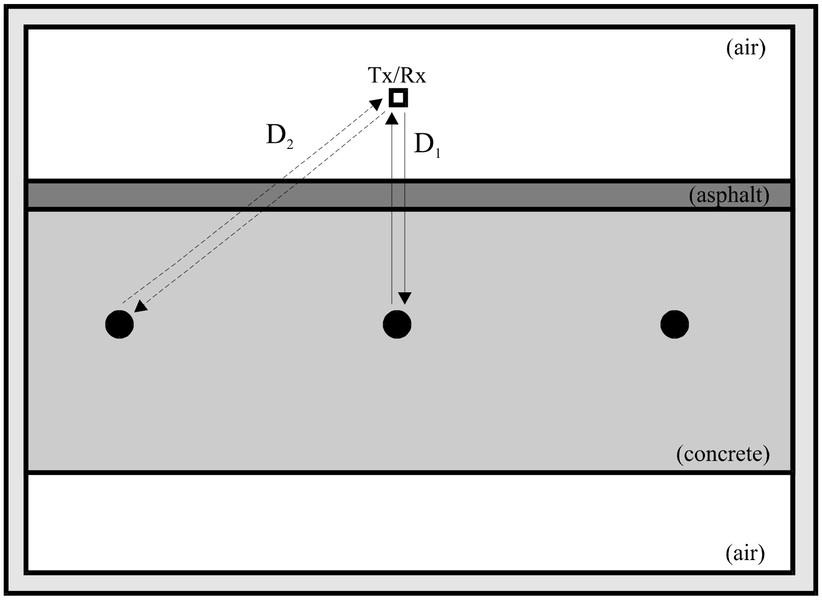

(a)

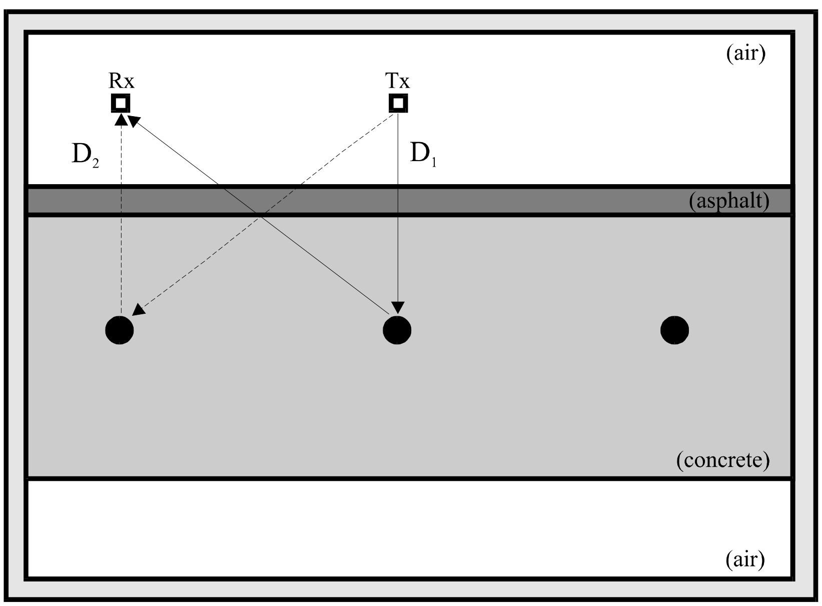

(b)

Figure 9.15 *Sketch of distances radar wave must travel for different antenna separations. (a) $D_1 \neq D_2$ (b) $D_1 = D_2$.*

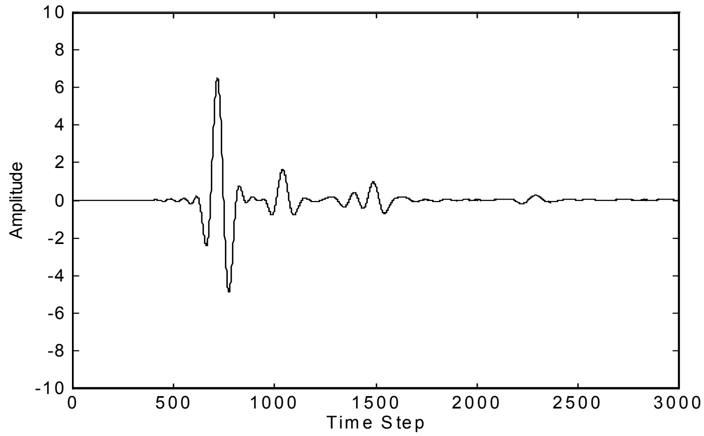

(a)

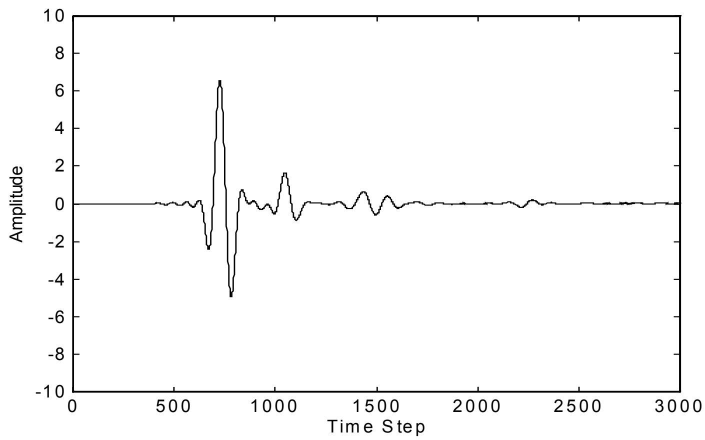

(b)

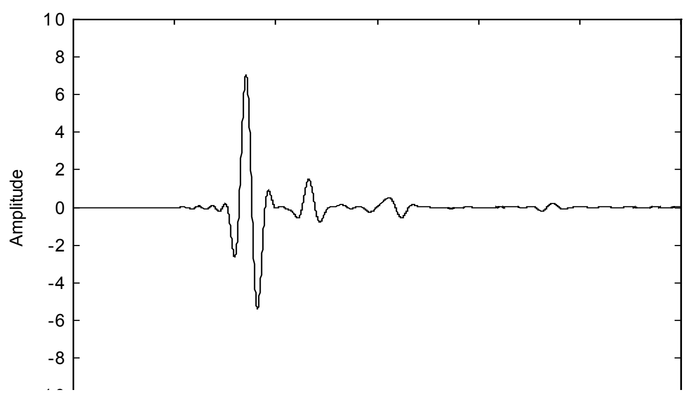

(c)

Figure 9.16 *2-dimensional finite difference simulation plots of the reflected waveform from a sound bridge deck at different transmitter/receiver separation distances. (a)co-located (b) separation distance = 65 mm (c) separation distance = 260 mm.*

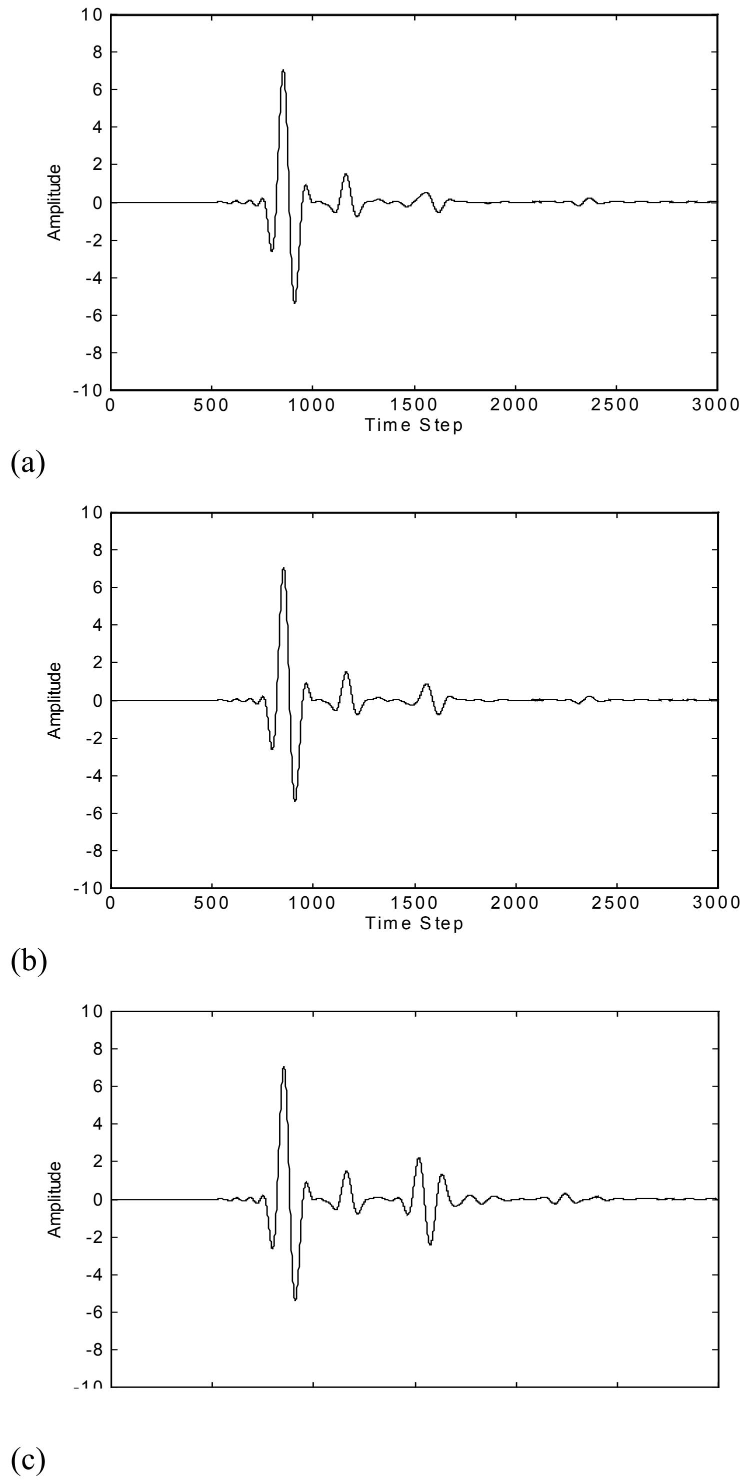

Figure 9.17 *Simulated reflected waveforms at a transmitter/receiver separation distance of 260 mm (a) sound deck (b) deck with air-filled delamination (c) deck with water-filled delamination.*

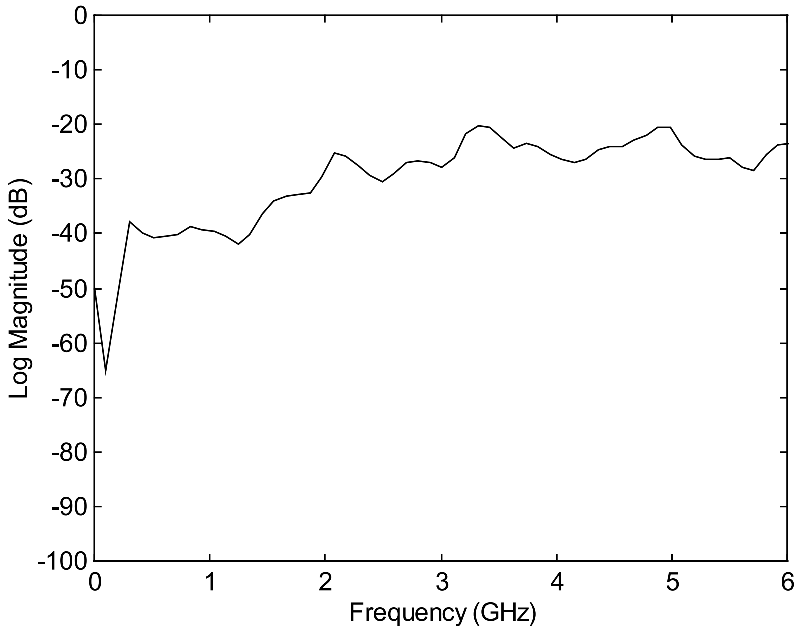

(a)

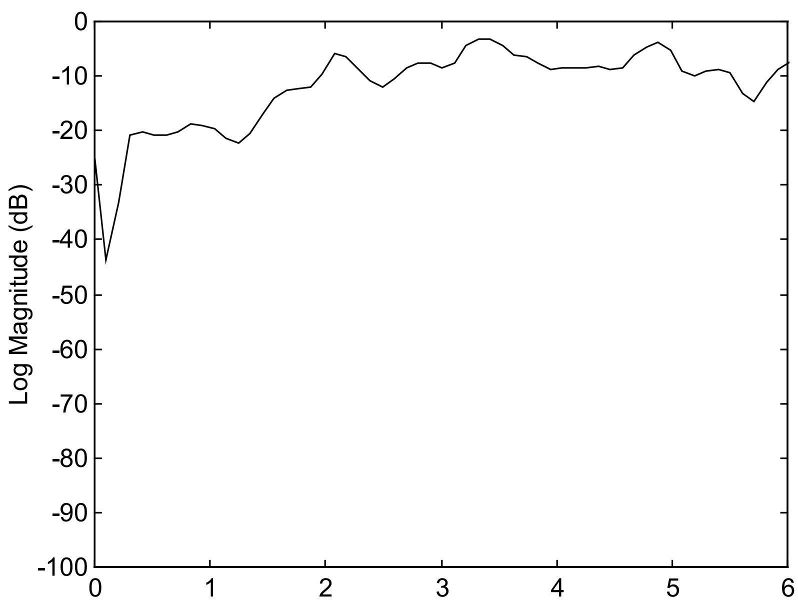

(b)

Figure 9.18 *Scattering amplitude spectra for antenna height of 152 mm and a transmitter/receiver separation of 260 mm (a) air-filled delamination (b) water-filled delamination.*

10. SIGNAL PROCESSING AND IMAGING ALGORITHMS

The mixing and convolution of effects that go into the formation of GPR return signals, often makes them difficult to interpret without some level of signal processing to put them in a format that is amenable to human examination. Processing procedures for the conditioning, display and interpretation of GPR signals range from the fairly simple to complex. Each technique has its own particular advantages and disadvantages. The following is a description of the most common GPR signal processing algorithms.

10.1 SURFACE REFLECTIVITY MEASUREMENTS

Possibly the simplest, and perhaps the most effective signal processing technique, is to calculate the dielectric constant of bare concrete, ε_c, from a measurement of the amplitude of the GPR signal that reflects off the surface of the concrete. The computed value of ε_c is one indicator of concrete deterioration. Normal concrete has a dielectric constant ranging from 7.5 to 10.5, depending on air content, moisture content, and aggregate type. Deteriorated concrete will show a higher dielectric constant (Carter, et al., 1986; Maser, 1990; Maser and Rawson, 1992). The quantity of deterioration is then inferred from the percentage of deck area exceeding a threshold dielectric constant.

As indicated in Chapter 8, the dielectric constant of a material can be calculated from GPR data using the amplitude of reflection between layers. This computation is based on the "reflection coefficient" between any two layers (1 and 2), R_{12}, which is defined as the ratio of the amplitude of the incoming wave to the amplitude of the reflected wave. The reflection coefficient (R_{12}) is related to the contrast in dielectric properties between the two layers, as follows:

$$R_{12} = (\sqrt{\varepsilon_1} - \sqrt{\varepsilon_2})/(\sqrt{\varepsilon_1} + \sqrt{\varepsilon_2}) \qquad (10.1.1)$$

where ε is the dielectric constant, and the subscripts 1 and 2 refer to the successive layers.

The dielectric constant of the concrete in a bare concrete deck can be determined at the air/concrete interface by recognizing the dielectric constant of air is 1. Using the reflection from a metal plate on the pavement surface to represent the incident wave (since the metal plate reflects 100%), equation (10.1.1) can be rearranged to yield the concrete dielectric constant, ε_c, as follows:

$$\varepsilon_c = [(1 + A/A_{pl})/(1 - A/A_{pl})]^2 \qquad (10.1.2)$$

where A = amplitude of reflection from concrete, A_{pl} = amplitude of reflection from metal plate (= negative of incident amplitude).

The surface reflection techniques is limited in its effectiveness if the concrete is saturated with water. In this case, the water will tend to absorb the GPR waves and distort the measurement of the dielectric constant. The surface reflection measurement technique is also limited by the use of asphalt overlays.

10.2 1-D LAYERED MEDIA MODELS

As noted earlier, the concrete dielectric constant measured by a surface reflection amplitude, may not be an adequate indicator of concrete condition due the surface drying. Asphalt overlays further complicate the situation. Under these circumstances, it is often effective to extend the surface reflection amplitude technique by considering the reflections off of subsurface layers. Based on an assumption that the roadway has a 1-D layered structure, such as an asphalt overlay or a rebar mat, the amplitudes and timing of the reflections off of subsurface layers can be highly indicative of the underlying features and conditions of the pavement. The simplicity of the algorithms associated with 1-D layered media identification enable the use of automated signal processing and interpretation algorithms. The primary limitations of the technique are that the subsurface features must have a 1-D layered geometry, and that the reflections are properly correlated with the appropriate underlying features.

10.2.1 ASPHALT OVERLAYS

If the deck has an overlay, then the reflection amplitude equation (10.1.1) can be used to calculate the reflection amplitudes from the air-asphalt interface and the asphalt-concrete interface. Combining the reflection amplitude expressions for both cases yields an expression for the dielectric constant of the concrete, ε_c, and the dielectric constant of the asphalt overlay, ε_0,

$$\varepsilon_c = \varepsilon_o \left[(F - R_2)/(F + R_2)\right]^2 \qquad (10.1.3)$$

where

$$F = (4\sqrt{\varepsilon_o})/(1 - \varepsilon_o) \qquad (10.1.4)$$

10.2.2 REBAR DEPTH

The arrival time of the reflection from the top rebar is used to calculate rebar depth. If the path between the rebar and the radar antenna were strictly vertical, the calculation would be simply the difference between the arrival time at the concrete surface and the arrival time at the rebar, multiplied by the velocity of the radar wave. However, since the reinforcement is a cylindrical target, reflections from bars that are not directly under the antenna are also received. A study was carried out sponsored by the Wyoming Transportation Department, in which the directly vertical calculation of rebar depth was correlated direct measurement of rebar depth using cores. The results of the correlation are shown in Figure 10.1 below. This figure shows that due to the longer paths to the side rebar, an adjustment factor of 0.88 needs to be applied to the calculation to obtain an accurate correlation. This factor has been incorporated into the analysis presented in this project.

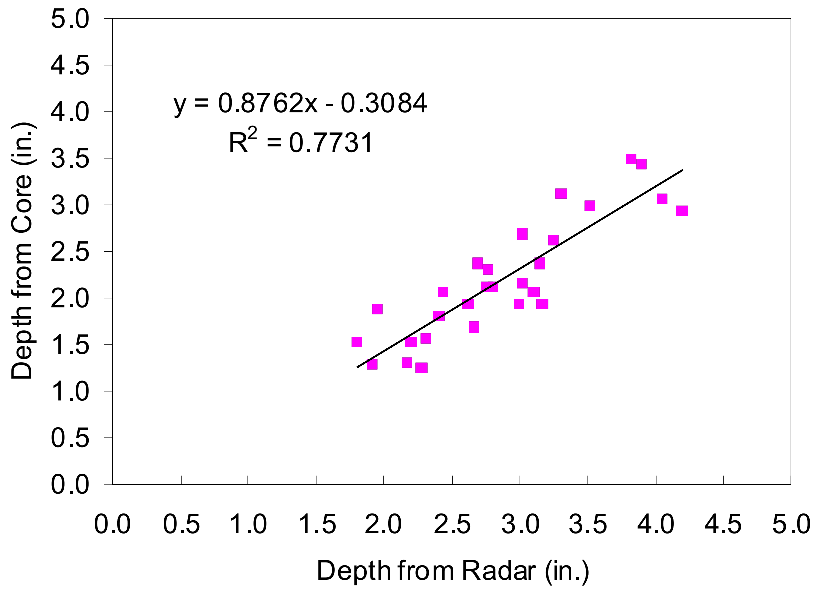

Figure 10.1 *Correlation of GPR to cores measurement of rebar depth based on Wyoming Transportation Department study.*

10.2.3 AASHTO TP36-93

A variety of products were tested and developed for the evaluation and condition assessment of pavements as part of the Strategic Highway Research Program (Scannell et al., 1996; Alongi et al., 1993). SHRP Product #2015: Ground Penetrating Radar was developed in an attempt to produce a standard method of measuring concrete deterioration with GPR. These efforts resulted in the provisional specification AASHTO TP36-93. The signal processing portions of the specifications are based on a 1-D layered pavement hypothesis. The principal parts of the specification are:

1. Use a GPR system that uses short monocycle pulses (1.0 ns) that are produced with air-coupled TEM linearly-polarized horn antennas.
2. At each scan point along the bridge deck measure
   a. V_i = applied signal strength at the deck surface.
   b. V_b = bottom echo signal strength.
   c. V_{rb} = bottom reinforcing layer signal strength.
3. From the set of measurements taken across the deck, calculate

a. V_{bs} = maximum bottom echo signal strength.
b. V_{avg} = average value of bottom steel signal strength.
4. The GPR scan signals have sufficient strength if $V_{bs} > 0.0264\ V_i$. (0.0264 is an empirically derived constant.) If the GPR signals do not have sufficient strength, they cannot be used.
5. The concrete is considered to be delaminated if $V_b < 0.385\ V_{bs}$.
6. The concrete is considered to be delaminated if $V_{rb} > 1.5\ V_{avg.}$

An advantage of the method outlined in TP36-93 is that it is fairly easy to automate. Algongi et al (1993) claim that the method is capable of detecting a delaminated sections with a 75% accuracy. A similar algorithm was automated and used to detect debonds, delaminations, and scaling on the Papineau Bridge in Ontario by Carter et al. (1986).

10.2.3 ITERATIVE METHODS

The 1-D layered media model technique can be extended to the identification of material properties by using iterative techniques. The method works by estimating the material properties of the pavement in a manner that produces a simulated waveform that forms the 'best' match to the original waveform. Halabe et al. (1995a, and 1997) describe an inverse identification procedure on concrete bridge deck that is fairly effective in locating cracks. Similarly Lazaro-Mancillo et al. (1998) describe a 1-D nonlinear iterative algorithm.

10.3 B-SCANS

The B-scan (Brightness-scan) is a standard representation technique that is used for the identification of a sweep of radar signals that consists of a set of pulses (Skolnik, 1988). For GPR, the sweep consists of a motion of the antenna along a line. This results in a set of traces that form a 2-D array of data. The amplitudes of the traces are plotted as intensities on a gray scale. Plotting data in an intensity format usually results in a compression of information that often forms a low-quality image. A variety of amplitude stretching and correction algorithms are available to enhance the images (Russ, 1999).

10.4 SYNTHETIC APERTURE RADAR AND MIGRATION

The 2-D and 3-D nature of radar signals and subsurface features often makes it difficult to discern the nature of the underlying features from a direct examination of the B-scan images. A major difficulty is the distortion due to hyperbolic nonlinearities that result from the extended distance of cross-range objects, as described in section 8.7. The problem of reconstructing subsurface features from measurements made of the surface of a structure is often called an inverse problem. The development of algorithms to solve inverse problems have been of tremendous importance to a wide range of fields, such as medicine, geophysics – including oil exploration, and air borne radar. A survey of the state-of-the-art in solving inverse problems can be found in Cheney (1997). The mathematics underlying the solution of inverse problems can be found in Isakov (1998).

The development of 2-D and 3-D imaging algorithms that are applicable to GPR has occurred along two independent paths – geophysical oil exploration and airborne radar. The geophysical oil exploration algorithms usually go by the name migration (Robinson, 1982; and Stolt, 1978). The airborne radar applications are usually called synthetic aperture radar (SAR). Migration and SAR refer to a whole set of algorithms that attempt to deconvolve the mixing of the cross-range hyperbolic nonlinearities by various integral transforms and manipulations of entire sets of B-scan data. One of the earlier reported applications of the SAR technique to the imaging of subsurface features in concrete is that due to Mast (1993). Mast and Johansson (1994a) have further extended this work into 3-D imaging of subsurface features. A related approach using multi-frequency diffraction tomography is also reported by Johansson and Mast (1994b). The results of the use of these algorithms can be quite striking, Figure 10.2 shows the results from a test on a slab with embedded rebars. The system is able to image rebars quite nicely. Imaging defects, such as cracks, is not as well demonstrated. These methods have been further extended to the application of a moving roadway test system using a multichannel microwave impulse radar system (Chase 1999).

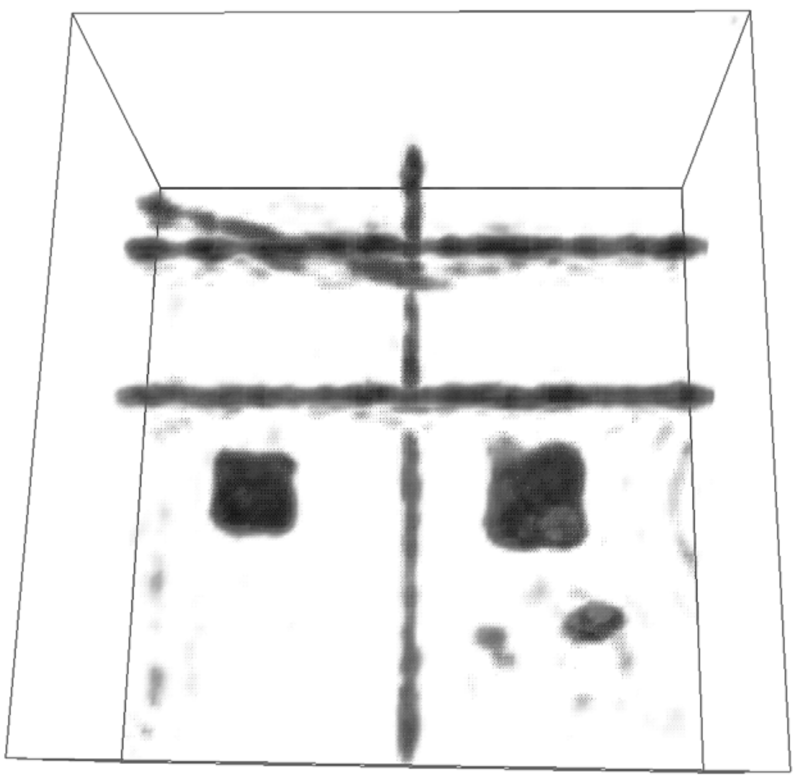

Figure 10.2 *Image of rebars and defects inside of a concrete slab by Mast and Johansson (1994a).*

A flowchart for the basic SAR algorithms as described by Soumekh appears in Figure 10.3. Some of the key features are that the hyperbolic nonlinearity is removed algebraically in the frequency and wavenumber domain by first Fourier transforming the B-scan data with respect to time and cross-range. A mathematical problem arises because the Fourier transform involves spatial, time, frequency and wavenumber domains that are infinite in extent, while the measurement system deals with data that have domains of finite extent. One method of correcting for the mismatch is to use the matched filter algorithm (Soumekh, 1999; and Papoulis, 1968).

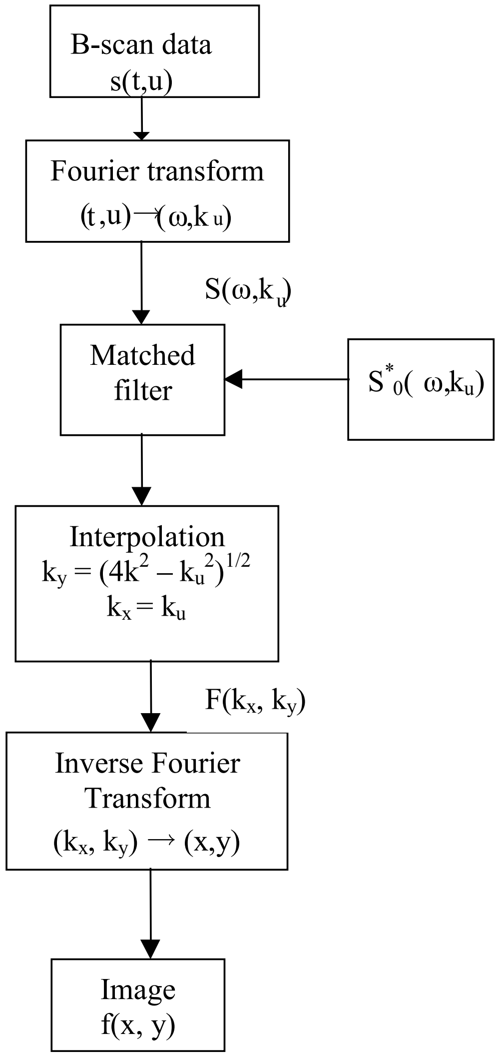

Figure 10.3 *Flowchart of synthetic aperture algorithm (Soumekh, 1999).*

The geometry of the hyperbolic nonlinearity in wavenumber space is shown in Figure 10.3. The key relations are

$$k_y^2 + k_u^2 = 4k^2 \qquad (10.4.1)$$

or

$$k_y = (4k^2 - k_u^2)^{1/2} \qquad (10.4.2)$$

and

$$k_x = k_u \qquad (10.4.3)$$

where k_x = downrange image wavenumber, k_y = crossrange image wavenumber, k_u = downrange wavenumber, and k = ω/c = wavenumber. This transforms the data into a form that represents the geometry of the reflective features. Finally, the data are inverse Fourier transformed into the spatial x-y domain to form an image.

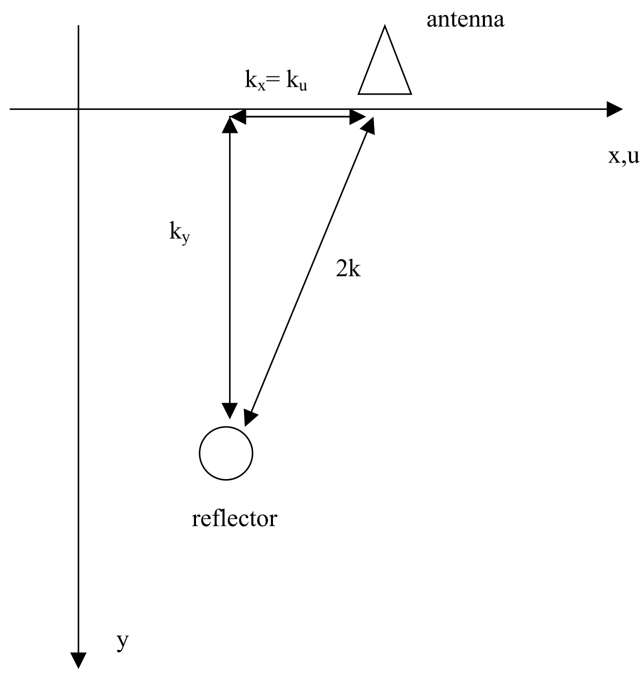

Figure 10.4 *Geometry of wavenumbers associated with the synthetic aperture imaging hyperbolic nonlinearity.*

10.5 WAVELETS AND NEURAL NETS

There have been a few cases reported where some of the other modern signal processing techniques, such as wavelets and neural networks have been used to analyze GPR signals. Most of the results from using these techniques are fairly preliminary and have yet to significantly increase the state-of-the-art. Shaw et al. (1998) used neural networks to examine concrete structures in the laboratory. Al-Nuiaimy et al. (1998) used a Hough transform on the front end of a neural network to remove the hyperbolic nonlinearities. This technique worked quite well and has the potential of reducing the computational effort of the signal processing. Liu and Oristaglio (1998) used wavelets on GPR data. It was suggested that this method is potentially superior to Hilbert transforms.

11. GROUND PENETRATING RADAR SYSTEM

This chapter is a description of the GPR system that was used for most of the tests reported here. The system underwent several stages of development. The following is a description of the final prototype version and some of the design steps and decisions that were made to reach this level of development.

11.1 SIGNAL SOURCE AND RECEIVER

An HP 8753D Network Analyzer produces the signals. It has a frequency range of 30 kHz to 6 GHz, with a dynamic range of 105 dB. The system is loaded with a wide variety of test features and data display options, the majority of which are not used for GPR testing. The basic test mode is that the system sends signals out of a test port, the signals interact with a system under test (antennas, cables, pavement, etc.); and the signals are received back at a test port for analysis, display and storage. The system has two test ports that are both capable of sending and receiving signals. This enables four measurement modes: S_{11}, S_{12}, S_{21}, and S_{22}, where the first index indicates the output port and the second index indicates the input port. The most common test mode is where the analyzer sends sine waves to the system under test. The sine waves are then reflected and transmitted with a system-specific frequency-dependent amplitude and phase shift. The amplitude and phase of the reflected or transmitted signal is picked up and measured at the test port. The analyzer performs this test by sweeping over a range of frequencies. The operator sets the frequency spacing and range. The maximum signal output power is 0.01 W. The total test time increases with the width of the frequency and decreases with the width of the frequency spacing. A test involving 201 frequency points evenly-spaced over a 6 GHz bandwidth takes 0.43 s to complete.

11.2 ANTENNA

The antenna that is used is a horn antenna that has been specifically designed to transmit and receive signals in the 0.5 to 6.0 GHz bandwidth. Two factors that significantly affect the performance of the antenna are the impedance match at the apex and the impedance match at the aperture. The apex is where the antenna connects to the cables and then to the analyzer. The aperture is the part of the antenna that launches the waves into the air.

The apex is designed to minimize the reflections that occur with the impedance mismatch as the coaxial cable is connected into the antenna. The geometry of the coaxial cable, and the unipolar nature of the source signals, makes it difficult to create an impedance-balanced connection by attaching it directly to the antenna. One method of balancing the attachment point is to use a balun. Commercially available baluns were evaluated as an aid for improving the impedance match at the apex. The baluns appeared to balance the signals by converting them from a unipolar to a bipolar format. However, the signals suffered from a 10-dB power loss whenever it ran through the balun. The total loss was 20 dB for a round trip signal. An alternative to a separate balun is to balance the connection by the inclusion of specific geometric details in a direct connection. Balanis (1997) lists several such balun direct-connect configurations. Aurand (1998) provided an apex design that worked quite well. This detail involved using a perpendicular bulkhead through mount to attach the coaxial cable to each of the sides of the antenna, figure 11.1. Balancing is achieved by making the horn plate areas asymmetric at the apex. The side that is connected to the outer conductor of the coaxial cable has a larger area than the side that connects to the inner conductor. The asymmetric areas create a situation where the effective lengths of both conductors are equal. The asymmetric geometry is determined by an empirical tuning process with aviator snips, files and an impedance analyzer. With care, an apex geometry can be found that produces a negligible impedance mismatch.

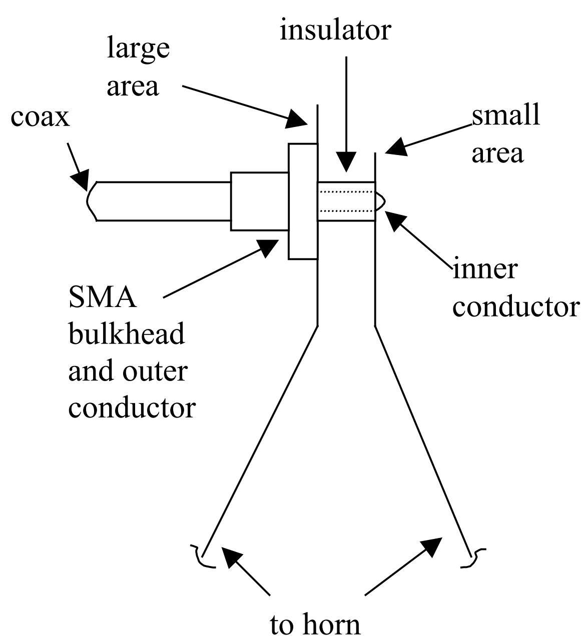

Figure 11.1 *Detail of impedance-matching low-loss antenna apex connection.*

After a variety of iterations, several different geometric details of the launch point were examined. The results of these studies are discussed in detail in section 12.1. The design of the aperture is a compromise between impedance matching and secondary end reflections. A tapered and flared configuration offers excellent impedance matching (Huston et al., 1999; and Hu 2000). However, the flared antenna has the drawback that it produces secondary reflections off of the flares. A compromise configuration that has no end reflections and a decent impedance match is to use a horn that has tapered, but not fixed ends. A schematic of the 'best' horn antenna design is shown in figure 11.2. A photo appears in figure 11.3.

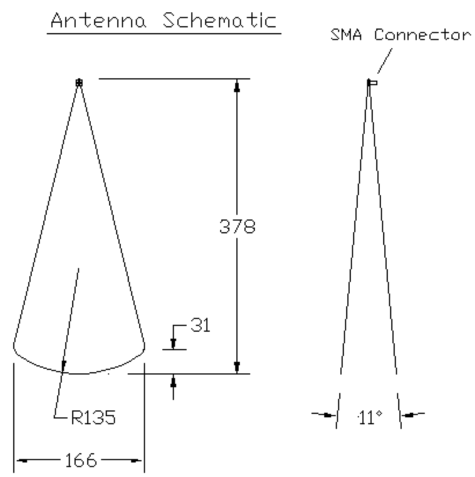

Figure 11.2 *Schematic of horn antenna.*

Figure 11.3 *Photo of horn antenna before mounting and encasement.*

11.3 CABLES

A key feature to the performance of the system is the cables and connectors that run from the signal source and receives the antenna. The ideal situation would be to have the cables and connectors transmit the signals without any impedance mismatch, loss and distortion. Of course, this is impossible for any real materials. Instead, the cables and connectors should be manufactured in such a way that there are minimal losses and reflections throughout the transmission path. Since the cables inevitable have a characteristic impedance, this impedance will cause a phase and amplitude shift for a sinusoidal signal that is passed through the cable. The ideal cable is one that has a minimal change in phase angle with bending of the cable. The reason for this criterion is because the cable is flexed into different positions as the antenna is articulated into different positions for air shot and road test measurements. The phase angle distortion should be identical for each case. Initially, 2 m cables were purchased from Gore. These were expensive top-of-the-line cables with a minimal phase distortion. They worked quite well and were quite flexible, but were fairly fragile. In spite of moderately gentle treatment, they sustained damage in day-to-day usage. The Gore cables were replaced with less expensive cables from Insulated Wire Inc. These cables worked quite well and were used in the latter half of the experiments reported in this project.

At least three connector options are available: 7mm, N and SMA. Nominally, the 7mm has the best fidelity at high frequencies followed by the N and SMA connectors. The 7mm connectors have the attractive feature in that they connect by a differential screw mechanism that creates a genderless connection. The 7mm and N connectors are considerably bigger and more expensive that the SMA connectors. Laboratory testing indicates that for the frequency range and amplitudes necessary for GPR testing, the SMA connectors operate with minimal spurious reflections and losses. SMA connectors were used predominantly throughout this project.

11.4 POSITION MOVEMENT AND MEASUREMENT

All of the components of the system, except for the power supply (120VAC), are housed in a moveable cart, Figure 11.4. This cart is designed to hold the antenna at a variable, but fixed, height and angle relative to the road surface. A principal feature of the cart is the position measurement system, which uses a measuring wheel. The operating principle of the measuring wheel is that the wheel rolls without slipping, by direct contact with roadway. As the wheel rolls, it sends an electric pulse to the signal processor for every 13 mm of linear motion of the cart. The signal processor uses the pulse to trigger the radar system and to record the cart position. The measuring wheel was fabricated by modifying a 305 mm diameter measuring wheel. The modifications included switching to a 152 mm diameter wheel while setting the electronics up as if the wheel was 305 mm diameter. The altered wheel size effectively doubled the resolution of the system. In addition, the initial pulse signals at TTL voltage levels were picked up from the system and connected to the parallel printer port of the PC for measurement.

11.5 SIGNAL PROCESSOR AND CONTROLLER

The measuring system was controlled with a Win95 Pentium PC. The PC would simultaneously trigger the HP8753D network analyzer, based on a signal from the measuring wheel, display the results, and then store the results. The steps are listed below:

Figure 11.4 *Picture of cart with GPR system.*

1. Operator positions the antenna and cart as desired.
2. Operator selects the operating parameters for the HP8753D Network Analyzer. The setup parameters affect the frequency range, and penetration depth.
3. Antenna is pointed upward into the air for an air shot system calibration.
4. Measurement process is started when operator clicks upon the appropriate screen icon.
5. PC opens a data file and stores initial setup data.
6. Cart is slowly rolled forward.
7. Measuring wheel sends a TTL pulse to the PC.
8. PC increments position counter.
9. PC sends trigger signal to HP8753D Network Analyzer via GPIB interface.
10. HP8753D performs radar scan by sending a series of sine waves to the antenna, measuring the magnitude and phase of the return signal, and then converting to the time domain with a hardware-based Fast Fourier Transform.
11. HP8753D sends synthesized time-domain radar reflection to PC via GPIB interface.
12. PC plots trace on screen in B-scan format and stores the data on the hard disk by appending to the open file.
13. Operator views the B-scan output and decides whether to continue or terminate the test.

14. If the test is continued, the process is repeated starting at Step 6.
15. If the test is terminated, the data file buffers are written to the disk and it is closed.

A schematic diagram of the data flow appears in Figure 11.5

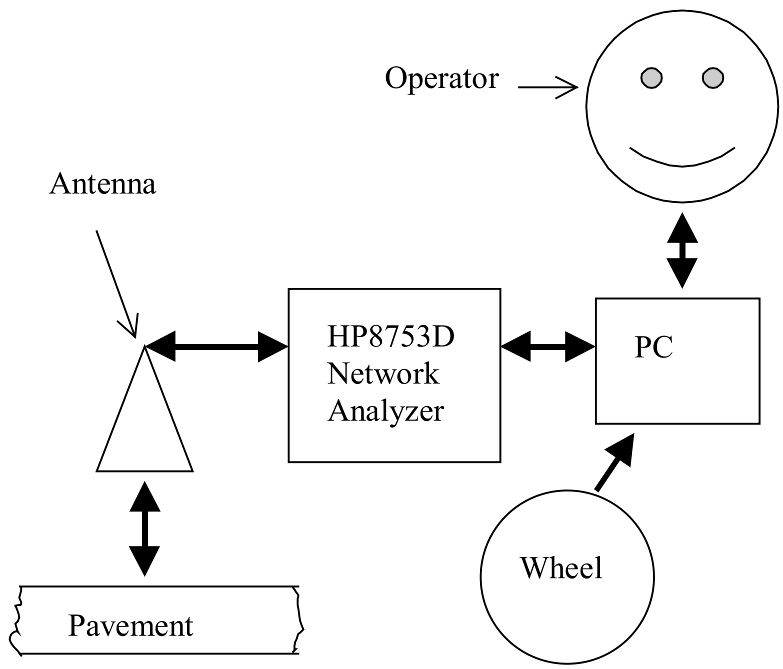

Figure 11.5 *Schematic of information flow in UVM GPR system.*

12. LABORATORY TEST RESULTS

12.1 ANTENNA PERFORMANCE ANALYSIS

Antennas are integral components of GPR systems. Various antenna designs were examined for selection as the one that is best suited for the examination of roadways. Several antennas were tested in the lab. A summary of the results follow. More details can be found in Adam (1997), Hu (2000) and Huston et al. (1999).

12.1.1 VIVALDI ANTENNAS

The first set of antennas to be examined were a pair of 2-12 GHz Vivaldi antennas that were designed and built by Weedon (1994). The antennas had good impedance matching and produced a clean signal with minimal time domain ringing. A disadvantage of the Vivaldi antenna design is that it is a flat plate antenna with a finite aperture in only one direction. This results in a large beam width that can be defined as the angle at which the amplitude of the signal decreases by $\sqrt{2}$. The half beam width was measured to be 54º in the E-plane and 82º in the H-plane. In spite of its wide beamwidth, the Vivaldi antennas were quite useful in system shakedown and time of flight measurements.

12.1.2 TEM HORN ANTENNAS

The TEM (transverse electromagnetic) horn antenna is an attractive design because it has the potential for transmitting narrow beamwidth, broadband, short pulse signals with a minimum of distortion.

12.1.2a NIST Design: The initial design to be evaluated followed the design guidelines developed at NIST (Ondrejka et al. 1995). The basic design includes a balun, which functions to create a balanced signal from the unbalanced signal generated by the network analyzer, the horn, and a set of parallel plate extensions, which improve the low frequency performance (Weedon,1997). A diagram of the NIST design TEM horn antenna can be seen in Figure 12.1. The half beam width was measured to be 30º in the E-plane and 39º in the H-plane.

Initially, two horn antennas were designed, built, and tested. These tests included an S_{11} measurement to examine the internal reflections of the horns, an S_{21} measurement between the two horns, an S_{21} measurement between a horn antenna and a Vivaldi antenna, and an S_{21} between the Vivaldi antennas. The S_{21} measurements were of pulses transmitted between the antennas.

The S_{11} measurements used a step response to examine the internal reflections from the TEM horns. The results showed that there was a small reflection from the feed point, and a larger reflection from the end of the antenna.

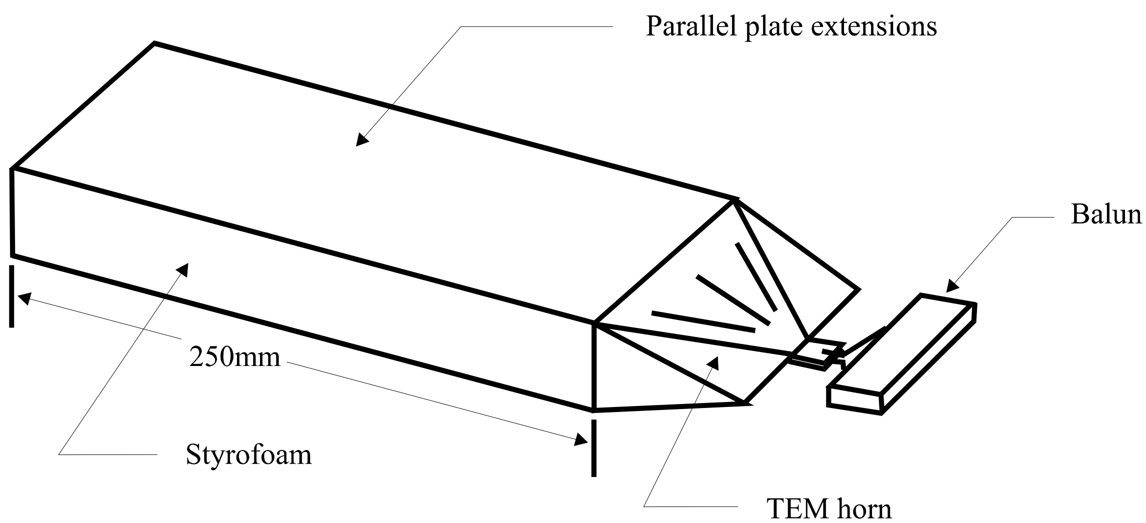

Figure 12.1 - *Diagram of NIST design TEM horn antenna.*

The S_{21} measurement between the horns resulted in a waveform that showed a reflection approximately 3 ns after the main impulse. It was believed that this reflection was caused by low-frequency moding. S_{21} measurements between the two horn

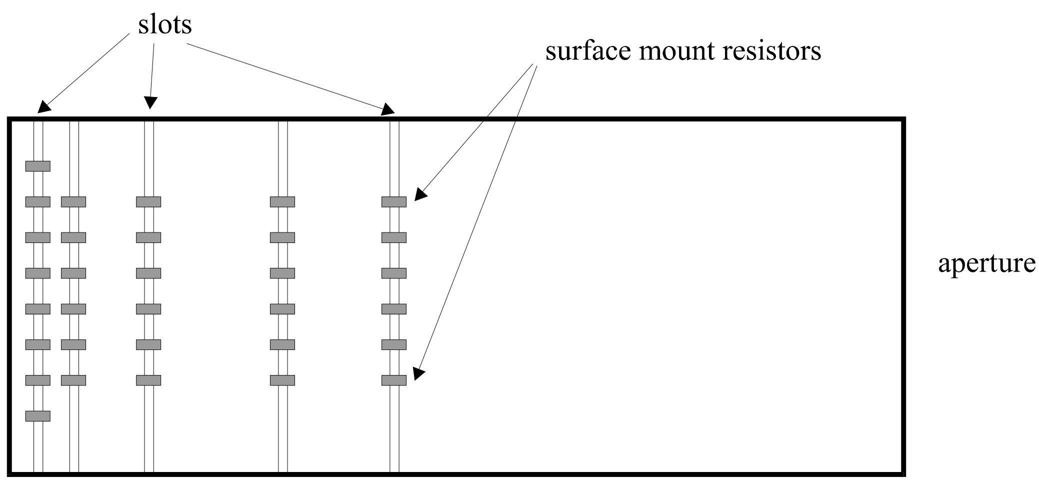

Figure 12.2 *Diagram of parallel plate extensions with resistive loading used with the NIST design TEM horn antenna.*

antennas, a horn and a Vivaldi antenna, and two Vivaldi antennas indicated that the transmitted signal from the Vivaldi antennas was more powerful than that of the horn antennas. It is believed that the use of baluns and the internal reflections at the end of the horn caused the loss of energy.

According to the design specifications of Ondrejka et al. (1995) the addition of resistive loading to the parallel plate extensions eliminates low frequency moding, resulting in a cleaner signal. The antennas were modified to include resistive loads by moding. This was accomplished by the parallel plate extensions made from RT/Duroid 5880 and inserting resistors.

The antennas were retested with the resistive loads in place. The S_{21} measurement showed that the resistive loads decreased the amount of noise. A pronounced reflection from the end of the horn remained. This was confirmed by S_{11} measurements using both the step response and the bandpass impulse response technique. Although the pulse was cleaner, a significant amount of ringing after the initial impulse was still present. When compared to the signal generated using the Vivaldi antennas, the horns built according to the NIST design exhibited a smaller peak amplitude and a wider pulse width.

12.1.2b Sandia Design: A second TEM horn antenna horn was design and built according to a procedure outlined by Aurand (1996). This design replaced the balun with a direct feed from the 50Ω coaxial line through an SMA connector. Because of the direct feed design, the antenna transitions from a 50 Ω impedance at the feed point to a 100 Ω impedance at the aperture. This impedance change improves the gain while making the antenna more compact. Figure 12.3 is a diagram of the Sandia design TEM horn antenna. The half beam width for this design was measured to be 20º in the E-plane and 45º in the H-plane. Due to the increased size of this design, only one antenna was initially built.

S_{21} measurements were performed using an impulse response. The results showed a clean time domain pulse that was similar to that of the Vivaldi antennas. There was a slight second peak that occurred approximately 1.75 ns after the main peak. The results of the S_{11} impulse response measurements, revealed a substantial reflection from the feed point, and a second smaller internal reflection at the end of the antenna. Also noteworthy is eliminating the balun decreased the number of internal reflections was decreased from three to two, with a corresponding decrease in lost energy.

As an additional test, an S_{11} measurement was performed with a metal plate placed 310 mm(12.25") from the end of the antenna. The reflection from the plate resulted in a peak approximately 2 ns after the reflection from the end of the antenna. Based upon the two way travel time of ~2 ns and the distance that the radar wave had to travel, the speed of propagation can be calculated as ~305 mm/ns (~12"/ns). This value correlates well with the speed of electromagnetic wave propagation in air.

Following the initial tests, the antenna was tuned to improve the characteristics of the transmitted pulse. Tuning included trimming the center conductor of the SMA launcher so that it was flush with the upper plate and filing the edges of the top plate into a rounded "V" shape. Tuning resulted in a decrease in the feed point reflection of approximately 38% that led to an approximate increase of 20% in the magnitude of the transmitted pulse. Additionally the transmitted signal was significantly "cleaner."

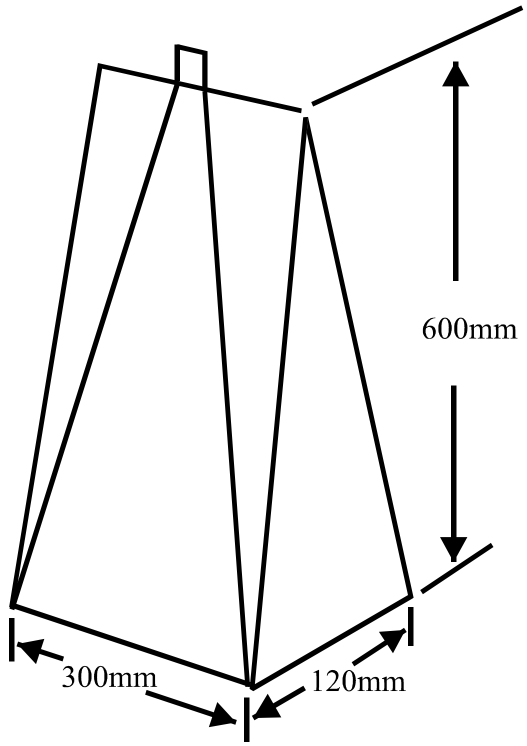

Figure 12.3 *Diagram of Sandia design for TEM horn antenna (Aurand, 1996).*

12.1.2c GIMA Design: A novel design for a horn antenna is the Good Impedance Match Antenna (GIMA) that was designed at UVM as part of this project. The following is a summary of the results of the testing. Details concerning the design and results of extensive performance studies can be found in Hu (2000) and Huston et al. (1999).

The penetrating capability and resolution of the antenna was tested using four 305 by 305 mm concrete slabs of differing thickness stacked on top of one another. The small gap in between the stacked slabs due to a flatness mismatch simulated air-filled cracks.

After an extensive series of performance tests on a series of GIMA antennas with different dimensions, the antenna denoted GIMA-6 performed the best. The key dimensions of GIMA-6 are α = 13 deg., ß = 6 deg., θ = 150 deg., a = 60 mm, b = 60 mm, and l = 180 mm.

A typical result appears in figure 12.5. In this test, the thickness of a concrete slab with a dimension of 305 mm by 305 mm by 89 mm (3.5”thick) was tested. Pulse 1 is the front surface of the slab, and Pulse 2 is the rear surface of the slab. Since the reflections are due first to a transition of dielectric values from low to high and then from high to low, the sign of the pulses is reversed.

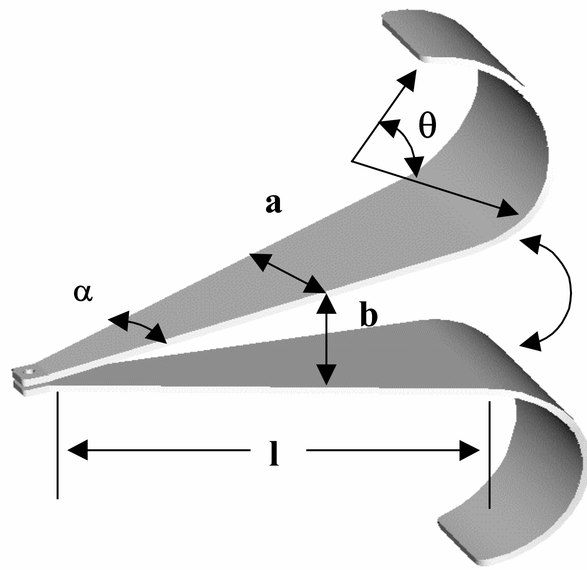

Figure 12.4. *Schematic of GIMA horn antenna design.*

Two slabs were then stacked flush to simulate an artificial crack that was approximately 1 mm thick. The data appear in figure 12.6. The first pulse is the front surface of the first slab; the third pulse is the rear surface of the second concrete slab. The pulse in between represents the artificial crack. However, because the crack is so small, there is not enough distance to resolve the two pulses. The two pulses merge together to form the second pulse in the plot.

When the two slabs are placed 50 mm apart, the front and rear surface of the air gap in between can be distinguished, figure 12.7. Pulse 1 is the front surface of the first slab. Pulse 2 is the front surface of the air gap. The sign of Pulse 3 is negative of Pulse 2. Pulse 4 is the rear surface of the second slab.

An earlier version GIMA antenna (GIMA-1) was also tested on a high-frequency (1 to 16 GHz) impulse GPR system from Sandia National Laboratories. The results demonstrate that with a higher frequency range using the GIMA-1, the rear surface of the first slab and the front surface of the second slab appear as distinct reflections, even though the separation between them is less than 1 mm. Figure 12.8 displays the resolution test results using the system from Sandia National Labs. Peak 1 is the front surface of the first slab. Peak 2 is the rear surface of the first slab. Peak 3 is the front surface of the second slab. Peak 4 is the rear surface of the second slab. Peaks 2 and 3 are partially merged.

The thickness of concrete bridge decks generally varies between 20 mm(8") to 30.5mm (12"). In order to study the signal penetrating capability in this thickness range, four concrete slabs were stacked together to form a 330 mm thick slab with three artificial cracks within it. The first and third slab are 89 mm (3.5") thick. The second and the fourth are 76 mm (3") thick. The sizes of the cracks are approximately 1 mm. Figure 12.9 shows the time domain real format data. The first peak is the front surface of the first concrete slab. The second peak is the artificial crack created by the first and second slabs. The third peak indicates the artificial crack shaped by the second and third slab. The fourth peak represents the gap created by the third and fourth slab. The last envelope indicates the location of the rear surface of the concrete stack.

In order to verify the location of the rear surface of the stack, a metal plate that is one foot wide by two feet long was placed closely to the rear surface of the stack. By doing this, the fifth envelope should have a larger magnitude and a reversed sign. Figure 12.10 verified the prediction. The fifth envelope in figure 12.10 is double the size of the one in Figure 5.2-5 and has a reversed sign. This indicates that the radar signal of the GIMA system traveled through 660 mm of concrete as well as 10 cm of air and still produced a high-resolution pulse.

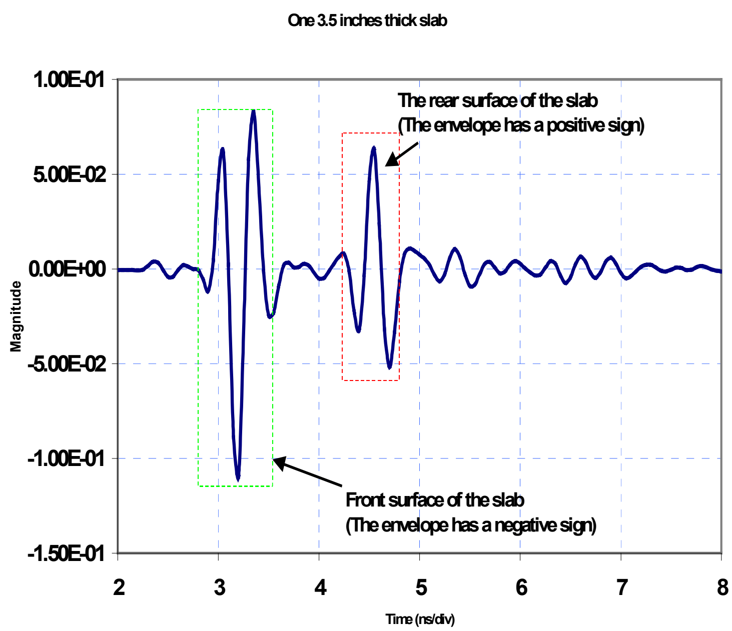

Figure 12.5 *Reflected signal versus time for one 90mm slab using GIMA-6 antenna and the HP8753D. The negative envelope denotes the front of the slab, while the positive envelope corresponds to the rear of the slab.*

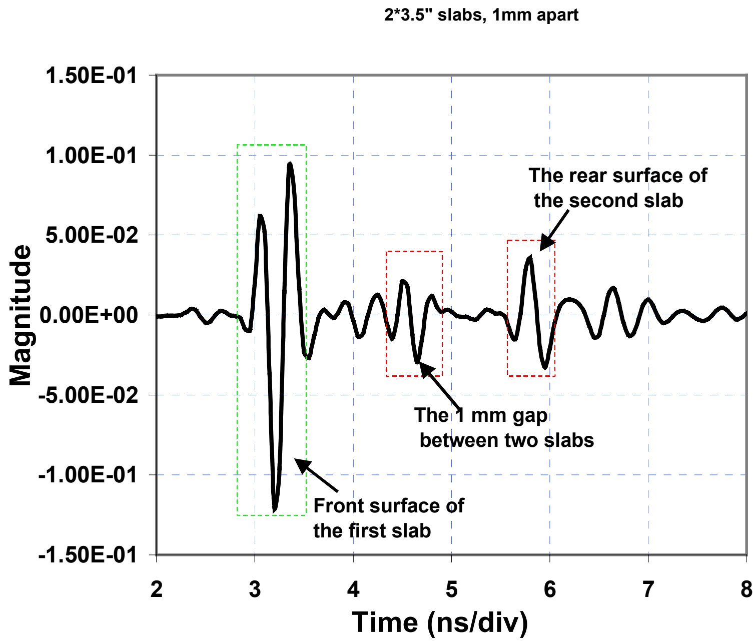

Figure 12.6. *Reflected signal versus time for two 90mm slabs stacked with a 1mm gap using GIMA-6 antenna and the HP8753D. A signal from the 1mm gap is apparent.*

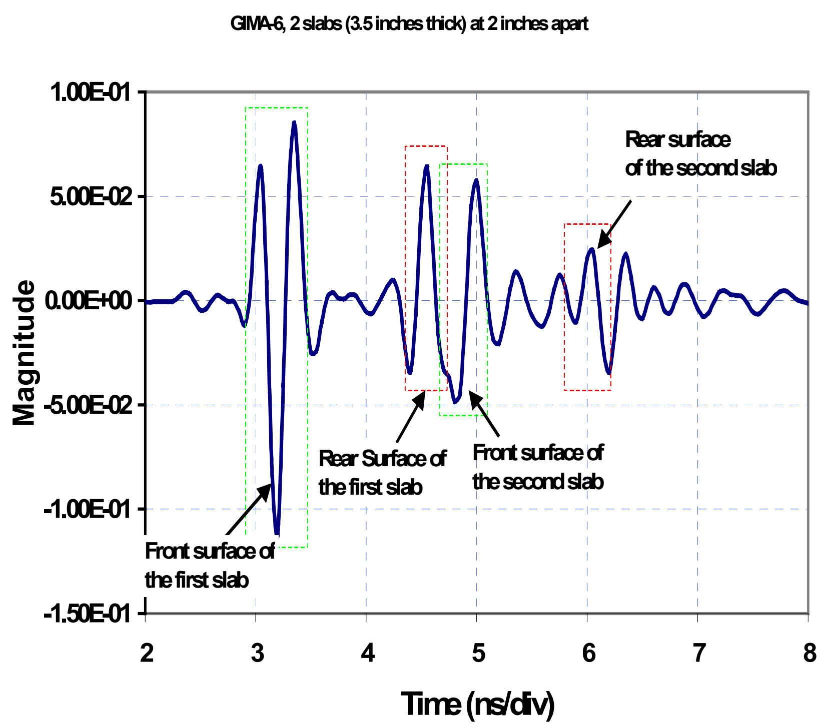

Figure 12.7. *Reflected signal versus time for two 90mm slabs stacked with a 50mm gap using the GIMA-6 antenna and the HP8753D. Signals from both surfaces of the gap are apparent.*

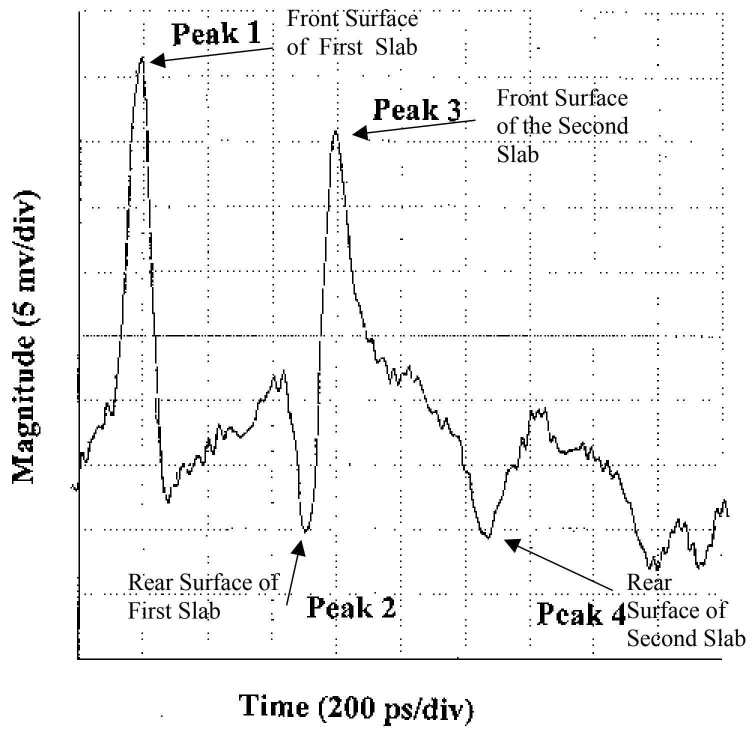

Figure 12.8. *Reflected signal versus time for two 38mm slabs stacked with a 1mm gap using the GIMA-1 antenna and the Sandia National Labs 1-16 GHz impulse GPR system. Both surfaces of the gap are apparent.*

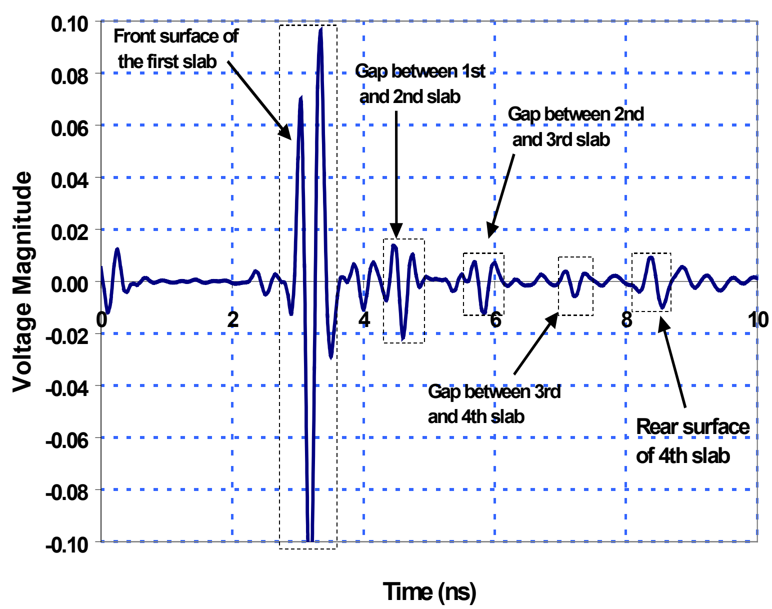

Figure 12.9 *Reflected signal versus time for two 90mm and two 76mm slabs stacked with 1mm gaps using the GIMA-6 antenna and the HP8753D. Signals from all three gaps are apparent.*

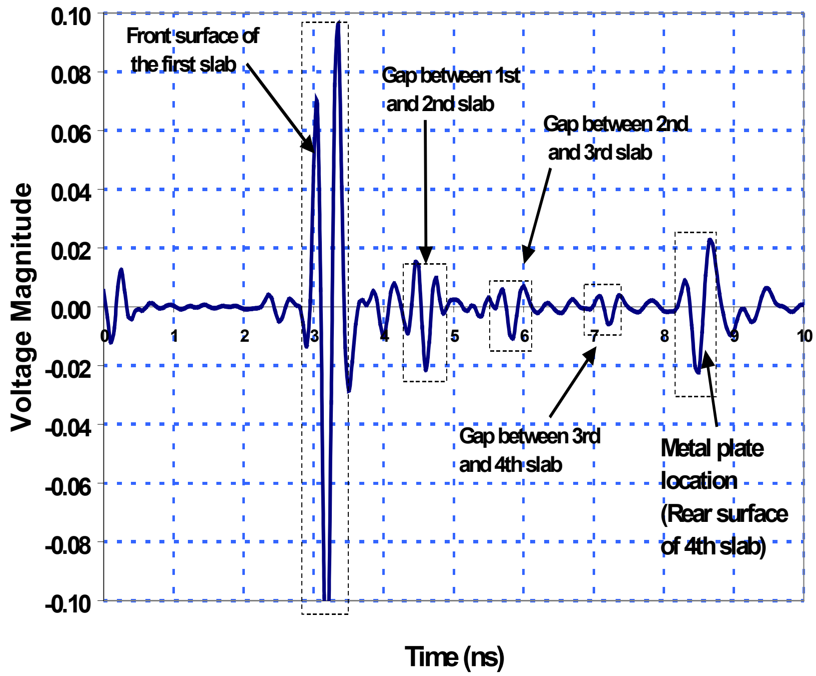

Figure 12.10 *Reflected signal versus time for two 90mm and two 76mm slabs stacked with 1mm gaps using the GIMA-6 antenna and the HP8753D and a metal plate reflector at the bottom of the stack. Signals from all gaps and the metal plate are apparent.*

12.2 SINGLE POINT SLAB TESTS

Four laboratory test slabs were cast using Sakrete concrete mix. The dimensions of the slabs were 117.5 cm (46.25") x 81.3 cm (32") x 15.25 cm (6"). Each slab was cast with simulated defects as shown in figure 12.11.

Additional tests were conducted on relatively small reinforced concrete specimens, which were rectangular slabs with dimensions 137 mm (5.39") x 230 mm (9.05") x 305 mm (12"). Two identical slabs were cast, one was subjected to accelerated electrolytic corrosion.

12.2.1 TRANSMISSION MEASUREMENTS

Time of flight transmission measurements were using the time domain capability of the HP8753D, with a synthesized 500 MHz to 6 GHz broad band pulse. The first measurements were used an identical pair of Vivaldi antennas. The second measurements used a pair of identical TEM horn antennas. For all measurements, the antennas were placed 76 mm from the surface of the concrete slabs. Figure 12.12 is a diagram of the setup.

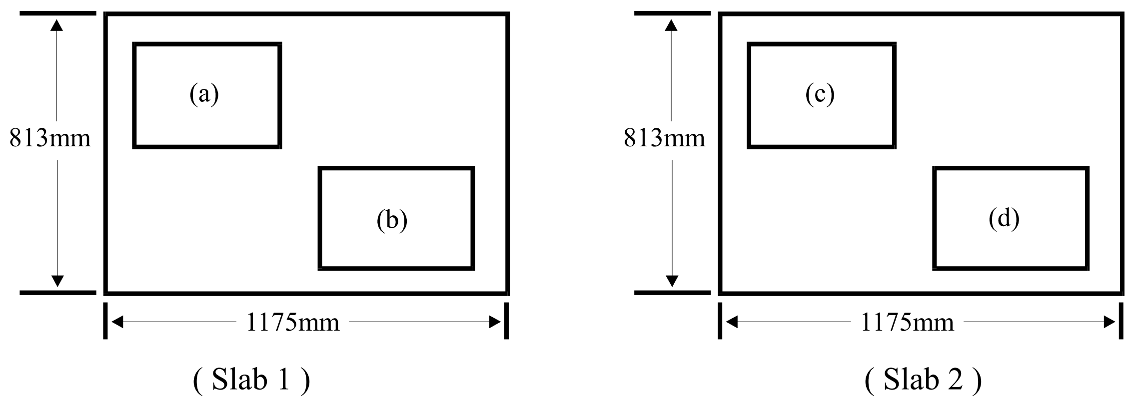

Figure 12.11 - *Diagrams of Slabs 1 and 2. (a) diagram thickness- 13 mm(0.5"), measured thickness – 13 mm(0.5") (b) diagram thickness - 6 mm(0.25"), measured thickness - 19 mm(0.74") (c) diagram thickness - 13 mm(0.5"), measured thickness - 6 mm(0.25") (d) diagram thickness - 19mm(0.75"), measured thickness - 10 mm(0.40").*

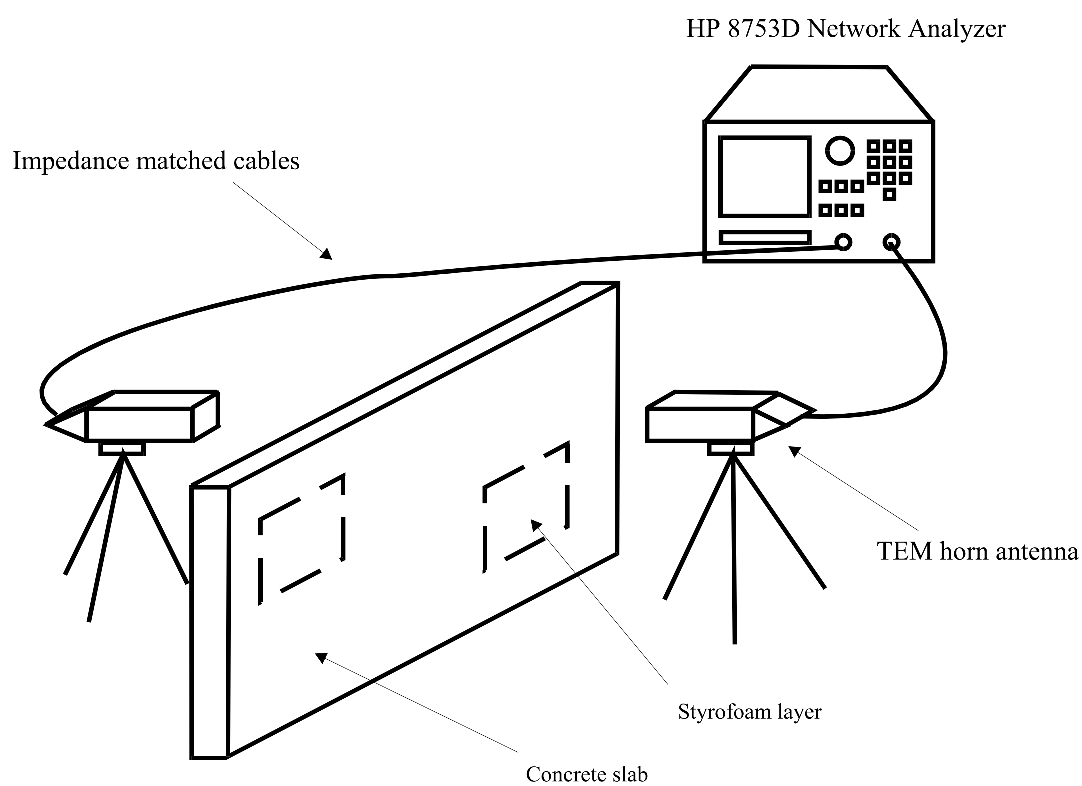

Figure 12.12 *Setup for transmission measurement using TEM horn antennas.*

Transmission measurements were taken in areas of solid concrete and in areas containing Styrofoam, and other defects, such as corrosion. These measurements were taken between the rebar layers so as to minimize rebar reflections. Based upon the velocity change going from concrete (velocity~100mm/ns) to Styrofoam (velocity~305mm/ns), and the time shift in the transmitted peaks caused by the presence of the Styrofoam, it was possible to determine the approximate thickness of the air void (Styrofoam) using the following relation,

$$h \approx \Delta V \cdot \Delta t \qquad (12.2.1.1)$$

where h is the thickness of the Styrofoam layer, ΔV is the velocity change in going from concrete to Styrofoam, and Δt is the time shift in the transmitted pulse.

Because the dielectric properties of Styrofoam are almost identical to those of air, sheets of Styrofoam were cast in the test slabs to simulate air filled delaminations. The first two slabs contained 6 mm (1/4"), 13 mm (1/2"), and 19 mm (3/4") layers of Styrofoam. The third slab contained 6 mm (1/4") and 13 mm (1/2") layers of Styrofoam, a sheet of packing foam approximately 2 mm thick. The locations of the various defects were documented.

12.2.2 TESTS OF SLABS WITH STYROFOAM DEFECTS

The measurements taken from Slab 1 confirmed the presence of the Styrofoam layers. However these measured thicknesses did not match the thicknesses as indicated on the slab documentation. The original diagram indicated that the first layer of Styrofoam had a thickness of 13 mm (0.5"). Time of flight measurements through this section showed a time shift of 0.065 ns relative to a Styrofoam-free section of the slab. Using equation (12.2.1.1), this time shift corresponds to a thickness of 13 mm (0.52"). A second set of time delay measurements were taken through the section of concrete which nominally contained a 6 mm (0.25") layer of Styrofoam, according to the diagram. Time of flight measurements resulted in a time shift of 0.093 ns relative to a Styrofoam-free section of the slab. This time shift corresponds to a thickness of 19 mm (0.74"), which disagrees with the nominal recorded thickness. Figure 12.11 shows a diagram of Slab 1, including the Styrofoam layers with the thickness as indicated on the original drawings and the thickness measured by the transmission measurements.

Transmission measurements were taken through Slab 2 in a manner identical to those taken for Slab 1. The first time of flight measurement was taken through a layer of Styrofoam which was 13 mm (0.50") thick as indicated on the diagram. This time shift was 0.031 ns relative to a Styrofoam-free section of the slab. This time shift corresponds to a measured thickness of 6 mm (0.25"), which disagrees with the nominal thickness as indicated on the diagram. The second measurement for Slab 2 was taken through the section of concrete that contained a 19 mm (0.75") layer of Styrofoam according to the diagram. The difference in the time of flight for the concrete containing the Styrofoam layer versus the concrete that did not was 0.050 ns for this case. This time shift corresponds to a measured thickness of 10 mm (0.40"), which does not agree with the thickness as indicated on the diagram. A diagram of Slab 2, including the Styrofoam layers with the thicknesses indicated on the original drawings and the measured thicknesses, can be seen in figure 12.11.

In addition to the transmission measurements that were taken using the Vivaldi antennas, a transmission measurement was taken using the NIST design TEM horn antennas without the parallel plate extensions or resistive loading. This measurement examined the layer of Styrofoam with a measured thickness of 6 mm (0.25"). The results of this measurement showed a time shift of 0.036 ns caused by the presence of the Styrofoam layer. This time shift corresponds to a measured thickness of 7 mm (0.3"), which supports the findings of the measurements taken with the Vivaldi antennas.

The drawings of the concrete slabs indicate the presence of two 13 mm (0.50") thick layers of Styrofoam, and individual Styrofoam layers of thickness 19 mm (0.75") and 6 mm (0.25"). The results of the transmission measurements agree with these thicknesses, however their locations differ from those on the drawings. This being the case, it is believed that the measurements were accurate and that the nominal locations of the Styrofoam defects were drawn in a mirror image format.

A third slab was cast to corroborate the results obtained in the first two experiments. The dimensions of this slab were identical to the first two. The defects introduced into this slab included a 6 mm (0.25") piece of Styrofoam, a 13 mm (0.50") piece of Styrofoam, and a 2 mm (.08") piece of Styrofoam.

Testing of Slab 3 using the transmission technique proved difficult because the top surface was not cast flat and level. Due to the accuracy required to detect a time shift on the order of ~0.05 ns and the fact that the thickness of the slab was not constant, it was difficult to obtain accurate time of flight data for this slab.

12.2.3 CORROSION MEASUREMENTS

In order to examine the effect of corroded rebar has upon the transmitted signal, two identical slabs, as described in Section 12.2 were cast. The first slab was placed in an electrolytic accelerated corrosion cell for seven days. The second slab was left untreated. After allowing the corroded slab to dry for a period of two weeks, so as to equalize the moisture contents of both slabs, transmission measurements were taken.

Measurements were taken using a pair of Vivaldi antennas which were positioned approximately in the center of the blocks at a distance of 76 mm (3") from the surface on either side. The transmitted pulse did not show a time shift. However there was a marked change in the magnitude of the transmitted pulse. The transmitted signal for the uncorroded slab had a magnitude which was ~50% less than that of the transmitted signal for the corroded rebar. This data suggests the hypothesis that as corrosion progresses and cross-section is lost, less of the transmitted signal is lost due to the reflection from the rebar. An alternative hypothesis is that the electrolytic accelerated corrosion treatment altered the concrete so as to make it more transmissive. This hypothesis is not borne out by other studies, which have shown that the absorption of radar waves increases with chloride content in the concrete.

12.2.4 CURE MEASUREMENTS

It has been shown that the relative dielectric constant of concrete exhibits a measurable change during the curing cycle (Al-Qadi et al., 1995a, 1995b, and 1996). The use of radar to monitor this change would prove useful in field analysis of newly constructed concrete structures. By correlating the measured relative dielectric constant of concrete to the degree of cure, it would be possible to determine when the concrete had reached a fully-cured or sufficiently-cured for more construction operations.

For a constant antenna separation, it is possible to determine the dielectric constant, ε_r, for a sample of known thickness using the following formula (Aurand, 1996)

$$\varepsilon_r \cong \left[1+\frac{\Delta\tau}{\tau_o}\right]^2 = \left[1+\frac{\Delta\tau}{d/c}\right]^2 \qquad (12.2.4.1)$$

Where $\Delta\tau$ is the time shift in the transmitted pulse caused by placing the sample between the antennas, d is the sample thickness, and c is the speed of light. Using this equation an experiment was designed in order to examine the change in dielectric constant of concrete due to curing. The additional purpose of this experiment was to examine the consistency of the NIST design TEM horn antennas, as well as the effects that the antenna modifications had on the final results.

For the dielectric constant measurements, three test slabs, 229 mm(9") x 279 mm (11") x 76 mm (3"), were cast using Sakrete™ mix. The slabs were allowed to cure and set for four hours before the first measurement. The NIST-design TEM horn antennas without the parallel plate extensions or resistive loading were used for these measurements. A test stand ensured a constant antenna separation. After the initial measurement, additional measurements were taken every twenty four hours over the next seven days. During the curing cycle, the slabs were kept moist with damp layers of cloth.

A second and third set of experiments were performed using the TEM horn antennas with the parallel plates both with and without resistive loading. For these experiments, additional slabs were cast. The three slabs that were tested using the unloaded parallel plates were identical to the slabs used in the first experiment. The three slabs that were tested using the resistively loaded parallel plates were 229 mm (9") x 279 mm (11") x 86 mm (3.375").

The change in dielectric constant followed a trend similar to that of the first set of data, however the measured values over the same frequency range were lower by a factor of 2. Additional measurements taken with the Vivaldi antennas after seven days of curing supported the values for the dielectric constant obtained in the first set of measurements using the horn antennas without the parallel plate extensions and resistive loads. That value was approximately 8.0 after a curing period of seven days.

A fourth set of slabs were built in an attempt to replicate the initial data. For this experiment the parallel plates were removed from the horn antennas. Measurements were taken with both the horn antennas and the Vivaldi antennas for a period of seven days. For this experiment three more slabs were cast which were 229 mm (9”) x 279 mm (11”) x 86 mm (3.375”).

The results of the tests performed using the Vivaldi antennas showed that the dielectric constant over the test period of seven days decreased consistently from an average initial value of 13.14 to an average final value of 8.88. The TEM horn antennas read an average initial value of 8.5. Subsequent measurements exhibited an increase to an average maximum value of 9.93 after 2 days of curing. The values then decreased in the remaining five days to an average final value of 9.06.

The inconsistency in the data obtained using the NIST design TEM horn antenna emphasizes the problems that were encountered using this design. As previously discussed, these problems lead to the subsequent re-design of the antennas.

The results of the measurements taken with the Vivaldi antennas were consistent with curing measurements taken by Al-Qadi et al. (1995a). The decrease in dielectric constant is believed to be caused by the decrease in unbound water content due to hydration during curing.

12.3 B-SCAN SLAB STUDIES

This section describes the GPR data taken from a set of concrete slabs subjected to real and artificial damage. Included in this section are B-scan images of the radar scans along the slabs. Four large slabs were created and subjected to different environmental conditions. In addition, three thin slabs were built and tested for crack identification studies.

12.3.1 METHOD OF SCANNING THE SLABS

The radar system was supported on a customized mobile cart. A 1524 mm (5’) boom arm supported the antenna approximately 100 to 200 mm above the test slab. The body of the cart that held the network analyzer, PC controller and measuring wheel. The cart was pushed at a slow rate and the antenna traversed the slab along a designated line. This traverse was done at several locations along the length of the slab.

A set of five scan lines was drawn with chalk on each of the four large test slabs. Figure 12.13 shows the location of the scans on the top of the slabs.

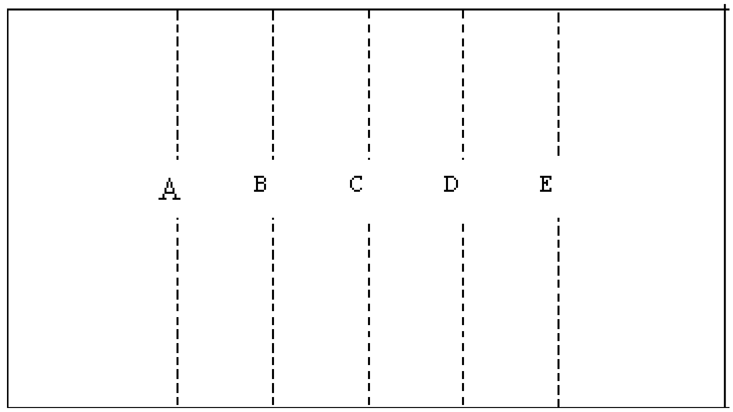

Figure 12.13 *Schematic of the scan lines drawn on each test slab.*

A digital measuring wheel triggered the system to take data every 13 mm (0.5”) along the scan line. This resulted in a high-resolution image that could be easily evaluated. The data are plotted in a B-scan intensity representation of the transverse scan. Features within the concrete are shown as a peak on the recorded waveform and as bright or dark bands on the B-scan image.

12.3.1a Data Processing: The B-scan images were smoothed with a moving average algorithm and an image enhancement program in MATLAB v.5.3. The technique involves first saving the raw data as a waveform matrix where the columns represent the resulting waveform in the time domain and each row is the waveform at every 13 mm of the scan line. This matrix was smoothed with a moving average filter to enhance the viewing of the B-scan image. The smoothing equation used on each element of the matrix is:

$$\tfrac{1}{4} x_{i-1} + \tfrac{1}{2} x_i + \tfrac{1}{4} x_{i+1} \qquad (12.3.1a.1)$$

This equation blends each column of the matrix so that it appears less ‘pixilated’ in the B-scan image. In MATLAB v.5.3, the matrix is plotted on a B-scan intensity map. This intensity map can be manipulated to enhance the features present in the image. This is done by analyzing the raw data, and manually selecting the proper intensity ranges to amplify the features on the image.

12.3.2 CRACKS IN CONCRETE SLABS

Three concrete slabs with a thickness of 51 mm were made for the purpose of simulating delaminations. The interface that exists at the contacting surfaces of these slabs when stacked on top of each other represents a thin delamination, approximately 1mm. The slabs measured, 914 mm x 610 mm x 51 mm. Radar scans were made across the transverse direction of the slabs.

The radar scans of this simulation revealed the cracks existing between the slabs. This is evident in the B-scan images where a feature can be seen which corresponds to the location of the slab-to-slab interface. It is necessary to validate the assumption that the feature seen in the image is, in fact, the surface interface between the slabs. This was done by placing a thin sheet of metal in-between the slabs. The metal acts as a perfect reflector. It can be seen by a high amplitude return signal. First, it was placed between the first and second slabs. The metal sheet was placed at the back end of the scan to see if it aligned with the feature seen when no metal was present. The metal was then placed between the second and third slabs for the same reason. Then it was placed on the bottom of the third slab to confirm that the radar was accomplishing full penetration of this apparatus. The scans can be seen in the following figures.

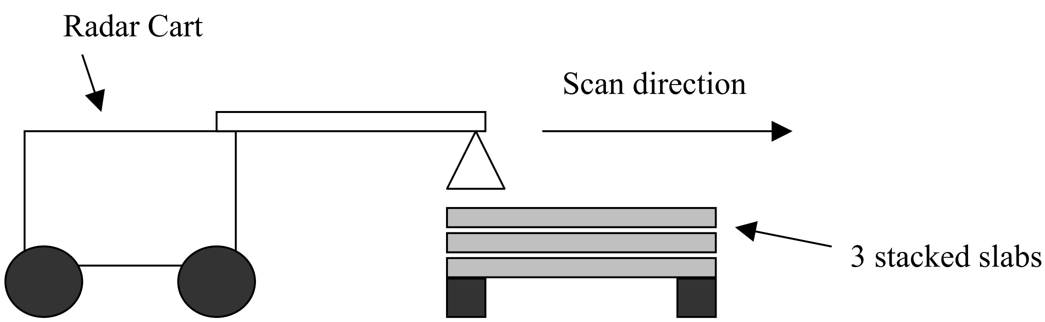

Figure 12.14. *Schematic of the cart with antenna and the layout of the three thin test slabs.*

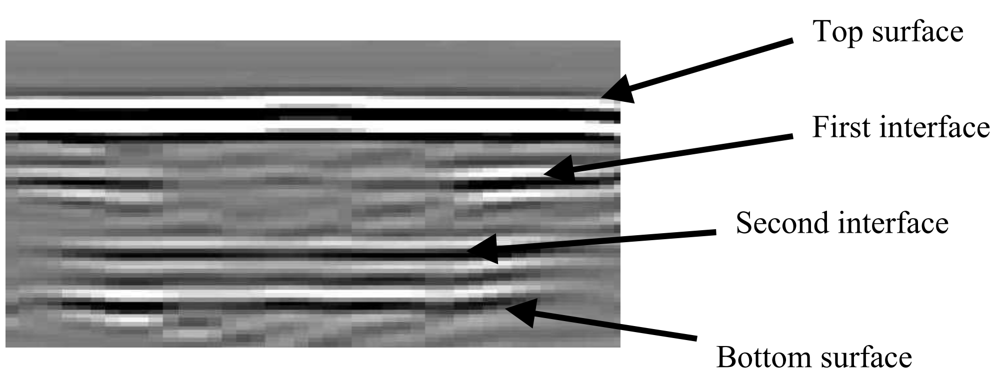

Figure 12.15a *B-scan image resulting from a scan across the center of the three- slab stack.*

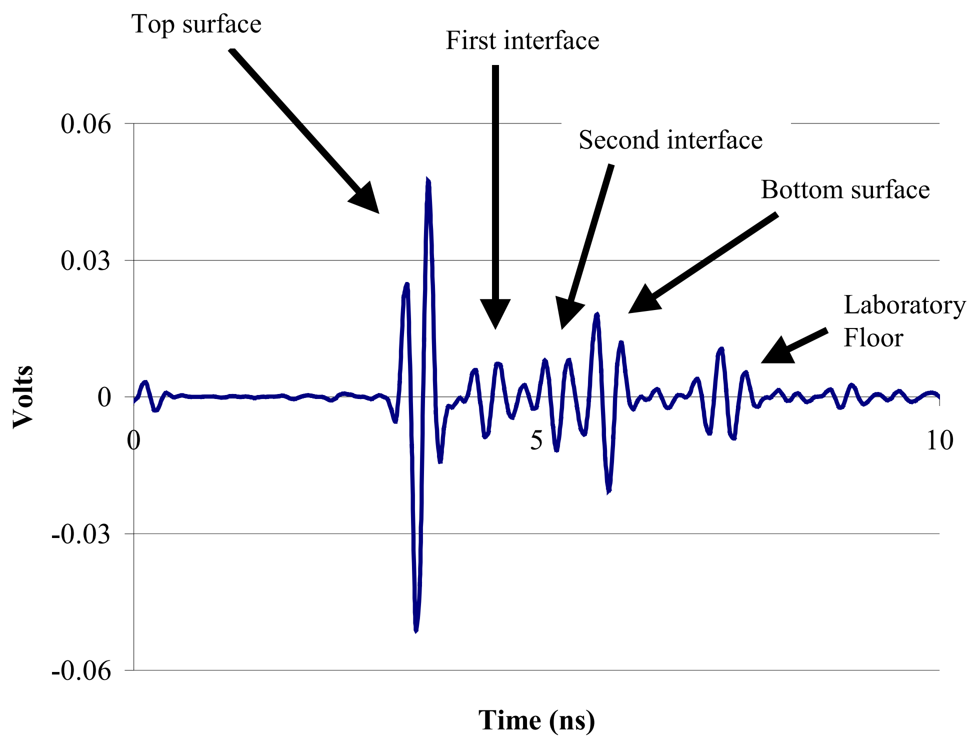

Figure 12.15b *Example waveform from one of the columns of data corresponding to the marked section in the three-slab stack.*

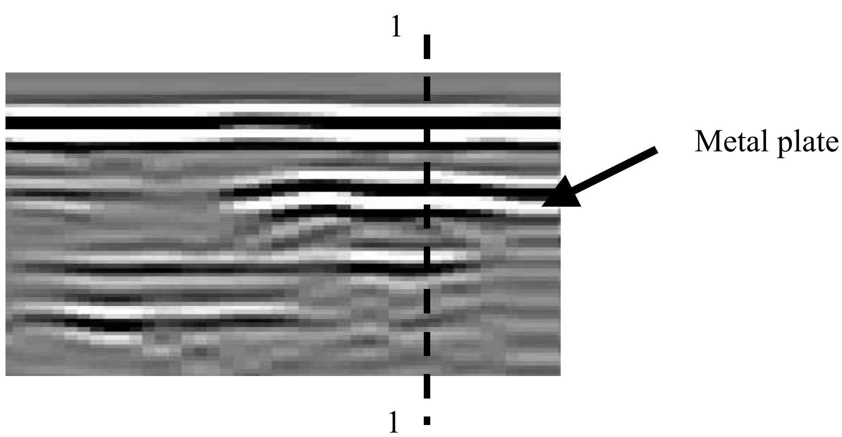

Figure 12.16a *B-scan of three-slab stack with metal placed in-between the first and second layers.*

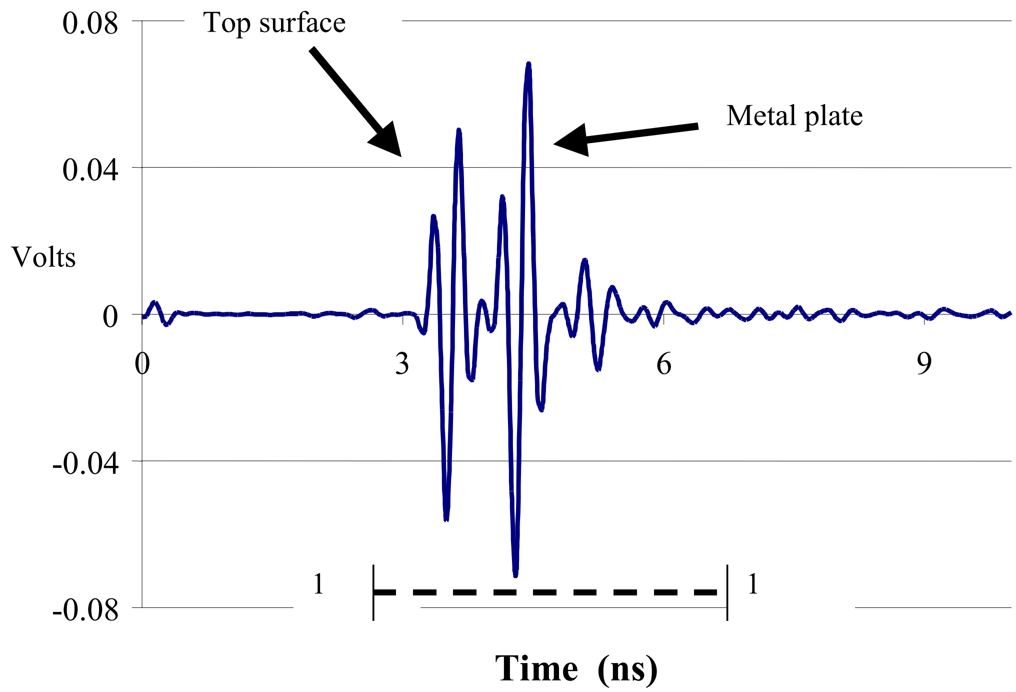

Figure 12.16b *Waveform corresponding to section 1-1 of three-slab stack with metal placed in-between the first and second layers.*

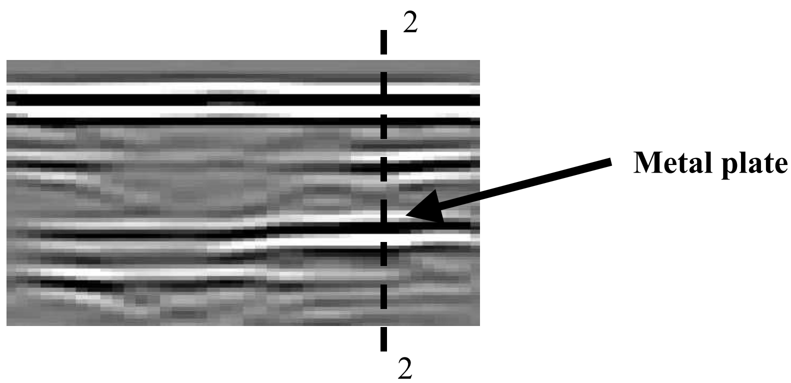

Figure 12.17a *B-scan of three-slab stack with metal placed in-between the second and third layers for section 2-2.*

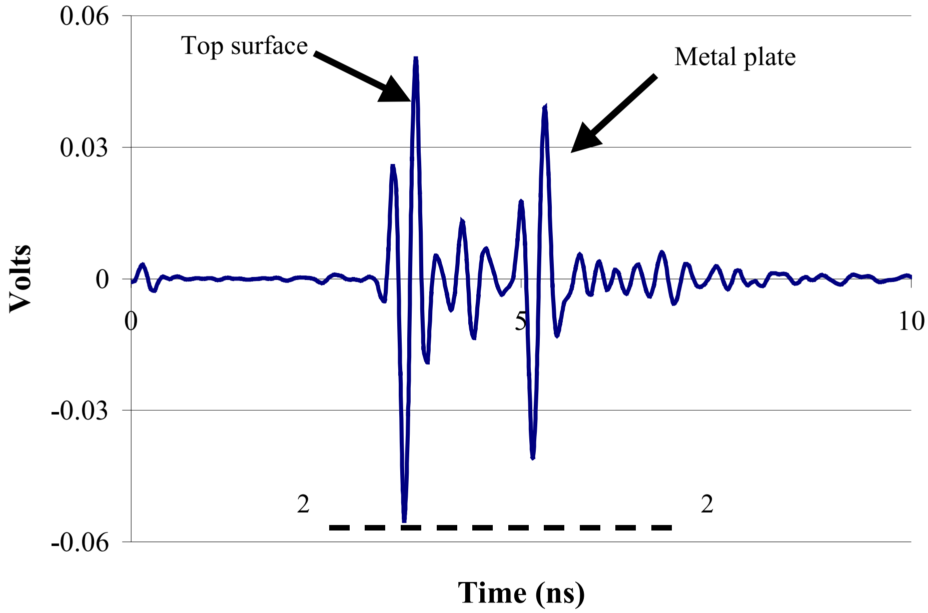

Figure 12.17b *Waveform corresponding to section 2-2 for three-slab stack with metal placed in-between the second and third layers.*

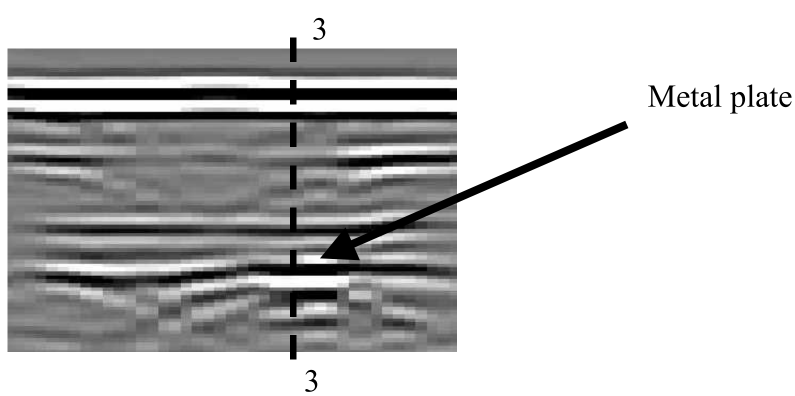

Figure 12.18a *B-scan of three-slab stack with metal placed at the bottom of the stack for section 3-3.*

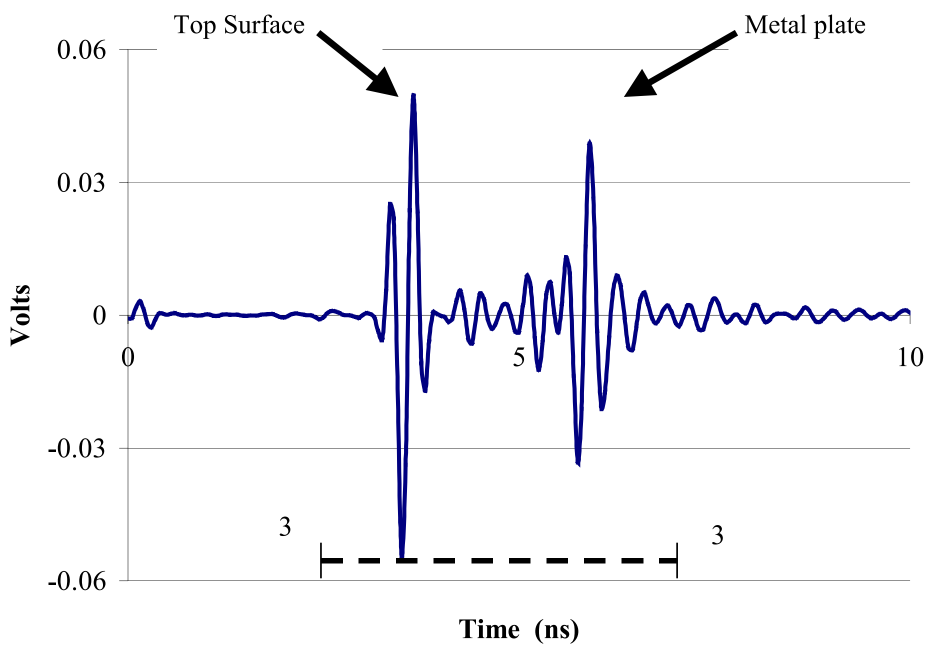

Figure 12.18b *Waveform corresponding to section 3-3 for three-slab stack with metal placed at the bottom of the stack.*

The above images show that the system is able to resolve a crack that is formed by setting two of the slabs flush on top of each other. The first two slabs were made with the same batch of concrete, while the one on the bottom was made at a different time. The dielectric mismatch between the second and third slab is represented by the larger reflection seen at that interface.

12.3.3 FOUR CONDITIONED TEST SLABS

The study in Section 12.3.2 demonstrated that the radar system can detect very thin air-filled cracks (less than 1mm) existing with in a concrete structure, under ideal circumstances. The environmental conditions that affect bridge decks often include additional effects that must be accounted for. In order to simulate field conditions better, the following study subjected four test slabs to different conditions.

The four slabs have the dimensions; 1168mm x 813mm x 152mm. A perpendicular grid of half-inch diameter rebar was supported at mid-depth in the form. The individual layouts can be seen in the subsequent figures. Three of the test slabs have different sizes of foam just above the rebar layer to simulate an embedded defect. The fourth slab is free of known defects. In the descriptions that follow, the slabs are designated as numbers, 1, 2, 3, and 4. Three slabs were poured in 1996 and the fourth was poured in July 1999.

12.3.3a Test Slab 1: Test Slab 1 underwent a rapid corrosion technique twice during its lifetime, once in June of 1998 and again in July of 1999. The purpose was to accelerate the aging process and to corrode the rebar inside the concrete to a dramatic point simulating an aged bridge deck with large chloride residue. The process of rapid corrosion included attaching an anode (+) to the rebar and the cathode (-) to the salt water soaked surface of the slab with a 20V electric potential. The slab was soaked with salt water, which migrated into the concrete and made contact with the rebar. This caused the embedded rebar to undergo accelerated oxidation. The result was a test slab with visibly evident corrosion and chloride build-up. The following schematic shows the form diagram for Slab 1. The pictures below were taken after the second corrosion cycle.

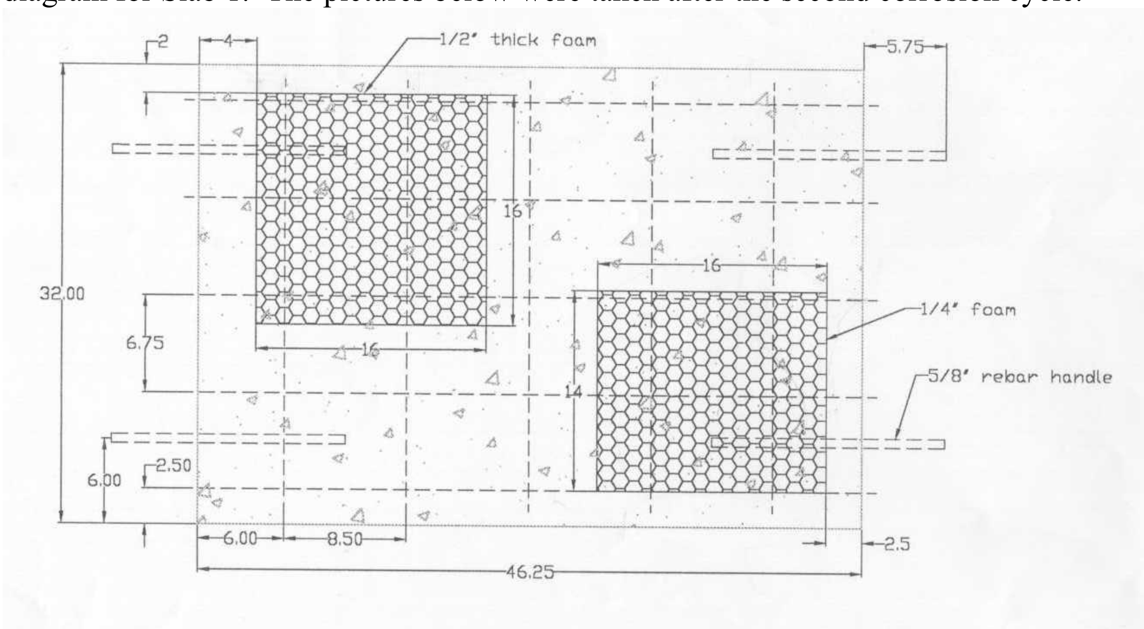

Figure 12.19 *Schematic of Test Slab 1 with a description of the embedded foam defects.*

Figure 12.20 *Top view of Slab 1 with scan lines drawn with chalk.*

Figure 12.21 *Crack in the corner of the slab resulting from the expansion of the rebar during due to corrosion.*

Test Slab 1 was scanned with the radar system in the same way that the three stacked slabs were scanned. The five scan lines were selected to give an overall picture of what exists in the slabs. The resulting data correspond well with the schematic drawing of the slab with embedded defects. The features can be seen in the B-scan images below.

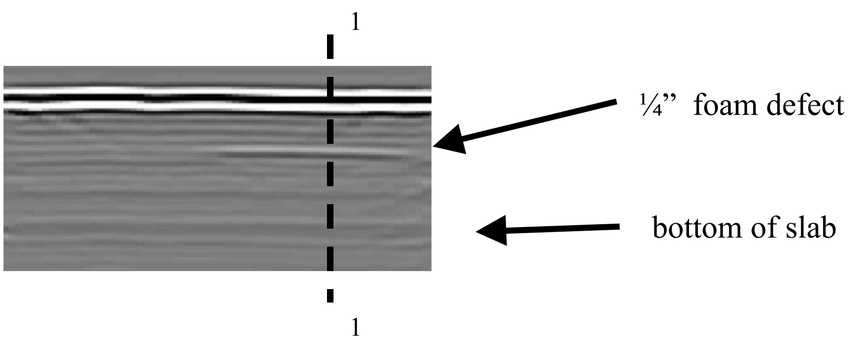

Figure 12.22a *B-scan of Slab 1 for scan line A.*

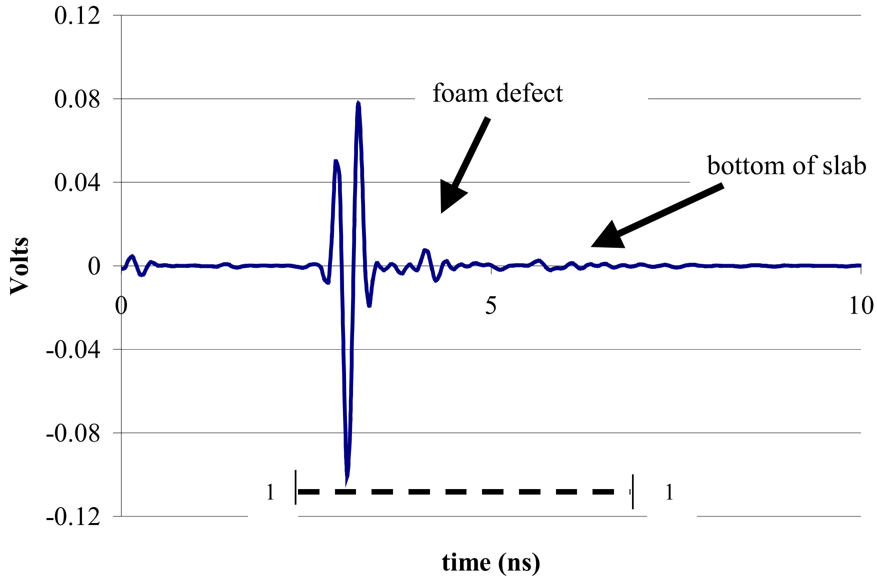

Figure 12.22b *Waveform corresponding to section 1-1 for Slab1 along scan line A.*

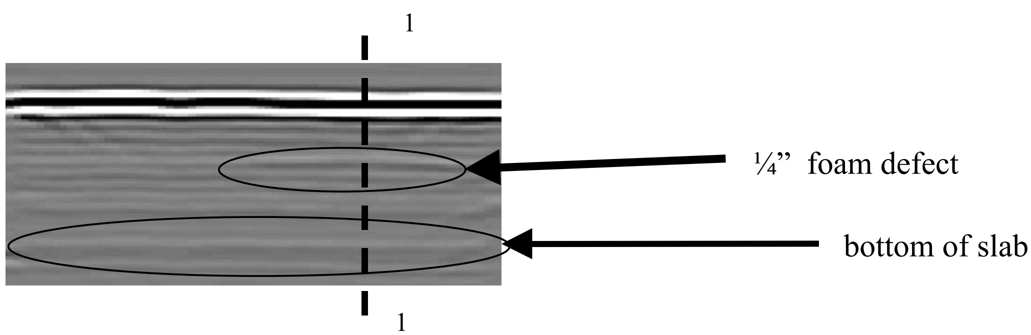

Figure 12.23a *B-scan of Slab 1 for scan line B.*

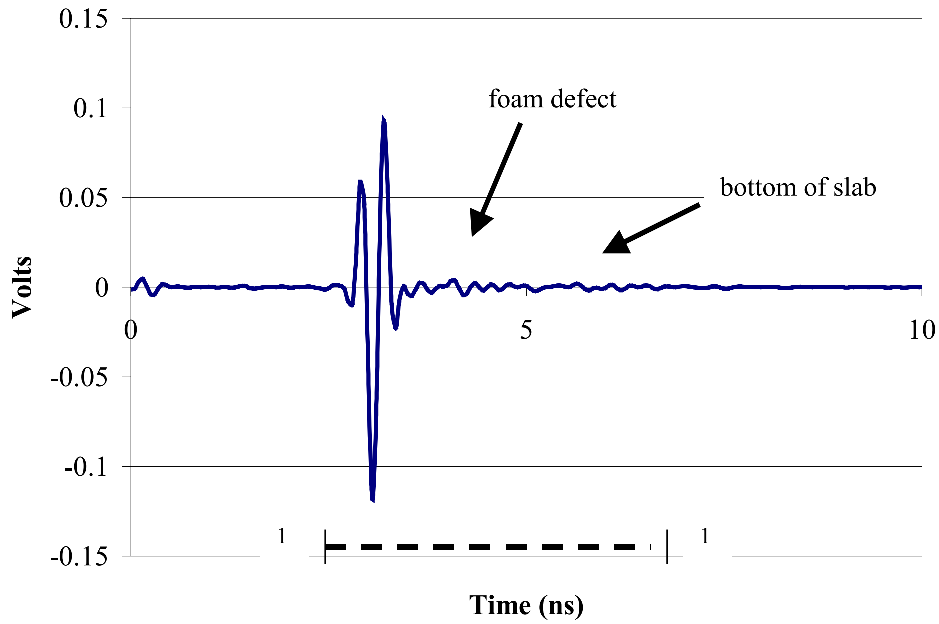

Figure 12.23b *Waveform corresponding to section 1-1 for Slab 1 along scan line B.*

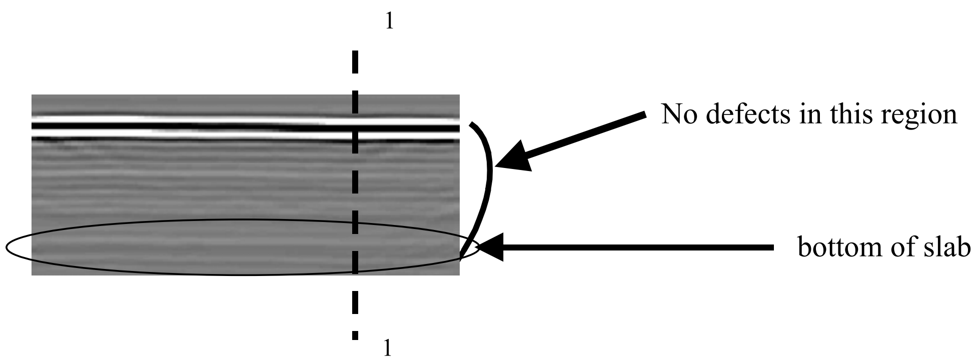

Figure 12.24a *B-scan of Slab 1 for scan line C.*

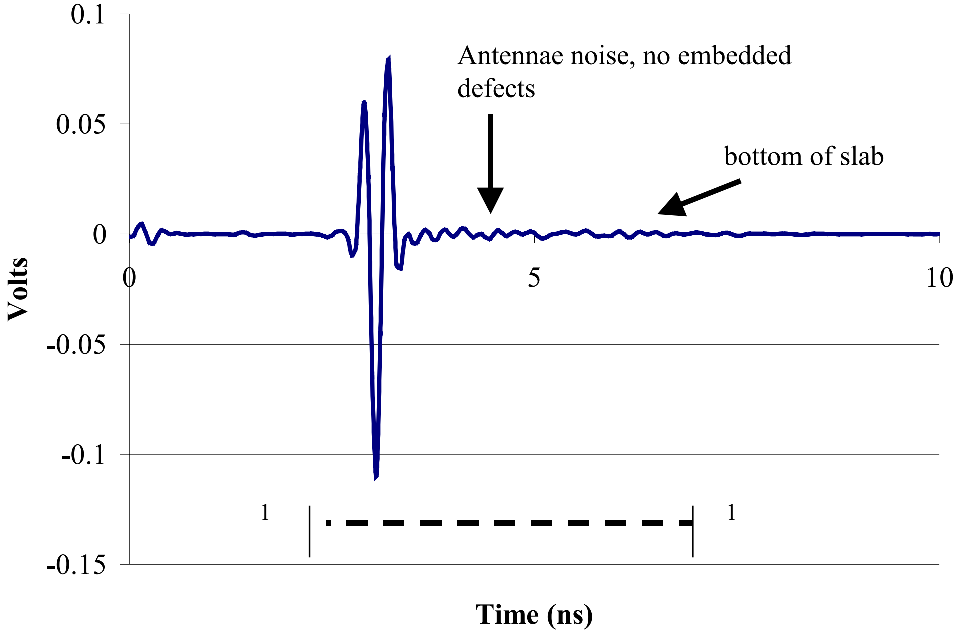

Figure 12.24b *Waveform corresponding to section 1-1 for Slab 1 along scan line C.*

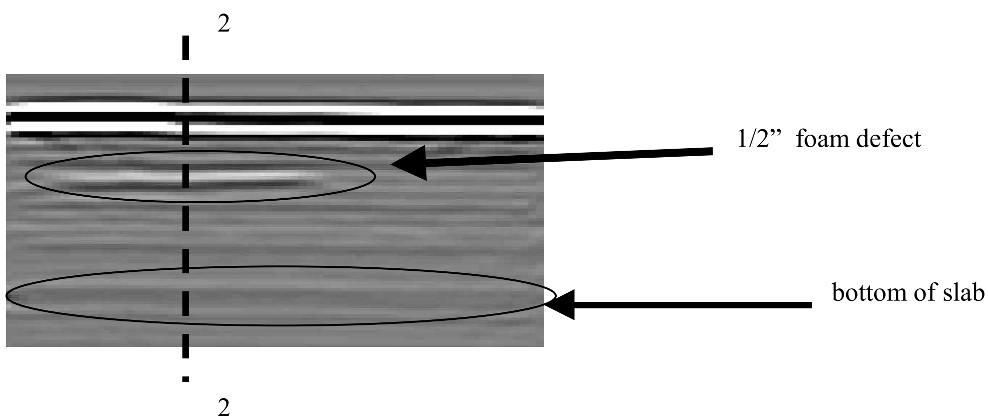

Figure 12.25a *B-scan of Slab 1 for scan line D.*

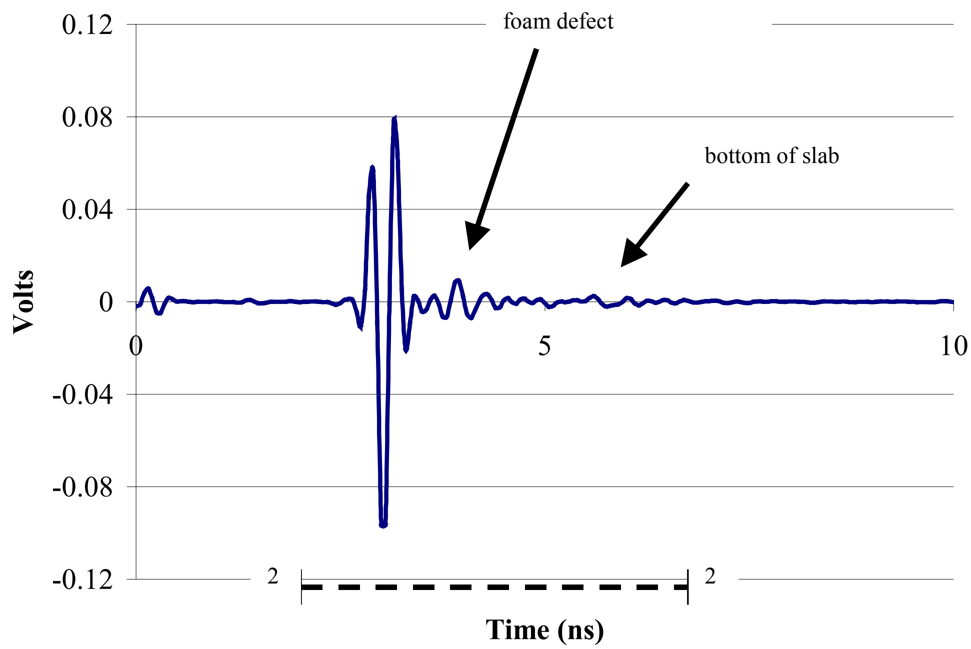

Figure 12.25b *Waveform corresponding to section 2-2 for Slab 1 along scan line D.*

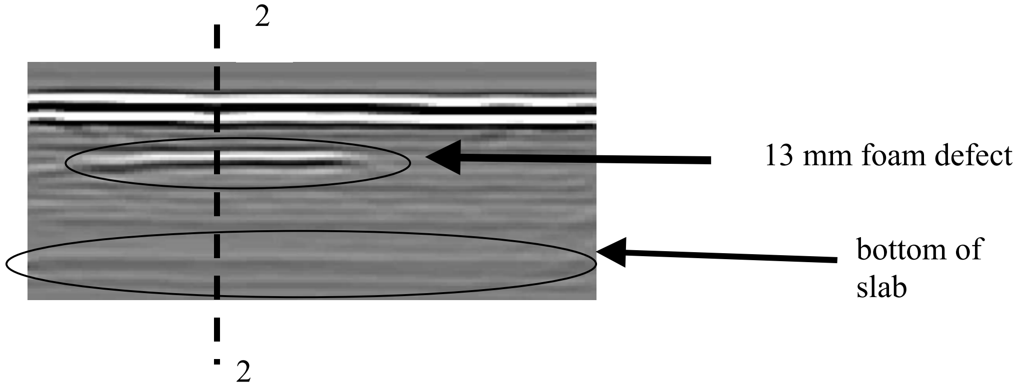

Figure 12.26a *B-scan of Slab 1 for scan line E.*

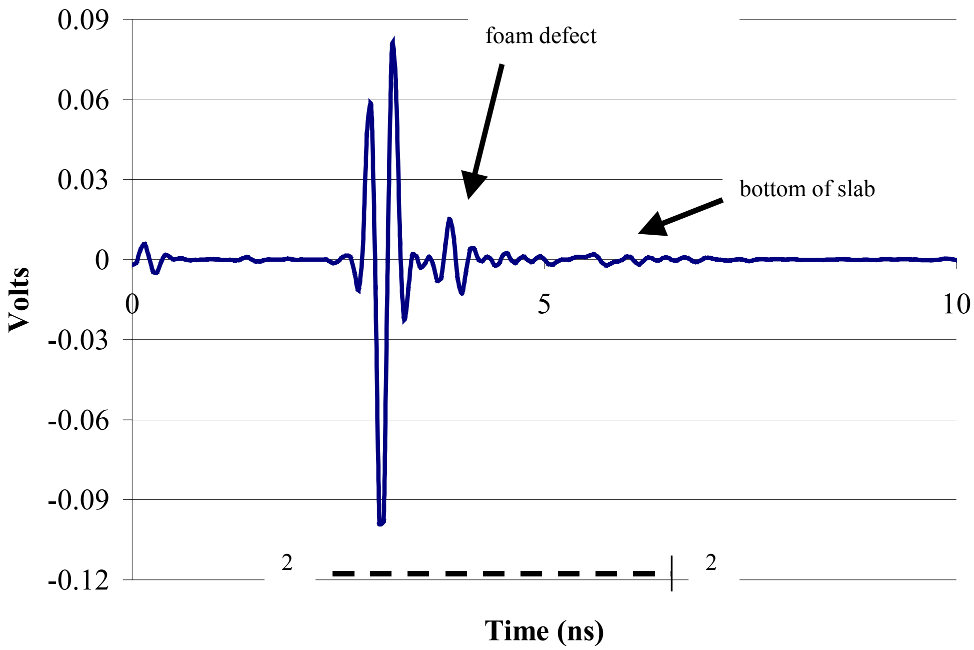

Figure 12.26b *Waveform corresponding to section 2-2 for Slab 1 along scan line E.*

12.3.3b Test Slab 2: Test Slab 2 was poured around the same time that Slab 1 was poured. It also contains embedded foam defects. However, it did not undergo any environmental stressing. Instead, Slab 2 was coated with 38 mm of Quick Patch™ asphalt. This was done to represent an overlay of asphalt on a bridge deck surface. The schematic that follows shows the location and size of the foam defects embedded with in the concrete form. The pictures of the slab were taken before the asphalt overlay was added, so that the scan lines can be seen.

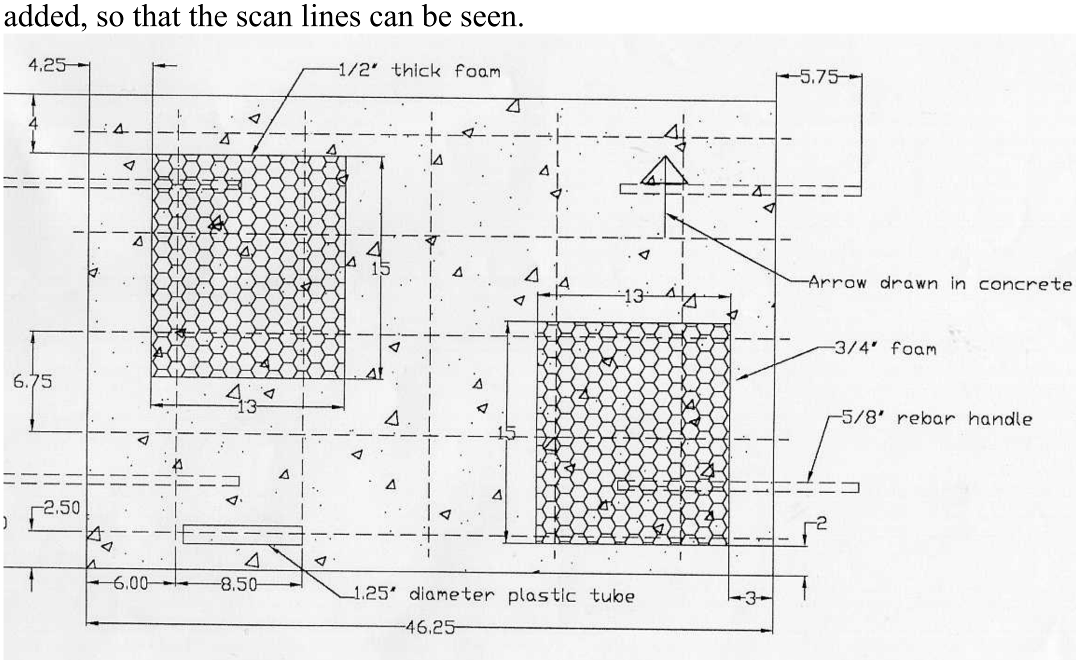

Figure 12.27 *Schematic of Slab 2 with location and size of the foam defects.*

Figure 12.28 *Picture of Slab 2 prior to the addition of a 38 mm thick layer of asphalt.*

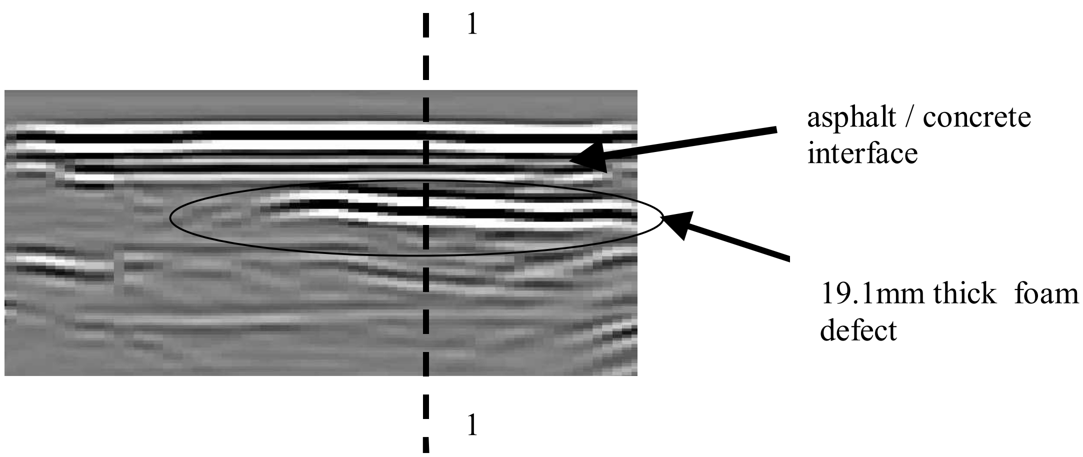

Figure 12.29a *B-scan of Slab 2 for scan line A.*

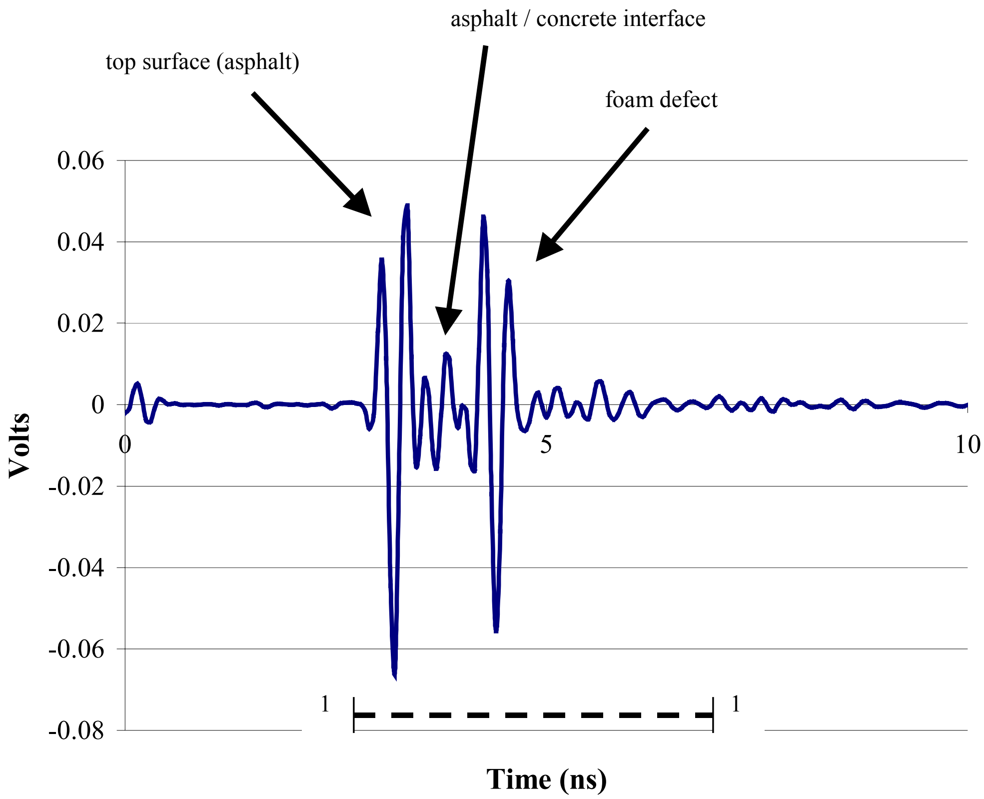

Figure 12.29b *Waveform corresponding to section 1-1 for Slab 2 along scan line A.*

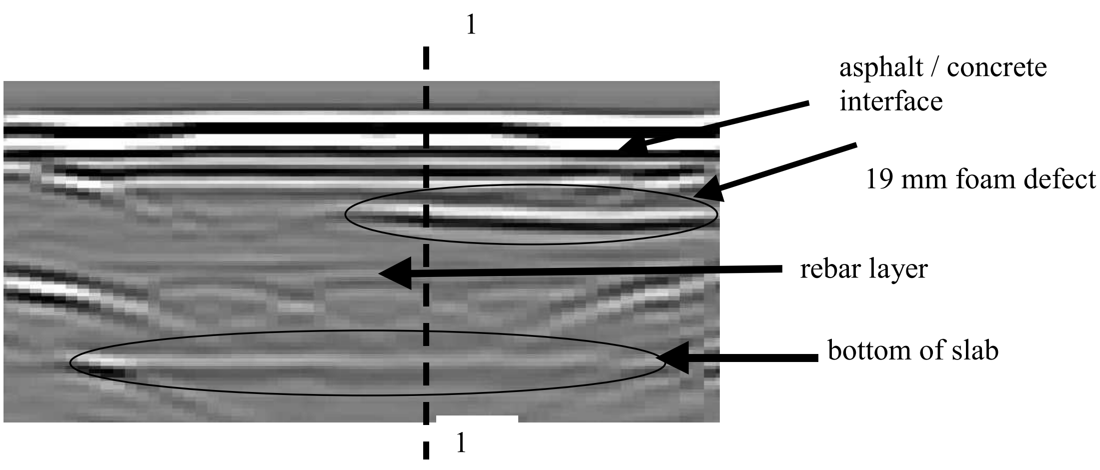

Figure 12.30a *B-scan of Slab 2 for scan line B.*

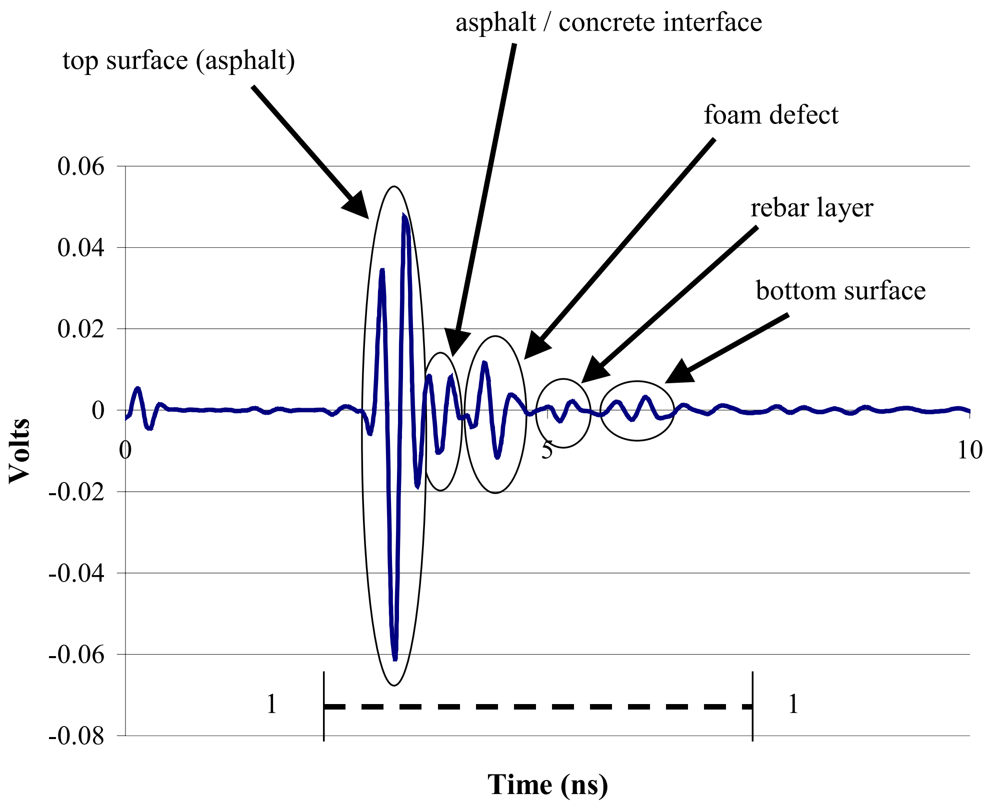

Figure 12.30b *Waveform corresponding to section 1-1 for Slab 2 along scan line B.*

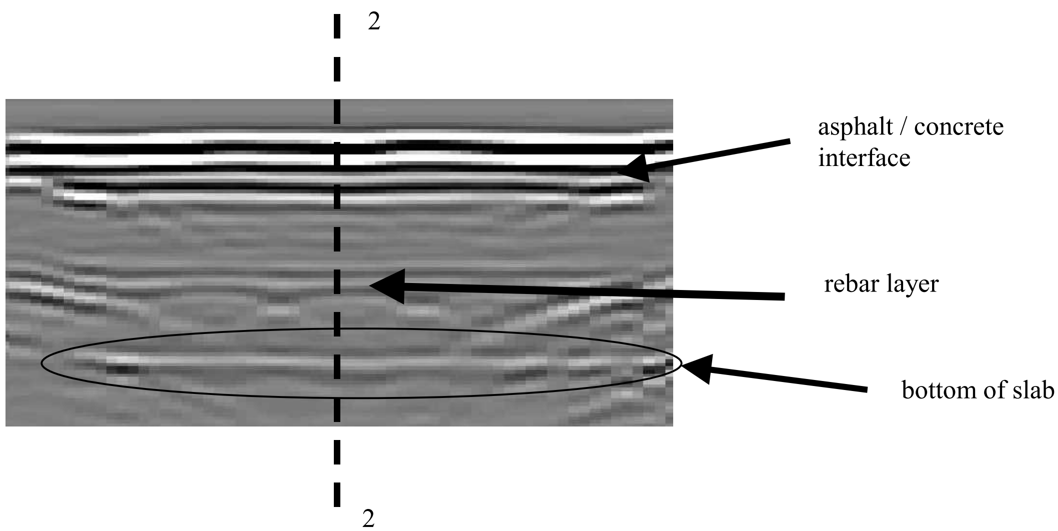

Figure 12.31a *B-scan of Slab 2 for scan line C.*

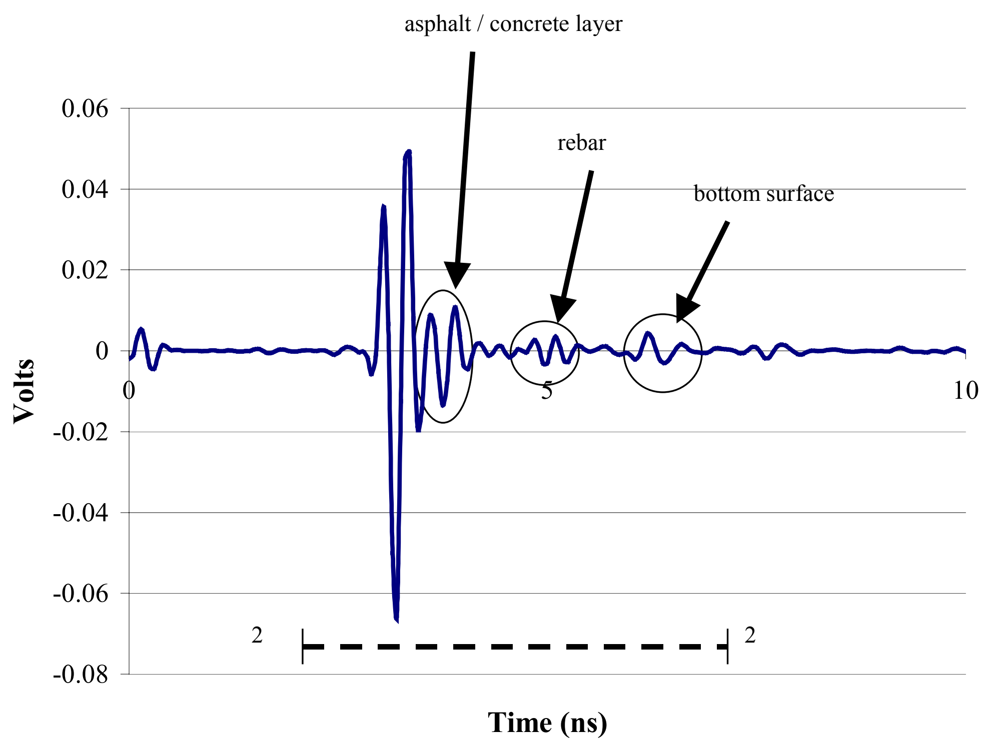

Figure 12.31b *Waveform corresponding to section 2-2 for Slab 2 along scan line C.*

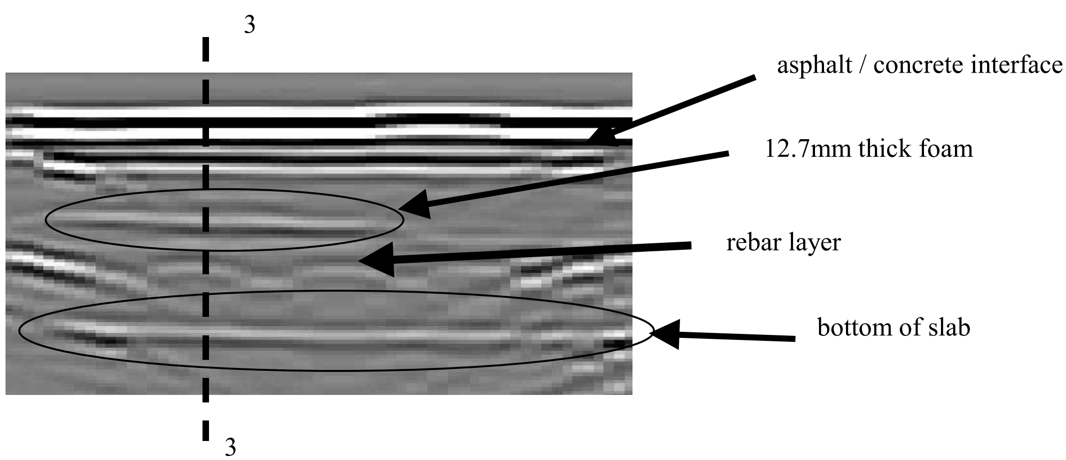

Figure 12.32a *B-scan of Slab 2 for scan line D.*

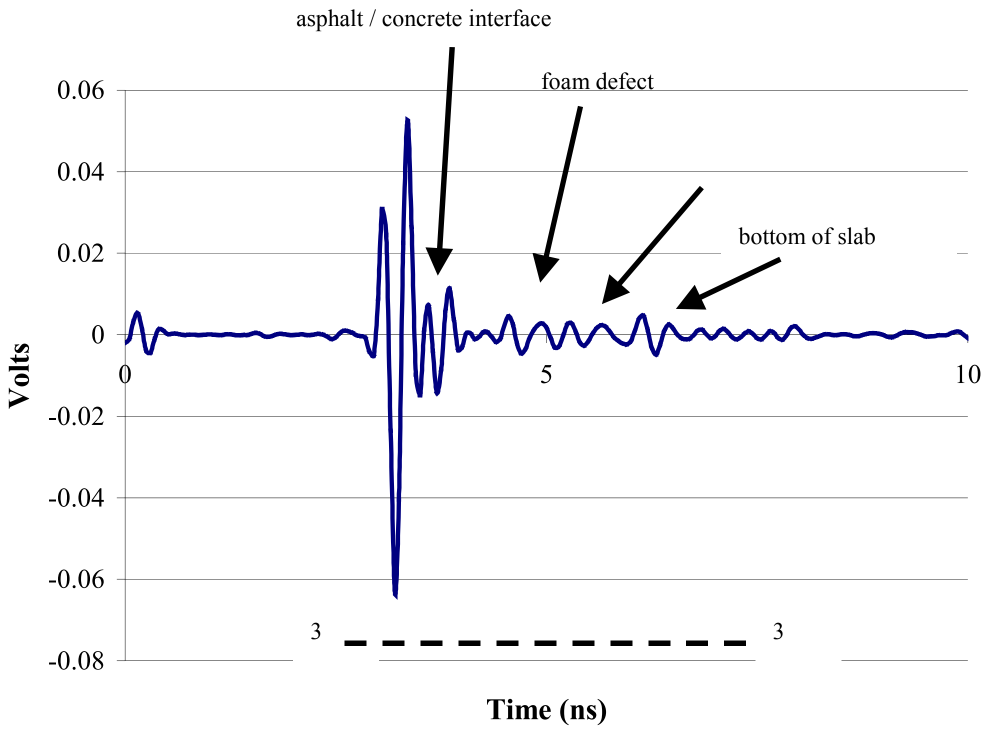

Figure 12.32b *Waveform corresponding to section 3-3 for Slab 2 along scan line D.*

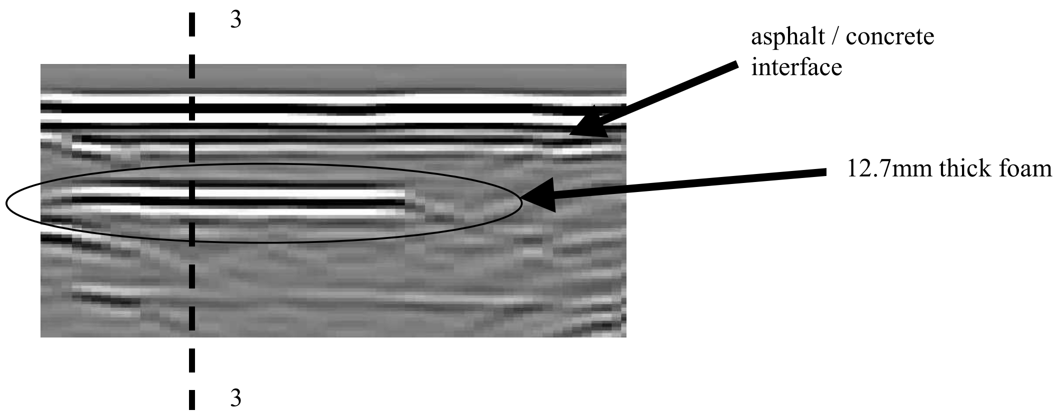

Figure 12.33a *B-scan of Slab 2 for scan line E.*

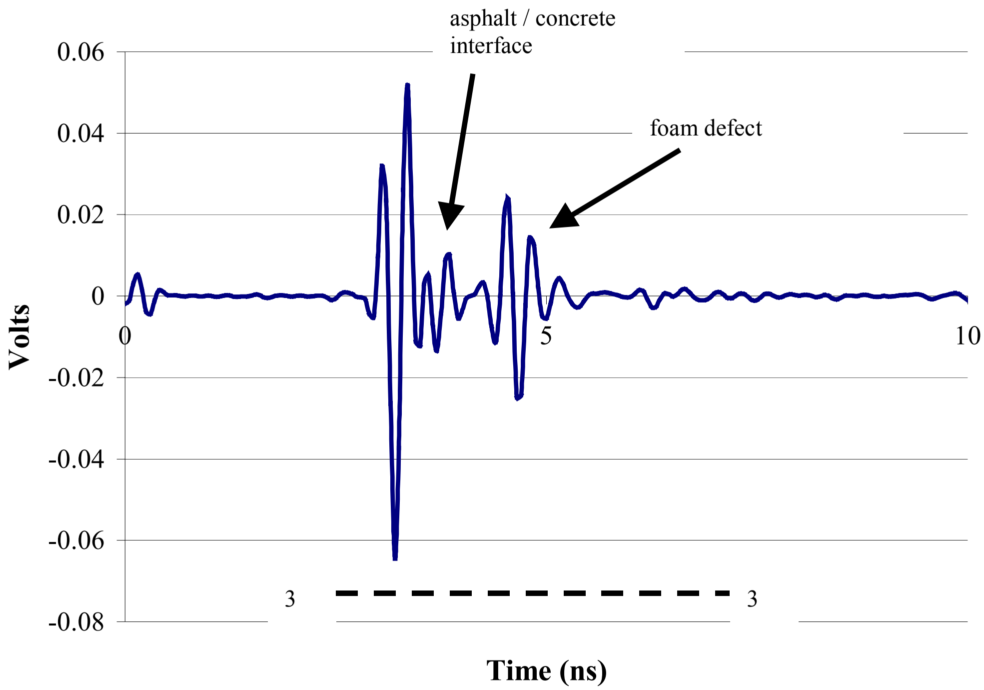

Figure 12.33b *Waveform corresponding to section 3-3 for Slab 2 along scan line E.*

12.3.3c Test Slab 3: Slab 3 is a bit of a mystery slab. It was poured sometime between 1996 and 1997. When it was tested in the lab, documentation concerning its inner construction was lacking. The following plots and interpretations of the data are based on a blind understanding of what is inside. These interpretations were later confirmed when documentation concerning Slab 3 was located. It was determined that Slab 3 included a 6 mm (0.25") piece of Styrofoam, a 13 mm (0.50") piece of Styrofoam, and a 2 mm (.08") piece of Styrofoam. Slab 3 was tested in a manner identical to that of Slabs 1 and 2.

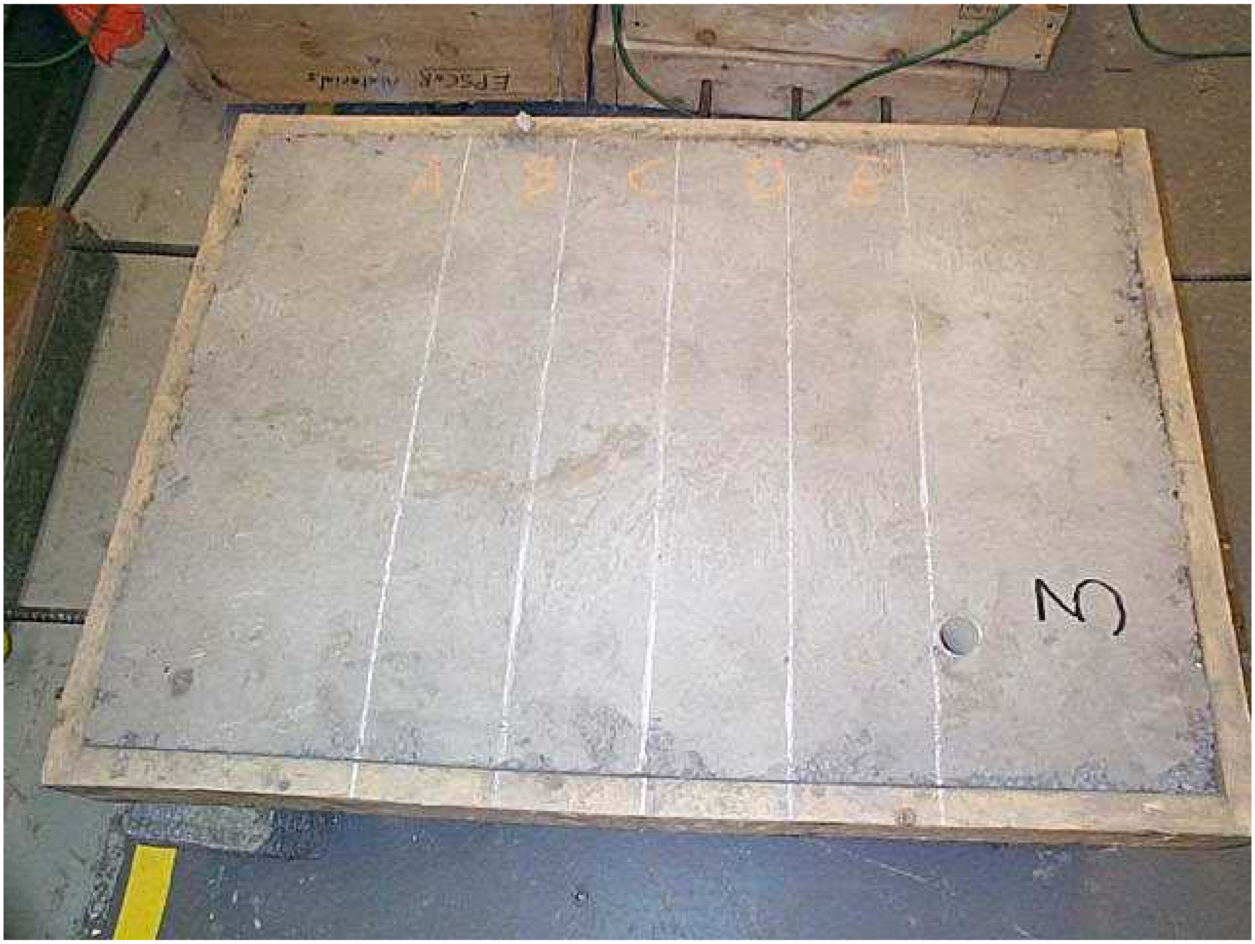

Figure 12.34 *Picture of Slab 3.*

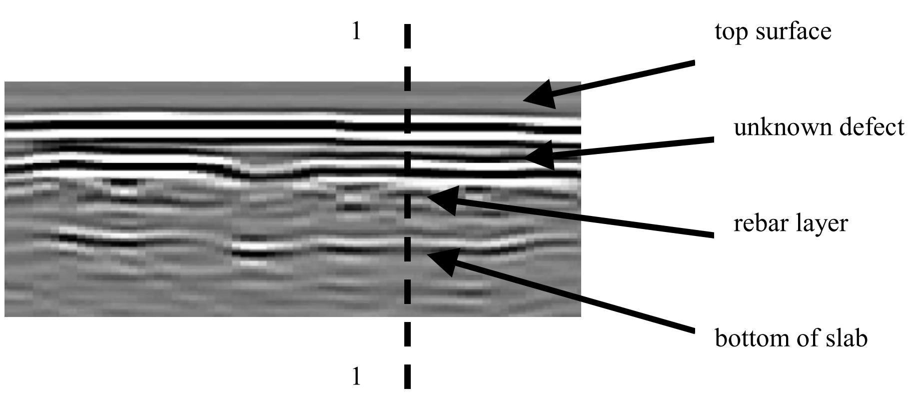

Figure 12.35a *B-scan of Slab 3 for scan line A.*

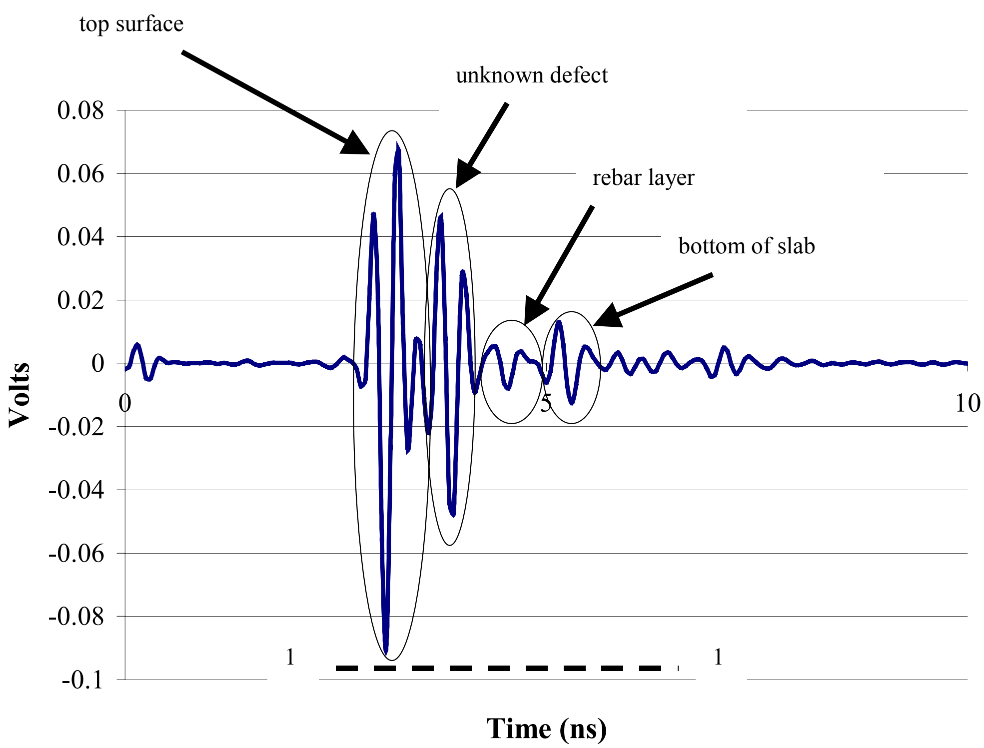

Figure 12.35b *Waveform corresponding to section 1-1 for Slab 3 along scan line A.*

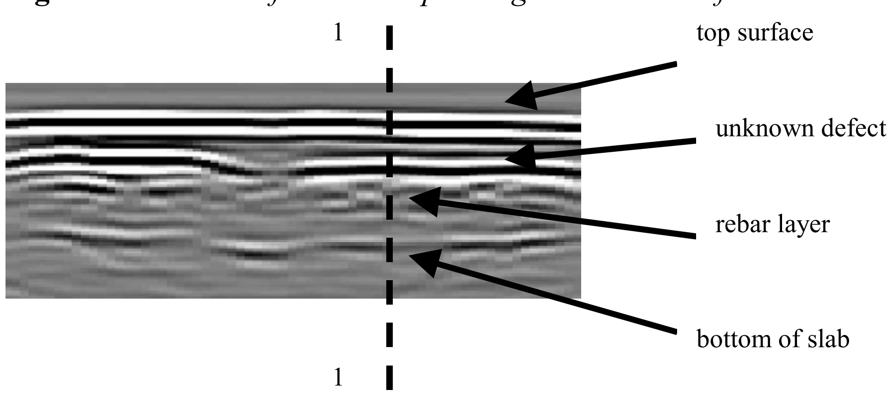

Figure 12.36a *B-scan of Slab 3 for scan line B.*

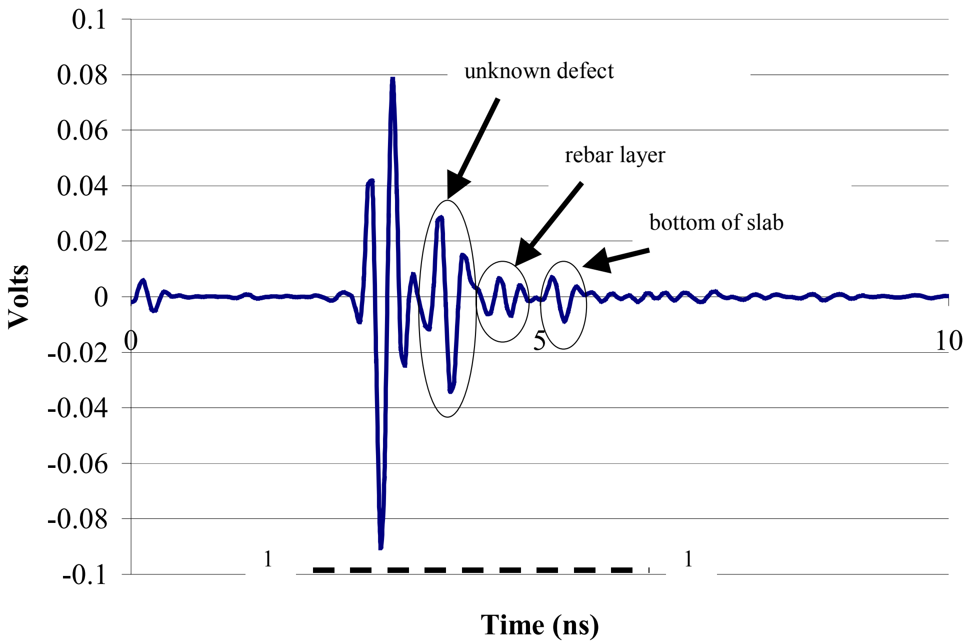

Figure 12.36b *Waveform corresponding to section 1-1 for Slab 3 along scan line B.*

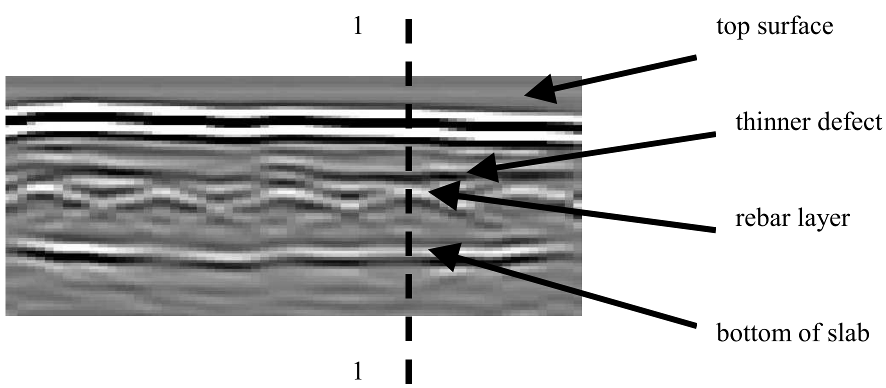

Figure 12.37a *B-scan of Slab 3 for scan line C.*

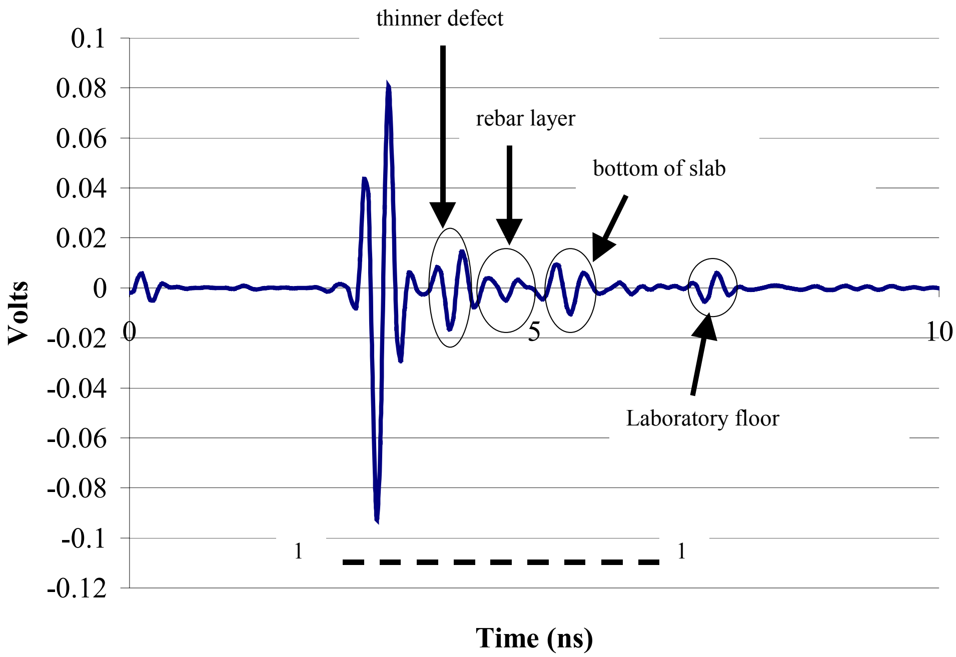

Figure 12.37b *Waveform corresponding to section 1-1 for Slab 3 along scan line C.*

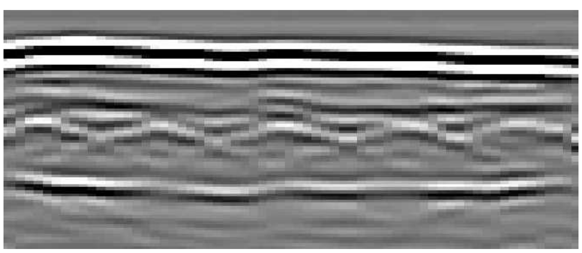

Figure 12.38 *B-scan of Slab 3 for scan line D.*

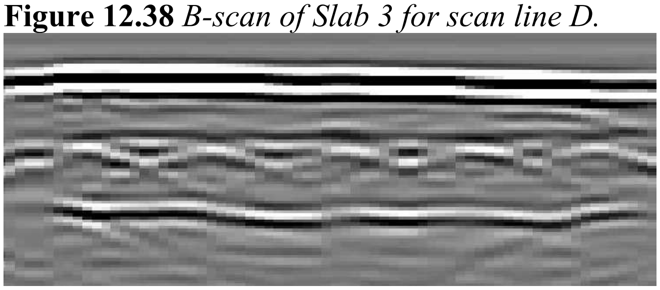

Figure 12.39 *B-scan of Slab 3 for scan line E.*

The waveforms corresponding to scan lines D and E are not supplied because they are similar to the other three figures for this test slab. The top surface, foam defect rebar, layer and the bottom of the slab can be seen clearly in the gray scale images.

12.3.3d Test Slab 4: Test Slab 4 was poured in July 1999, and the radar scans seen in the B-scan images were made in September of 1999. This slab is a new compared to the other test slabs, and very young in terms of bridge lifespan. Slab 4 was made with the same 90 degree 13 mm diameter rebar grid as the other slabs, but there are no defects present with in the slab. The only abnormality is the existence of PVC tubing for the central rebars in both the longitudinal direction and the transverse direction. This can be seen in the figure below. The age of this slab makes it a valuable study tool to test the effects of a newly poured concrete form on the radar system.

Figure 12.40 *Picture of Slab 4.*

The two central reinforcing bars are made of hollow PVC tubing. The initial plan was to use the hollow void created in the concrete as a place to add and remove steel rebar. The purpose was to monitor the difference in the returned signal of the void containing either air or steel. The age of the slab complicated the penetration of the deck with the rebar. This concrete was mixed with a high water to cement ratio and took a long time to cure, which directly affects the dielectric constant and the penetrating radar signal amplitude.

The following B-scan images do not have subsequent waveforms for each scanline due to the similarity of the five scan lines in the absence of any defects. On each B-scan, the PVC tube is clearly visible. The waveform provided is marked at the location of this transverse hollow tube.

Figure 12.41 *Picture of Slab 4 reinforcement including hollow tubes.*

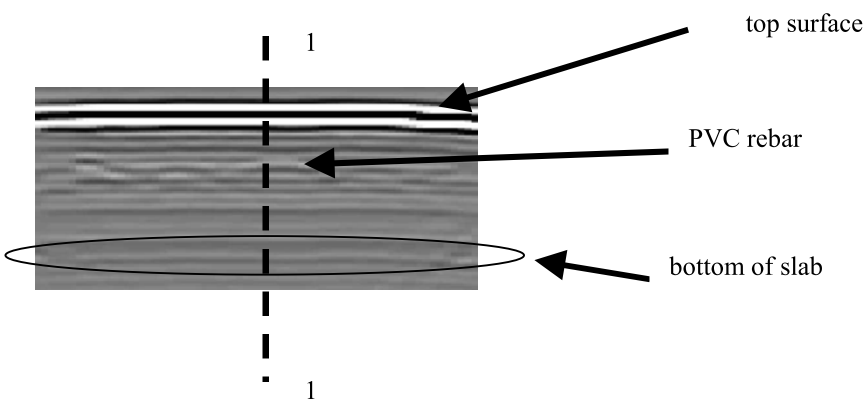

Figure 12.42a *B-scan of Slab 4 for scan line A.*

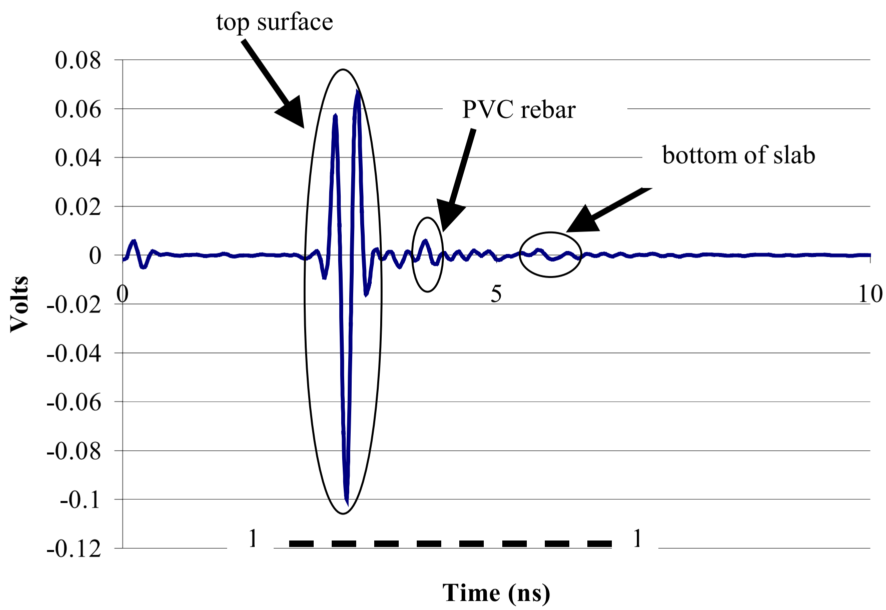

Figure 12.42b *Waveform corresponding to section 1-1 for Slab 4 along scan line A.*

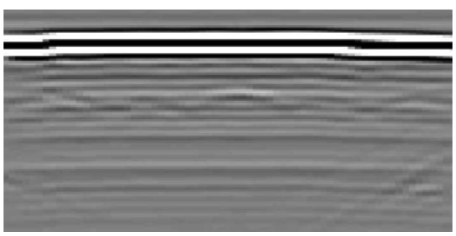

Figure 12.43 *B-scan of Slab 4 for scan line B.*

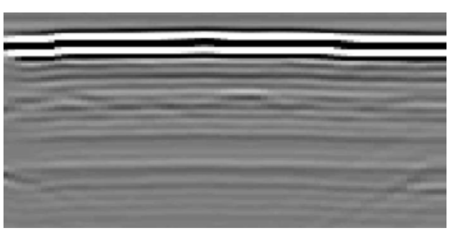

Figure 12.44 *B-scan of Slab 4 for scan line C.*

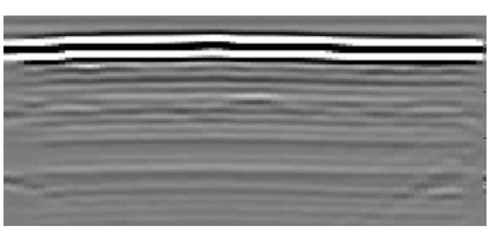

Figure 12.45 *B-scan of Slab 4 for scan line D.*

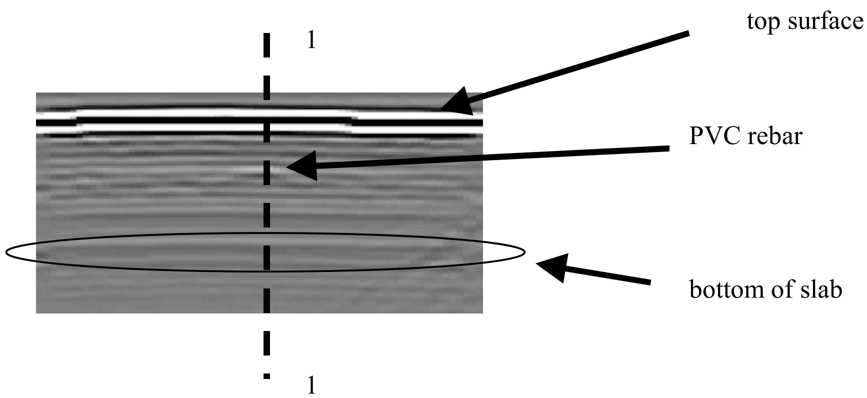

Figure 12.46 *B-scan of Slab 4 for scan line E.*

12.4 FREEZE / THAW TEST

Concrete bridge decks are exposed to many brutal environmental conditions over the life span of the deck. One such condition that is very prevalent in the northeast is freeze / thaw cycling. During the winter months there is a constant temperature fluctuation between night and day and during storms the moisture absorbed by the porous nature of the concrete tends to cycle through freeze and thaw stages. Usually during the night when traffic is low and the temperature is below freezing the trapped moisture freezes and expands in volume, causing localized internal stresses. During the day with the heat of the sun and increased traffic, the moisture thaws and become liquid again. The effects of the freeze / thaw cycling on concrete can be observed with the radar unit designed for this project.

The dielectric constant of concrete is variable, with values ranging from 5 to 11. The dielectric constant can be influenced by a variety of effects, as discussed in Section 8.5. The tests reported in this section, involve the change in dielectric constant of concrete test specimens due to moisture absorption and freeze / thaw cycling.

The dielectric constant of concrete is measured with GPR by comparing the reflection of the radar signal off the concrete surface and the total reflection of the radar signal off of a metal plate placed on the surface of the concrete sample. This comparison is determined from the ratio of the amplitude of the reflected signal off of the concrete surface to the amplitude of the total reflection off of the metal plate.

$$R_{12} = {}^{-V_2}\!/_{V_1} \tag{12.4.1}$$

The dielectric constant is then calculated using the ratio above and the following equation.

$$\varepsilon_r = \left[\frac{(1 - R_{12})}{1 + R_{12}}\right]^2 \tag{12.4.2}$$

Three concrete samples were used to study the effects of freeze / thaw cycling. Initial GPR scans were made of the samples, and of a metal plate placed on the surface of the samples. Then the samples, numbered 1,2, and 3, were placed in a water bath. Sample 3 was placed in a salt water solution while samples 1 and 2 were simply put in fresh (tap) water. The samples soaked in the water baths for 2 days before they were placed in a freezer. Over the course of a week the samples were brought in and out of the freezer ten times. Thus, completing ten freeze / thaw cycles. After ten cycles, the samples were set aside to dry for two days. They were then scanned under the radar to acquire the reflective amplitude of each samples surface. Subsequently, the metal plate was scanned to acquire the maximum reflection of the radar system at that time. The samples were soaked again for two days with sample 3 still soaked in salt water. After the pre-soak, the samples were subjected to eighteen more freeze / thaw cycles. With the total cycles now at twenty-eight, the samples were set to dry for three and a half days. Then they were scanned under the radar, as well as, the metal plate.

The following plot shows the resulting dielectric constant for each concrete sample. The initial point is the value calculated before any conditioning was performed. The two other points were taken after ten and twenty eight freeze / thaw cycles, respectively.

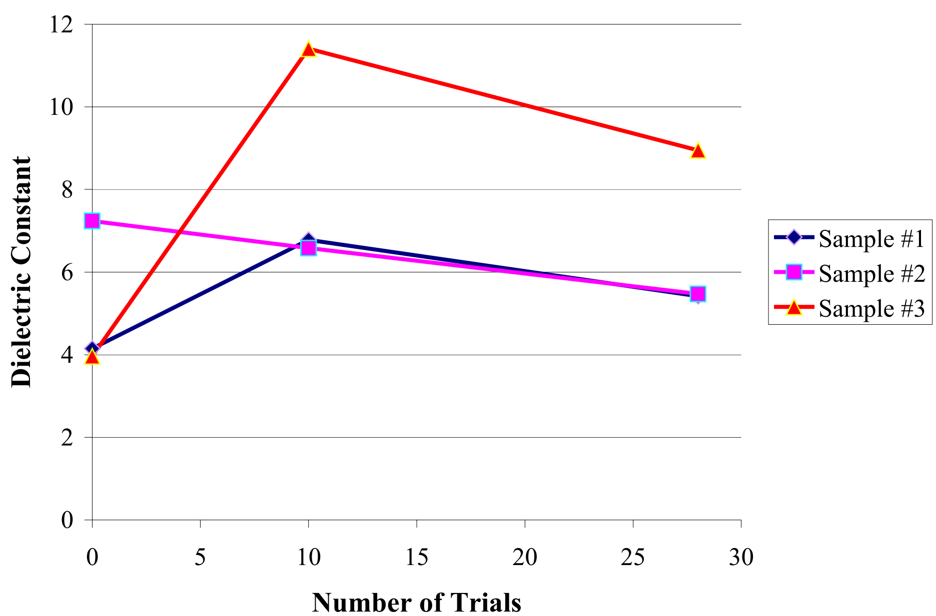

Figure 12.47 *Dielectric constant of slabs vs. number of freeze/thaw cycles. Slabs 1 and 2 were soaked in tap water. Slab 3 was soaked in salt water.*

The above plot shows the effects of twenty eight freeze / thaw cycles on the dielectric constant of concrete. The amount of cycles does not add up to the equivalent of one season, therefore, there exists inconsistency in the above figure. This is a minimal amount of cycles compared to the life-span of bridge decks which is on the order of fifty years. However, some trends can be noted from this experiment. First, the dielectric constant of Sample 3 increased dramatically after the initial soaking in the saltwater bath and ten subsequent freeze / thaw cycles. This is an expected trend because the addition of chloride to the concrete does significantly raise the dielectric constant. The plot shows the effect of moisture content on the dielectric constant of the samples. Initially the samples were dry slabs, prior to the water bath. The lower initial dielectric constant is an indication that absorbed moisture increases the dielectric constant. This holds self evident for Samples 1 and 3. The samples were allowed to dry for two days after the first ten cycles before they were scanned with the radar. The samples were allowed to dry for three days after the second set of freeze / thaw cycles which might account for the decrease in the dielectric constant seen at point three. Sample 2 does not follow the expected dielectric constant trend after any amount of cycles. This is most likely due to the fact that twenty eight cycles is simply not enough cycles to start analyzing the effects of freeze / thaw on concrete samples. To continue studying these effects, the samples are being subjected to additional freeze / thaw cycling.

13. FIELD TEST RESULTS

Several bridges were examined with the GPR system. The quality of the bridges ranged from new to highly-distressed.

13.1 PRELIMINARY STUDIES

An initial series of tests were conducted on local bridges in an effort to benchmark and develop the GPR system. The first bridges to be tested were a new reinforced post-tensioned concrete bridge in Milton, VT and an old truss bridge undergoing rehabilitation in Waterbury, VT. These studies indicated that it was possible to use a network analyzer as the source, receiver, and signal processor. It was also determined that an improved antenna positioning system and improved data processing software were needed. Figure 13.1 is a picture of testing at the Waterbury Bridge.

The next field test was performed at the Bostwick Bridge, Shelburne, Vermont, on December 2, 1998. The Bostwick Bridge, was built in 1954. The bridge had a condition rating of four. This means that the deck had > 5% spalls, or the sum of the deteriorated and/or contaminated concrete was between 40% to 60 % of the bridge. Figure 13.2 shows the deck condition of the Bostwick Bridge. The deck had numerous asphalt and concrete patches, along with some undamaged sections. The combination of damaged and undamaged sections, along with the low traffic volume, made the Bostwick bridge an ideal candidate for GPR testing.

Figure 13.1 *Field test conducted at the Waterbury Bridge, before a new concrete deck is placed.*

Figure 13.2 *Bostwick Bridge, Shelburne, VT roadway.*

13.2 SECOND BOSTWICK BRIDGE TEST

13.2.1 PROCEDURE

The GPR survey system and set up is shown in figure 13.3. The system consisted of a GIMA-1 antenna, an HP 8753D Network Analyzer, a measuring wheel, and a computer. It was powered by a power generator through an uninterruptable power supply. The system was set up to collect a scan every 25.4-mm.

First, four lines spaced 610mm apart were drawn along the span of the bridge deck for the GPR cart to track. Cross lines were drawn every 1220 mm. The aperture of the antenna was set at a 15-degree angle with respect to the ground to prevent multiple reflections between the ground and the antenna. A system baseline correction measurement was taken by pointing the antenna upward into open air. The cart was then pushed slowly at a speed of approximately 100 mm/s per second from one end of the bridge to the other, while collecting data. Four strips of pavement were tested along the bridge.

The test data appeared on the computer screen simultaneously as the test was conducted. A Matlab program was used to plot the data.

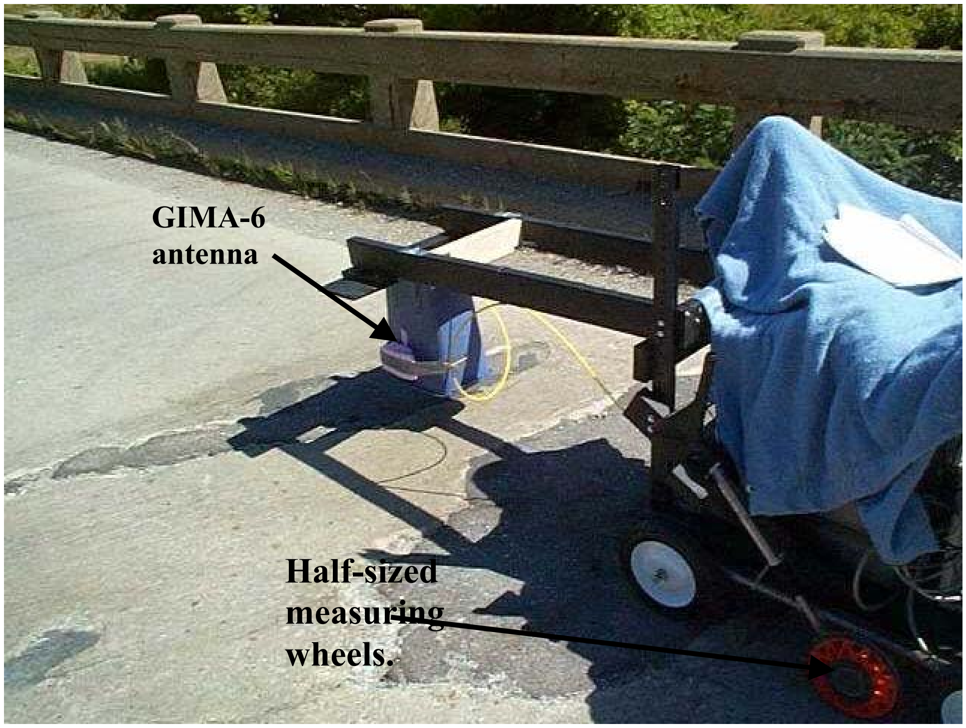

Figure 13.3 *Second Bostwick Bridge, Shelburne, VT deck survey.*

13.2.2 RESULTS OF THE SECOND BOSTWICK BRIDGE FIELD TEST

The GPR system worked well on the field-test, except for occasional data dropouts due to a malfunction of the measuring wheel. Some data points were also missed when the cart was pushed too fast and the data were not recorded properly.

For these tests the data were plotted in a waterfall format. The Z-axis is the magnitude of the reflection coefficient. The X-axis is the distance along the bridge deck. The Y-axis is the penetrating depth relative to time of flight.

Figure 13.4 is the GPR signal from a deck section with a relatively good condition. It contains a regular first main peak due to the reflection from the top of the deck surface. The sub-surface structure is consistent. Figure 13.5 is the data taken from an asphalt filled patch. The irregular main peak is due to difference in the reflection coefficient between the asphalt and concrete. The dropout of the main peaks indicates the asphalt filled area. It also shows that there are peak rises right after the main peak. These peaks indicate the change in the substructure near the surface. Figure 13.6 shows the GPR data taken from a section of the deck where several small patches are filled with different materials, such as asphalt, and concrete. Changes in the height of the main peak correspond to changes in the material. However, because the dielectric constants of the old concrete and new concrete are not significantly different, the magnitude of the main peaks do not change as severely in some places. Changes in the subsurface condition can be recognized from the subsurface waveforms.

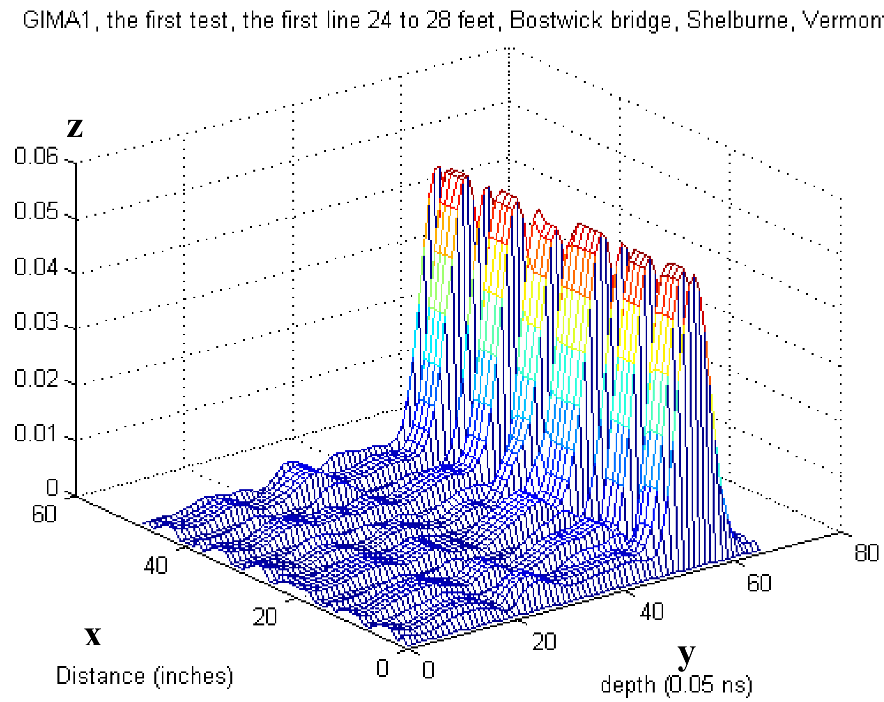

Figure 13.4. *GPR waterfall plot of the results obtained over a relatively good condition portion of the deck of the Bostwick Bridge, Shelburne, VT.*

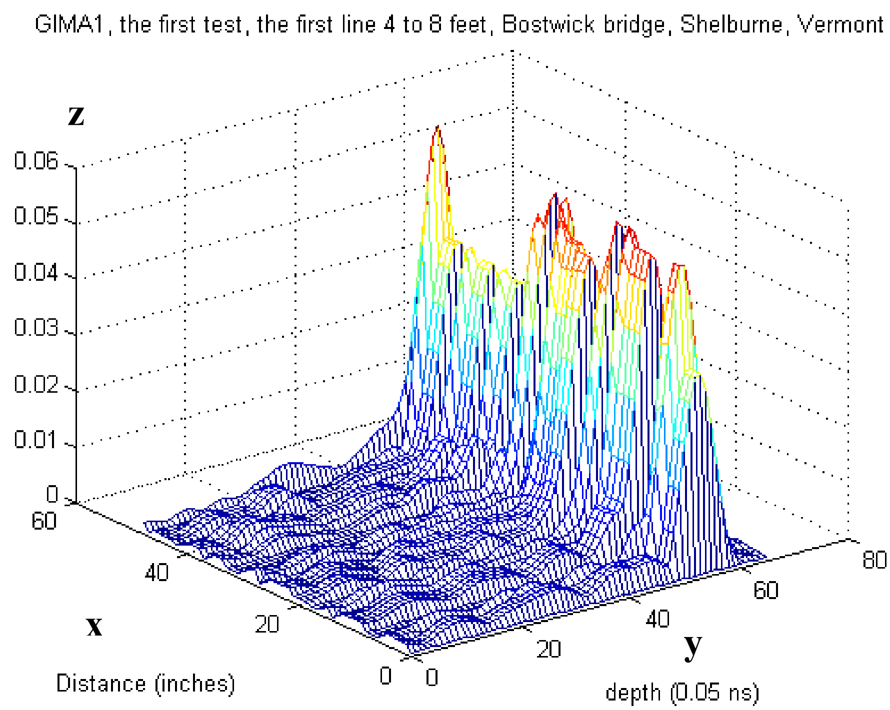

Figure 13.5 GPR *waterfall plot of the results obtained over an asphalt-filled patch of the deck of the Bostwick Bridge, Shelburne, VT.*

.

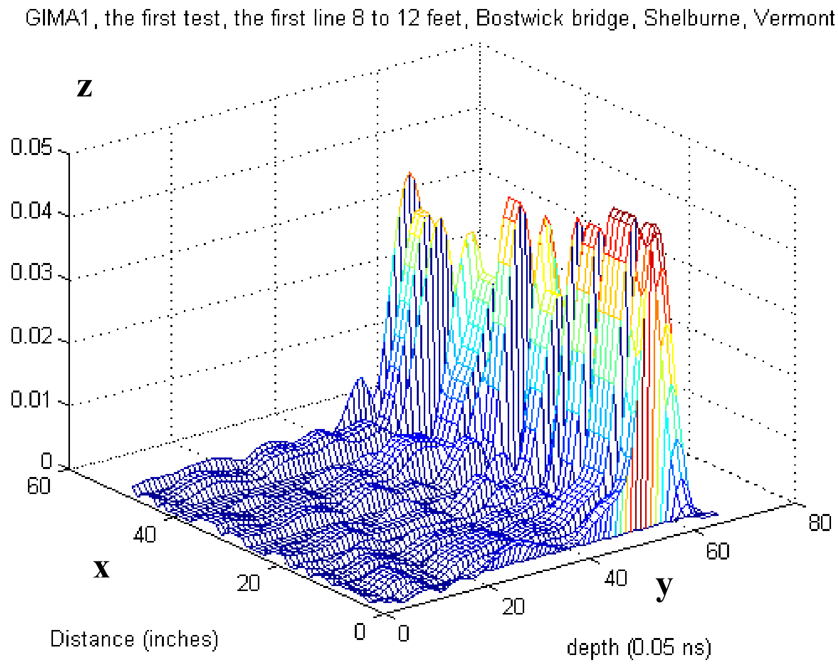

Figure 13.6 GPR *waterfall plot of the results obtained over several small asphalt-filled patches on the deck of Bostwick Bridge, Shelburne, VT.*

13.3 THIRD BOSTWICK BRIDGE FIELD TEST

13.3.1 PROCEDURE

Prior to the next field test, the system was upgraded significantly. This involved using a better antenna, mounting the antenna on a wooden boom, using bigger wheels on the cart, decreasing the horizontal resolution to 13 mm and modifying the software. The software was upgraded to allow the operator to view the data in real time in a B-scan format.

The third test of the Bostwick Bridge, Shelburne, VT occurred on August 12, 1999. There were no major repairs or changes in the condition of the bridge from the previous tests. A chalk line was drawn along the bridge that covered several surface features. Some deck areas were in good condition, such as repaired patches and spalls, as shown in figure 13.7. From A to B was an asphalt filled area. From B to C was an area with a good surface condition. From C to D was a quickrete filled patch. From D to E was another area with good surface condition. From E to F was a quickrete filled area.

For a more detailed examination, a measured grid was drawn on a small area that had several surface spalls and large repaired asphalt patches, figure 13.8. Scan No.1 crossed one perpendicular spalling and covered a large area of asphalt filled patch. Scan 2 covered two severe spalls at a close distance and a smaller portion of the asphalt patch. Scan 3 covered two spalls, at about 300 mm apart, and 100 mm of patched area.

13.3.2 FIELD TEST RESULTS AND DISCUSSIONS

Figure 13.9 shows the result of the long scan along the Bostwick bridge. Section AB, as circled, corresponds to the asphalt filled area, starting from an asphalt-filled patch across some area having a good surface condition at B. There is a delamination or spalling show between B and C. The rest of the area within section BC, as circled, is identified as being in good condition. CD as circled has a subsurface delamination.

Figure 13.7 Direction *and path of the long scan on the Bostwick Bridge, Shelburne, VT.*

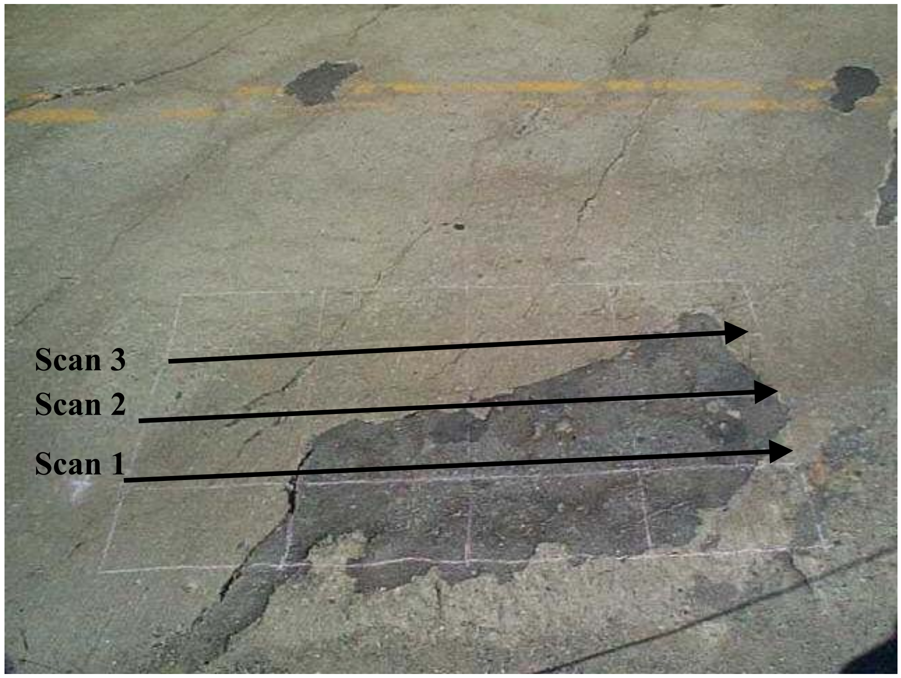

Figure 13.8 *Measured grid over a small deck area with spalling and repaired patches on Bostwick Bridge, Shelburne, VT.*

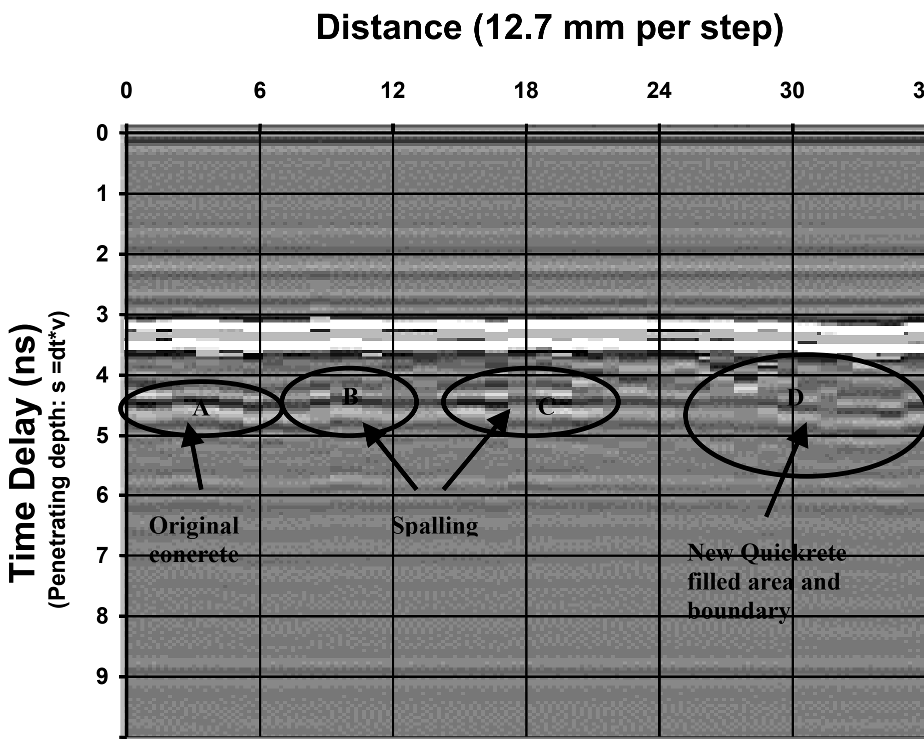

Figure 13.9 Results *of Scan 2 over the measured grid on Bostwick Bridge, Shelburne, VT. Correlations with subsurface structures are noted.*

13.4 TURKEY LANE BRIDGE TEST

The Turkey Lane bridge over Lewis Creek in Hinesburg, VT was chosen on the basis of the age of the bridge, low traffic and high rated condition. The bridge was built in 1995. It has a concrete surface that carries an estimated 50 motor vehicles per day. The current bridge deck condition rating is eight out of ten. The purpose behind choosing a high rated bridge was the assumption that the bridge suffered minimal damage due to standard environmental aging effects. The expectations were that the data would show that the concrete surface and the rebar layers were largely undamaged.

For these tests, the GPR cart was fitted with a new antenna. This antenna appears in figures 11.2 and 11.3. This antenna design significantly improved the performance of the system. Figures 13.10 through 13.13 show the Turkey Lane bridge and the scan locations. Figures 13.14 through 13.17 show the B-scan plots of the data that were collected on scans A, B, C, and D. The surface layer and the rebar layer, represented by the hyperbolic features, can clearly be seen, in the B-scan images. The change in the depth of the rebars near the end of the bridge surface is apparent in figures 13.14 and 13.15. No defects were visible on the bridge deck. This corresponds to no GPR features being apparent that may be correlated with defects.

Figure 13.10. Photo of Turkey Lane bridge with GPR cart in the background.

Figure 13.11 Side *shot of the Turkey Lane bridge.*

Figure 13.12 Scanning *the Turkey Lane bridge deck.*

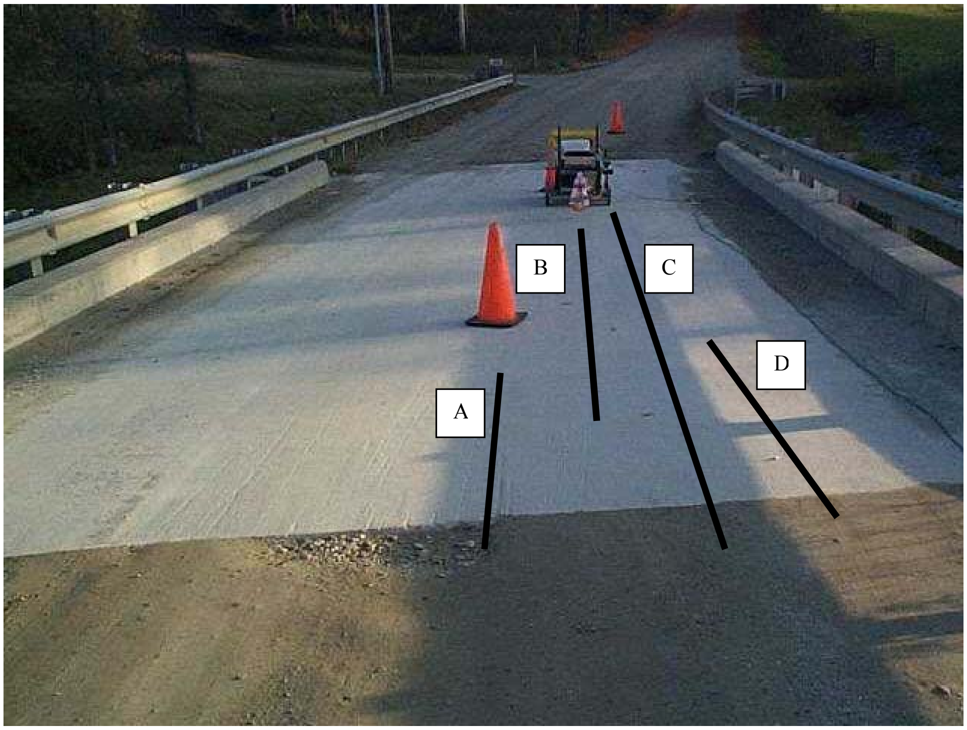

Figure 13.13 *Scan lines shown on the Turkey Lane bridge that correspond to the following B-scan images.*

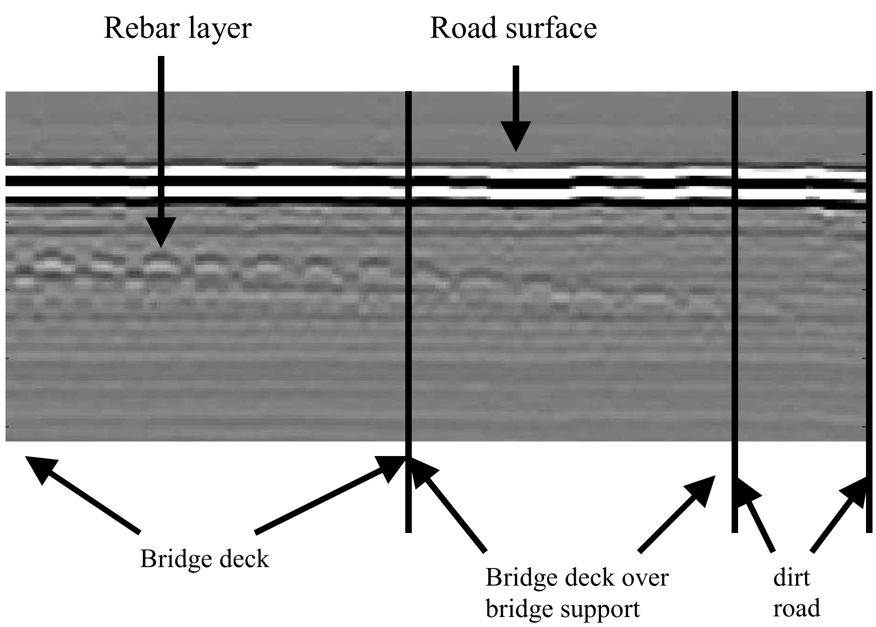

Figure 13.14 *Turkey Lane Bridge scan line A.*

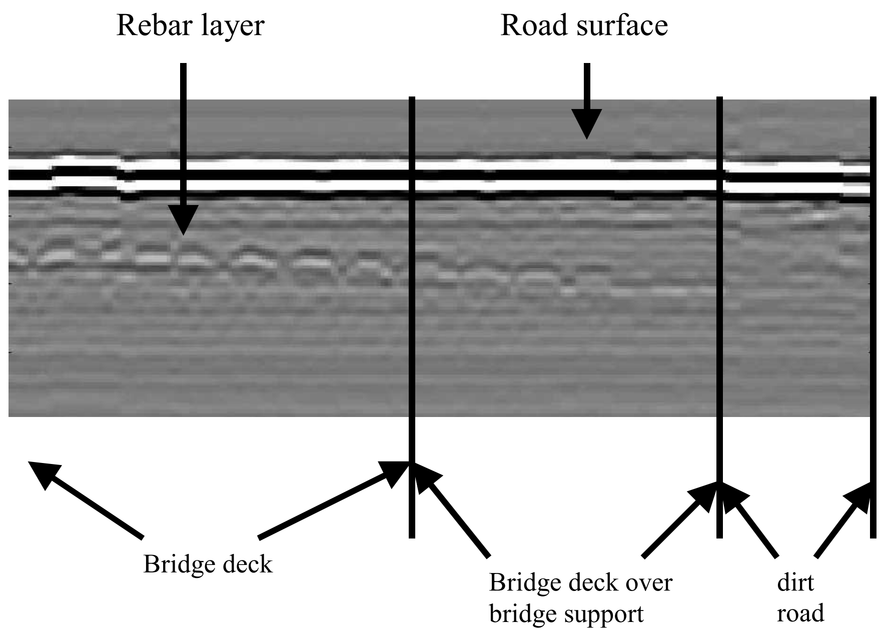

Figure 13.15 *Turkey Lane Bridge scan line D.*

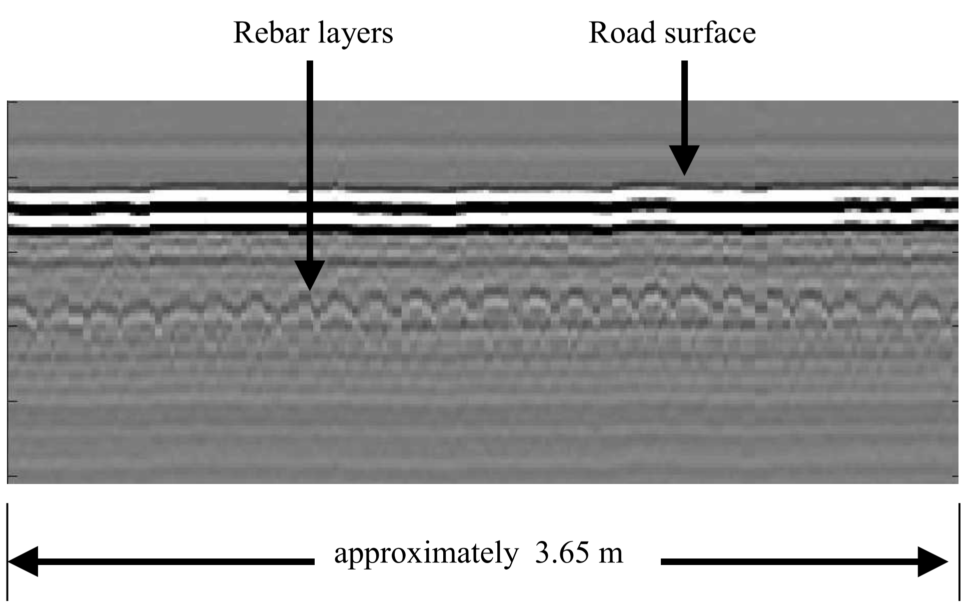

Figure 13.16 *Turkey Lane bridge scan line B.*

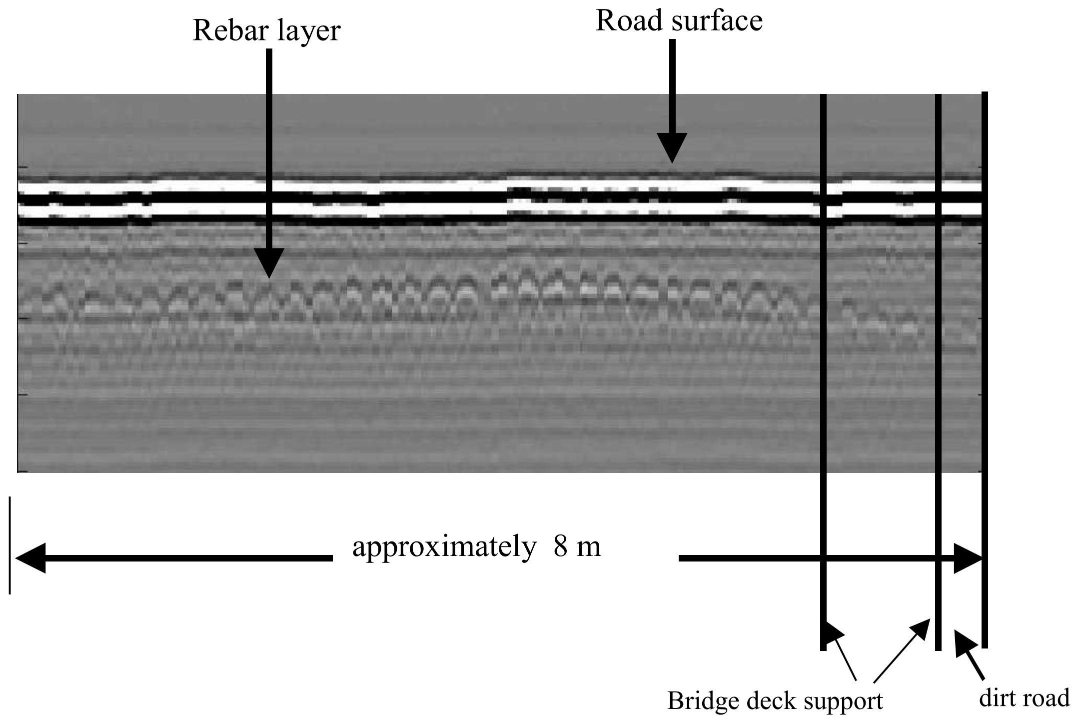

Figure 13.17 *Turkey Lane bridge scan line C.*

13.5 FOURTH BOSTWICK BRIDGE TEST

Following the successful modifications that resulted in improvements to the system, and the successful testing on the Turkey Lane bridge, the Bostwick bridge was retested. Figures 13.18-13.22 show B-scans of data taken from the Bostwick bridge. The asphalt patches, rebars and end of the roadway can be located on the following B-scan images of scans across the bridge.

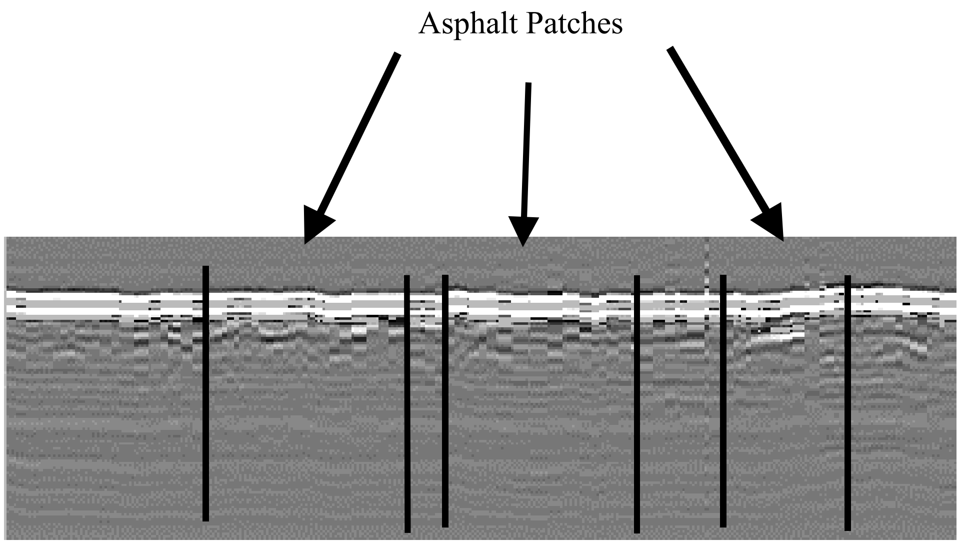

Figure 13.18 *Scan line 1 of Bostwick bridge deck with asphalt patches. Approximately 5 meters in length.*

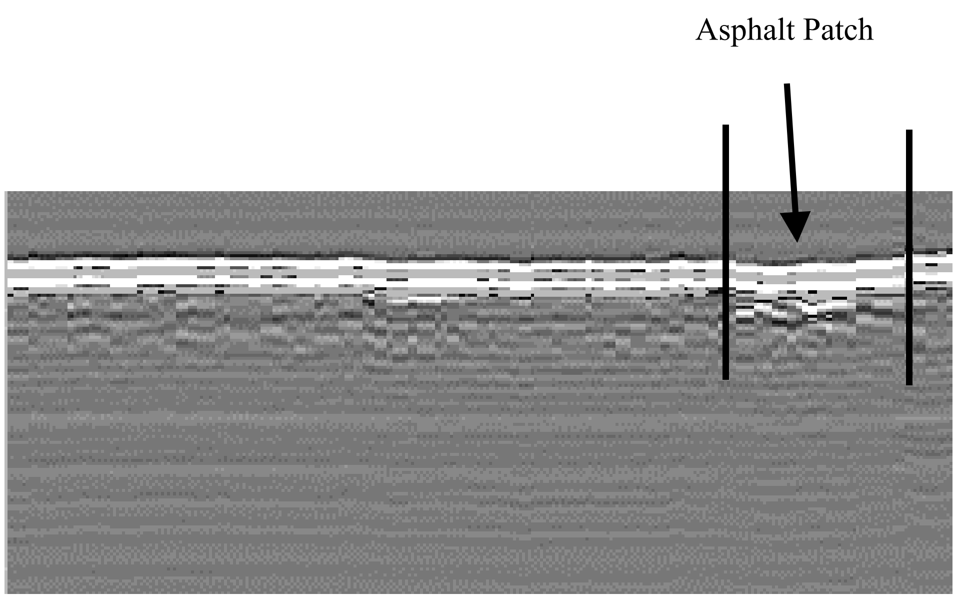

Figure 13.19 *Scan line 2 of Bostwick Bridge that was parallel to scan line 1. The same asphalt patch was present in both scan lines. (5 m)*

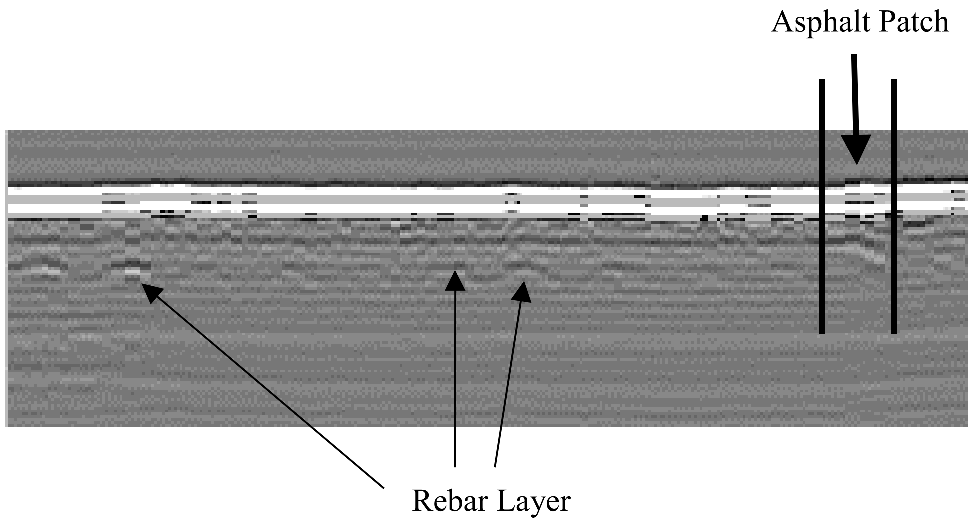

Figure 13.20 *Scan line 3 of Bostwick bridge, approximately 5 meters in length.*

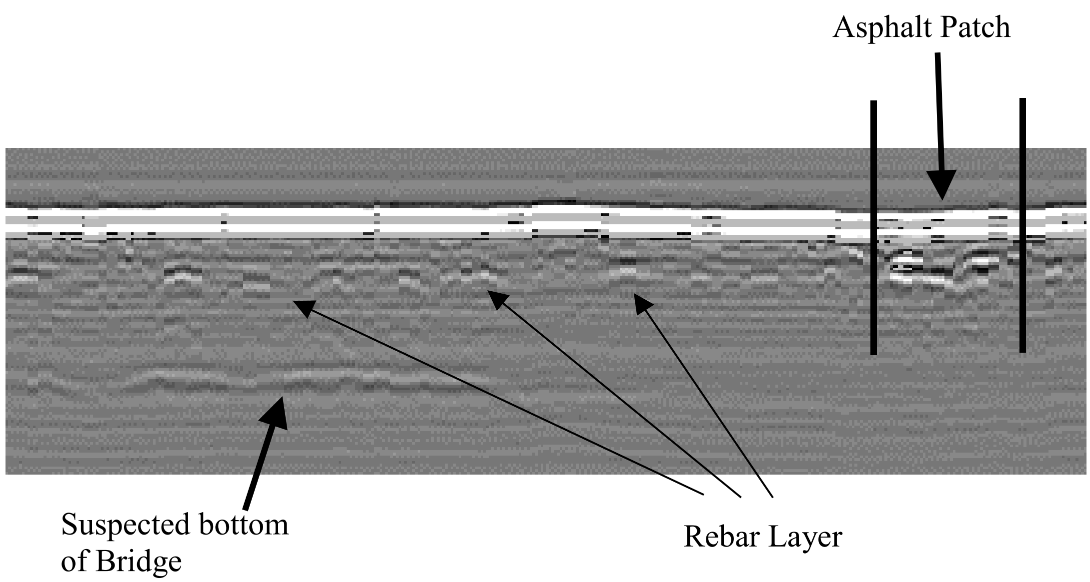

Figure 13.21 *Scan line 4 of Bostwick bridge, approximately 7.5 meters in length.*

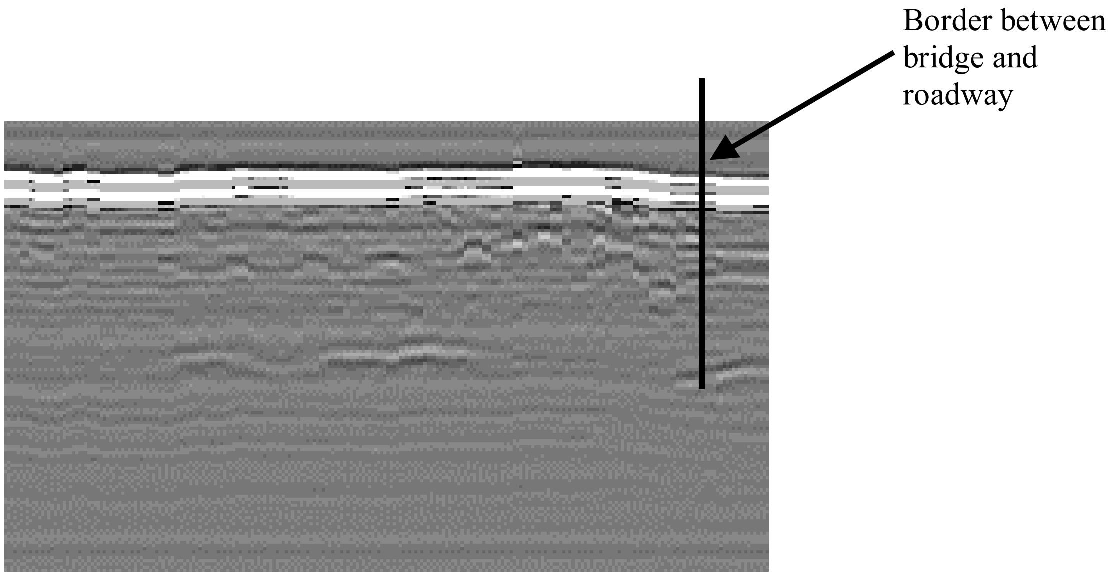

Figure 13.22 Scan line 5 of Bostwick bridge (approx. 3m). This scan line shows the meeting of the bridge and the roadway.

13.6 I-89N EXIT 12A BRIDGE NEAR SUNAPEE, NH

The following are results from a dielectric analysis and grayscale image evaluation for GPR scans taken on the I-89 Northbound Exit 12A bridge in New Hampshire, Figure 13.23. Scans were taken with the asphalt overlay in place and after the asphalt was removed one week later.

Figure 13.23 *Exit 12A Bridge undergoing GPR test.*

Figure 13.24 shows the layout of the bridge scanning grid. Three scan lines were drawn on the surface of the bridge at the spacing described. The bridge was scanned in a northbound direction parallel to the direction of traffic. The horizontal grid indicate the intervals for which the scan was stopped and the data were saved to disk on the PC. This process speeds the data acquisition process and keeps the file size small. Data points were taken every ½ inch along the scan line.

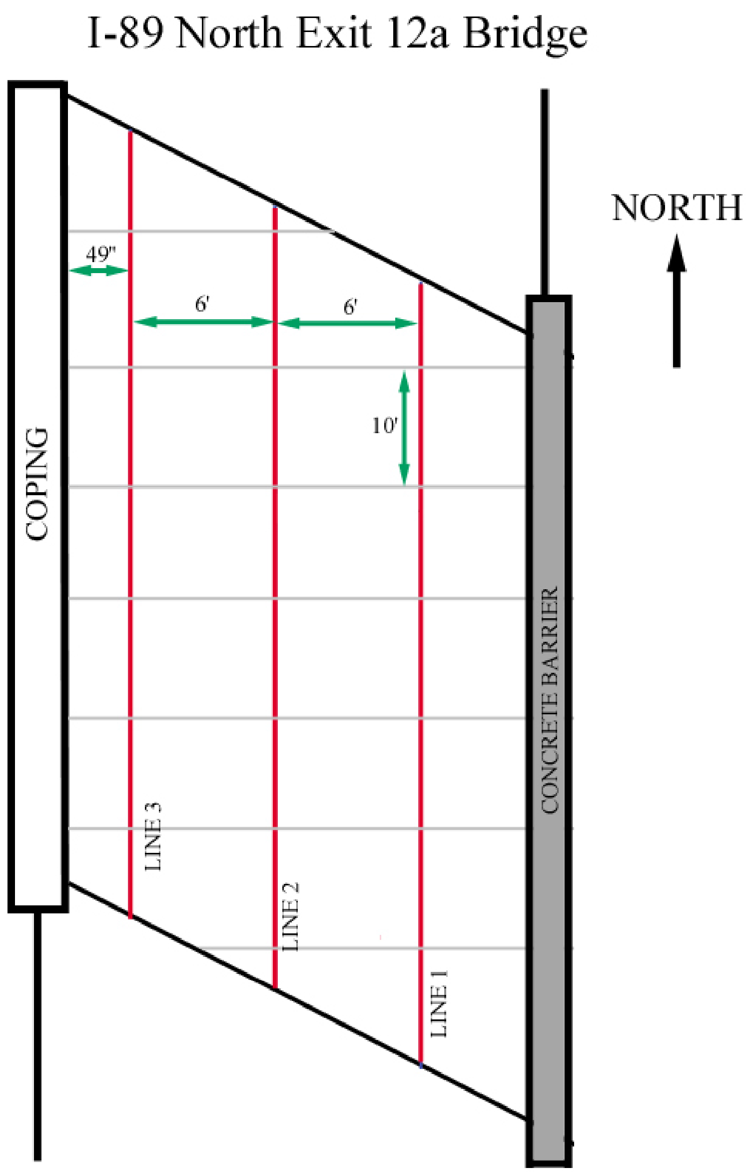

Figure 13.24 *Schematic of the bridge surface showing the main scan lines that accompany the data.*

Figure 13.25 shows the areas of delamination that were determined by the hammer tap method after the asphalt was removed. The hammer tap technique was conducted by experienced personnel from the construction crew (Hydro Demolition). Additional scan lines were added to focus on the suspected delamination areas.

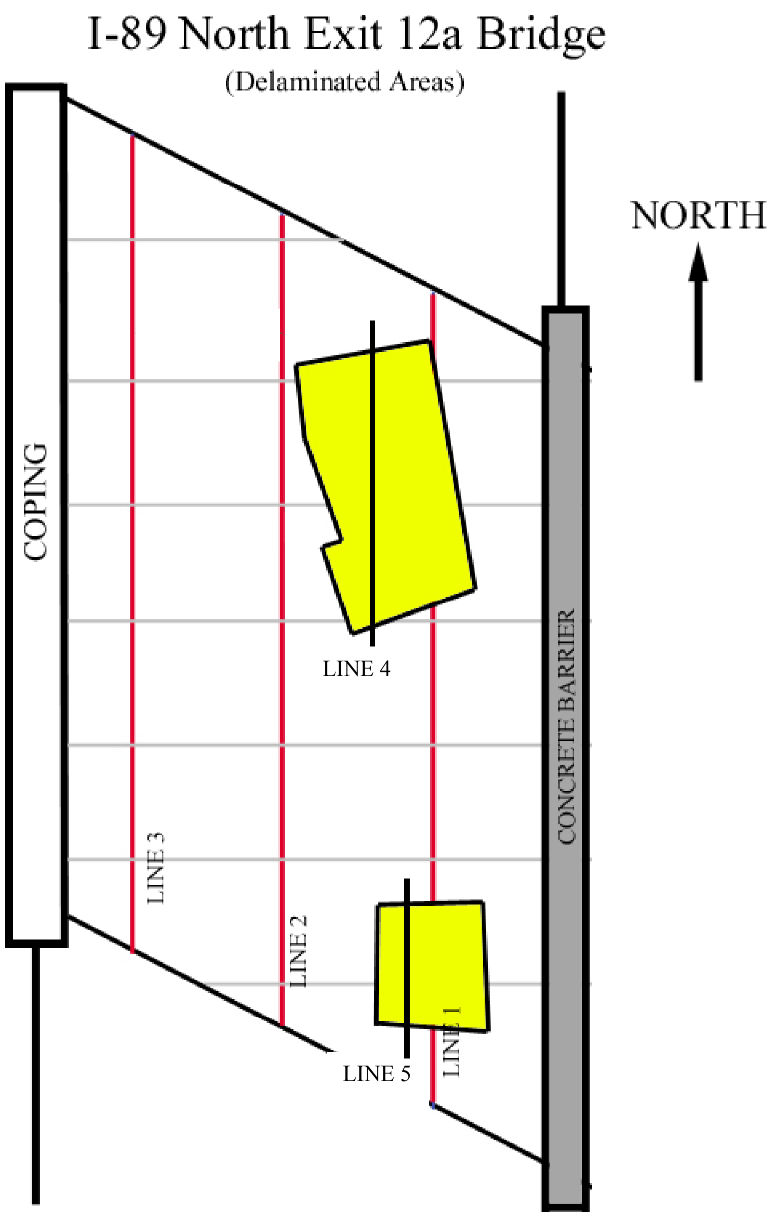

Figure 13.25 *Schematic of Bridge with shaded areas indicating delaminations determined by a hammer tap test.*

The data were processed to extract the dielectric constant of the deck surface and presented in a B-scan format, as described in Chapter 10. The corresponding files were pieced together to yield a full section of the bridge, which is approximately 90 feet in length. Figures 13.26 through 13.29 show the dielectric properties of the surface of the pavement along scan lines 1 through 5.

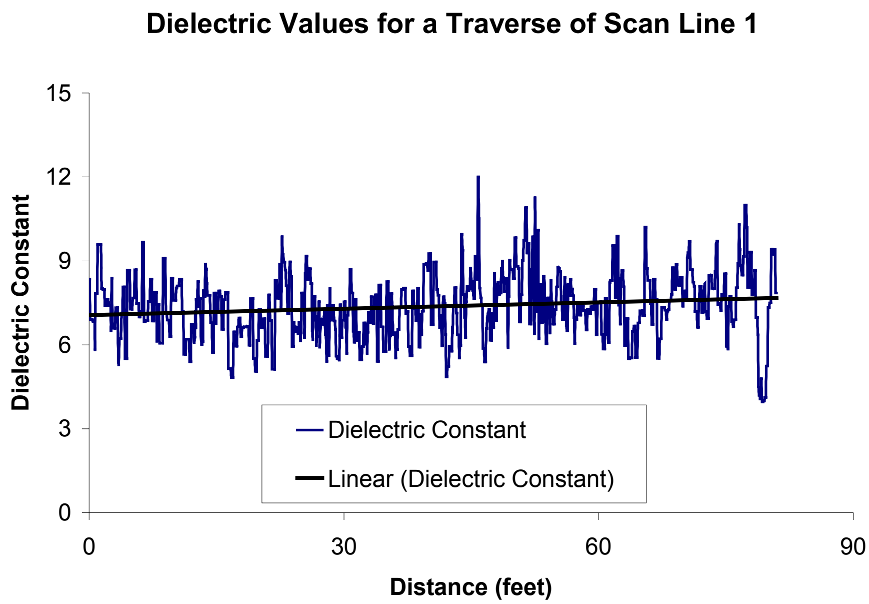

Figure 13.26 *Plot of Dielectric Values along Scan Line 1.*

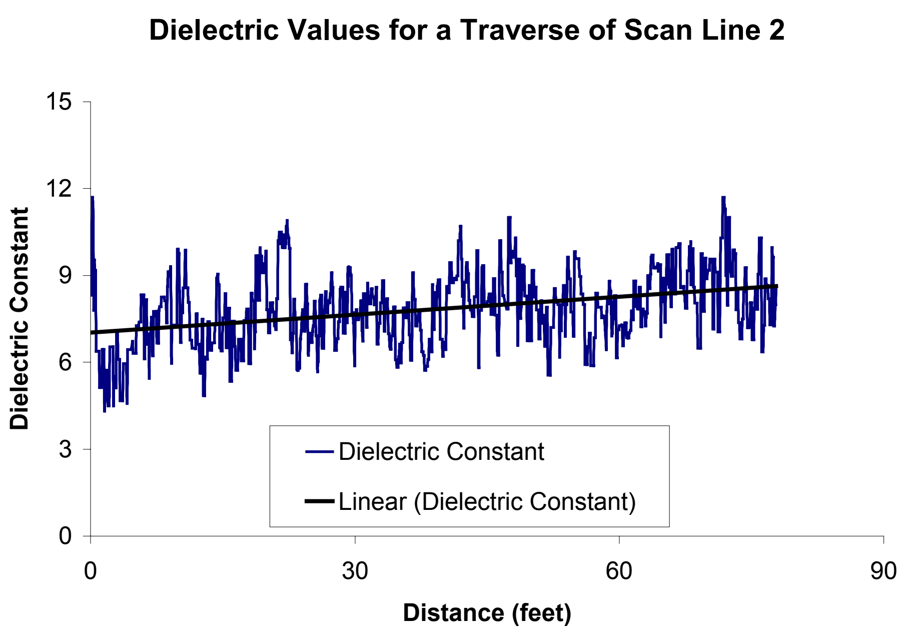

Figure 13.27 *Plot of Dielectric Values along Scan Line 2.*

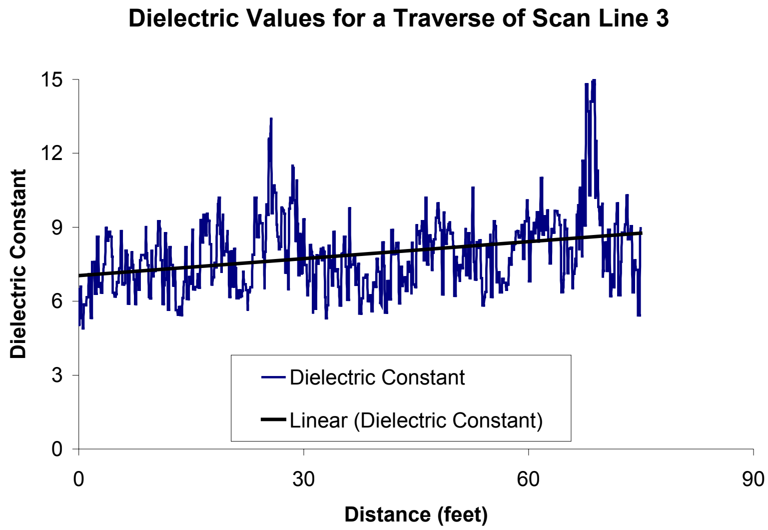

Figure 13.28 *Plot of Dielectric Values along Scan Line 3.*

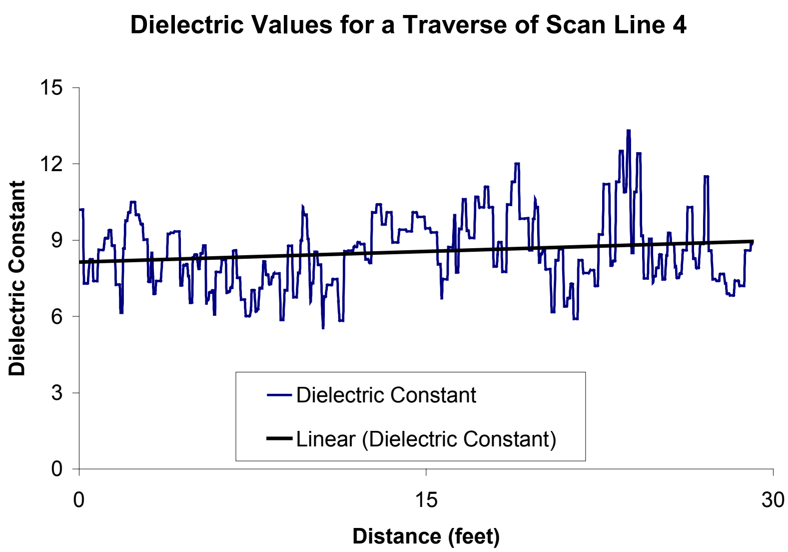

Figure 13.29 *Plot of Dielectric Values along Scan Line 4.*

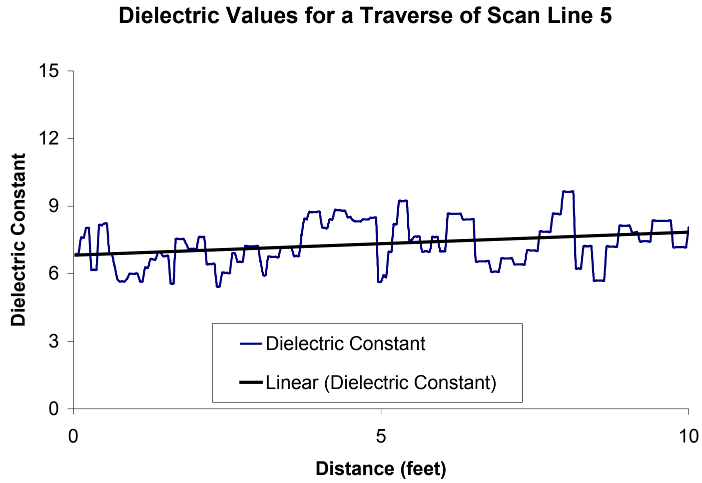

Figure 13.30 *Plot of Dielectric Values along Scan Line 5.*

Dielectric data can be used to determine the condition of the concrete by quantifying the amplitude of the surface reflections, however it does not offer any clues as to the state of the bridge deck beneath the surface. Delaminations are usually the defects of importance when scheduling bridge maintenance. To see delaminations in the concrete several B-scans are taken and printed as grayscale images. The following figures show the grayscales prepared from the exit 12A bridge.

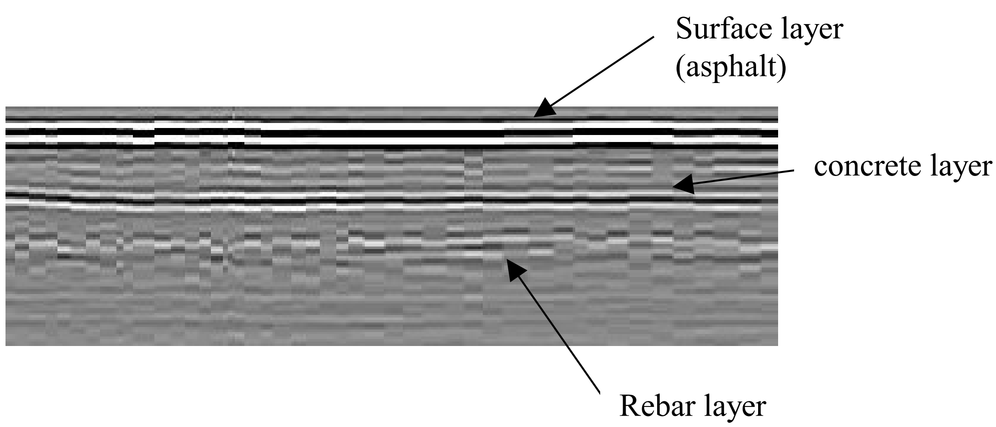

Figure 13.31 *Sample grayscale of a portion of Scan line 2 with asphalt overlay intact.*

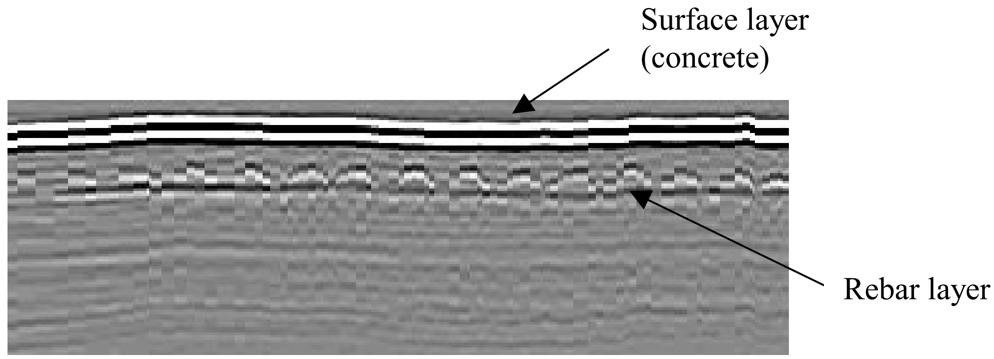

Figure 13.32 *Sample grayscale of a portion of Scan line 2 with asphalt overlay removed.*

The tests conducted on the Interstate 89 Northbound Exit 12A bridge in Sunapee, New Hampshire were the first tests on an interstate highway with the UVM Ground Penetrating Radar Unit. The results were able to be compared with a conventional hammer check for delaminations by a Hydro Demolition worker. Some correlation can be seen in the areas where the delaminations were assumed to be by interrogating the grayscales for the length of the bridge. In scan line 1 a section of poor rebar reflection can be seen in the same area as the delaminations. It should be also noted that in scan line 2 which is outside of the proposed delamination area that the rebar also shows up poorly in the grayscales in the same region. This could suggest that degradation of the rebar similar to the delaminated region is infecting that area. The lower portion of scan 1 also shows a poor rebar reflection which is in the same area as delamination 5 as found by Hydro Demolition via the hammer check. Another item to note is the larger than normal rebar reflection seen in scans 2 and 3. They occur in roughly the same area. An explanation of this phenomenon cannot be given at this stage in the testing.

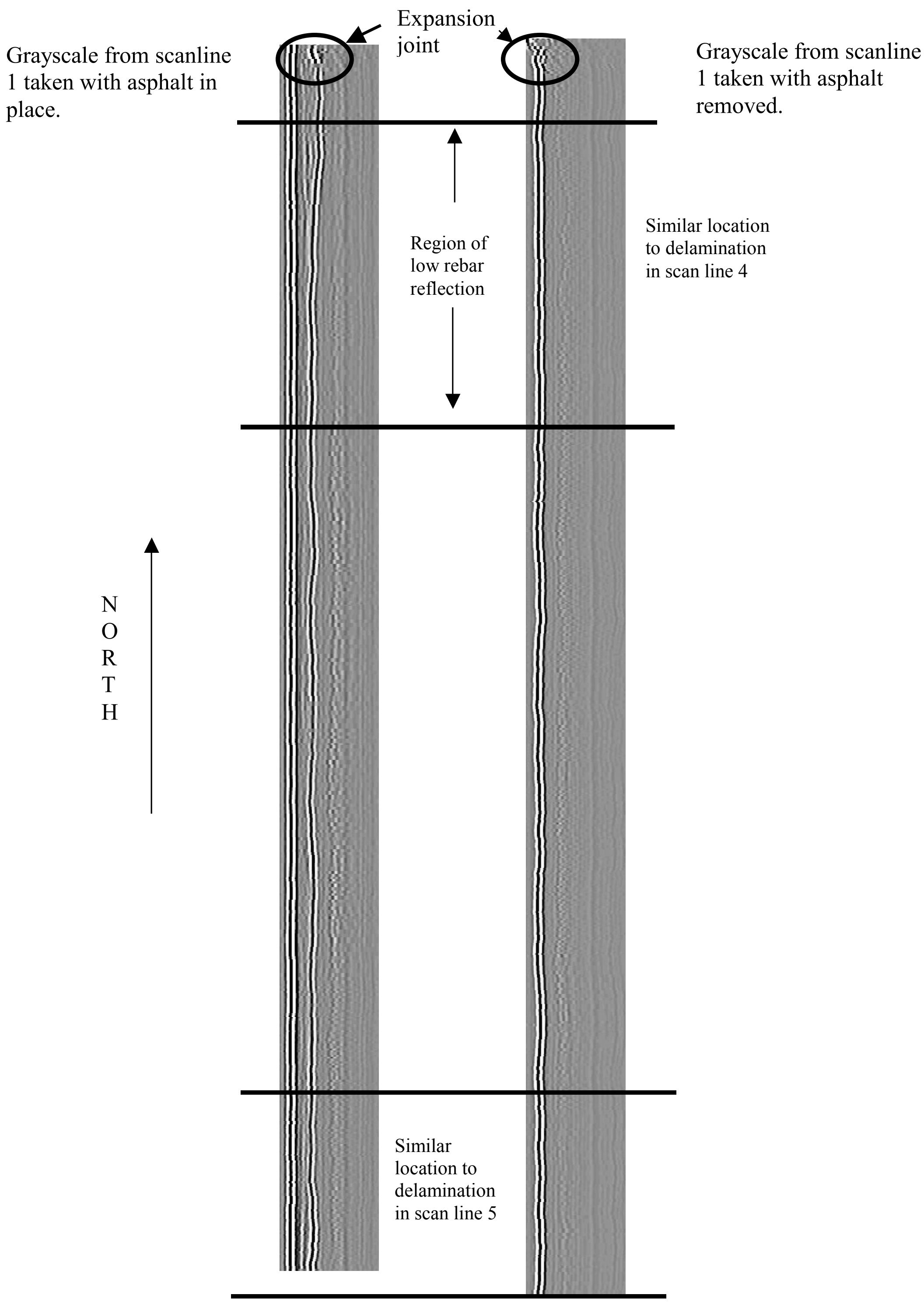

Figure 13.33 *B-scans of scan line 1 with and without asphalt overlay.*

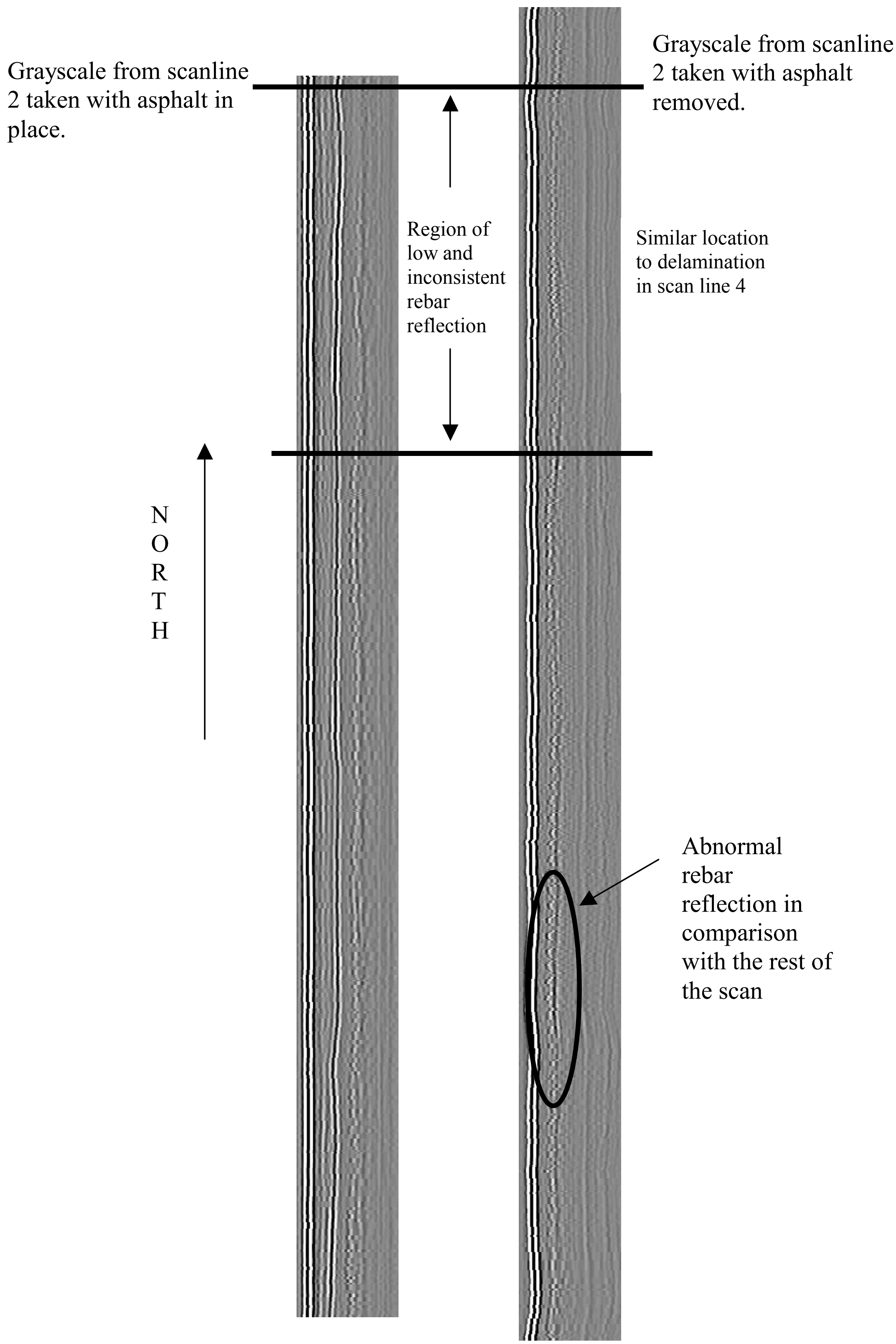

Figure 13.34 *B-scans of scan line 2 with and without asphalt overlay.*

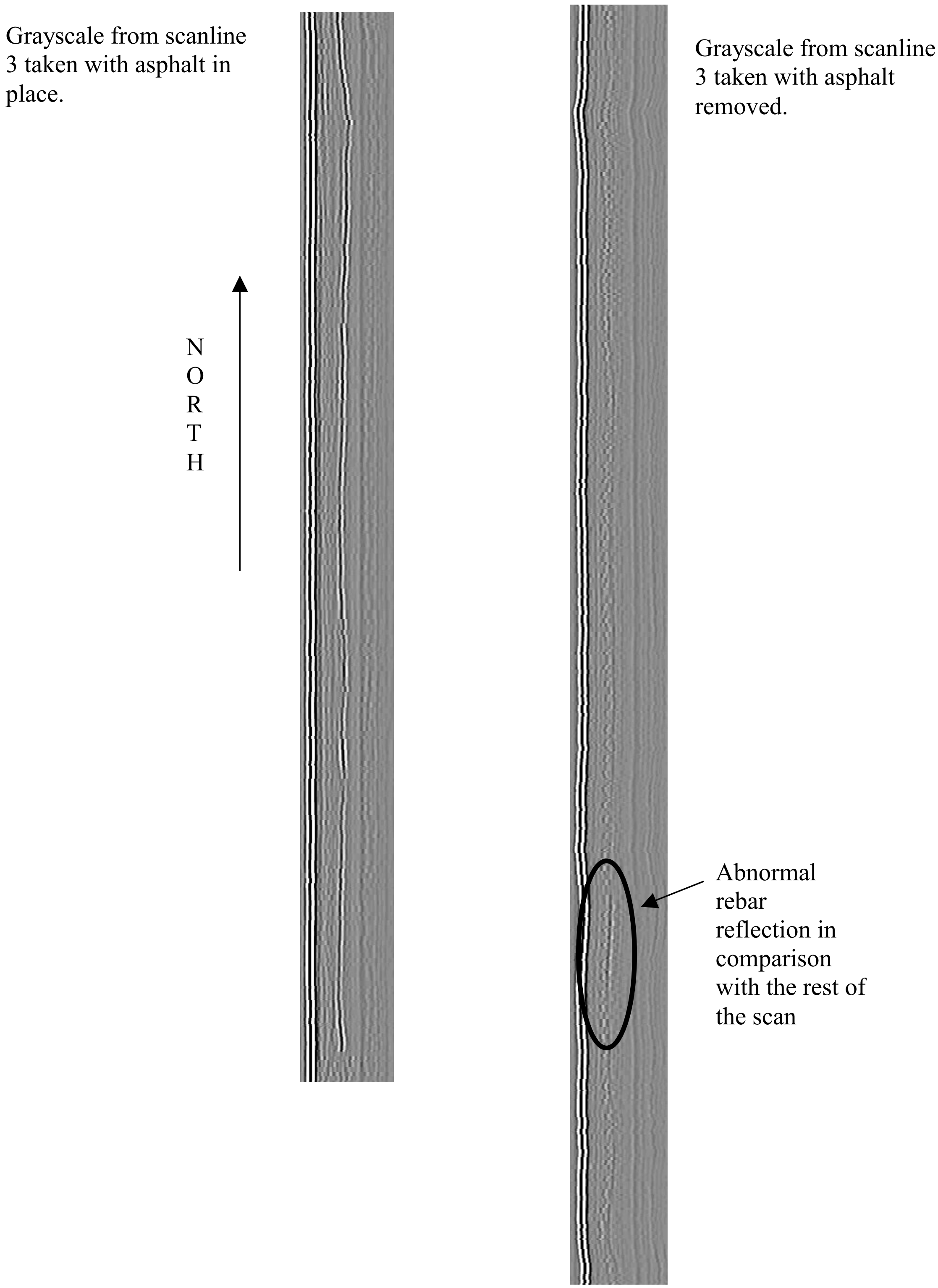

Figure 13.35 *B-scans of scan line 3 with and without asphalt overlay*.

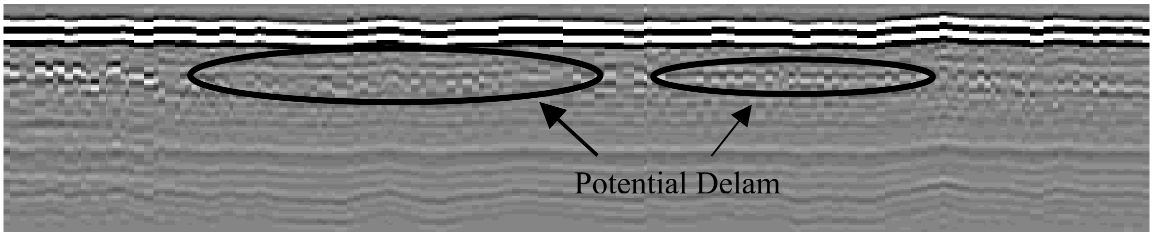

Figure 13.36. *Grayscale of scanline 4. A known delamination exists in this region as verified by a hammer tap test.*

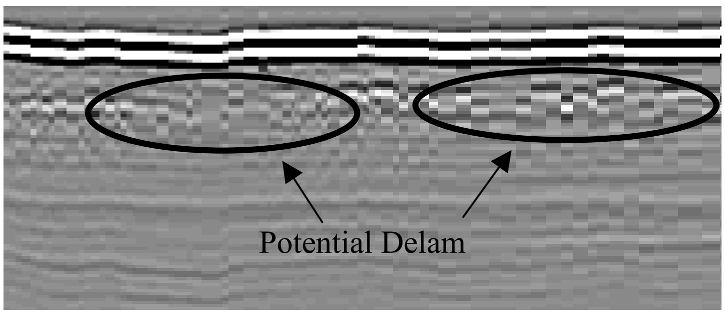

Figure 13.37. *Grayscale of scanline 5. A known delamination exists in this region as verified by a hammer tap test.*

These data show that rebars can be imaged through an asphalt overlay. However, once the overlay is removed, the rebars are more readily imaged. The dielectric constant was not strongly correlated the location of delaminations. The reduction in reflection strength from the rebars was consistent with the presence of rebar delaminations.

13.7 I-189 SPEAR ST. OVERPASS COLUMN TEST

In order to assess non-horizontal concrete surfaces, such as columns and retaining walls, a handheld GPR system was developed and tested on columns and retaining walls in the field, as well as in the laboratory. The system uses a measuring wheel to measure the relative position of the antenna and wall, Figure 13.38, and the same GPR system described in the above tests.

Following a series of preliminary tests on concrete walls inside the Votey Building on the UVM campus, a field trial was conducted on the reinforced concrete columns of the I-189 Spear St. overpass bridge in South Burlington, VT. Figure 13.39 shows the columns and the associated scan lines. These columns are interesting because they have recently been retrofitted with a two to three inch layer of concrete cover over older columns that had been distressed due to deicing salts. Figure 13.40 shows a B-scan of the column. Rebars and a possible location of a cover seam are visible. Similar results appear in Figure 13.41.

Figure 13.38. *Test of handheld system on a retaining wall.*

Figure 13.39. *Columns of I-189 Spear St. overpass bridge in South Burlington, VT. Scan lines are indicated.*

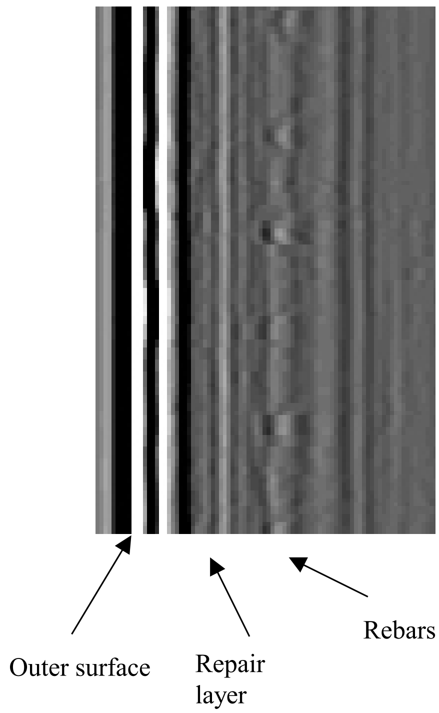

Figure 13.40. *B-scan of column of of I-189 Spear St. overpass bridge in South Burlington, VT along scan line 1. The seam of the new cover repair layer and underlying rebars are visible.*

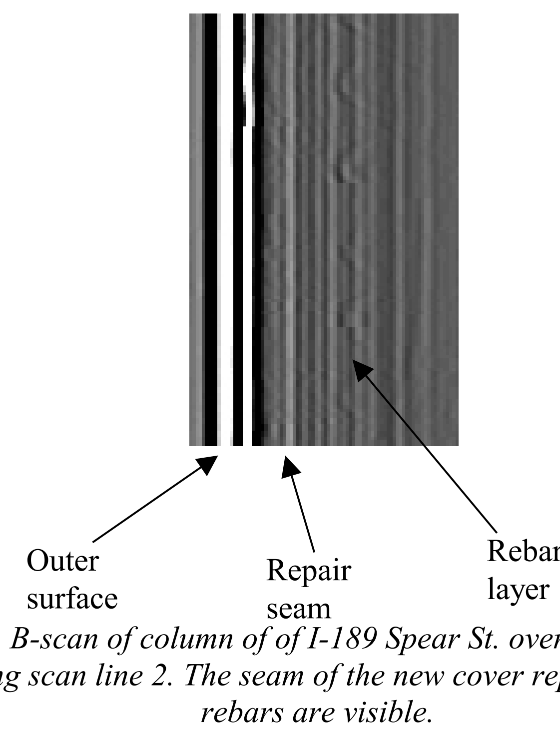

Figure 13.41. *B-scan of column of of I-189 Spear St. overpass bridge in South Burlington, VT along scan line 2. The seam of the new cover repair layer and underlying rebars are visible.*

13.8 I-189 FARELL ST. OVERPASS RETAINING WALL TEST

The second test of the handheld system was conducted on a retaining wall of the I-189 Farrell St. overpass bridge in South Burlington, VT. This retaining wall is fairly old and is showing signs of distress, such as cracking, probably due to rebar corrosion. The retaining wall has a set of three horizontal joint like features. The purpose of these features is probably architectural. A set of vertical scans was conducted on the retaining wall. The location of the vertical scans appears in Figure 13.42. Figures 13.43 – 13.50 show the presence of concrete joints, an underlying rebar layer, and an unexplained feature between the concrete surface and the rebar layer.

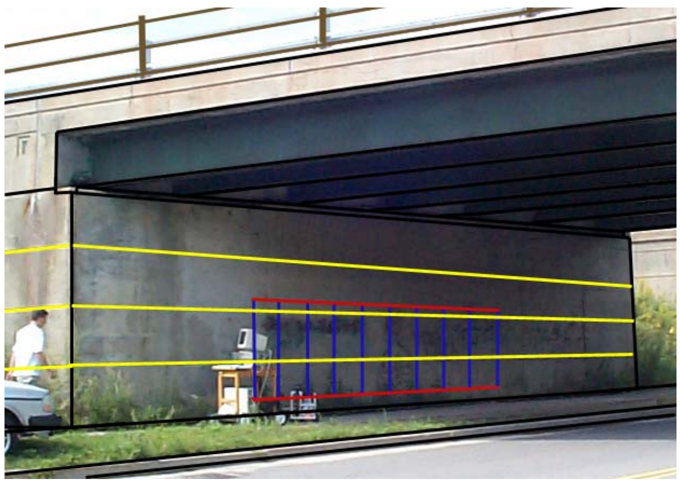

Figure 13.42. *Retaining wall on I-189 Farrell Street Bridge with vertical lines indicating scan locations.*

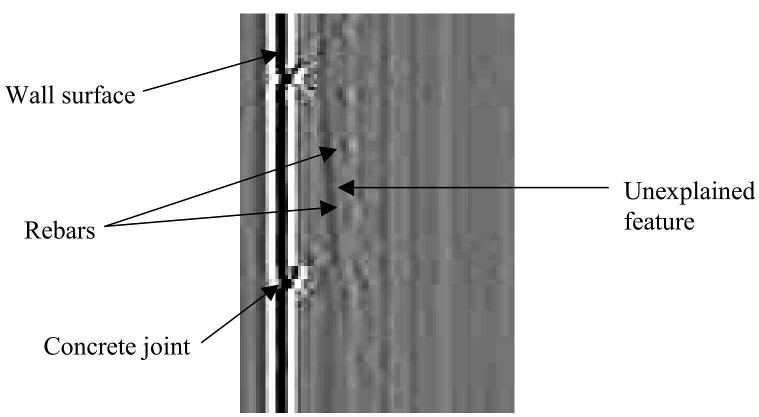

Figure 13.43. *B-scan of retaining wall on I-189 Farrell Street Bridg ealong scan line 1 with rebars, concrete joints and an unexplained feature visible.*

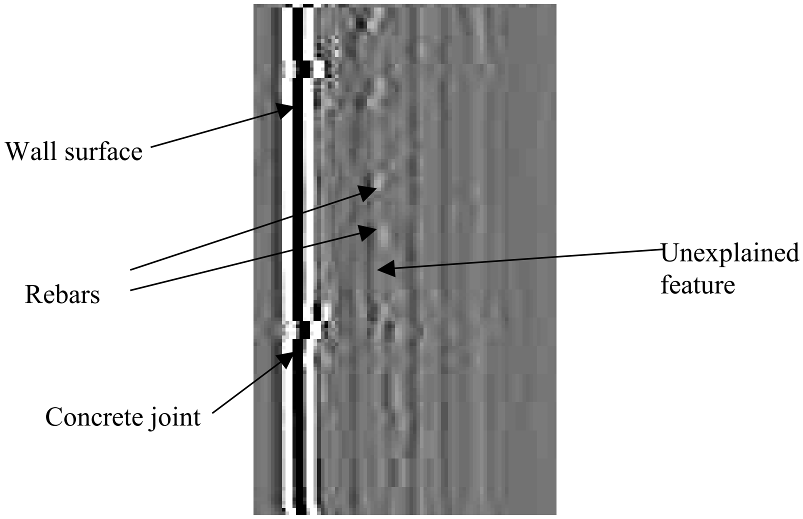

Figure 13.44. *B-scan of retaining wall on I-189 Farrell Street Bridge along scan line 2 with rebars, concrete joints and an unexplained feature visible.*

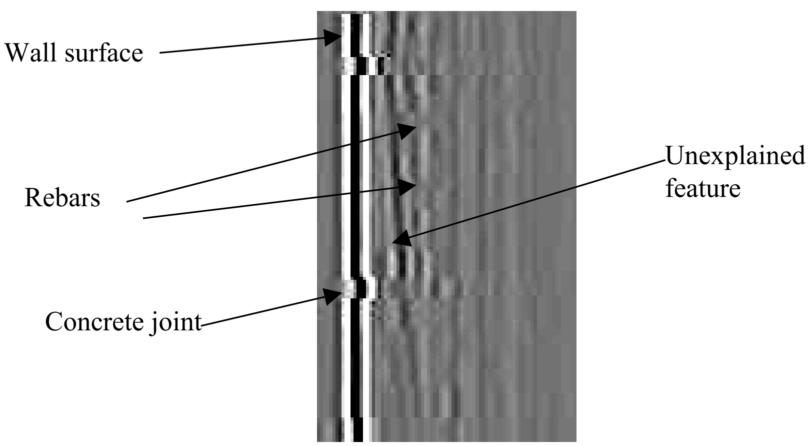

Figure 13.45. *B-scan of retaining wall on I-189 Farrell Street Bridge along scan line 3 with rebars, concrete joints and an unexplained feature visible.*

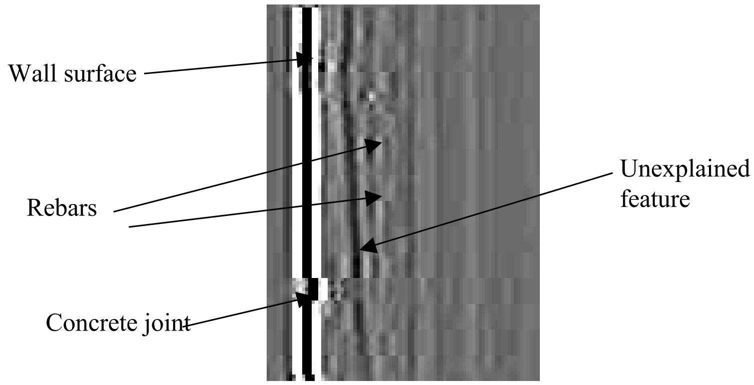

Figure 13.46. *B-scan of retaining wall on I-189 Farrell Street Bridge along scan line 4 with rebars, concrete joints and an unexplained feature visible.*

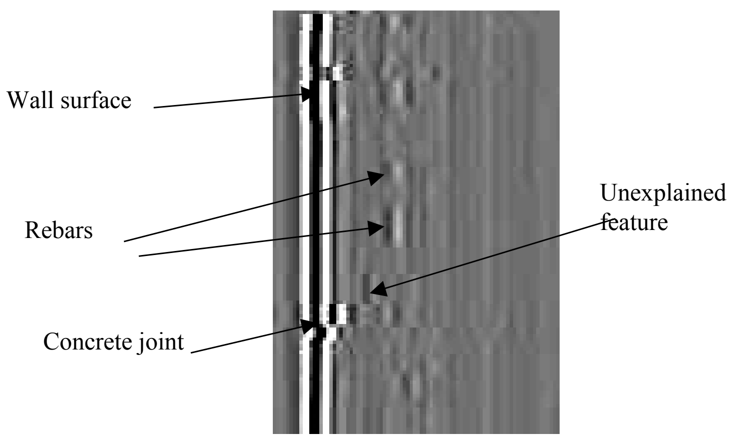

Figure 13.47. *B-scan of retaining wall on I-189 Farrell Street Bridge along scan line 5 with rebars, concrete joints and an unexplained feature visible.*

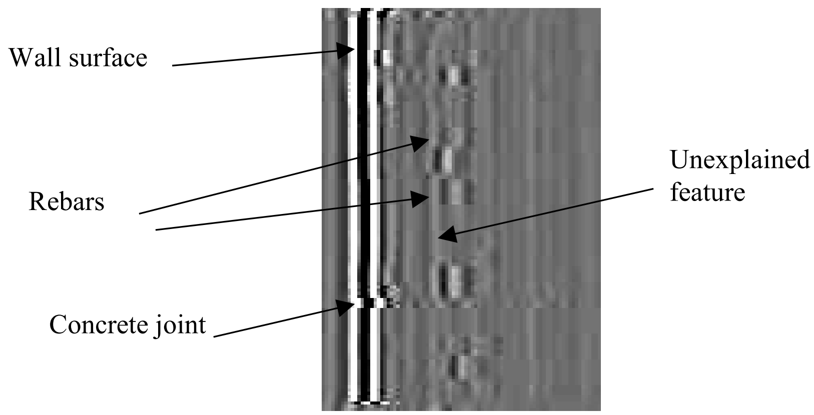

Figure 13.48. *B-scan of retaining wall on I-189 Farrell Street Bridge along scan line 6 with rebars, concrete joints and an unexplained feature visible.*

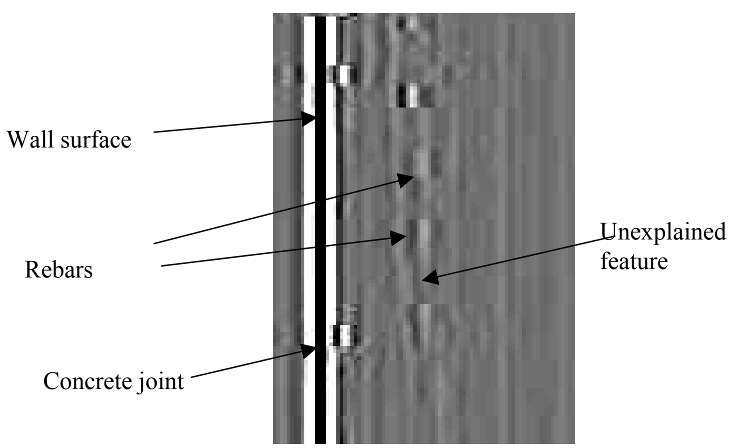

Figure 13.49. *B-scan of retaining wall on I-189 Farrell Street Bridge along scan line 7 with rebars, concrete joints and an unexplained feature visible.*

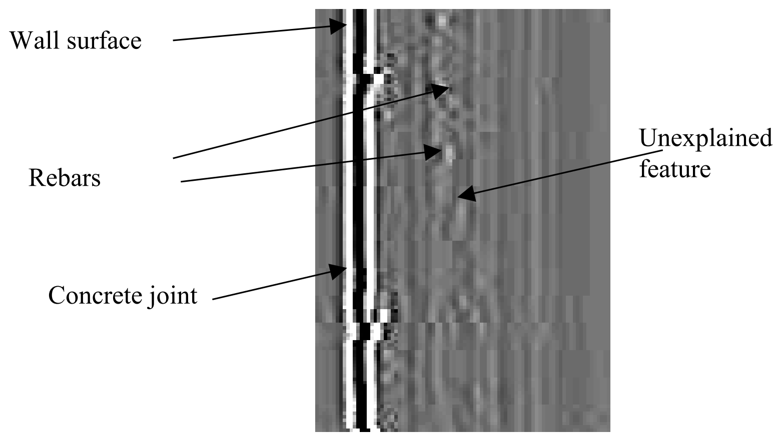

Figure 13.50. *B-scan of retaining wall on I-189 Farrell Street Bridge along scan line 8 with rebars, concrete joints and an unexplained feature visible.*

14. RECOMMENDATIONS FOR FIELD TEST SYSTEM

One purpose of this study was to develop a series of specifications for a reliable bridge deck GPR inspection system. Based on the results of the laboratory and field experiments that are reported in the previous sections of this report, the following specifications have been developed.

14.1 RECOMMENDED SPECIFICATIONS

The field test system must have the following capabilities:

1. Able to scan an entire lane at a speed of at least 32 km/h (20 mph). Highway speeds would be preferable.
2. Horizontal cross-range position resolution of 13 mm (1/2 in) or better.
3. Absolute position resolution relative to the bridge deck of 25 mm (1 in) or better.
4. Ability to correlate with visual condition of the bridge deck, such as through a synchronized video recording of the deck.
5. Data analysis software with the following capabilities.
    a. Logging of the raw GPR scan data.
    b. Real-time plotting of B-scan images.
    c. Damage indication by comparing the amplitudes of the surface reflections and of the lower layer reflections.
    d. Depth of layer calculations.
    e. Synthetic aperture imaging of underlying features (desirable).

6. The system must be compliant with the new FCC regulations governing ultrawideband systems. (FCC, 2002; see Section 14.3)

It should be noted that the state of the art for ground penetrating radar systems is in many respects fairly immature. At the moment there exists no set of standard specimens or statistical-based thresholding of conditions, known as discriminant analysis. Such procedures are now routinely used in medical radiology (He, 2001; He et al., 2001; Minitab, 1997)

14.2 GENERIC FIELD TEST SYSTEM

The field test system is a compromise between cost, complexity and ease of use. The data reported in the previous chapters of this report used a single antenna that was operated with a GPR system that worked primarily in the step-frequency mode. Such a system is capable of collecting good GPR data, but is limited in speed and area coverage. The system also required using an expensive network analyzer to perform the step-frequency scans and the Fourier transforms that were necessary to transform the data to equivalent time domain pulses. A more cost-effective approach is to use multiple antennas that operate in a time domain mode without using a network analyzer. The number of antennas is a compromise between resolution, cost, complexity and ease of use. The effectiveness of multichannel systems was demonstrated with the Concorr system (Payne, 1999) and with the FHWA PERES and HERMES systems (Chase, 1999). A viable system that can measure over a full width of a deck is one that uses a single-line array of antennas. If the high-frequency (0.5 – 6 GHz) horn antennas are used, then the small footprint (and associated higher resolution) requires an antenna every foot of horizontal span. Covering a 12 foot lane, requires 12 antennas. The following is a possible configuration.

Figure 14.1 shows a block-diagram of a time-domain multi-monostatic radar system that may be used for bridge-deck nondestructive evaluation. An antenna array to be attached in front of or behind the GPR vehicle contains several antenna elements spanning a 12 foot traffic lane. Although only six antenna elements are shown in the diagram, between six and twelve elements would be used in the actual system.

The system shown here is multi-monostatic (as opposed to multi-bistatic) because the same antenna elements are used for transmit and receive. In a multi-bistatic system, separate transmit and receive antenna elements would be used in pairs. A multi-bistatic system could be used instead, but would require more antenna elements.

The radar system is controlled by a radar control unit (RCU). Data is collected from the RCU and stored in a personal computer (PC). The PC also “talks” to the RCU providing configuration settings (RF ON/OFF command, averaging factor, etc). A distance measuring instrument (DMI), such as one connected to the odometer of the GPR vehicle, provides distance marks to the PC, which are stored with the data scans collected from the RCU.

The radio frequency (RF) transmit signal is gererated by a pulse generator. The pulse gererator generates an RF pulse with a very fast rise time on the order of 50 picoseconds (ps) and an amplitude of approximately 10 Volts. The transmit waveform should be either a step or an impulse. The TEM horn antennas that we use will actually convert a step function to an impulse function, since the antennas have the effect of taking the time derivative of the transmit waveform.

The pulse generator is controlled by a trigger, which produces a rectangular waveform with a repetition rate selectable between 1 KHz and 1000 KHz. The trigger signal has a slow risetime compared to the pulse generator (10 - 100 ns). Hence, the pulse generator has the effect of “sharpening” the trigger signal rising (or falling) edge. The trigger signal repetition rate is controlled by the RCU.

The signal from the pulse generator passes through a broadband directional coupler, and to a coaxial RF switch. The directional coupler passes the transmitted signal from the pulse generator directly to the coaxial switch, and has minimal effect on the transmit signal. The coaxial RF switch sequentially selects the various antenna elements in the antenna array and is controlled by the RCU.

The reflected signal from the selected antenna element passes again through the coaxial RF switch onto the directional coupler. The directional coupler "couples off" or separates the reflected signal from the transmit signal. The reflected signal is passed to a sampler, which can be thought of as a very high-speed analog-to-digital (A/D) converter. The hardware implementation of the sampler is quite different than an A/D converter, however, and allows the "sampling" of time-domain signals as high as 12 GHz! Our sampler would, of course, only need to sample signals up to 6 GHz, since signals above that frequency would effectively be attenuated by the asphalt or concrete in the bridge deck. The "sampled" signals are then passed to the radar control unit. The RCU stores the sampled pulses in a first-in-first-out (FIFO) memory, averages sequencial scans, and transmits them to the PC.

The various components needed for the time-domain system are listed below, with suggested part numbers and a price estimate.

Component	**Vendor**	**Price Estimate**
Personal Computer	Various	\$2000.
Radar Control Unit	Custom	\$5000.
Trigger	Hewlett-Packard	\$500.
Pulse Generator	Picosecond Pulse Labs	\$8000.
Directional Coupler	Hewlett-Packard	\$500.
Coaxial RF Switch	Loral	\$800.
Antenna Array	Custom	\$2000.
Sampler	Tektronics	\$6000.
Power Supply	Various	\$700.
	Total	**\$18,300**

Table 14.1 Parts list for generic GPR system.

14.3 NEW FCC REGULATIONS

The GPR system must be compliant with new FCC regulations (FCC, 2002). These regulations affect a wide variety of systems that use ultrawideband electromagnetic radiation. GPR is one such system. The regulations govern two applications of GPR to concrete bridge monitoring. One is when the system is pointed downwards and used to examine a bridge deck. The FCC calls this system a 'GPR' system. The other mode of operation is when the system is pointed horizontally and used to image a wall or column. The FCC calls this a 'Wall Imaging System.' For both GPR and Wall Imaging Systems, they must be operated with their –10 dB bandwidth below 960 MHz or in the frequency band 3.1 – 10.6 GHz. In order to comply with these new regulations, the pulse generator listed above would have to be configured to produce regulation compliant pulse shapes.

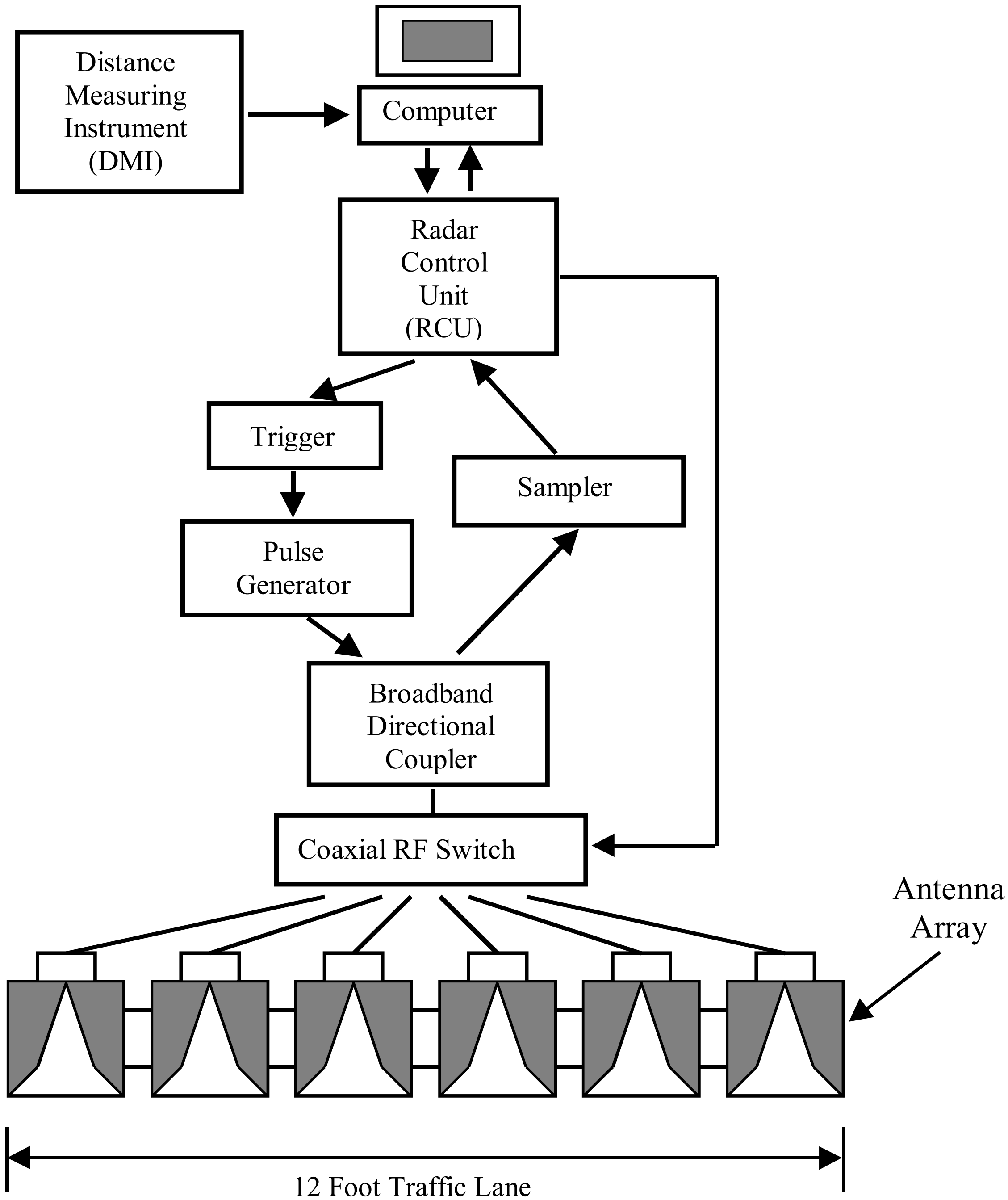

Figure 14.1 *Schematic diagram of generic GPR system.*

15. REFERENCES

AASHTO. (1993) *Standard Test Method for Evaluating Asphalt-Covered Concrete Bridge Decks Using Pulsed Radar*, AASHTO Designation: TP36-93, Edition 1A, September 1993.

Adam C (1997) *Ground Penetrating Radar for Nondestructive Evaluation of Concrete Bridge Decks*, MS Thesis, Department of Mechanical Engineering, University of Vermont. September 1997.

Al-Nuiaimy W, Huang Y, Nakhkash M, Fang M, Nguyen VT, Eriksen A. (1998) "Automatic Detection of Buried Utilities and Solid Objects using Neural Networks and Pattern Recognition" Proc 7th Intl Conf on Ground Penetrating Radar, Lawrence, KS pp. 425-430.

Alongi AV, Cantor TR, Kneeter CP, Alongi, Jr A. (1982) "Concrete Evaluation by Radar Theoretical Analysis," Transportation Research Board Record No. 853.

Alongi AJ, Clemena GG, Cady PD. (1993) "Condition Evaluation of Concrete Bridges Relative to Reinforcement Corrosion. Volume 3: Method for Evaluating the Condition of the Asphalt Decks" Report No. SHRP-S/FR-92-105, Strategic Highway Research Program, National Research Council, Washington DC.

Al-Qadi IL, Hazim OA, Su W, Riad SM. (1995a) "Dielectric Properties of Portland Cement Concrete at Low RF Frequencies," *Journal of Civil Engineering Materials*, ASCE, Vol.7 No.3, pp.192-198, Aug.1995.

Al-Qadi IL, Riad SM, Mostafa R, Su W. (1995b) "Design and Evaluation of a Coaxial Transmission Line Fixture to Characterize Portland Cement Concrete" *Proc. of 6th International Structural Faults and Repair*, Vol. 2, London, UK, pp.337-348, July 1995.

Aurand JF. (1996) "A TEM Horn Antenna With Dielectric Lens for Fast Impulse Response" *Ultra-Wideband, Short-Pulsed Electromagnetics 3*, Proceedings of the 3rd International Conference on Ultra-Wideband, Short-Pulsed Electromagnetics, May 27-31, 1996, Albuquerque, NM.

Aurand JF. (1998) personal communication.

Balanis CA. (1997) *Antenna Theory,* 2nd ed., Wiley, New York.

Barton DK, Cook CE, Hamilton P. eds. (1991) *Radar Evaluation Handbook*, Artech House, Inc., Boston.

Berenger JP. (1994) "A Perfectly Matched Layer for the Absorption of Electromagnetic Waves" *J. Comp. Phys.*, Vol. 114, pp.185-200.

Bhandarkar VA (1993). "Detection of Sub-Surface Anomalies in Concrete Bridge Decks Using Ground Penetrating Radar," Masters Thesis, Dept. of Civil Engineering, West Virginia University.

Cady PD, Weyers RE (1983) "Chloride Penetration and the Deterioration of Concrete Bridge Decks" *Cement, Concrete, and Aggregates*, CCAGDP, Vol. 5 No.2, pp. 81-87.

Cantor TR, Kneeter CP. (1982) "Radar as Applied to the Evaluation of Bridge Decks," Transportation Research Board Record No. 853, January 1982.

Carrier RE, Pu DC, Cady PD. (1975) "Moisture Distribution in Concrete Bridge Decks and Pavements" *Durability of Concrete*, ACI SP 47-8, pp.169-190.

Carter CR, Chung T, Holt FB, Manning DG. (1986), "An Automated Signal Processing System for the Signature Analysis of Radar Waveforms From Bridge Decks," *Canadian Electrical Engineering Journal*, Vol. 11, No. 3, pp. 128-137.

Cartz L (1995), *Nondestructive Testing*, ASM International, Materials Park, OH, 1995, pp.15-16.

Chase S. (1999) "Tomographic Imaging of Bridge Decks Using Radar," *Proc. ASCE Structures Congress*, New Orleans, pp. 280-283.

Cheney M. (1997) "Inverse Boundary-Value Problems" *American Scientist*, Vol. 85, pp. 448-455, Sept.-Oct., 1997.

Chung T, Carter CR, Manning DC, Holt FB (1984) "Signature Analysis of Radar Waveforms Taken on Asphalt Covered Bridge Decks" Canada Ministry of Transportation and Communications, Report ME-84-01.

Clemena GG. (1984) "Non-destructive Inspection of Overlaid Bridge Decks with Ground-Penetrating Radar" Transportation Research Board Record No. 899.

Condon EU, Odishaw H, eds. (1967) *Handbook of Physics*, 2nd Ed., McGraw-Hill, New York.

Davis III CW. (1979) "Computational Model for Subsurface Propagation and Scattering for Antennas in the Presence of a Conducting Half Space," Technical Report 479X-7, Dept. of Electrical Eng., Ohio State University, Columbus Ohio.

Escalante E, Cohen M, Kahn AH. (1984) "Measuring the Corrosion Rate of Reinforcing Steel in Concrete," NBSIR 84-2853, U.S. Dept. of Commerce.

Feng S, Sen PN. (1985) "Geometrical Model of Conductive and Dielectric Properties of Partially Saturated Rocks," *Journal of Applied Physics*, Vol. 58, No. 8, pp.3236-3243.

Feynman RP. (1977) *The Feynman Lectures on Physics*, Addison Wesley Longman, Inc., Reading, MA.

Halabe U, Chen HL, Bhandakar V, Sami Z. (1997) "Detection of Subsurface Anomalies in Concrete Bridge Decks Using Ground Penetrating Radar" *ACI Materials Jnl*. Sept/Oct p 396.

Halabe UB, Maser KM, Kausel E. (1990) "Condition Assessment of Reinforced Concrete Structures Using Electromagnetic Waves," *Technical Report*, Contract No. DAAL 03-87-K005, MIT, Department of Civil Engineering, Cambridge, MA.

Halabe UB, Sotoodehnia A, Maser KR, Kausel EA. (1993) "Modeling the Electromagnetic Properties of Concrete," *ACI Materials Journal*, Vol.90, No.6, Nov./Dec., pp. 552-563.

Halabe UB, Chen HL, Bhandarkar V, Sami Z. (1995a) "Detection of Sub-Surface Anomalies in Concrete Bridge Decks Using Ground Penetrating Radar," accepted by *ACI Materials Journal*, August 1995.

Halabe U, Chen HL, Bhandarkar V, Sami Z. (1997) Detection of Sub-Surface Anomalies in Concrete Bridge Decks Using Ground Penetrating Radar ACI Materials Jnl. Sept./Oct. 1997, pp 396.

Halabe UB, Maser KR, Kausel EA. (1995b) "Condition Assessment of Reinforced Concrete Structures Using Electromagnetic Waves," *ACI Materials Journal*, Vol. 92, No. 5, Sept./Oct., 1995, pp. 511-523.

He R. (2001) *Quantitative Sonographic Prostate Cancer Characterization* MS Thesis, Department of Mechanical Engineering, University of Vermont.

He Z, Skljarevski, G, Trainer T, Tuthill JM, Wear KA, Wagner RF, Huston D, Garra BS. (2001) "Classification Of Benign And Malignant Prostate Tissue Using Radio Frequency Ultrasound Data: Preliminary Results Of In Vitro Studies Of Radical Prostatectomy Specimens" US Tissue Characterization Symposium 2001.

Hu JQ, Huston D, and Fuhr P. (1999) "GIMA Antenna Design for Ground Penetrating Radar in Concrete NDE Application" SPIE paper 3670-63, SPIE Conf. on Sensory Phenomena and Measurement Instrumentation for Smart Structures and Materials, Newport Beach, CA, March 1999.

Hu JQ. (2000), Good Impedance Match Antenna (GIMA) Design And Its Applications For Ground Penetrating Radar In Concrete Structures NDE Applications, MS Thesis, Department of Mechanical Engineering, University of Vermont, March 2000.

Huston D, Maser K, Weedon W, Fuhr Adam C. (1997) "Bridge Deck Evaluation with Ground Penetrating Radar" *Structural Health Monitoring,* F Chang ed., Technomic

Publishing, pp. 91-103 Proc. International Workshop on Structural Health Monitoring, Stanford, CA, Sept. 1997.

Huston D, Maser K, Hu JQ, Weedon W, Adam C. (1998) "Bridge Deck Evaluation with Ground Penetrating Radar" Proc. GPR '98 7th International Conference on Ground-Penetrating Radar, The University of Kansas, Lawrence, KS, May 27-30, 1998.

Huston DR, Hu JQ, Maser K, Weedon W, Adam C. (1999a) "GIMA Ground Penetrating Radar System For Infrastructure Health Monitoring" to appear Jnl. of Applied Geophysics 1220(1999).

Huston D, Hu J, Maser K, Weedon K, Adam C. (1999b) "Ground Penetrating Radar for Concrete Bridge Health Monitoring Applications" SPIE 3587-23 Proc. SPIE NDE Techniques for Aging Infrastructure and Manufacturing, Newport Beach, CA, March 1999.

Isakov V. (1998) *Inverse Problems for Partial Differential Equations* Springer-Verlag Applied Mathematical Science Vol. 127, New York.

Johansson E, Mast JE. (1994) "Three-dimensional ground penetrating radar imaging using synthetic aperture time-domain focusing," SPIE 2275-24 *Adv. Microwave and Millimeter-Wave Detectors.*

Joyce RP (1984) "Rapid Non-Destructive Delamination Detection," Federal Highway Administration FHWA RD-84/076.

Klein LA, Swift CT. (1977) "Improved Model for the Dielectric Constant of Seawater at Microwave Frequencies," *IEEE Transactions on Antennas and Propagation*, Vol. AP-25, No.1, Jan. 1977, pp.104-112.

Kong JA. (1986) *Electromagnetic Wave Theory*, John Wiley & Sons, NY.

Landau LD and Lifshitz EM. (1980) *The Classical Theory of Fields*, Pergamon Press, Oxford.

Lau CL. (1991) *Thickness Estimation of Subsurface Layers in Asphalt Pavement Using Monostatic Ground Penetrating Radar*, Masters Thesis, Department of Electrical Engineering, Texas A&M University, Dec. 1991.

Lazaro-Mancilla O, Gomez-Trevino E. (1998) "One-Dimensional Ground Penetrating Radar Inverse Problem" *Proc. 7th International Conference on Ground Penetrating* Radar, Lawrence, KS, May 1998.

Liu L, Oristaglio M. (1998) “GPR Signal Analysis Instantaneous Parameter Estimation using the Wavelet Transform” *Proc. 7th International Conference on Ground Penetrating Radar*, Lawrence, KS.

Madden TR, Williams E. (1993) “Role of Size Distributions in Physical Properties of Inhomogeneous Materials” *Journal of Geophysical Research*, Vol. 98, No. 9, Sept. 1993, pp.15,951-15,964.

Manning DG, Holt FB. (1980), “Detecting Delamination in Concrete Bridge Decks,” *Concrete International*, pp.34-41, November 1980.

Manning DG, Holt FB. (1984), “Detecting Deterioration in Asphalt-Covered Bridge Decks,” Transportation Research Board Record No. 899.

Maser KR. (1989) “New Technology for Bridge Deck Assessment,” New England Transportation Consortium Phase I Final Report, Center for Transportation Studies, MIT.

Maser KR. (1990) “New Technology for Bridge Deck Assessment,” New England Transportation Consortium Phase II Final Report, Center for Transportation Studies, MIT.

Maser KR and Rawson A. (1992) "Network bridge decks surveys using high speed radar: case studies of 44 decks" *Transportation Research Record No. 1347*. Transportation Research Board. National Research Council. 1992.

Maser KR, and Kim Roddis WM. (1990) “Principles of Thermography and Radar for Bridge Deck Assessment,” *ASCE Journal of Transportation Engineering*, Vol.116 No.5, pp. 583-601, Sept./Oct.

Mast J. (1993) *Microwave Pulse-Echo Radar Imaging for the Nondestructive Evaluation of Civil Structures* Ph.D. Dissertation, Electrical Engineering, University of Illinois at Urbana-Champaign.

Mast J, Johansson EM. (1994b) “Three-dimensional ground penetrating radar imaging using multi-frequency diffraction tomography,” SPIE 2275-23 *Advanced Microwave and Millimeter-Wave Detectors.*

Matthews S, Goodier A, Massey S, Veness K. (1998) “Permittivity Measurements and Analytical Dielectric Modelling of Plain Structural Concretes” *Proc. 7th International Conference on Ground Penetrating Radar*, pp 363-368.

Minitab (1997) *Minitab User’s Guide*, Minitab, Inc.

Moffatt DL, Puskar RJ. (1976) “A Subsurface Electromagnetic Pulse Radar” *Geophysics*, Vol. 41, No. 3, pp. 506-518.

Narayanan RM, Hudson SC, Kumke CJ. (1998) “Detection of Rebar Corrosion in Bridge Decks using Statistical Variance of Radar Reflected Pulses” Proc. GPR '98, Seventh International Conference on Ground Penetrating Radar, Lawrence, KS 1998.

Moon P, and Spencer DE (1960) *Foundations of Electrodynamics*, van Nostrand, Princeton, NJ.

NCHRP (1979) "Durability of Concrete Bridge Decks." *Synthesis 57,* National Cooperative Highway Research Program, Transportation Research Board, National Research Council, Washington, D.C.

Ondrejka AR, Ladbury JM, Medley HW. (1995) *TEM Horn Antenna Design Guide*, NIST Technical Report, Boulder, CO, 1995.

Papoulis A, Systems and Transforms with Applications in Optics, McGraw-Hill 1968, New York.

Payne W. (1999) private communication, Concorr Inc., Ashburn, VA.

Robinson E. (1982) “Spectral Approach to Geophysical Inversion by Lorentz, Fourier and Radon Transforms” *Proc. IEEE*, Vol. 70, No. 9, September 1982, pp. 1039-1054.

Russ J. (1999) *The Image Processing Handbook*, 3rd ed. CRC Press

Sansalone M, Carino NJ. (1988) “Laboratory and Field Studies of the Impact-Echo Method for Flaw Detection in Concrete,” *Nondestructive Testing*, SP-112, American Concrete Institute, Detroit, N.J., pp.1-20.

Sansalone M, Carino NJ. (1989) “Detecting Delaminations in Concrete Slabs with and without Overlays Using the Impact-Echo Method,” *ACI Materials Journal*, Vol.86, No.2, March-April, pp.175-184.

Scannell WT, Sohanghpurwala AA, Islam M. (1996) *FHWA – SHRP Showcase: Assessment of Physical Condition of Concrete Bridge Components*, USDOT, FHWA, July 1996.

Serway RA. (1990) *Physics For Scientists and Engineers: with Modern Physics*, 3rd ed., Saunders College Publishing, Philadelphia, pp. 970-972.

Shaw M, Molyneaux TC, Millard SG, Bungey J, Taylor MJ. (1998) “Automatic Analysis of GPR Scans on Concrete Structures” *Proc. 7th Intl Conference on Ground Penetrating Radar*, Lawrence, KS, pp 449-453.

Shlager KL, Schneider JB. (1995) “A Selective Survey of the Finite-Difference Time Domain Literature,” *IEEE Antennas and Prop. Mag.*, Vol. 37, No. 4, pp.39-45, August 1995.

Skolnik MI. (1988) *Radar Applications*, IEEE Press, New York.

Slater JC, Frank NH. (1969) *Electromagnetism*, Dover, New York.

Smith SS. (1995) "Detecting Pavement Deterioration with Subsurface Interface Radar," *Sensors*, pp.29-40, September 1995.

Sotoodehnia A. (1989) "Experimental Verification of Three Models for the Permittivity of Concrete," B.Sc. Thesis, Dept. of Electrical Engineering and Computer Science, MIT, May 1989.

Soumekh M (1999) *Synthetic Aperture Radar Signal Processing,* Wiley-Interscience.

Steinway WJ, Echard JD, Luke CM. (1981) "Locating Voids Beneath Pavement Using Pulsed Electromagnetic Waves," National Research Council.

Stratton J. (1941) *Electromagnetic Theory*, McGraw-Hill Book Co., New York, pp.1-78.

Stogryn A. (1971) "Equations for calculating the Dielectric Constant of Saline Water" *IEEE Transactions on Microwave Theory and Techniques*, Vol. MMT-19, Aug. pp.733-736.

Stolt R. (1978) "Migration by Fourier Transform" *Geophysics*, Vol. 43, No. 1, Feb. 1978, pp. 23-48.

Taflove A (1988) "Review of the Formulation and Applications of the Finite-Difference Time-Domain Method for Numerical Modeling of Electromagnetic Wave Interactions With Arbitrary Structures," *Wave Motion*, Vol. 10, pp.547-582.

Udd E. (1991) *Fiber Optic Sensors*, Wiley, New York.

Ulaby FT, Moore RK, Fung AK. (1986) *Microwave Remote Sensing*, Vol. 3, Artech House Inc., MA..

Ulricksen, CP. (1982) *Application of Impulse Radar to Civil Engineering*, Doctoral Thesis, Lund University, Dept. of Engineering Geology, Sweden.

Weedon WH. (1994) *Broadband Microwave Inverse Scattering: Theory and Experiment*, Ph.D. Dissertation, University of Illinois at Urbana-Champaign, 1994.

Weedon WH. (1997) "High-Frequency TEM Horn Antenna Design," Technical Report NETC-9701, Applied Radar Analysis, Watertown, MA.

Wiener N (1958) *The Fourier Integral and Certain of Its Applications*, Dover, New York.

Yee KS. (1966) "Numerical Solution of Initial Boundary Value Problems Involving Maxwell's Equations in Isotropic Media," *IEEE Trans. on Antennas and Propagation*, Vol. AP-14, No. 3, pp. 302-307.

Zoughi R, Cone GL, Nowak PS. (1991) "Microwave Non-destructive Detection of Rebars in Concrete Slabs," *Materials Evaluation*, Vol.49 No.11, Nov.1991, pp.1385-1388.

Zoughi R, Gray SD, Nowak PS (1995). "Microwave Nondestructive Estimation of Cement Paste Compressive Strength," *ACI Materials Journal*, Vol. 92 No. 1,

APPENDIX

A.1 OPERATION MANUAL FOR UVM GPR SYSTEM

The following is an operations manual for the ground penetrating radar system developed at the University of Vermont.

A.1.1EQUIPMENT

The following equipment are required for the system.

1. Network Analyzer HP8753D with hardware FFT option
2. GPIB cable
3. Windows based PC with CM software loaded and GPIB card.
4. Antenna with integrated balun
5. Digi-Roller
6. Microwave coaxial cable with SMA connectors that is fabricated with minimal phase shift due to flexing.
7. Zip Drive/Disk or other removal mass storage media
8. Wood GPR cart
9. Generator/power source with power cables and strips

A.1.2 EQUIPMENT SET-UP

Setup the equipment in the following sequence.

1. Attach coaxial cable to network analyzer using SMA connector. Clean the connectors first with pressurized air.
2. Connect the network analyzer to the PC using the GPIB cable
3. Attach the Zip drive to the PC.
4. Attach the digi-roller to the Zip drive
5. Turn on digi-roller (make sure fresh batteries were used and the parallel cable connection to the zip drive is good)
6. Make sure the PC, Network Analyzer, and Zip drive are plugged into the power strip and power strip is off
7. Start generator. Plug in power source. Make sure to keep generator as far from antenna as possible to minimize interference.
8. Turn on power strip
9. Boot up PC
10. Calibrate the cable. Instructions for cable calibration are listed below.
11. Attach coaxial cable to antenna using SMA connector. Clean the connectors first with pressurized air.
12. Attach antenna to antenna arm of cart using shock cord

A.1.3 CALIBRATION OF ANTENNA CABLE

The following is the procedure for calibrating the antenna cable. This step is necessary so as to remove artifacts from the data due to the frequency-dependence impedance of the cable. The **square brackets [***key name***]** represent a HARD KEY to be pressed on the front panel of the network analyzer and the **parentheses (***button name***)** represents a SOFT KEY to be pressed that is located on the side of the screen which has a value shown on the screen corresponding to the key, Figure A.1.1.

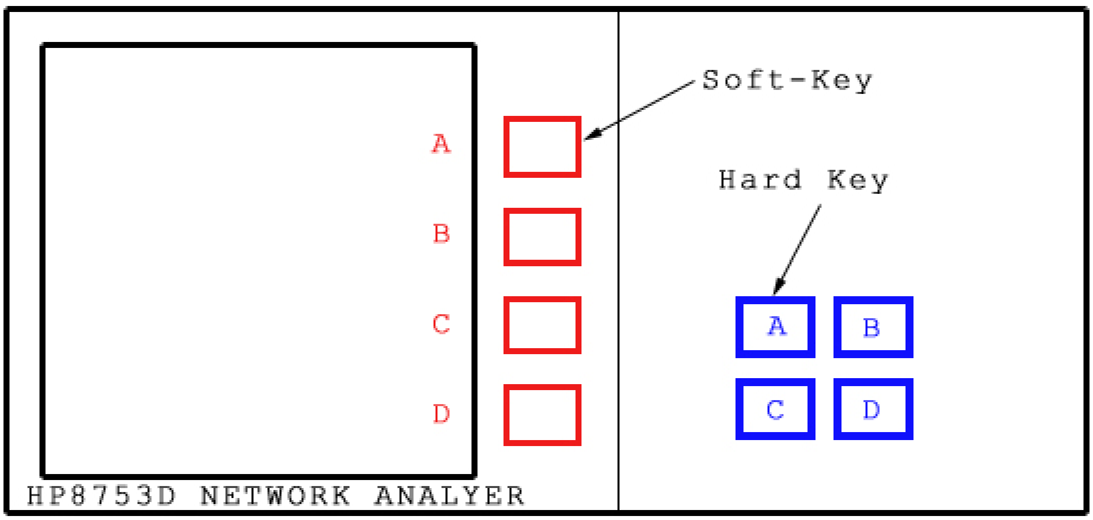

Figure A.1. *Front panel of the HP 8753D Network Analyzer*

1. Make sure system has power
2. Press [start] → [500Mhz] → [system] → (transform menu) → (transform on) → [start] → [0 ns] → [format] → (more) → (real) → [cal] → (calkit 7mm) → (3.5mm D) → (return) → (calibration menu) → (s11 1 port)
3. Use Dust Off or similar pressurized air to clean the connections. Attach the cable to "O" on the calibration tool. Press (**o**pen)
4. Do the same for "S", (**s**hort) and "L", (**l**oad)
5. Press (done) → [save recall] → (save state)
6. Calibration will have designation "reg ##" . A calibration file will be saved on the network analyzer as "reg##", where the "##" is the number of the calibration file and needs to be written down (i.e. reg09, reg13). It will be used later in the network analyzer initialization process.
7. Press (define disk save) → (format on) → (ascii) → (return) → (select disk) → (internal disk)

A.1.3 OPERATION OF CM.EXE GPR SYSTEM CONTROL SOFTWARE

The following is a description of how to operate the cm.exe GPR system control software. This software is available free of charge from the principal author (Huston) or can be downloaded from the web site www.emba.uvm.edu\~huston\gpr .

1. Double click on "Shortcut to CM".
2. Select **Measurement** from the **View** menu.
3. Go to the **Edit** menu and select **Options.**
4. Select **Network Analyzer Control Panel** tab.
5. Type "**recareg*XX*; refp 0; refv 0; scal .002;**" and click "**enter**". The "reg*XX*" in the "*recaregXX*" is the calibration file name and number that you wrote down in the cable calibration process. The network analyzer screen should change a few times if the command was entered correctly. If there is any red text on the screen, the command was inputted incorrectly. Keep in mind there is nothing wrong with typing the command over and over again. It will not effect your data collection.
6. Select **New** from the **Selections** menu. If you're taking an air-shot, make sure you aim the antenna skyward before clicking "**Yes**" at the computer's air-shot prompt. After the air-shot is complete the computer will beep. It is now safe to flip the antenna arm over so the antenna faces the ground. (Note: the air-shot is momentary data sample used to zero the antenna. The digi-roller wheel does not need to be turned during the air-shot).
7. Push the cart over you testing area. As you move the cart you will see a bitmap image of the data on the PC monitor. (Note: If the digi-roller is rolled backwards there is a possibility of an error in the data and/or a possible program crash).
8. When finshed select **Stop** from the **Selections** menu.
9. To save the data in a ASCII file in matrix form, select **Save As** from the **File** menu. CM will save the data with a ".**Sav"** file extension.
10. To save the data as a picture, select **Save a Copy** from the **File** menu. Enter the name you would like the file to have and then add a **.bmp** after the file name.